Faculdade de Engenharia da Universidade do Porto

Simulation of the Blood Flow in Aortic Aneurysms Using Advanced Discretization Meshless Techniques

Joana Marisa Lopes da Silva

Dissertation carried out under the Master's in
Biomedical Engineering

Supervisor: Prof. Jorge Américo Oliveira Pinto Belinha
Co-supervisor: Prof. Renato Manuel Natal Jorge

June, 2019

Abstract

Computational simulations of blood flow are highly motivated by the prevalence of cardiovascular diseases (CVD), which are the leading cause of death worldwide. Among the several diseases concerning the cardiovascular system, there is one particular that affects the largest artery of the human body (the aorta) and which vague symptoms can make it lethal - the aortic aneurysms. Predominant in the elderly population, the aortic aneurysms are a result of multifactorial processes, which includes variations in hemodynamics. It has been studied that aneurysms cause disturbances in the blood flow, potentiating the artery enlargement, which can lead to its rupture. Therefore, the simulation of blood flow is essential to understand the pathophysiological processes occurring in blood vessels, analyse the evolution of the diseases and assess the need for surgical intervention. Regardless of the extent of studies that exist concerning this topic, there are few that focuses on the hemodynamics in aortic aneurysms.

Within this context, this dissertation aims to simulate blood flow in two and three-dimensional aortic aneurysm models using advanced discretisation computational methods, such as meshless methods. Contrary to the Finite Element Method (FEM), meshless methods discretise the problem domain into a set of arbitrary nodes without any pre-established relation, which allows them produce more accurate results.

In this work, two meshless methods are presented, the Radial Point Interpolation Method (RPIM) and the Natural Neighbour Radial Point Interpolation Method (NNRPIM). In the end, it is expected to conclude if meshless methods are suitable for simulating blood flow.

Resumo

As simulações computacionais do fluxo sanguíneo são em grande parte motivadas pela prevalência de doenças cardiovasculares que, por sua vez, são a maior causa de morte do mundo. De entre as várias patologias relacionadas com o sistema cardiovascular, há uma em particular que afeta a maior artéria do corpo humano (a aorta) e cujos vagos sintomas a podem tornar letal – os aneurismas da aorta. Predominante na população idosa, os aneurismas da aorta resultam de um processo multifatorial, onde estão incluídas alterações na hemodinâmica. Vários estudos afirmam que os aneurismas provocam alterações no fluxo sanguíneo, potenciando a dilatação das artérias, o que pode resultar na sua rutura. Desta forma, a simulação do fluxo sanguíneo é relevante para o entendimento do processo patofisiológico dos vasos sanguíneos, da análise da evolução de doenças e na aferição da necessidade de intervenção cirúrgica. Apesar dos vários estudos que existem acerca deste tópico, poucos se focam na hemodinâmica nos aneurismas da aorta.

Nesta sequência, este projeto tem como objetivo simular o fluxo sanguíneo em modelos tridimensionais do aneurisma da aorta, utilizando métodos computacionais de discretização avançados, tais como os métodos sem malha. Ao contrário do Método dos Elementos Finitos (MEF), os métodos sem malha discretizam o domínio do problema através de um conjunto de nós arbitrariamente distribuídos e sem nenhuma relação pré-estabelecida, o que os faz produzirem resultados mais precisos.

Neste projeto, dois métodos sem malha são discutidos, o *Radial Point Interpolation Method (RPIM)* e o *Natural Neighbour Radial Point Interpolation Method (NNRPIM)*. No final, é esperado aferir se os métodos sem malha são adequados para a simulação do fluxo sanguíneo nos aneurismas da aorta.

Agradecimentos

Um genuíno obrigada ao Professor Jorge Belinha por todo o acompanhamento e dedicação infindável na realização deste projeto. Agradeço especialmente por todas as reuniões semanais, pela paciência demonstrada, mesmo quando os resultados eram menos animadores, e pelas palavras de incentivo que me ajudaram a encarar este percurso com mais entusiasmo.

Aos meus pais e à minha madrasta, por me incentivarem a dar sempre o melhor de mim e por me terem dado asas para seguir os meus sonhos, mesmo que isso signifique estar longe de casa. Aos meus avós, pelo exemplo de compromisso, justiça e determinação que me transmitiram desde pequena. Agradeço especialmente à minha avó, pela boa disposição e pelas brincadeiras que me fizeram rir, mesmo nas fases menos boas do meu percurso académico. Um profundo agradecimento à minha tia, pelas sábias palavras ao longo destes anos e por sempre me aconselhar na tomada de decisões ponderadas e conscientes.

Este percurso académico não seria a mesma coisa sem os amigos que fiz pelo caminho, e por isso expresso a minha gratidão a todos os que me acompanharam nesta jornada, especialmente à Diana e à Beatriz, por serem as melhores parceiras e confidentes que podia ter tido.

Por fim, agradeço ao meu namorado, Paulo, por toda a paciência ao longo destes anos. Obrigada por me ensinares a ser mais otimista, pelas vezes em que tiveste de ouvir-me a treinar para apresentações, pelas opiniões sinceras e por cada abraço, tanto nos meus piores momentos, como nas minhas conquistas.

Joana Lopes da Silva

Institutional Acknowledgments

The author truly acknowledges the work conditions provided by the Applied Mechanics Division (SMAp) of the department of mechanical engineering (DEMec) of Faculty of Engineering of the University of Porto (FEUP), and by the MIT-Portugal project "MIT-EXPL/ISF/0084/2017", funded by Massachusetts Institute of Technology (USA) and "Ministério da Ciência, Tecnologia e Ensino Superior - Fundação para a Ciência e a Tecnologia" (Portugal).

Additionally, the authors gratefully acknowledge the funding of Project NORTE-01-0145-FEDER-000022 - SciTech - Science and Technology for Competitive and Sustainable Industries, co-financed by Programa Operacional Regional do Norte (NORTE2020), through Fundo Europeu de Desenvolvimento Regional (FEDER).

Furthermore, the author acknowledges the inter-institutional collaboration with clinical partners of the Vascular Surgery department of "Hospital de São João do Porto" – Dr. Isabel B. Vilaça and Dr. João Rocha Neves.

Finally, the author acknowledges the synergetic collaboration with the collaborators of "Computational Mechanics Research Laboratory CMech-Lab" (ISEP/FEUP/INEGI), and its director, Prof. Dr. Jorge Belinha, and its senior advisors, Prof. Dr. Renato Natal Jorge and Prof. Dr. Lúcia Dinis.

Joana Lopes da Silva

"It's the possibility of having a dream come true that makes life interesting."
Paulo Coelho in *The Alchemist*

Contents

List of Figures

List of Tables

List of Abbreviations and Symbols

List of abbreviations

2D	Two-dimensional
3D	Three-dimensional
AAA	Abdominal Aortic Aneurysm
CFD	Computational Fluid Dynamics
CT	Computed Tomography
CVD	Cardiovascular Diseases
DEM	Diffuse Element Method
EFGM	Element-free Galerkin Method
EVAR	Endovascular Repair
FDM	Finite Difference Method
FEM	Finite Element Method
FSI	Fluid-structure Interaction
FVM	Finite Volume Method
ILT	Intraluminal Thrombus
MFEM	Meshless Finite Element Method
MLS	Moving Least-Squares
MRA	Magnetic Resonance Angiography
MRI	Magnetic Resonance Imaging
NEM	Natural Element Method
NNRPIM	Natural Neighbour Radial Point Interpolation Method
OR	Open Repair
PDEs	Partial Differential Equations

PIM	Point Interpolation Method
SPH	Smoothed-particle Hydrodynamics
RBF	Radial Basis Function
ROI	Region of Interest
RPIM	Radial Point Interpolation Method
RKEM	Reproducing Kernel Element Method
WSS	Wall Shear Stress

Symbols

$\dot{\gamma}$	shear rate
$\dot{\gamma}_c$	characteristic shear rate
λ	characteristic time constant
μ	fluid viscosity
μ_c	fluid viscosity
μ_p	plasma viscosity
μ_0	zero-shear-rate viscosity
μ_∞	infinite-shear-rate viscosity
τ	shear stress
τ_c	characteristic shear stress
τ_0	yield-stress
$\emptyset$	volume concentration
A	Carreau-Yasuda index
K	flow consistency index
k_0	maximum volume fraction for zero shear rate
k_∞	maximum volume fraction for infinite shear rate
M	Cross model index
N	Power-law index
α	Womersley number
ω	fundamental frequency
ρ	fluid density
d	blood vessel diameter
L	distance between two points
Q	flow rate
E	Young's modulus
υ	Poisson ratio

Chapter 1

Introduction

Computational simulations of blood flow are highly motivated by the prevalence of cardiovascular diseases (CVD), which are the leading cause of death worldwide. These diseases were the cause of 17.3 million deaths in 2008 and, by 2030, this number is estimated to rise up to 23.6 million [1]. The most predominant pathologies included in the CVD are atherosclerosis (accumulation of fatty constituents), stenosis (vessel compression), thrombosis (clot formation), hypertension (high blood pressure) and aneurysms (vessel dilation).

Despite the high prevalence of CVD in all population, there is one silent pathology that develops, grows and, in a rupture's event, has a death probability of 80% - the aortic aneurysm [2]. Predominant in the elderly population, the aortic aneurysms are a result of several factors, such as ageing, smoking, sedentarism, gender (male), genetics and hemodynamics. Alterations in hemodynamics inside the blood vessel have been proven to potentiate not only thrombus deposition, but also the enlargement of the vessel, leading to its rupture [3], [4]. Therefore, the study of blood flow inside healthy and diseased vessels is of major importance in order to understand the need for surgical intervention.

Thus, aneurysms have a substantial influence on cost in the healthcare sector. It is crucial to understand the fundaments regarding their pathophysiology and treatment. In Portugal, between 2001 and 2013, it was spent an average of 9.955,70€ to 11.404,00€ per patient on aortic aneurysm's surgery, depending on the adopted procedure [5]. In the USA, the scenario is identical, with costs ranging between 12.342 and 21.250 US dollars, which correspond to, approximately, 10.830€ and 18.647€, respectively [6].

The three-dimensional imaging techniques and the refinement of numerical methods have enabled a range of new applications in the study of blood vessels. Additionally, the emergence of more powerful computers has permitted faster outcomes, allowing the scientific community to obtain more responses to the disease's characterisation, evolution and prediction.

In blood flow studies, it is established that zones with flow turbulence can lead to disease scenarios, like aneurysms. Furthermore, blood is simulated according to a rheological model, that varies whether it is considered a Newtonian or a non-Newtonian fluid.

Within this context, this dissertation aims to simulate blood flow in aortic aneurysms with advanced discretisation computational techniques and demonstrate that meshless methods are an efficient alternative numerical technique.

1.1 Motivation

Studies on the behaviour of blood flow inside blood vessels have been conducted since the end of the 1960s [7]. In the specific case of simulations in aortic aneurysms, the first publication refers to 1996 [8], where the problem was discretised using one of the most used numerical methods, the finite element method (FEM). Nevertheless, there are other numerical methods that have been successfully applied in blood flow problems – the meshless methods.

Despite the applications and improvements on numerical methods applied to blood flow in aortic aneurysms, since its first publication, there are still many opportunities for the research community.

In a research performed on *Scopus* database (www.scopus.com) concerning the publications on blood flow in aortic aneurysms (see Figure 1. 1), it is verified that FEM and meshless methods have not been widely used. It is also noted that, until this date and based on what was found in the database research, meshless methods have never been applied for simulating blood in aortic aneurysms.

As such, another motivation of this project is to comprehend the performance of these methods in the numerical simulation of blood in aortic aneurysms, enhancing the state-of-the-art of meshless methods.

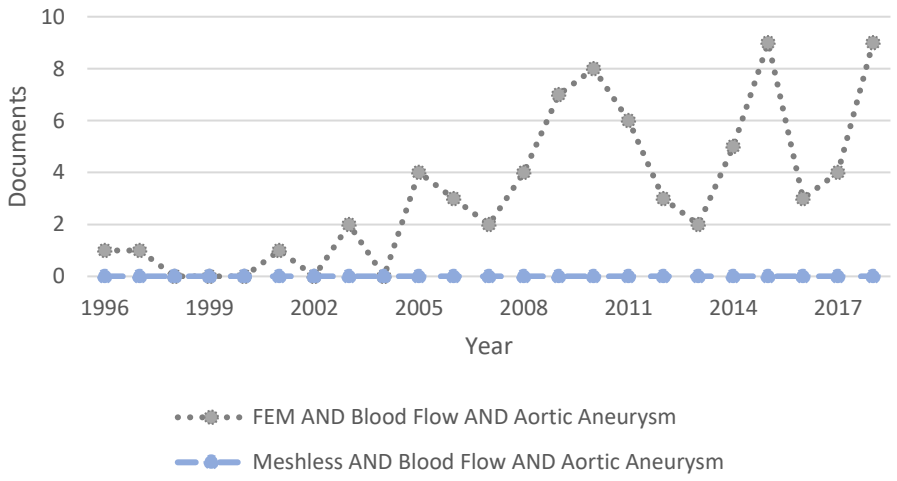

Figure 1. 1 – Number of documents published throughout the years, in the keywords indicated. The data was collected from *Scopus* database (www.scopus.com).

1.2 Objectives

The main objective of this thesis is to study the blood flow in two and three-dimensional geometrical models with and without aneurysm, using advanced discretization meshless techniques, and understand how the aneurysms influence blood dynamics.

To accomplish these goals, secondary objectives were defined:

- Perform a fluid flow analysis in a two and three-dimensional healthy branched aorta and comprehend how curvatures influence the blood flow patterns in those regions;
- Calibrate the parameters of simulation for RPIM and NNRPIM, both in 2D and 3D models;
- Study the increase of the diameter in a fusiform aortic aneurysm, in two and three-dimensions, and evaluate the alterations of the blood flow with the modifications of the blood vessel;
- Understand the influence of regular and irregular meshes in fluid flow numerical results;
- Analyse the blood flow of patient-specific geometries and compare the results of the numerical methods with the clinical values;
- For all the previous steps, compare the results between FEM, RPIM and NNRPIM and conclude if meshless methods are an efficient alternative approach for fluid flow problems.

Furthermore, this thesis aims to perform a detailed review in the following subjects:

- Cardiovascular system (cardiac cycle);
- Aorta artery (anatomy, mechanical properties and diseases);
- Blood flow (physiology and mathematical models to describe it);
- Aortic aneurysms (pathophysiology and treatments);
- Discrete numerical techniques (mathematical formulation and state-of-the-art).

1.3 Document Structure

This dissertation is composed of ten chapters, as follows. In the first chapter, **Introduction**, a brief introduction on the subject is given, as well as the motivational factors for the accomplishment of this thesis. Furthermore, the goals of this work are stated.

In Chapter 2, **Cardiovascular System**, a biological description of the human circulation and its components are presented. Also, it is delivered a description of the cardiac cycle and an introduction to a specific blood vessel – the aorta.

In Chapter 3, **Blood Flow**, it is explained the blood constitution and detailed the features inherent to hemorheology.

In Chapter 4,**Aortic Aneurysms**, a detailed explanation of the mechanisms that lead to aortic aneurysm's formation is shown, as well as a correlation between hemodynamics and disease evolution. In addition, it is presented the most common treatment techniques and the economic resources involved.

In Chapter 5, **Mathematical and Numerical Methods**, the governing equations and mathematical models to simulate blood are presented. Then, a brief exposure of the numerical methods formulation is given.

In Chapter 6, **Fluid Mechanics**, the fundamentals of flow formulation and the fluid's discretisation procedure is explained.

In Chapter 7, **Numerical Methods in Hemodynamics**, it is described the first techniques to access blood flow features, the evolution of numerical methods in the fluid mechanics field

and, particularly, the principal applications that have been developed in the study of hemodynamics in aortic aneurysms.

In Chapter 8, **Preliminary Work**, the software used in this thesis is presented. Then, it is performed the static fluid flow simulation in simple and aneurysmal 2D and 3D geometries, which comprises a convergence analysis and the calibration of the parameters of simulation.

In Chapter 9, **Abdominal Aortic Aneurysms – Clinical Cases**, it is studied the blood flow in 2D and 3D realistic aortic aneurysm's geometries. The results are then compared with the ones from the clinics and also between the mesh-dependent and meshless methods.

In Chapter 10, **Conclusions and Future Work**, the main conclusions of this thesis are mentioned, as well as the limitations encountered along the development of this project. Furthermore, prospections regarding the future works to be developed are presented and discussed.

Chapter 2

Cardiovascular System

This chapter begins with a brief contextualization of blood circulation's history. Formerly a broad overview of the constituents of the cardiovascular system is presented, along with the description of the cardiac cycle. Then, it is emphasised a specific artery – the aorta -, including the discussion of its anatomy, structure, biomechanical properties and pathologies. The knowledge of the normal aorta's features will be fundamental for the posterior understanding of aneurysm evolution, which is the pathology under study in the dissertation.

2.1 General Introduction

The circulation of the blood has been documented for thousands of years: between 384 and 322 BC, Aristotle, an early scientist and philosopher that lived in Greece, wrote that the heart was the focus of blood vessels, however, he did not distinguish between veins and arteries; further, Paxagoras, a physician also from Greece, was the first to recognize the difference between veins and arteries and to reference on the pulse; in 1628 it was published the first document concerning that blood is pumped from the heart. This study was authored by William Harvey, court physician to King James I and King Charles I, from England [9].

Since ancient times that the circulatory system has intrigued the scientific community to find responses to how blood travels in the human body. Nowadays, questions are still asked, and answers have been sought using new tools, such as computational methods.

2.2 Constitution and Functions

The cardiovascular system is a closed loop of blood distribution, comprising three main subsystems: the heart, the systemic system, and the pulmonary system, as it is represented in Figure 2. 1. As a low-pressure system, the pulmonary circulation is responsible for oxygenating the blood via lungs, while in systemic circulation the oxygenated blood is pumped in the aorta with high pressure and delivered to all parts of the body [10]. The most significant function of circulation is to provide oxygen and nutrients to cells and tissues and to remove carbon dioxide

and additional waste from them. Besides, it also regulates body temperature by transferring extra temperature to body parts that dissipate it into the environment [9], [11].

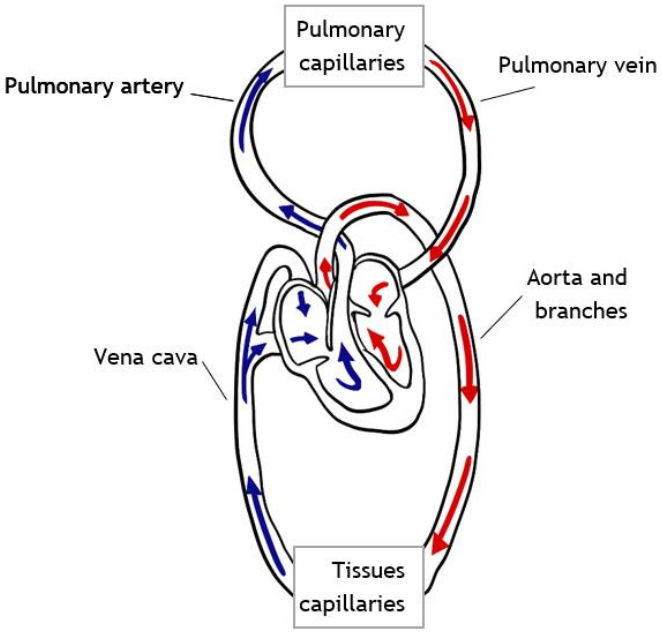

Figure 2. 1 - Representation of pulmonary and systemic circulation. The red colour represents the arterial blood and the blue colour represents the venous blood.

The heart is the muscle responsible for inflating the blood through the complex network of the cardiovascular system, and it is divided into four cavities – two ventricles and two atria, as seen in Figure 2. 2. Both systemic and pulmonary circulations are composed by a network of five types of blood vessels: veins, venules, arteries, arterioles and capillaries, each one with a specific function and, consequently, unique properties and structure. The larger blood vessels are the arteries, which deliver blood from the heart to the body, whereas the veins are responsible for bringing the blood back to the heart. The capillaries, the smallest blood vessels, exchange oxygen and nutrients between blood and tissues [12].

2.3 The Cardiac Cycle

In normal conditions, a cardiac cycle, also known as pulse, takes about 1s and it is divided into two phases: systole and diastole. The first one is a contraction period where the blood ejection takes place, while the last one corresponds to the cardiac muscle relaxation, that lasts, approximately, 2/3 of the cardiac period. In Figure 2. 2 it is described the three main phases of the cardiac cycle.

Blood is pumped at a rate of 5,2 litres per minute and its pressure changes in the heart during the cardiac cycle [13]. The pressure that is generated by the contraction of ventricles and the resistance of the arterial system reaches 120 mmHg in the aorta during systole and 80 mmHg during diastole (in normal conditions), decreasing as blood travels into the capillaries [14]. As it is seen in Figure 2. 3, at the end of the atrial systole, the ventricular pressure rises above the atrial pressure, and the mitral valve closes. At that point, occurs blood ejection to the ascending aorta. When the pressure difference between aorta and ventricle is reversed, the aortic valve closes, and the diastole phase begins. With the analysis of the cardiac cycle,

it is possible to understand that blood pressure and the velocity of blood can be related, being one of the most complex concepts in the study of cardiovascular fluid dynamics [15].

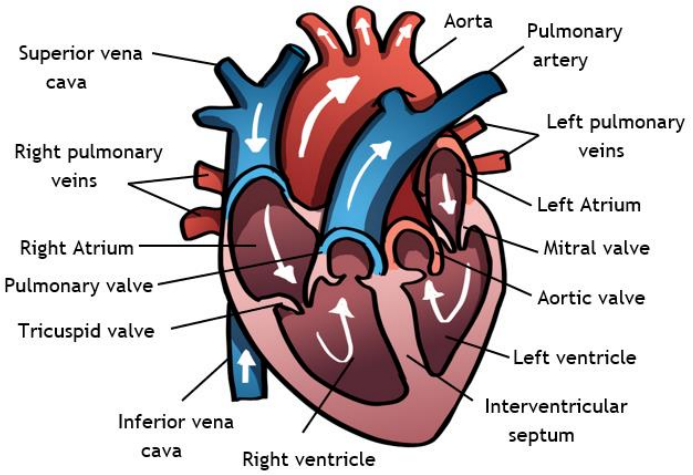

1. Cardiac diastole: all cavities are relaxed and blood flows into the atria via pulmonary veins, superior and inferior vena cava.

2. Atrial systole, ventricular diastole: atria contract, pushing blood into the ventricles.

3. Atrial diastole, ventricular systole: the ventricles contract, pumping blood out of the heart via pulmonary artery (pulmonary system) and aorta (systemic system).

Figure 2. 2 - Representation of the heart anatomy and description of the cardiac cycle.

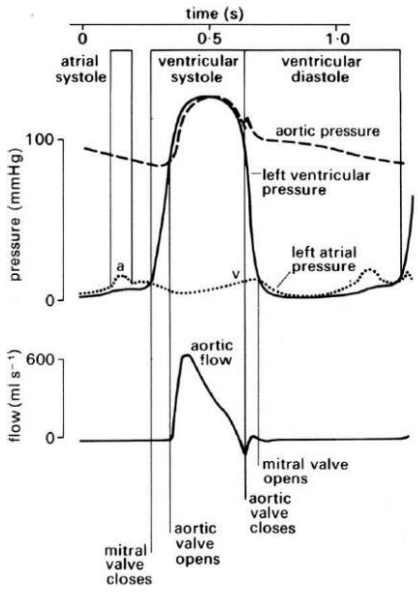

Figure 2. 3 - Correlation between blood flow velocity and pressure in the heart during a cardiac cycle [7].

Despite the several types of blood vessels that exist in the human body, in this dissertation, the focus is directed to the study of blood flow in a specific artery – the aorta -, more precisely, an aortic aneurysm. Hence, it is essential to first require a detailed knowledge of the healthy wall vessel in order to comprehend the mechanisms that lead to the aneurysm formation.

2.4 The Aorta

In this subchapter, it is briefly described the aorta's anatomy, the structure and functions of the arterial wall and its mechanical properties. Further, some of the most common pathologies that occur in this blood vessel are presented, including an aneurysm.

2.4.1 Anatomy

The aorta is the largest artery in the human body, starting at the top of the left ventricle and extending down through the torso to the iliac bifurcation, where it splits into the iliac arteries. The dimensions of blood vessels vary according to its distance from the heart [12], [15]. The Table 2. 1 presents typical dimensions and properties of human vessels. Among different blood vessels, it is visible the existent variations on the vessels': diameter, wall thickness, blood volume and pressure. Notice that aorta has the highest values in blood pressure and dimensions.

Table 2. 1 - Dimensions and properties of the human vessels (data obtained from [12]).

Vessel	*Lumen's diameter (mm)*	*Wall thickness*	*Blood volume (%)*	*Mean pressure (kPa)*
Aorta	25	2	2	12.5
Large arteries	1-10	1	5	12
Small arteries	0-5-1	1	5	12
Capillary	0.006-0.01	0.001	5	3

The aorta can be divided into three parts: the ascending aorta, the aortic arch and the descending aorta, that includes both thoracic and abdominal aorta, as shown in Figure 2. 4. In adults, the ascending aorta is, approximately, 5 cm length and 2.5 cm diameter, continuing to the aortic arch, curving 180 degrees laterally left and slightly posteriorly. The arch is typically 4-5 cm in length and has a smaller diameter comparing to the ascending aorta. The arterial branches from the aorta arch are responsible for delivering oxygenated blood to the neck, head and upper limbs. The descending aorta is, approximately, 35 cm length: 20 cm in the thoracic segment and 15 cm in the abdominal portion. The diameter is nearly 2.5 cm, getting smaller along the descending blood vessel [16], [17]. The majority of internal organs are supplied by the abdominal aorta via numerous branch arteries, therefore, the well-functioning of this segment is crucial for maintaining organ functions.

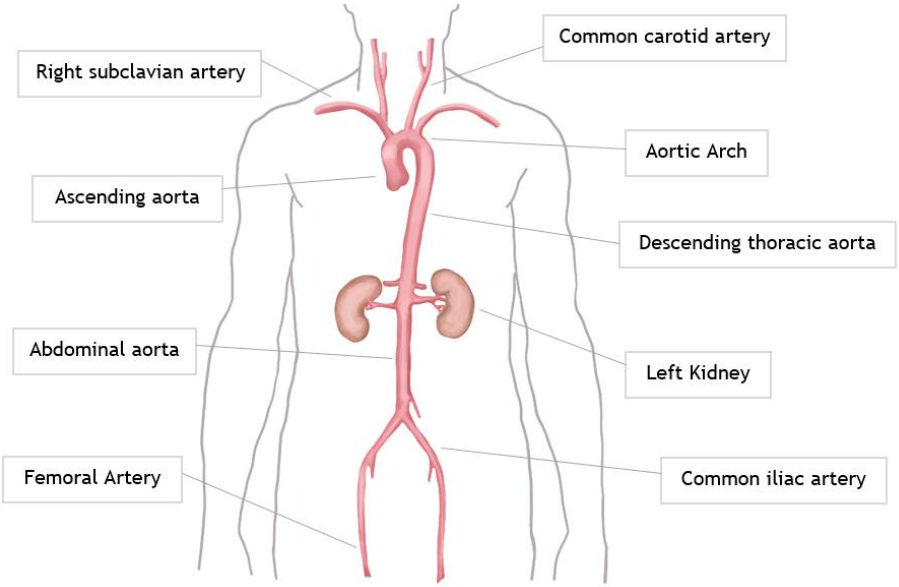

Figure 2. 4 – Front view of the complete aorta.

2.4.2 Structure and functions of the arterial tissue

According to the structure and size of the arteries, they can be classified into three types: (1) **elastic arteries**, such as the aorta, that have a larger diameter and higher number of elastic fibres; (2) **muscular arteries**, that are smaller in diameter, but larger than arterioles and have more muscle than elastic tissue; (3) **arterioles**, that are the smallest and have almost no connective tissue and a few layers of smooth muscle tissue [9].

The normal arterial wall is composed of three layers - tunica intima, tunica media and tunica adventitia, as shown in Figure 2. 5. The inside of the vessels is called lumen and is the region where blood flows. The lumen is lined with the endothelium – a slick layer of epithelium cells in close contact - that forms the interface between the vessel wall and the blood [9], [18].

The innermost layer of the artery wall, the intima, is a monolayer of endothelial cells attached to a basement membrane constituted of laminin and type IV collagen, and it is the layer that makes contact with blood. The middle layer is the thickest layer, and it is composed of smooth muscle fibres embedded in an extracellular matrix consisting of elastin, proteoglycans and multiple types of collagen. This layer does not exist in capillaries. The outermost layer, the tunica adventitia, consist of fibroblasts surrounded by type I collagen and elastin and serves as a protective case that thwarts over-distension of the media layer [19]. It is important to notice that, the closer arteries are to the heart, the more elastin they have, and the farther away, the more smooth muscle.

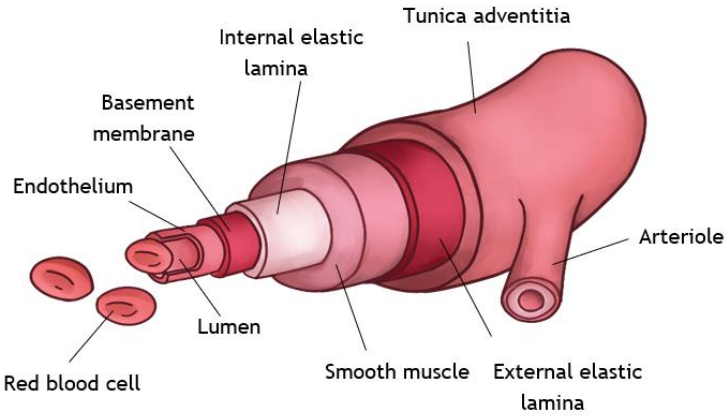

Figure 2. 5 - Representation of a muscular artery. The tunica intima is composed by the endothelium, the basement membrane and the internal elastic lamina. The tunica media comprehends the smooth muscle and the external elastic lamina.

The endothelium, contrary to what was thought, is a biologically active single layer of cells, that plays an essential role in the blood flow mechanics, leukocyte adhesion and blood clotting and it is responsible for the regulation of the wall stiffness. Besides, it also secrets vasoactive substances that are responsible for the contraction and relaxation of vascular smooth muscle and modify transport of lipids into the wall which has a major role in atherosclerosis. Many functions that are performed by the endothelium are triggered by the shear stress induced by blood flow, whereby the study of hemodynamic is important in the comprehension of many vascular disorders [9], [11].

Smooth muscle is mainly responsible for contraction or expansion of a blood vessel, allowing a change in blood flow. The hypertrophy, hyperplasia, apoptosis and migration of smooth muscle play an essential role in pathologies such as aneurysms, atherosclerosis and hypertension. Elastic fibres, on its turn, support and allow recoil of an expanded blood vessel when pressure is removed [19].

2.4.3 Mechanical properties

Despite in this work the structural behaviour of the arterial wall is not considered (the arterial wall will be considered as a rigid body, i.e., as the essential boundary condition), in order to complement the arterial wall information, in this subsection a brief description regarding its mechanical properties and commonly used constitutive models is presented.

The first reports of the study of the blood vessel's mechanical behaviour date back to the end of the 19th century [20]. The primary notable characteristic of an unloaded blood vessel is the presence of residual stress, circumferentially and axially. In further studies, it was stated that internal pressure equilibrates the compression applied in the luminal part, and the tension, that exists in the external part of the vessel. Secondly, when the vascular tissue is under a load-free configuration, it is considered anisotropic due to the different behaviour observed in circumferential and axial directions. Since the vascular wall has a high content of water – 70 to 80 per cent – it is taken as incompressible, despite the presence of some exceptions in cases of large deformations [20]. Other studies have reported that soft tissues have a viscoelastic response, discovered by the stress relaxation they present due to hysteresis under cyclic loads and when they are subjected to sustained deformations. The vessel wall is considered

hyperelastic, however, since it behaves differently in loading and unloading, it can be regarded as pseudoelastic [15], [20].

Despite being anisotropic and hyperelastic, for simulations purposes and to better understand its mechanical behaviour, the vessel wall is frequently considered isotropic and homogeneous (the material properties are identical in all directions), with constant wall thickness. Examples of the implementation of these assumptions are the studies on computed fluid dynamics (CFD) performed by Scotti et al. [21] and Ene et al. [22] concerning aortic aneurysms.

It is important to notice that the artery mechanics does not depend only on its geometry, but also on its material properties. In this sequence, Hooke's law for uniaxial loading relates stress to strain and, for a one-dimensional model, can be described as in Equation (2. 1) [9].

$$\sigma = E\varepsilon \tag{2. 1}$$

Where σ is the stress, E is de modulus of elasticity and ε is the strain.

In a typical linearly elastic material, the stress-strain curve is shown in Figure 2. 6 (a), being the slope the modulus of elasticity (E). Since arteries are not linearly elastic, the stress-strain curve is defined as in Figure 2. 6 (b), where it is observed that the elastic modulus is not constant and varies with stress and strain: as stress increases, the material becomes stiffer and resists strain. Another aspect is that smooth muscle can contract or expand to resist strain. Since the modulus of elasticity of arterial wall is not continuous, Hooke's law is no longer applicable.

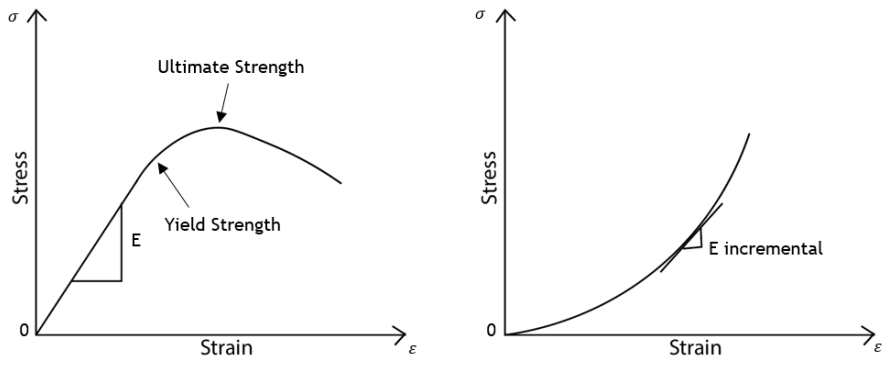

Figure 2. 6 – (a) Stress-strain curve for a material with a linear elastic behaviour below the yield stress; (b) Artery's stress-strain curve (hyperelastic behaviour).

The walls of arteries and veins comprise 70% water and the rest consist of a mesh of fibres that have elastic properties. The three types of fibres - elastin, collagen and smooth muscle – determine the elastic properties of the vessel walls. The Young's modulus of each fibre is summarised in Table 2. 2 [15]. Depending on the proximity of the artery to the heart, the structure of the vessel wall changes and, consequently, so does its mechanical properties. For modelling purposes, the Young's Modulus of the aorta wall is often considered 2.0 – 9.0 MPa and the Poisson's coefficient is 0.45 [23], [24].

Table 2. 2 – Young's Modulus for each type of artery fibre.

Type of fibre	Young's Modulus
Elastin	$3 \times 10^6 MPa$
Collagen	$10^8 MPa$
Smooth muscle	$1 \times 10^5 MPa \ - \ 2 \times 10^6 MPa$

The mechanical properties of the vessel's wall and the influence of blood flow in its remodelling and disease formation is an important scope of investigation. However, in this dissertation the solid mechanics concerning the study of the aneurysmal wall will not be deepened. For more information and better comprehension of this topic, it can be consulted the books of Caro et al. [15] and Yuan C. Fung [25].

2.4.4 Common pathologies of the aorta

Inflammation, atherosclerosis and aneurysms are the three main diseases that occur in the aorta [18]:

Inflammation – aortitis is an inflammatory process of the aorta that cause thickening of the vessel layers and, in its turn, can potentiate aneurysm formation;

Atherosclerosis - large calibre arteries are prone to develop atherosclerosis, that forms at areas of branch points, bifurcations or regions of turbulent flow. In the aorta artery, the arch and the infrarenal part are the two zones that generally contain plaque;

Aneurysms – aneurysm is a dilation of 50% of the healthy blood vessel's diameter and affect all three layers.

In this work, it will be studied the blood flow in aortic aneurysms, so this pathology is explained further in Chapter 4. Before understanding the aneurysm's formation, it is necessary to comprehend how blood flow behaves inside the vessels since it is known to potentiate diseases in specific zones. In this sequence, the next chapter will approach blood flow in detail.

Chapter 3

Blood Flow

Hemodynamics has been shown to play a crucial role in the vessel wall, leading to its remodelling, weakness and, posteriorly, the possible development of arterial disease, such as atherosclerosis and aneurysms. Therefore, it is important to understand blood's properties and its behaviour in the human body in order to comprehend the pathophysiological process that leads to diseases [26], [27]

Thus, this chapter starts with a brief description of the blood's composition, followed by the explanation of the hemorheology and then, more specifically, it is described the dynamic properties that characterise blood flow.

3.1 Blood Constitution

Blood is a heterogeneous multi-phase suspension of formed elements (erythrocytes, leukocytes and platelets) in a liquid plasma and comprises 6% to 8% of the body weight of normal and healthy individuals [28]. In the approximately 5 L of blood volume that exists in an adult, 55% to 60% is plasma, and the remaining fraction is cellular, as it can be seen in Table 3. 1 [11], [29].

Table 3. 1 – Blood components.

Cellular Component (~40%)	**Cell Type**	**Cell Concentration**	**Characteristic Shape/ Dimensions**
	Red Blood Cell (Erythrocyte ~ 99.7%)	$\sim 5{,}000{,}000/\mu L$	Biconcave Discs $8\ \mu m$ Diameter $2.5\ \mu m$ Thickness
	White Blood Cell (Leukocyte ~ 0.2%)	$\sim 7{,}500/\mu L$	Spherical $20-100\ \mu m$ Diameter
	Platelet (Thrombocyte ~ 0.1%)	$\sim 250{,}000/\mu L$	Ellipsoid $4\ \mu m$ Long Axis $1.5\ \mu m$ Short Axis
Plasma Component (~60%)	**Composition**	**Major Contributors**	**Function**
	Water (~ 92%)	H_2O	Reduce Viscosity

Plasma Proteins (~ 7%)	Albumin (~ 60%)	Osmotic Pressure
	Globulins (~ 35%)	Immune Function
	Fibrinogen (~ 3%)	Clotting
	Others (~ 2%)	Enzymes/ Hormones
Other Solutes (~ 1%)	Electrolytes	Homeostasis
	Nutrients	Cellular Energy
	Wastes	Excretion

Red blood cells, or erythrocytes, are the most numerous cells in blood and are responsible for transporting oxygen and carbon dioxide. The transport of oxygen is performed by haemoglobin, a protein of the red blood cells that also maintains the blood's pH between 7,35 and 7,45. White blood cells, or leukocytes, represent a reduced amount of blood cells (less than 1%). Despite their minor proportion, they are involved in the immune responses of the body by producing antibodies, identifying and phagocyting external substances, and for these reasons, they are crucial for protecting the human organism. There are five types of leukocytes – neutrophils, eosinophils, basophils, lymphocytes and monocytes -, each one with its own function [12], [29].

Platelets, or thrombocytes, are the main cells for haemostasis. They control the conversion of the protein fibrinogen to fibrin, that is a relevant structural element in a blood clot. Local hemodynamic loads influence the platelets stimulation, aggregation and accumulation, which are significant for vessel healing/ haemostasis and atypical events that can lead to thrombosis. Plasma is the amber-coloured liquid, majorly composed of water, in which blood elements are suspended. It also contains electrolytes, sugars, hormones cholesterol, urea, phospholipids and proteins. The main plasma protein is albumin, which accounts for over 60% of the total protein concentration and its principal function is to maintain the blood's osmotic pressure. With an account of, approximately, 35% of the plasma protein, globulin play an important role in immunology. The about nearly 3% remaining protein is the fibrinogen, a precursor to fibrin and responsible for clot formation. The water of plasma allows the blood flow to occur, by reducing the viscosity of the blood's cellular component [11], [29]. Therefore, plasma plays a fundamental role in the function of the human body.

3.2 Blood Rheology

Rheology is the study of flow and physical properties of materials. Hence, hemorheology is the science that studies the flow properties of blood in living organisms [12], [28]. The rheological properties of blood are determined by its components and their interaction with each other, as well as with the surrounding blood vessels. The external factors, such as temperature and the intake of medication, fluids and nutrients also affects the rheological properties of blood, although it is not substantial [28].

The most well-studied property of the blood is **viscosity**, that is mainly determined by the deformation, aggregation, orientation and volume percentage (haematocrit level) of red blood

cells, which are the cells with higher concentration in blood [30]. The relation between haematocrit level and blood viscosity is represented in Figure 3. 1 and demonstrates that the more erythrocyte's volume percentage, the more viscous is the blood.

Also, blood viscosity is dependent on the thickness of plasma, on the total blood cell distribution and on the mechanical properties of blood cells. Despite these fluid properties, other mechanical factors alter the viscosity, such as the forces exerted in the fluid, boundary conditions of the vessel geometry and fluid motion [28], [29].

Another intrinsic property of flow is density, ρ (kg/m^3), that represents the mass of a fluid per unit of volume. For blood, the density is, generally, 1060 kg/m^3 at 20ºC [13].

According to the previous characteristics, the blood flow can be characterised in non-Newtonian or Newtonian, steady or pulsatile, and laminar or turbulent.

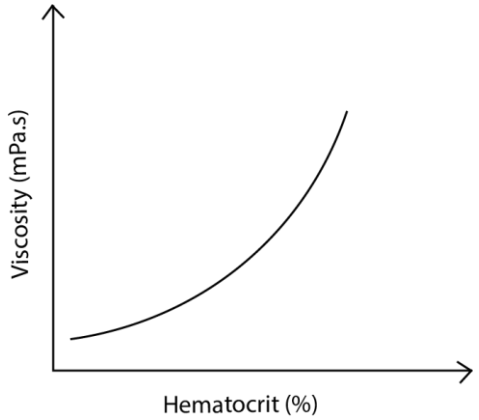

Figure 3. 1 - Influence of the haematocrit percentage in blood viscosity.

3.2.1 Non-Newtonian versus Newtonian

As mentioned before, the erythrocytes play a fundamental role in blood properties. When these cells are dispersed, the blood exhibit a Newtonian inelastic behaviour, which means that the viscosity is constant during flow and have a linear relationship with shear stress, as represented in the following equation [9]:

$$\tau = \mu\dot{\gamma} \tag{3. 1}$$

Where $\dot{\gamma}$ is the strain rate, τ is the shear stress, and μ is the viscosity.

The viscosity of blood along the arterial wall is not constant, leading to alterations in the shear stress. Also, blood properties such as **viscoelasticity**, **deformation rate**, **yield stress** and **thixotropy** resemble non-Newtonian fluids, which means that viscosity changes throughout the flow, being defined as a function of the shear rate, i.e. $\mu(\dot{\gamma})$ [12].

Viscoelasticity

The viscoelastic property of blood results from the red blood cells, which present elastic deformability and have the capacity to aggregate, forming rouleaux (three-dimensional structures). These red blood clusters are mostly formed under low shear rates and magnified by the pulsatile behaviour of blood flow [28].

Yield stress

Yield stress results from the formation of the previously mentioned three-dimensional red blood cell structures at low shear rates. It is also correlated with the amount of fibrinogen protein in plasma. Thus, it can be stated that yield stress contributes to blood clotting [28].

Thixotropy

Thixotropy is a blood's property in which the viscosity decreases under constant shear stress, which means that the viscosity is time-dependent [29].

Although blood is considered, in general, a non-Newtonian fluid, some particularities are observed in different blood vessels: in large calibre arteries, where shear rate is mostly high, blood is assumed to have constant viscosity, in other words, it is considered a Newtonian fluid [31]. This behaviour is explained by the fact that the red blood cells deform and align with the flow field, decreasing the viscosity. In contrast, small vessels have a very low shear rate, exhibiting non-Newtonian behaviour. In these cases, the viscosity increases due to the clustering of red blood cells [32]. In disease scenarios, like aneurysms, where there are slow recirculation zones, sometimes blood is considered a non-Newtonian fluid [28], [33]. Thus, it is important to state that the decreasing of viscosity with shear rate is a significant property of blood, named **shear-thinning behaviour**.

Although the evidence of blood's non-Newtonian behaviour, in large arteries, such the aorta, the shear rate is high (over $100s^{-1}$), which means that it is generally accepted the simulation of blood with Newtonian models (see Figure 3. 2). On the other hand, when the shear rate is lower than $100s^{-1}$, this assumption is not valid [34]. This is the case of capillaries, small arteries, stenosis and aneurysms. In these circumstances, slow flow can occur, which is better represented by non-Newtonian models.

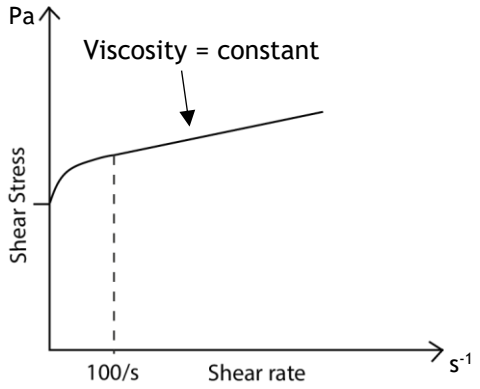

Figure 3. 2 - Shear stress as function of shear rate, for blood.

Another important concept about blood is that when it is assumed as a non-Newtonian fluid, blood can be represented as a combination of a Bingham plastic fluid and a pseudoplastic fluid (see Figure 3. 3). This means that, for blood starts to flow, it needs to surpass an initial yield stress, and as the shear rate rises, the viscosity decreases.

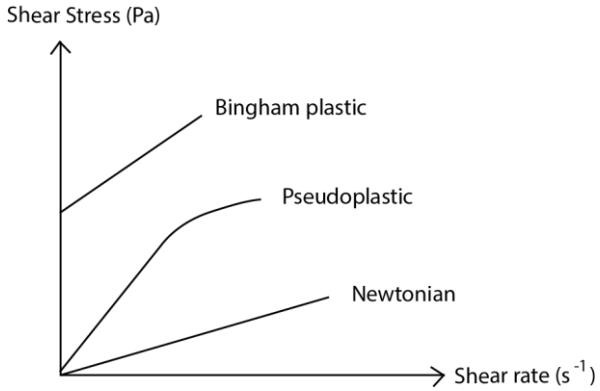

Figure 3. 3 - Shear stress as a function of shear rate, for different fluids.

3.2.2 Static versus Pulsatile

Flow in the body vasculature is complex since it consists of a pulsatile and non-Newtonian fluid in a domain with flexible walls (variable geometry). In most of the vessel tree, blood flow has a pulsatile behaviour that is caused by the cyclic pumping of the heart. These types of flow are governed by the Womersley solution [35], given by the expression:

$$\alpha = r\sqrt{\frac{\omega\rho}{\mu}} \tag{3. 2}$$

Where r is the vessel radius, ω is the fundamental frequency (typically the heart rate) and ρ is the fluid density.

The flow rate at the inlet periodically differs with time, so velocity in the vessel assumes only the axial component, when sufficiently distant from the inlet. Consequently, Womersley velocity outline is not parabolic. Furthermore, although the flow's total volume be always positive, there is a reversed flow near the wall, that function as a boundary layer, and occurs when the viscous traction forces are contrary to the dominant flow course, creating retrogressive flows [27], [35].

For low Womersley number ($\alpha < 1$), viscous forces dominate and flow in a cylindrical geometry (that can be approximated to the vessel geometry) will be characterised by a parabolic profile. In this case, the blood flow is considered steady, which means that it is governed by the Poiseuille solution. Despite the oscillating biological behaviour of blood flow, it is often regarded as steady, with a direction parallel to the vessel wall [15], [29].

In Figure 3. 4 it is schematized the Poiseuille flow in a straight tube with a constant cross section. The inlet velocity begins with a flat profile and then, when sufficiently distanced from the entrance region, develops to a parabolic profile. Once the velocity profile no longer changes along the extension of the tube, it progressively reduces to zero at the wall and reaches the maximum along the axis. That region of the tube is known as the region of fully developed flow, where the pressure gradient, $\Delta p/L$ (pressure difference between two points distanced L apart), is constant and increases linearly with the flow rate Q [9], [15]. The law that describes a steady flow through the tube is given by:

$$\Delta p = 128\,\frac{\mu L Q}{\pi D^4} \tag{3. 3}$$

Where μ is the fluid viscosity and D is the diameter of the tube.

Given the viscous property of blood, the velocity is not uniform, assuming the parabolic profile [29]. The values of the velocities in several segments of the aorta is described in Table 3. 2.

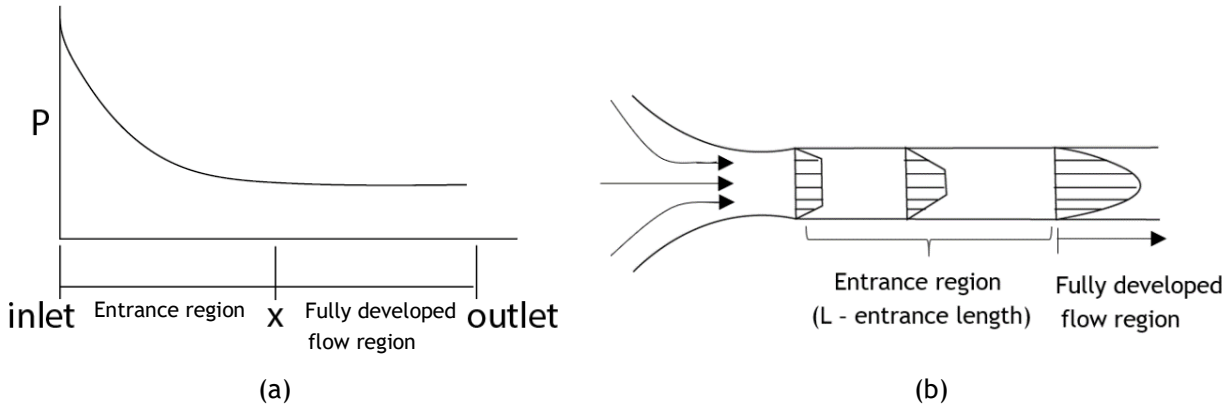

Figure 3. 4 - Schematization of the laminar fluid profile in a tube: (a) variation of the fluid's pressure with distance and (b) evolution of the flow's velocity profile.

Table 3. 2 – Values of velocities in several portions of the aorta (the data was obtained from [15]).

Vessel	Peak velocity (cm/s)	Mean velocity (cm/s)
Ascending aorta	20 - 290	10 – 40
Descending aorta	25 – 250	10 – 40
Abdominal aorta	50 - 60	8 - 20

Another flow behaviour can also be highlighted: the transitional flow. It occurs when flow changes from steady to pulsatile. The destabilising factor is the decelerating phase of the cardiac cycle that promotes transition. In contrast, the stabilising factor is flow's acceleration, where flow relaminarize. In these scenarios, turbulent patterns usually occur [27].

3.2.3 Laminar versus Turbulent

Blood velocity field usually has a laminar regime that flows parallel to the vessel centreline. Under conditions of high flow, such as during the systole period, turbulent regime takes place, especially in the ascending aorta. This disruption of the flow may also include vortices, known as recirculation zones. In the particular case of the aorta, curves and mainly branches exist along its extension, which also generates secondary flows [36]. Laminar flow is described by a parabolic velocity profile that, when velocity components are found in both nonaxial and axial directions, turns into a turbulent regime. The onset of turbulent flow can be estimated using Reynolds number (Re): for Re> 2000, the flow became turbulent and, in a cardiac cycle, this value can range from 6000 to $>10^{-3}$, from the heart to the periphery [9], [37].

$$Re = \frac{\rho V D}{\mu} \tag{3. 4}$$

Where ρ is the fluid density, V is the fluid velocity, D is the vessel diameter and μ is the fluid viscosity.

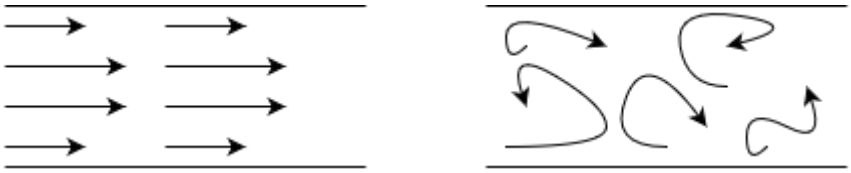

Figure 3. 5 - Schematization of laminar (left) and turbulent (right) flow regimes.

Chapter 4

Aortic Aneurysms

In the previous chapter, it was described the general blood flow's behaviour in the human body, that is related to some disease's formation and evolution. In this scope, it is known that aneurysms are a result of a multifactorial process, where hemodynamic plays an important role. Thus, this chapter aims to present an overall vision of aneurysm's incidence, the general concepts underlying this pathology, the process of the disease formation, including the risk factors and, at last, the assessment and treatment. After this chapter, it is expected a clearer correlation between blood flow and aneurysms.

4.1 Epidemiology

The number of detected abdominal aortic aneurysms has increased in the past two decades due to the surge in the total number of smokers, the ageing of the population, the introduction of improved diagnostic tools and the implementation of more regular screening programmes [38].

The population above 50 years old, especially the male gender, are the most susceptible to develop this disease, with an estimated incidence, for both genders, ranging from 5 to 9% [13]. The expected behaviour of an aneurysm is its expansion all over the years, which may lead to potentially lethal rupture [39]. Since the pathology usually remains asymptomatic or with vague indicators such as abdominal or back pain, it is difficult to detect until rupture [38], [41].

The Global Burden Disease 2010 Project concluded that the global mortality rate from aortic aneurysms and dissected aorta increased from 2,49 per 100 000 to 2,78 per 100 000 inhabitants between 1990 and 2010, with prevalence for men [42]. In the USA, abdominal aortic aneurysm (AAA) is the thirteenth leading cause of death, affecting 65% of patients with ruptured aneurysm [38]. In England, abdominal aortic aneurysm rupture causes 1,5% of the total mortality rate in males over 50 years old, which translates into 8000 deaths per year [43]. The global mortality rate for patients with AAA is estimated to vary between 65% and 85%, however, half of the deaths occur before patients reach surgery [38].

The diameter and growth rate of an aneurysm are the main factors for elective surgery, which is explained in more detail in subchapter 4.3.1. However, it is now understood that those criteria have several limitations, whereby biomechanical factors, such as hemodynamics, must be considered.

4.2 Disease Contextualization

An aneurysm is a chronic degenerative disease, characterised by a permanent and localised dilation of a blood vessel. This pathology is caused by a multifactorial process that leads to wall weakening and, consequently, its enlargement. Despite the complex vasculature that exists in the human body, this multifaceted disease mainly appears in arteries, primarily in the intracranial arteries and in the thoracic and abdominal (or infrarenal) portions of the aorta [40], [41]. Although the most common site of aortic aneurysms is the descending aorta, this pathology can also be found in the ascending aorta and in the aortic arch, as it can be seen in Figure 4. 1.

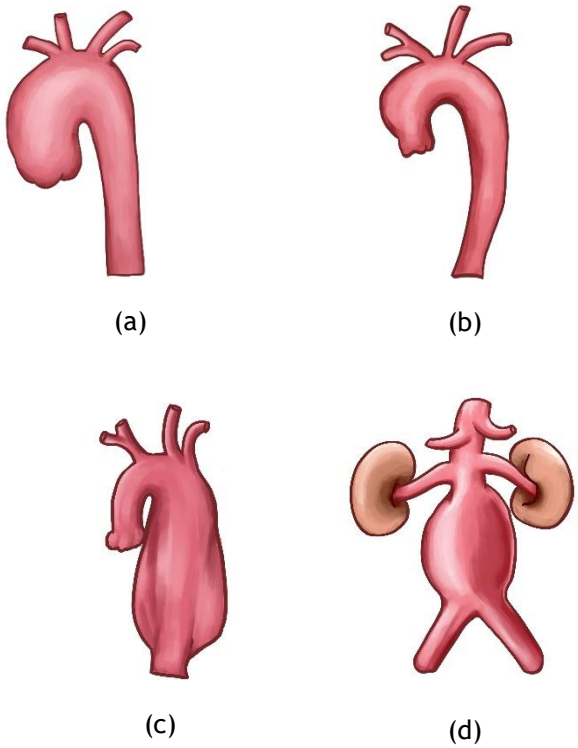

Figure 4. 1 – Representation of different locations for aortic aneurysms: (a) ascending aortic aneurysm; (b) aortic arch aneurysm; (c) descending aortic aneurysm (thoracic); (d) abdominal aortic aneurysm (AAA).

The average diameter of an aorta varies with body weight, age and sex and decreases gradually from the ascending portion to the iliac bifurcation. In the elderly, the width of the infrarenal aortic portion varies between 15 mm and 24 mm. In 1991, the Society for Vascular Surgery defined that an aortic aneurysm is represented by dilation of 1.5 times the typical diameter of the aorta, i.e., at least 30 mm. The three layers of the artery wall are affected, otherwise, the dilation is called a pseudoaneurysm [38].

The shape of the aneurysms can be classified into two main categories: fusiform and saccular aneurysm, as it is represented in Figure 4. 2 (a) and (b), respectively. The last is characteristic of cerebral arteries, while the former is predominantly found in the abdominal aorta or in the popliteal artery, behind the knee. Nevertheless, the abdominal aortic aneurysm

can also have an irregular shape, involving up to 90 mm of the infrarenal portion of the aorta [19], [38].

Since aortic and intracranial aneurysms have different conformations, it leads us to understand that both result from distinct pathophysiological processes. In this sequence, it is important to know which factors determine aortic aneurysm formation, growth and which risk factors are associated with the disease.

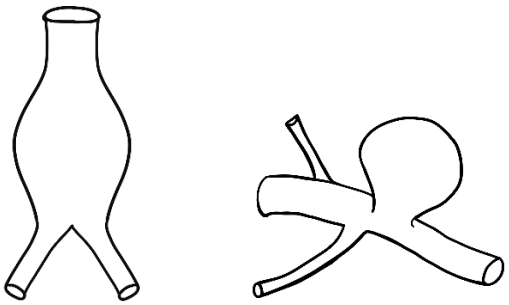

Figure 4. 2 – Shapes of aneurysms: (a) fusiform; (b) saccular. It is also important to state that, despite those two aneurysm conformations, aortic aneurysm tend to have an irregular shape.

4.3 Pathogenesis

The aortic aneurysms occur due to changes in the arterial wall. In a review made by Nordon et al. [44], it was stated that the three main processes that trigger aortic aneurysm phenotype are: (1) proteolysis (collagen and elastin degradation), (2) inflammation and (3) smooth muscle cell apoptosis. Alterations on the aortic wall composition cause changes in its mechanical properties that are strictly related to the elastin and collagen content that exists in the extracellular matrix of the wall and that control its elasticity. When an aneurysm forms in the aorta, there is a decrease of 91% in elastin content that, on its turn, can be related with the increase in elastase activity, that quickens the breakdown process of elastin. The collagen content, on its turn, decreases 77% compared to a non-aneurysmal aorta. With changes in the elastic fibres, the vessel wall becomes stiffer and less distensible, which alters the pulse wave propagation of blood flow through the aorta, leading to changes in hemodynamics [45].

Along with the process of aneurysm formation, there is another component that commonly appears in the vessel wall – the intraluminal thrombus (ILT). Over 75% of the aortic aneurysms contain an ILT, which development comprises mainly three phases: change in the platelet activity, the formation of a fibrin clot and a possible fibrinolysis (clot destruction) [46]. This thrombus deposition over the aneurysm wall achieve a thickness up to 3 cm or more, however, it never covers the lumen completely [47]. In this sequence, the thrombus remains in permanent contact with the blood, which promotes its continuous remodelling, and, on the other hand, the endothelial layer of the aneurysm wall is degraded by hypoxia because the blood is no longer in contact with the vessel walls [48]. Because of that, the composition and mechanical behaviour of the vessel can be modified, constituting a possible risk for rupture [49].

The presence of ILT is broadly discussed in the scientific community: some affirm that ILT functions as a protective barrier for aneurysm's wall shear stresses, preventing it from expansion and possible rupture [14]. Other defend that the thrombus promotes vessel wall

degradation by causing hypoxia of the meddle layer, necrosis of the smooth muscle cells and destruction of the endothelial cells [43]. A numerical study performed in 1997 concerning the role of ILT in AAA established a relation between the vessel wall stresses and the thrombus depth, in which it was proved that the deeper was the thrombus, the less wall stress in an aneurysm, preventing it from enlarge [50]. The scenario is different in a recent study of Haller et al., where it was proved that, for small abdominal aortic aneurysms and low stresses, the ILT potentiated rupture [51].

Thus, the alterations of the arterial wall that, in a first phase, leads to its expansion, can be associated with several factors like age, high blood pressure, obesity, diabetes, high alcohol consumptions, smoking and genetic factors. All the risk aspects that were nominated before are common to almost every cardiovascular disease, being difficult to understand which are the specific mechanisms that induce pathological wall remodelling causing aneurysm formation [14], [43].

4.3.1 Aneurysm Formation and Progression Risk Factors

The review made by Lindquist et al. [52] showed that the most strongly risk factor associated with aortic aneurysms, especially the AAA, is smoking. In another study performed by Lasheras [14], it was stated that the primary cause of AAA development is age. Although many other factors contribute to the disease development, progression and, eventually, aneurysm rupture, smoking seems to be the only factor that can be modified during the lifetime. Other causes that are related to the aortic aneurysms are age, hypertension, atherosclerosis, gender and genetics.

4.3.1.1 Age and Gender

The ageing of elastic arteries causes changes in the architecture of the vessel concerning diameter, length and wall structure. The significant changes occur in the tunica media, which loses the arrangement of fibres and elastin laminas, causing wall stiffening [14].

The aneurysms in the abdominal portion of the aorta affect mostly the population aged above 50 years old. Men are six times more expected to have this lesion, however, the risk of rupture in women are three times higher [19]. In men, the pathology starts to appear from 50 years old, reaching its peak at age 70 or 80; in women, it occurs later, however, it is generally associated with a worse prognosis [53].

A screening carried out in Portugal in 2012 revealed that 2,2% of the population with more than 60 years old has an AAA. This value arises to 3,94% in men above 65 years old [53]. Another study that was performed in Sweden showed that there is a prevalence of AAA in 65-year-old men and 0,5% in 70-year-old women [52]. In the USA the scenario is identical: the women have a prevalence rate between 1,0% and 2,2%, while in man it varies between 1,3% and 8,9% [38].

4.3.1.2 Smoking

Smoking is strongly related to AAA progression and rupture, however, the mechanisms by which this factor promote aneurysm development remain unknown. The prevalence of this pathology in tobacco smokers are three to five times greater than in lifelong non-smokers [38], [54]. The duration of smoking is more relevant than the number of cigarettes smoked per day:

each year of tobacco increases the relative risk of AAA by 4% in all populations. Also, the expansion rate of an aneurysm is greater in those individuals who continue to smoke [44].

In a review made by Lederle [54] concerning the ultrasonographic screening of abdominal aortic aneurysms, it was analysed the criteria used for screening programs. The main norms that were defined was age, gender (male) and smoking habits. In Figure 4. 3, it is described the prevalence of 4 cm or larger AAA in men with smoking history, proving that smoke is one of the most influential risk factors for aneurysm growth.

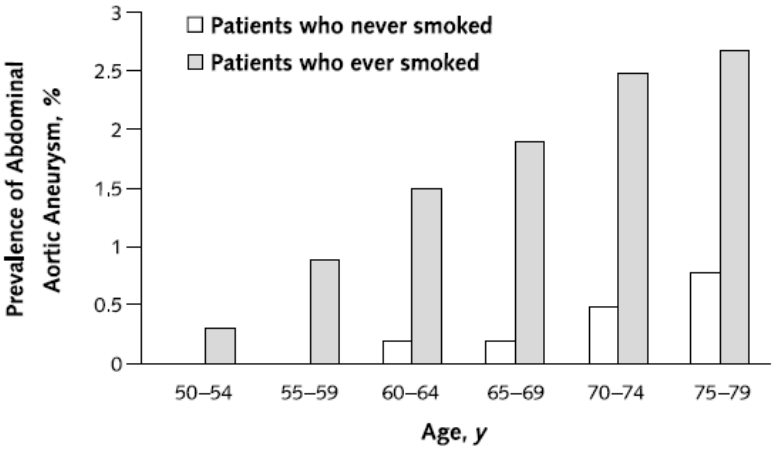

Figure 4. 3 – Prevalence of AAA with 4 cm or greater, in men with smoking habits [54].

4.3.1.3 Hypertension

Hypertension (diastolic blood pressure above 95 mmHg and systolic blood pressure above 160 mmHg) distends the vessel progressively, causing the gradual thickness of the wall and it is found twice as often in patients with aneurysms than without [14]. This structural stiffening disturbs the hemodynamic, that affects wall stress and can potentiate vascular disease processes [11].

4.3.1.4 Atherosclerosis

Atherosclerosis is the process in which fatty constituents are placed on the arterial walls, specifically in the intimal layer (atherogenesis). It is usually observed in sites of bifurcations and curvatures, as so in the infrarenal portion of the aorta [55]. For this reason, and because atherosclerotic plaque is usually detected in the presence of AAA, it is frequently related to its pathogenesis. In the locals where atherosclerosis is more propense, it has been stated that wall shear stress (WSS) and tensile stress play a fundamental role in the progression of the plaque formation. This is related to the fact that atherosclerosis happens mostly in regions of low blood flow velocity and shear stress, recirculation, turbulence and flow separation zones. Those factors are known as atheromatic factors [56], [57]. In this sequence, endothelial cells susceptible to extreme WSS are more prone to damage, favouring atherosclerosis deposition, altering wall physiology and, consequently, intimal wall thickening.

4.3.1.5 Hemodynamics

The tendency of aneurysm formation at curvatures and bifurcations suggest that the flow features in those sites play a fundamental role in the disease formation. In fact, similarly to what happens in atherosclerosis, blood flow recirculation and disruptions are observed in zones with an aneurysm, so this means that hemodynamics modulates disease progression [3], [4].

Mechanical parameters such as wall shear stress (WSS) and oscillatory shear index are believed to act in the genesis of vascular diseases, so they are the metrics usually considered when analysing blood flow in aneurysm scenarios [48]. The wall shear stress parameter is particularly important since the luminal side of blood vessels are constantly exposed to it. Also, the excess or lack of wall shear stress can generate pathological changes in the vessel wall, through the response that it induces on endothelial cells.

Regarding aneurysm expansion, there are two main hypotheses: one that shows that aneurysms are more expected to grow in regions of low shear stress and another that links the aneurysm expansion to the increase of blood flow. The former theory states that high WSS causes the initial development of the arterial wall and the consequent focal decrease of WSS potentiate biological processes that outcome in aneurysm evolution [58]. The explanation for the last theory is that high WSS causes destruction and remodelling of the arterial wall, which leads to a disruption of the equilibrium between the internal wall stress forces and the blood pressure forces, resulting in wall's dilation [30].

To schematize the previous information, see Figure 4. 4, where it is made a correlation between risk factors, mechanical factors and pathogenesis of aortic aneurysms.

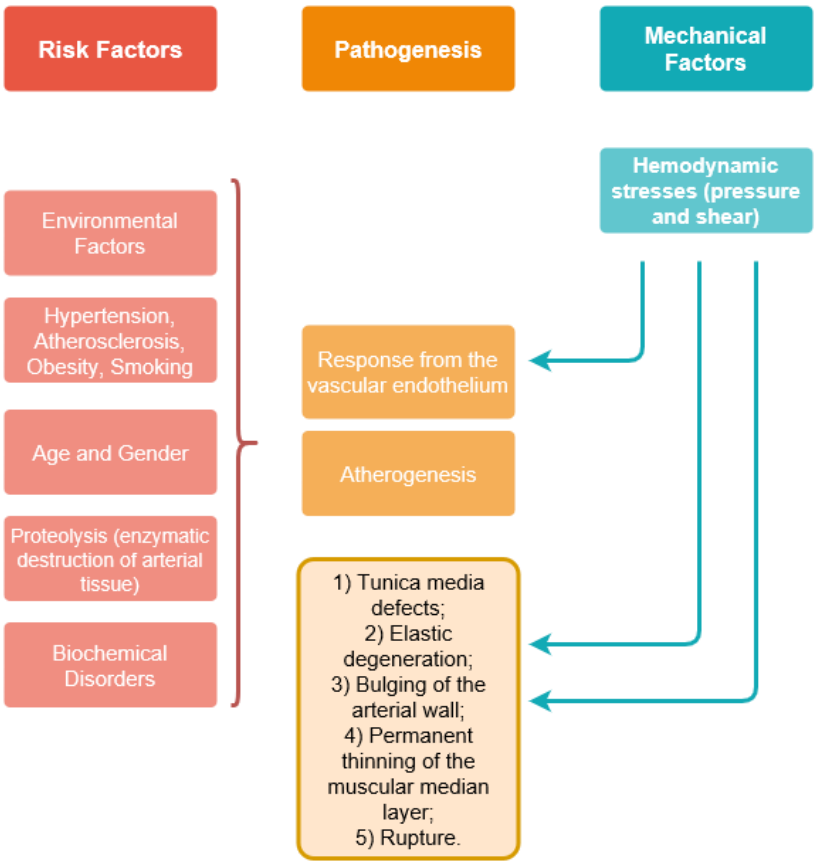

Figure 4. 4 - Correlation between the factors that contribute to abdominal aortic aneurysm formation and the pathogenesis process.

4.4 Diagnosis and treatment

Aortic aneurysms usually are detected incidentally on a routine check-up or on imaging ordered for other indications. A physical examination can also detect an aneurysm as a palpable and pulsatile mass in the abdomen, however, by palpation, it is not possible to access features as the size of the aneurysms, and it is also difficult to make a diagnosis in overweight patients [38].

In this sequence, diagnostic imaging modalities are crucial for detecting and monitoring the aortic aneurysms. The most used modalities are abdominal ultrasonography, computed tomography (CT) and magnetic resonance angiography (MRA). The former is the cheapest and the most straightforward method for diagnosis of aortic aneurysms and it is largely used not only for follow-up as also for population screening. Combined with doppler, both 2D and 3D ultrasonography obtain time-resolved blood velocities. As a disadvantage, the image obtained from this modality can be affected by fatty tissue and anatomy obstruction. CT is better in defining the shape and extent of the pathology than ultrasonography and for this reason, it is mostly used for surgery planning. CT scans can also measure the thickness of the intraluminal thrombus and the presence of blood inside it, that consists of a predictive marker of rupture. As for disadvantages, CT has higher cost and includes the utilisation of intravenous contrast substance and ionising radiation. Lastly, the MRA is usually used for patients with contraindications, such as allergies, since there is no need for contrast material. In summary, CT scanning and MRA are superior tools in detecting aortic aneurysms, since they provide images with better quality [24], [38], [41].

After aneurysm detection, it is imperial to evaluate its features, such as size, growth rate and risk of rupture for assessment of surgery necessity. The clinical decision for intervention is normally based on the diameter and the growth rate, that are the criteria believed to increase the risk of rupture [2]. The progressive growth of an aortic aneurysm is pointed as a significant risk factor, since it enlarges at rates up to 0,25 cm to 0,75 cm per year, initially slower, then faster as they grow [40]. In Table 4. 1, it is resumed the risk of rupture's percentage according to an abdominal aortic aneurysm diameter

Table 4. 1 – Abdominal aortic aneurysm rupture risk according to is diameter (Adapted from [5]).

Aorta's diameter (cm)	*Rupture Risk (%/year)*
<4	0
4 - 5	0,5 – 5
5 - 6	3 – 15
6 - 7	10 – 20
7 - 8	20 – 40
>8	30 – 50

Several proceedings can be adopted according to the aneurysm's diameter at the time of the scanning. In the scheme depicted in Figure 4. 5, it is represented a possible methodology for managing the specific case of the AAA.

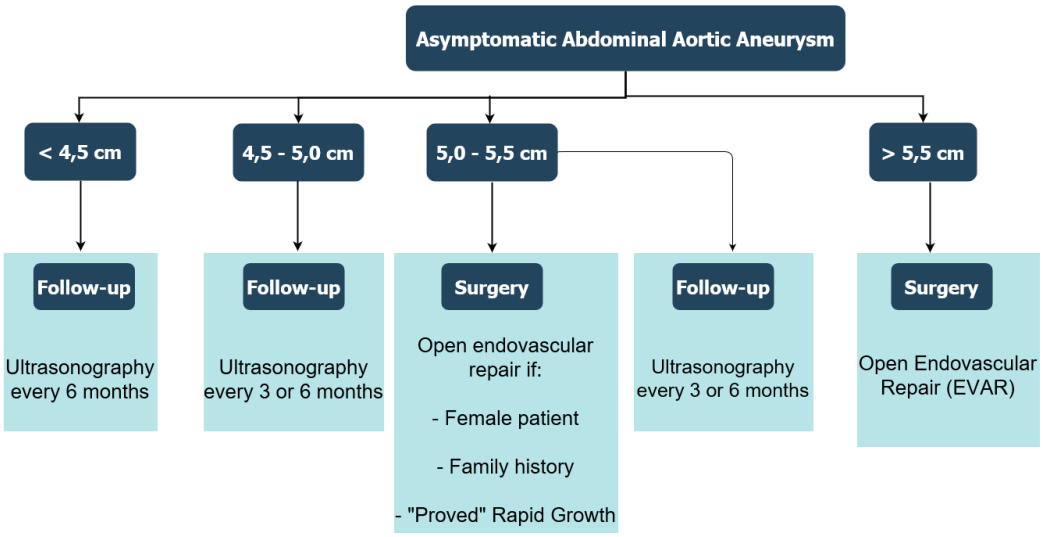

Figure 4. 5 – Abdominal aortic aneurysm management according to its diameter (Adapted from [38]).

The reliability of the previous criteria is questioned, since 60% of AAA with a diameter higher than 5,5 cm never rupture, while 10% - 20% of AAA with a diameter below 5,5 cm do rupture [59], [60]. Therefore, promising and new approaches to access aneurysm rupture is based on the analysis of hemodynamics inside the dilated artery through 3D reconstructions of an aortic aneurysm, acquired by imaging techniques. The wall shear stresses can be determined by a numerical method, such as finite element analysis, leading to the location of sites more prone to rupture, becoming a relevant tool in determining the timing for aneurysm's repair.

As it was previously observed in Figure 4. 5, surgery is recommended for patients with the aneurysm diameter exceeding 5,5 cm, but prior to surgery, medical supervision is indispensable to control the aneurysm growth. This implies close monitorization through CT scanning, reduction of the cholesterol levels and the decrease of hypertension by, for example, quit smoking. After these measures, if an aneurysm is still growing and presenting a risk of rupture, surgery is needed. The most common clinical procedure for an aortic aneurysm (more commonly AAA) treatment is open surgery, which appeared in 1952. In this invasive technique, the surgeon extirpates the aneurysmal aorta and substitutes it with a prosthetic graft [41]. Due to the significant morbidity and mortality (30% to 50%) associated with this procedure, an alternative approach emerged in 1991 – the endovascular repair (EVAR) – that consists in the percutaneous deployment of a stent-graft in an aneurysm [53], [61]. In Portugal, this procedure was performed for the first time in 1992, and since then, it has been improved, substituting the open repair gradually [5]. In Figure 4. 6 it can be observed the prevalence of EVAR between 2005 and 2010 in several regions of Portugal.

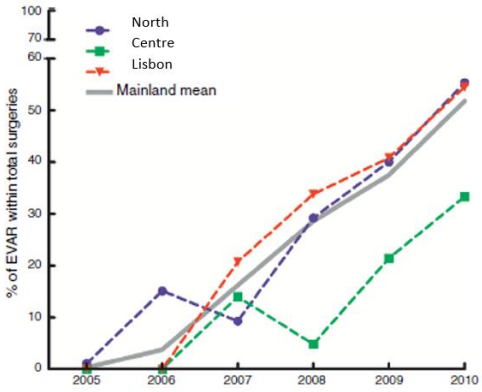

Figure 4. 6 – Evolution of EVAR treatment in Portugal in 5 years [5].

Another procedure that has been gained popularity is the personalised external aortic support, that consists in a mesh that is wrapped around an aneurysm. Currently, it is used only in specific cases of thoracic aortic aneurysms, so it is not regularly adopted in clinical practice [41]. In Figure 4. 7, it is represented the three main procedures for aneurysmal repair.

Technique	Real Image
Open Repair	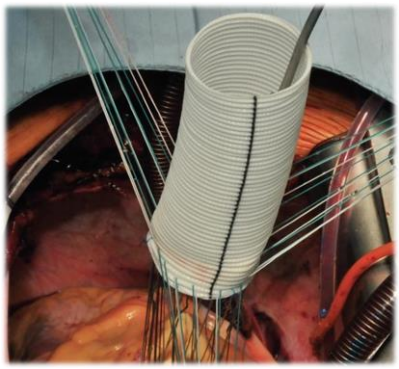 [62]
EVAR	 [63]

External aortic support

[64]

Figure 4. 7 – Surgical techniques for aortic aneurysm's treatment.

4.4.1 Economic Analysis

The open surgery and the EVAR are the most commonly used procedures for treating aortic aneurysms. Hence, there is an emergent need to perceive with certainty and clarity which aneurysms are at risk and which ones need surgery to avoid unnecessary economic, material and human expenses.

The management of the aortic aneurysm's disease comprehend several costs that go beyond surgery: screening, pharmaceutical, medical device maintenance, the procedure's planning and human costs are just a small amount of a panoply of expenses for treating this disease.

Regarding surgery, the EVAR has gaining popularity since it reduces the mortality and morbidity of the total surgeries. However, EVAR is considerably more expensive than the traditional open repair procedure, so this puts the medical community and the hospital managers under an impasse.

In order to access the evolution of the procedures and the correlation with its inherent costs, several studies have been made in many countries considering data from several health unities. For example, a paper published in 2000 concerning AAA repair costs in several centres in the USA revealed a detailed list of procedures and its expenses in EVAR and OR surgery (Table 4. 2), showing that EVAR is more expensive in almost all sectors.

Table 4. 2 – Hospital costs, in US dollars, for AAA repair. The ICU stands for "Intensive care unit" and OR stands for "operating room" (Adapted from [6]).

	Open repair (n=60)	Endovascular (n=190)
Procedure diagnostic	644	1100
Postprocedure diagnostic	698	1760
Total diagnostic	$1342	$2860
Room and board	1099	752
ICU	1210	639
Recovery	1898	1225
Total bed costs	$4207	$2616
OR	2642	2577
Anesthesia	940	1038
Medical/ surgical supplies	972	1094
Total OR costs	$4554	$4709
Pharmacy/ blood	1588	865
Device	653	10,200
Grand total	$12,342	$21,250

In Portugal, the impact of EVAR in the population with aortic aneurysms was also evaluated not only concerning survival rate, but also in the scope of costs associated with the trials related to the procedure implementation. The outcomes of 12 years of study revealed that the mean cost of EVAR surgery, per patient, was 11.404,00€ and conventional surgery was 9.955,70€ [5].

To summarise the information regarding the pros and cons of OR surgery and EVAR, it was constructed the Table 4. 3 with basis on the information collected from references [5], [6], [36].

Table 4. 3 – Comparison between ORS and EVAR.

Open Repair Surgery	**EVAR**
Suitable for almost any patient	Limited to aortic aneurysms with the "right shape"
Large incision in the abdomen	Small incision in groin
6 days stay in hospital (average)	2 days stay in hospital (average)
Full recovery after 6 weeks	Full recovery after 2 weeks
29% morbidity	18% morbidity
3,8% mortality rate	1,3% mortality rate
High blood transfusion	Low blood transfusion
No long-term surveillance required	Long-term surveillance required
Average total cost: $12,500 (US dollars)	Average total cost: **$20,000** (US dollars)

Chapter 5

Mathematical and Numerical Models

In much of the cardiovascular system, the unsteadiness and three-dimensionality of blood flow constitute a challenge in mathematical and numerical analysis. Besides, this can be difficulted by the fact that blood is a suspension of deformable cells in the plasma, in which its properties are altered according to many physiological and unpredictable factors. However, despite its complexity, numerical methods for the solution of the partial differential equations that govern flow fluids for three-dimensional, unsteady and complex geometries have been continuously developed.

In this sequence, this chapter begins with the presentation of the mathematical concepts for modelling blood flow, which includes the explanation of the governing equations, rheological models and similarity parameters. Then, it is described the formulation of advanced discretisation numerical methods - FEM, RPIM and NNRPIM.

5.1 Modelling of Blood Flow

5.1.1 Governing equations

The key components of hemodynamics modelling are the mathematical equations of fluid dynamics that, for each discrete point within the flow, solve the fluid's velocity and pressure. Once these two parameters are solved, forces and shear stresses applied by the blood to the vessel wall can also be estimated.

The set of partial differential equations that enables the previous calculations is the time-dependent fluid equations expressing the equilibrium of linear momentum (Navier-Stokes equations) and the solenoidality of the velocity field, resultant from the principles of conservation of the momentum and mass, respectively [12], [13].
Assuming a three-dimensional, unsteady and incompressible flow, the equations can be read as

Conservation of mass:

$$\operatorname{div} \boldsymbol{v} = 0 \quad in\ \Omega, \forall t > 0 \tag{5. 1}$$

Conservation of momentum:

$$\rho \frac{\partial \boldsymbol{v}}{\partial t} + \rho(\boldsymbol{v}.\nabla)\boldsymbol{v} + \nabla p - div\,\boldsymbol{\sigma} = \rho \boldsymbol{f} \quad in\,\Omega, \forall t > 0 \tag{5. 2}$$

Where $\Omega \subset \mathbb{R}^3$ is a 3D domain that represents the lumen of the vessel (or vessels) under study, ρ is the blood density, $\boldsymbol{f}$ is the possible action of external forces (N), p is the pressure (N/m^2) and $\boldsymbol{\sigma}$ is the Cauchy stress tensor.

$$\boldsymbol{\sigma} = -p\boldsymbol{I} + 2\mu(\dot{\gamma})D(\boldsymbol{v}) \tag{5. 3}$$

In this equation, $\boldsymbol{I}$ represent the identity matrix, μ is the dynamic viscosity and $\dot{\gamma}$ is the shear rate. For Newtonian fluids, the viscosity is constant and independent of the shear rate. In the other hand, for non-Newtonian fluids like blood in aortic aneurysms, D is the strain rate tensor and described by

$$D(\boldsymbol{v}) = \frac{1}{2}(\nabla \boldsymbol{v} + \nabla \boldsymbol{v}^T) \tag{5. 4}$$

In the differential equations presented, there are four unknowns: the three components of the velocity and the pressure. To obtain these values, the equations must be resolved according to a mathematical model of blood flow. There are several blood models, depending on whether it is considered Newtonian or non-Newtonian.

5.1.2 Non-Newtonian Models

Several rheological models can describe blood's rheology. These models are generally grouped into Casson, Carreau-Yasuda, Power-law, Herschel-Bulkley and Quemada models (see Table 5. 1).

There are other less applied models that also describe the rheology of blood, however, the most popular non-Newtonian hemorheologic models are Casson and Carreau-Yasuda. More detailed information about fluid models can be consulted in [28] and [65].

As it is seen in Table 5. 1, the Power-law model is the simplest and the most suitable for modelling a transition region. The viscosity tends to infinity as $\dot{\gamma}$ tends to 0 and to 0 as $\dot{\gamma}$ tends to infinity. For this reason, the model neither shows good correlation for low and high strain rates.

The Casson model is only valid for steady flows at a small range of low shear stress. This model, as well as the Herschel-Bulckley model, take into account the yield stress to start flowing. In the Carreau-Yasuda model, when $a = 2$, it becomes the Carreau model.

The parameters of the unknown variables were taken from studies in which the blood was modelled in arterial disease scenarios, as in aneurysms.

Table 5. 1 – Effective viscosity models of blood flow, μ, as a function of strain rate, $\dot{\gamma}$ and the respective parameters.

Rheological Model	Effective Viscosity	Parameters
Casson [28], [29], [65]-[68]	$\mu = \sqrt{\mu_c} + \sqrt{\frac{\tau_c}{\dot{\gamma}}}^2$	$\mu_c = 3.5\ mPa.s$ $\tau_c = 0.005\ Pa$ [69]
Carreau-Yasuda [28], [32], [34], [65], [66], [70]	$\mu = \mu_\infty + \frac{\mu_0 - \mu_\infty}{[1 + (\lambda\dot{\gamma})^a]^{\frac{1-n}{a}}}$	$\mu_0 = 51.9\ mPa.s$ $\mu_\infty = 4.76\ mPa.s$ $a = 0.409$ $n = 0.191$ $\lambda = 0.438$ s [70]
Cross [28], [65], [66], [71]	$\mu = \mu_\infty + \frac{\mu_0 - \mu_\infty}{1 + \lambda\dot{\gamma}^m}$	$\mu_0 = 56\ mPa.s$ $\mu_\infty = 3.45\ mPa.s$ $\lambda = 1.007\ s$ m $= 1.028$ [66]
Power-law [28], [33], [65]-[67], [72]	$\mu = k\dot{\gamma}^{n-1}$	$n = 0.48510$ $k = 0.20730$ kgs^{n-2}/m [33]
Herschel-Bulkley [28], [48], [66], [67], [72]	$\mu = \left(\frac{\tau_0}{\gamma}\right).[1 - exp(-m\dot{\gamma})] + k\dot{\gamma}^{n-1}$	$\tau_0 = 0.0035\ Pa$ $n = 0.8375$ k$= 0.008\ Pa.s^{0.8375}$ m$= 1000\ s$ [48]
Quemada [28], [49], [66]	$\mu = \mu_p\left(1 - \frac{k_0 + k_\infty\sqrt{\frac{\dot{\gamma}}{\dot{\gamma}_c}}}{2\left(1 + \sqrt{\frac{\dot{\gamma}}{\dot{\gamma}_c}}\right)}\emptyset\right)^{-2}$	$k_0 = 4.0$ $k_\infty = 1.5$ $\dot{\gamma}_c = 5.0$ [49]

The meaning of the symbols that are presented in the previous equations are listed below:

$\dot{\gamma}$ – shear rate
$\dot{\gamma}_c$ – characteristic shear rate
λ – characteristic time constant
μ – fluid viscosity
μ_c – fluid viscosity
μ_p – plasma viscosity
μ_0 – zero-shear-rate viscosity
μ_∞ - infinite-shear-rate viscosity
τ – shear stress
τ_c – characteristic shear stress
τ_0 – yield-stress
$\emptyset$ - volume concentration
a – Carreau-Yasuda index
k – flow consistency index

k_0 – maximum volume fraction for zero shear rate
k_∞ - maximum volume fraction for infinite shear rate
m – Cross model index
n – Power-law index

In Chapter 3, it was seen that blood in large vessels can be modelled as a Newtonian fluid. Since there is no transition from Newtonian to non-Newtonian flow as a function of shear rate, an initial choice must be made according to subjective and objective factors (for example, the type of vessel, presence/absence of disease state and the shear rate range). Usually, non-Newtonian effects are considered significant if the shear rate range is < 100 s^{-1}. For values above this limit, the blood is regarded as a Newtonian fluid [28].

Despite the existence of mathematical models for blood flow, it is not possible to capture faithfully all the features that describe blood's complexity, both for non-Newtonian and Newtonian assumptions. These different models can provide very different results.

5.1.3 Similarity Parameters

The simulation of the cardiovascular network presents many challenges, such as the reproduction of the flow characteristics, that aim to be close as possible to realistic scenarios. To guarantee this dynamic resemblance between the human system and the model under simulation, dimensionless parameters, acknowledged as the similarity parameters, are studied. The two most important parameters are the Reynolds and Womersley numbers, which were already introduced in the subchapter 3.2 to clarify the discrepancies between static and pulsatile, laminar and turbulent flow regimes.

5.1.3.1 Womersley number

The Womersley number is defined by equation (3. 2) and describes the oscillatory property of the flow: for α >>1 the flow is considered unsteady and for α <1 the flow may be assumed as steady [9], [25].

5.1.3.2 Reynolds number

The Reynolds number is described by equation (3. 4) and is used to identify whether the flow is laminar or turbulent. In the laminar regime, the flow is well organised and free of variations, which occurs when Re < 2000. In disparity, the turbulent flow presents random fluctuations in space and time and occurs when Re > 4000 [15], [37].

In small vessels, like capillaries, it is perceptible that the blood flows with low velocity, assuming a laminar and steady profile. In contrast, in vessels close to the heart, as the aorta, the blood is pumped with high velocity, creating turbulent flows. In Table 5. 2, it is presented the values of the two dimensionless parameters for different blood vessels [12].

Table 5. 2 – Similarity parameters for several blood vessels.

	Womersley Number	*Reynolds number*
Ascending aorta	10.5	4000
Thoracic Aorta	7.7	2500
Iliac artery	3.5	1000
Common carotid artery	2.8	800
Small artery	1.4	100
Capillary	0.007	0.003

5.2 Numerical Methods

The mathematical formulation of blood flow is generally based on two fundamental principles (conservation of mass and Newton's second law) that are expressed in differential equations with partial derivatives. The complexity of this governing equations requires numerical methods for reaching a solution. In this context, emerged a branch of science that studies the solving techniques of these equations – the Computational Fluid Dynamics (CFD). The problem is resolved by replacing the equations with discrete solutions, which are moved in time and space for an approximation of the flow in study.

In the dissertation, it will be implemented three numerical methods: The Finite Element Method (FEM) and two Meshless methods - the Radial Point Interpolation Method (RPIM) and the Natural Neighbour Radial Point Interpolation Method (NNRPIM).

5.2.1 Finite Element Method

The FEM is one of the most popular computational methods for spatial discretisation for solid mechanics. FEM allows to easily model complex geometries and to impose straightforwardly boundary conditions. Furthermore, when applied to problems governed by self-adjoint elliptic or parabolic partial differential equations (PDEs), FEM leads to symmetric stiffness matrix. Giving the success of FEM in solid mechanical problems, the same scenario was expected to fluid mechanics field [73].

In the 1970s, the FEM was introduced to fluid problems and, nowadays, it still continues to be applied. The technique consists in dividing the flow domain into discrete simpler parts (elements) that are connected by nodes (see Figure 5. 1), forming a mesh in which governing equations are applied. These equations are reworked in algebraic form to characterise the changes that occur in the variables due to incremental variations in position and time [73], [74]. The solutions are then adapted each cycle over the complete mesh until a converged result of the viscosity is obtained.

Regardless the current implementation of FEM in the numerical analysis of fluid problems, it is not the method that achieves the better results. This is because the governing equations present a convection operator, that is not self-adjoint, rendering the solution (velocity and pressure). These operators are non-symmetric, so the Galerkin FE method imposes a symmetry that does not exist in the partial differential equations, losing the best approximation property. To overcome this problem, stabilisation techniques were developed, such as the Galerkin Least-squares method. For more in-depth knowledge of stabilisation techniques, it can be consulted

the reference [74]. The mesh-based algorithms, when applied to complex models or analysis with large deformations (as in fluid flow) presents high computational cost due to the remeshing task. Consequently, meshless methods are preferred, since it does not need elements for discretising a problem.

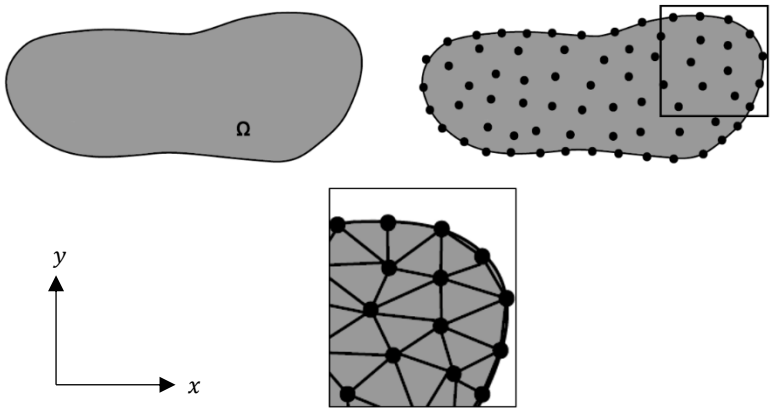

Figure 5. 1 - Process for the mesh creation. The domain is divided into elements, connected by nodes. The type, the arrangement and the number of elements influence the accuracy of the results. In this case, the mesh is constituted by triangular elements, however, the elements can have other shapes. For each of the finite element of the mesh, the field variables will be interpolated by shape functions.

5.2.1 Meshless Methods

The meshless methods were formulated to overcome some limitations of the FEM, usually associated with difficulties in the mesh generation. The main difference between a meshless method and FEM is that in the former, the domain is discretised by a group of randomly distributed nodes, with no pre-established connectivity relations between them [75]. The nodal connectivity is imposed by influence-domains, so the variable fields are approximated within an influence-domain, rather than an element. Contrary to the non-overlap rule between elements in the FEM, in meshless methods the influence-domains must overlap [76].

These advanced numerical methods comprise three phases: the construction of the shape function, the formulation and the integration [76]. A description of meshless methods origin and evolution is then presented in the State-of-the-art chapter.

5.2.1.1 General procedure

Meshless methods are nodal dependent discretisation techniques that allow solving partial differential equations. The analysis of this numerical methods relies on the nodal discretisation of a continuous domain and, similarly to other nodal dependent numerical methods, it follows the next outline.

First, the geometry under study is characterised by identifying the contour of the domain and its essential and natural boundary conditions. Then, the domain and boundary are numerically discretised with a regular or irregularly distributed set of nodes. This process is called nodal discretisation and is schematized in Figure 5. 2.

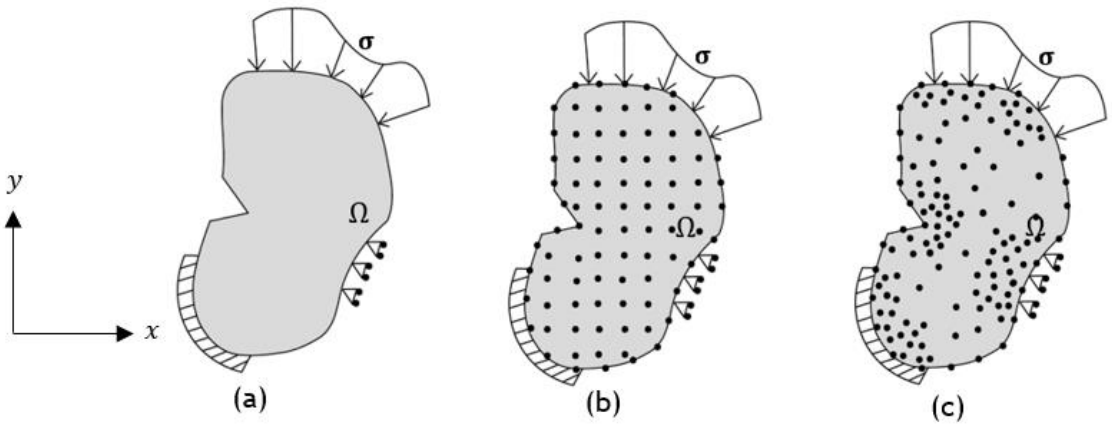

Figure 5. 2 - Representation of the nodal discretization of a domain: (a) solid domain; (b) regular discretization; (c) irregular discretization.

Contrary to FEM, these nodes do not form a mesh, since in true meshless methods it is not required any initial relationship between the nodes to construct the shape functions. Regardless of this nodal independency, their distribution and density in the domain affect the method's performance. A denser mesh will lead to more accurate results but, in return, it will increase the computational cost. Another important aspect is the spatial distribution of the nodes: an unbalanced distribution can result in lower accuracy so, to overcome this problem, a good practice referred in the literature is to establish a higher nodal density in areas of interest, where the field variable's gradients are more pronounced. These areas may be discontinuities, material interfaces, convex boundaries, etc. [76].

After discretising the domain into a set of independent nodes, it is necessary to construct a background mesh (nodal dependent or independent) to integrate the weak form equations correctly. The methods that need the background mesh are not true meshless methods, which is the example of RPIM. It is common to use a Gaussian integration mesh, as in the FEM, that fits the problem domain or can be larger than the problem domain, not affecting the results significantly (see Figure 5. 3). Also, there is an alternative approach to integrate the weak form equations that is by nodal integration, which resorts to the Voronoï diagrams for obtaining the integration weight of each node. Despite this nodal integration scheme being related to true meshless methods, it is often associated with a decrease in accuracy, creating the need for stabilisation methods that, in its turn, increase the computational cost [77], [78].

After the discretisation of the domain and the construction of the background mesh, it is imposed the nodal connectivity. In FEM, the nodes of each element interact directly between themselves and between the nodes of adjacent elements. This property is predefined in FEM by the element matrix, though, in meshless methods there are no elements, so each point of interest, $\boldsymbol{x}_I$, has its own influence domain [78]. Depending on the integration scheme, the point of interest can be an integration point, from the background integration mesh, or a node of the nodal discretisation, if the nodal integration method is used.

The influence domain is determined by defining concentric areas or volumes in each integration point and the nodes comprised inside each area or volume are part of the influence domain of that point, $\boldsymbol{x}_i$. Although the areas or volumes can have several shapes and dimensions, it is strongly recommended that all influence domains have an equal number of nodes inside [76]. In Figure 5. 4 it is observed three different scenarios for the selection of influence domains.

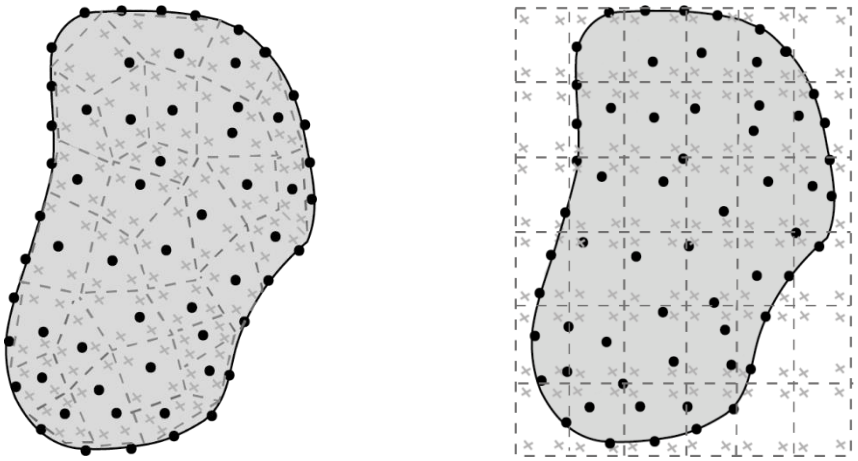

(a) (b)

Figure 5. 3 – Schematization of the background integration mesh: (a) fitted integration mesh; (b) general integration mesh.

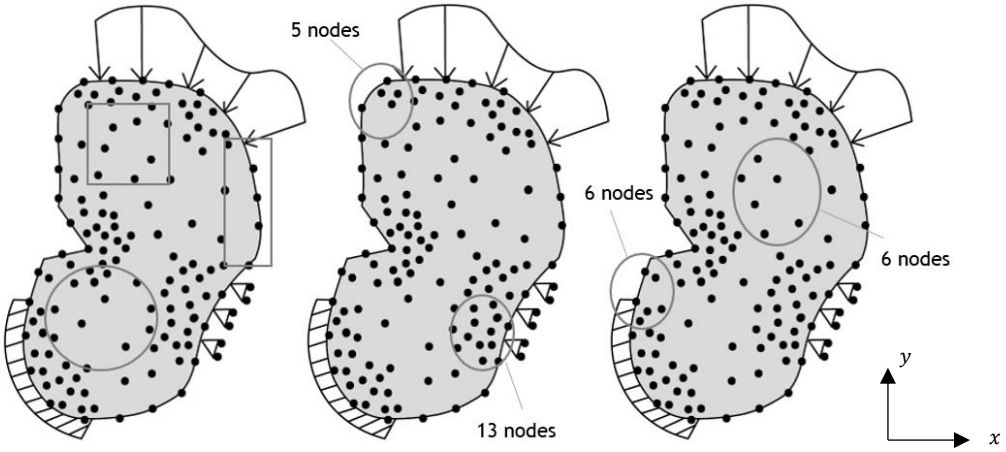

(a) (b) (c)

Figure 5. 4 - Examples of different selections of influence-domains: (a) influence-domain with different shapes; (b) influence-domain with circular shape and different sizes (bad choice); (c) influence-domain with variable size, circular shape and with the same number of nodes inside.

With the numerical discretisation of the domain defined, the integration scheme selected, and the connectivity of the nodes imposed, it can be obtained the variables field by calculating the shape functions, whether the method is approximant or interpolant. The RPIM is an interpolation method, which means that it uses interpolation shape functions (radial basis function). The major advantage of the interpolation functions compared to the approximation is that they are null in every node of the domain, except the node of interest, which assumes the value of one. This particularity gives the method the delta Kronecker property, that is useful when imposing constraints [76].

In sum, meshless methods involve the combination of three parts: nodal connectivity, numerical integration scheme and shape functions, which will be explained in detail for both RPIM and NNRPIM formulations. For the explanation of these three components, it will be assumed a 2D representation, which can easily be extended to higher dimensional spaces, as observed in [76].

5.2.2.2 Nodal Connectivity

- **RPIM**

After discretising the problem domain with an arbitrary set of nodes, the nodal connectivity is imposed by overlapping the influence-domain of each node. The influence-domains are found through the limitation of a uniform number of nodes with shapes of variable sizes. The initial nodal spatial distribution has a major influence in the influence-domains, since it can affect the final solution of the problem. To overcome this problem, RPIM uses influence-domains with variable sizes but with a constant number of nodes, as seen in Figure 5. 4 (c). It uses the Galerkin weak formulation to obtain the discrete equation system and the shape functions are constructed using radial basis functions, which performs a radial search using as centre the point of interest, $\boldsymbol{x}_I$, to find the n closest nodes [76].

- **NNRPIM**

Natural Neighbours

The NNRPIM uses the concept of natural neighbours to determine the nodal connectivity. The geometric construction is based on the Voronoï diagram of the nodal distribution, already mentioned in the meshless general procedure.

The problem domain ($\Omega \subset \mathbb{R}^2$) is discretised by N arbitrary distributed nodes – $\boldsymbol{N} = \{n_0, n_1, \dots, n_N\} \in R^2$ – which express the coordinates $\boldsymbol{X} = \{\boldsymbol{x_0}, \boldsymbol{x_1}, \dots, \boldsymbol{x_N}\}$, $\boldsymbol{x_i} \in \mathbb{R}^2$. The Voronoï diagram of $\boldsymbol{N}$ is a partition of the domain into closed and convex subregions, V_i, in which each one is associated with a node, n_i. Therefore, a Voronoï cell can be obtained for each node in the subregion and defined as the geometric place for which all belonging points are nearer to that node than any other [78]. The steps to obtain the Voronoï diagram is described in Figure 5. 5 and the determination of each cell can be represented by the following equation.

$$V_i = \left\{\boldsymbol{x_I} \in \mathbb{R}^2 : \|\boldsymbol{x_I} - \boldsymbol{x_i}\| < \left\|\boldsymbol{x_J} - \boldsymbol{x_j}\right\|, \forall i \neq j\right\} \quad (5.\ 5)$$

Where $\|\cdot\|$ is the distance between the interest point, $\boldsymbol{x}_I$, and the nodes defined by the coordinates $\boldsymbol{x_i}$ and $\boldsymbol{x_j}$.

The Voronoï diagram is then defined by: $\boldsymbol{V} = \{V_1, V_2, \dots, V_N\}$.

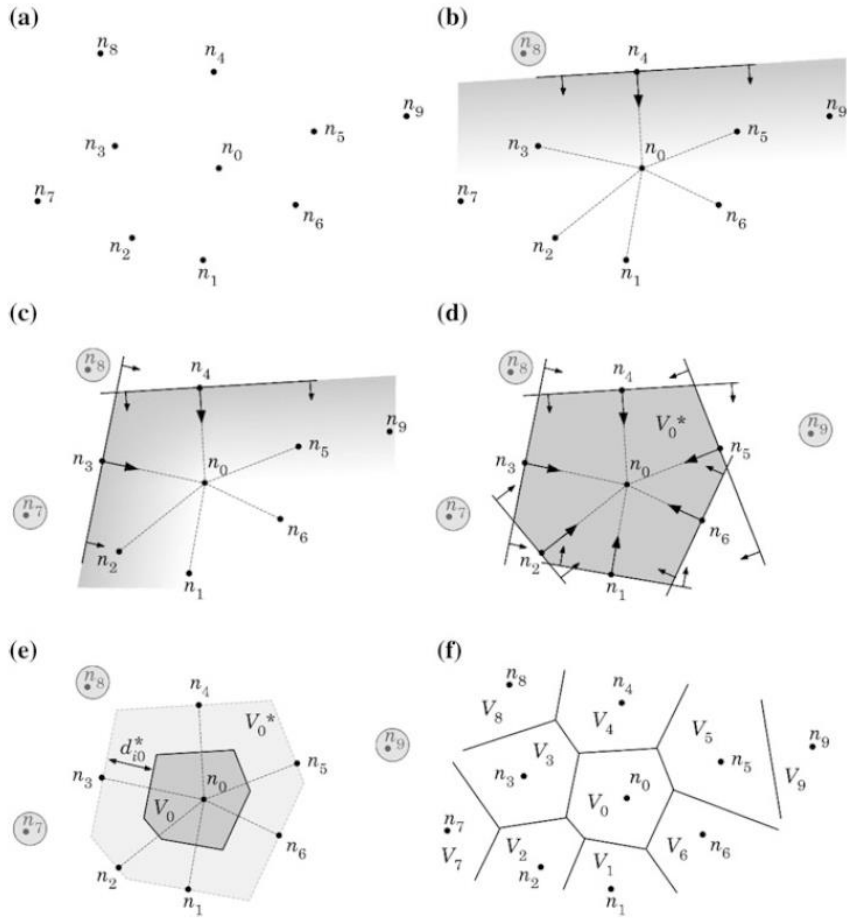

Figure 5. 5 – Process for obtaining the Voronoï diagram: (a) initial node set; (b) first experimental plane; (c) second experimental plane; (d) temporary Voronoï cell; (e) Voronoï cell from node n_0; (f) Voronoï diagram [76].

Taking as an example the scheme of Figure 5. 5, it is possible to obtain a provisional Voronoï cell that contains all neighbour's nodes of n_0. The nodes that are located outside of the region that comprehends the provisional selection are discarded. As a first step, a potential neighbour must be chosen, for example n_4 and the vector $\boldsymbol{u}_{40}$ must be determined:

$$\boldsymbol{u_{40}} = \frac{(\boldsymbol{x_0} - \boldsymbol{x_4})}{\|\boldsymbol{x_0} - \boldsymbol{x_4}\|} \tag{5. 6}$$

With $\boldsymbol{u_{40}} = \{u_{40}, v_{40}, w_{40}\}$. The nodes that do not meet the following relationship are excluded.

$$u_{40}x + v_{40}y + w_{40}z \geq (u_{40}x_4 + v_{40}y_4 + w_{40}z_4) \tag{5. 7}$$

This process is then repeated for each node included in the initial set of nodes in order to select the natural neighbours of node n_0. Therefore, the provisional Voronoï cell is obtained and converted into a definitive one. The distance between n_0 and the boundary of Voronoï cell is given by:

$$d_{n_0 n_i} = \frac{\|\boldsymbol{x_0} - \boldsymbol{x_i}\|}{2} \quad (5.\ 8)$$

Then, the other cells are obtained through a similar process for each node.

Influence-cell

In NNRPIM, there is a new concept for the nodal connectivity – the influence-cell concept. The cells are obtained using the information of the Voronoï diagram and the nodal connectivity is imposed by overlapping these influence-cells. The n nodes that compose these cells can interpolate the point of interest [76], [78].

In this sequence, there are two types of influence cells according to their level of nodal connectivity. The first-degree influence-cell of a point of interest comprises its natural neighbours, obtained from the Voronoï diagram. The second-degree influence-cells of a point of interest consists on the search for neighbouring nodes, similarly to first-degree influence-cells and, considering the Voronoï diagram, the natural neighbours of the first neighbours are added to the influence-cell (see Figure 5. 6) [78]. Since the size of the second-degree influence-cell is larger than the size of the first-degree influence-cell, it is predictable that using these cells would allow to obtain approximations with greater accuracy. The results documented in the literature confirm this anticipation.

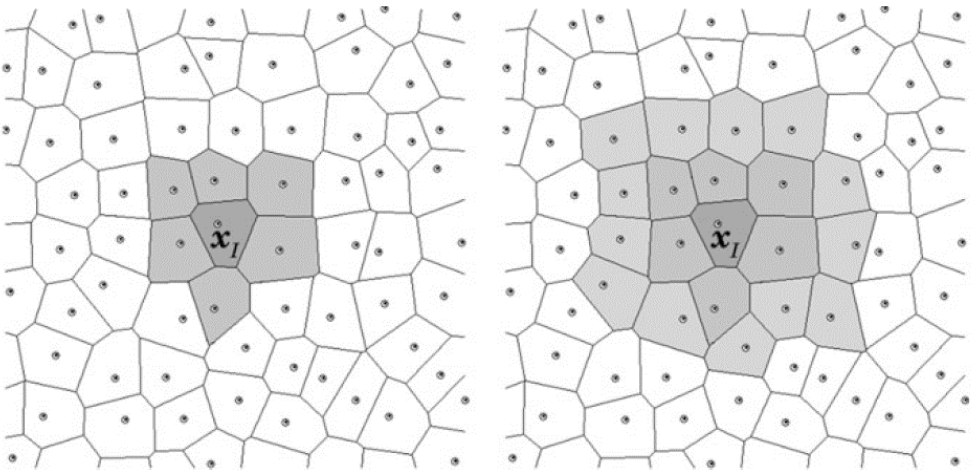

(a) (b)

Figure 5. 6 – (a) First-degree influence-cell; (b) Second-degree influence-cell [76].

5.2.2.3 Numerical Integration

- RPIM

RPIM uses the Gauss-Legendre quadrature scheme for numerical integration, requiring, for that purpose, a background integration mesh that is created according to one of the processes described in the general procedure. As seen in Figure 5. 3, the integration mesh can be obtained by the cells (quadrilateral or triangular) created to connect the nodes that discretised the problem's domain or by a larger regular mesh [76]. Inside each cell of the background

integration mesh, the integration points are distributed following the Gauss-Legendre quadrature rule, represented in Figure 5. 7.

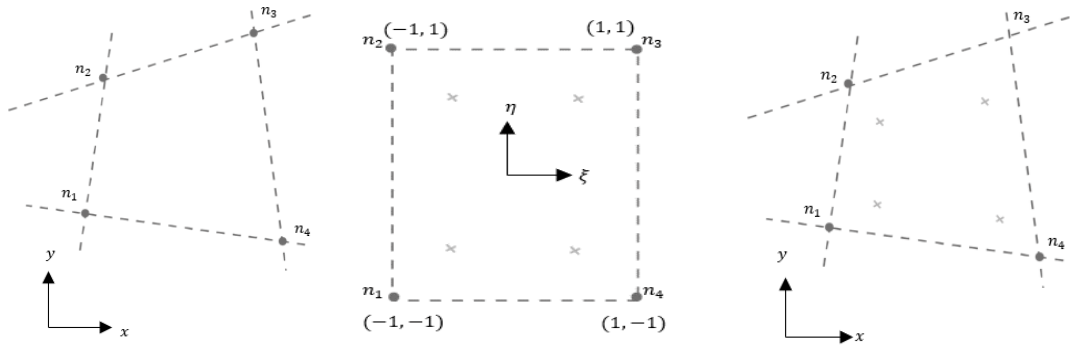

(a) (b) (c)

Figure 5. 7 – Gauss quadrature technique: (a) initial quadrilateral; (b) 2x2 scheme of the isoparametric square with 4 integration points; (c) return to Oxy.

After the distribution of the integration points in the isoparametric shape, its Cartesian coordinates are obtained using the following isoparametric interpolation functions, N_i:

$$\begin{aligned} N_1 &= \frac{1}{4}(1-\xi)(1-\eta) \\ N_2 &= \frac{1}{4}(1-\xi)(1+\eta) \\ N_3 &= \frac{1}{4}(1+\xi)(1+\eta) \\ N_4 &= \frac{1}{4}(1+\xi)(1-\eta) \end{aligned} \tag{5. 9}$$

Then, the Cartesian coordinates are expressed by:

$$\begin{aligned} x &= \sum_{i=1}^{m} N_i\,(\xi,\eta)\,.\,x_i \\ y &= \sum_{i=1}^{m} N_i\,(\xi,\eta)\,.\,y_i \end{aligned} \tag{5. 10}$$

Where m is the number of nodes that define the element and x_i and y_i are the Cartesian coordinates of nodes that defined the integration cells.

The integration weight of the integration point is given by equation (5. 12) and obtained by multiplying the isoparametric weight of the quadrature point with the Jacobian matrix determinant of the respective cell.

$$\boldsymbol{J} = \begin{bmatrix} \frac{\partial x}{\partial \xi} & \frac{\partial x}{\partial \eta} \\ \frac{\partial y}{\partial \xi} & \frac{\partial y}{\partial \eta} \end{bmatrix} \tag{5. 11}$$

The differential equation integration is then given by:

$$\int_{-1}^{1}\int_{-1}^{1} f(\boldsymbol{x})dxdy = \sum_{i=1}^{m}\sum_{i=1}^{m} \omega_i \omega_j f(\boldsymbol{x}) \tag{5. 12}$$

Where ω_i and ω_j are the weight in each direction of the integration point $\boldsymbol{x}$. This integration method can be reasoned for three dimensional problems using tetrahedral solids instead.

- **NNRPIM**

Once constructed the Voronoï diagram, an integration mesh can be obtained considering the nodal distribution. Therefore, the area of each Voronoï cell is divided by lines that intersect the central node of each neighbourhood node. The partition results are triangles, if the mesh is regular, or quadrilaterals in the case of the mesh being irregular. This process is called the Delaunay tessellation, and is represented in Figure 5. 8 [78].

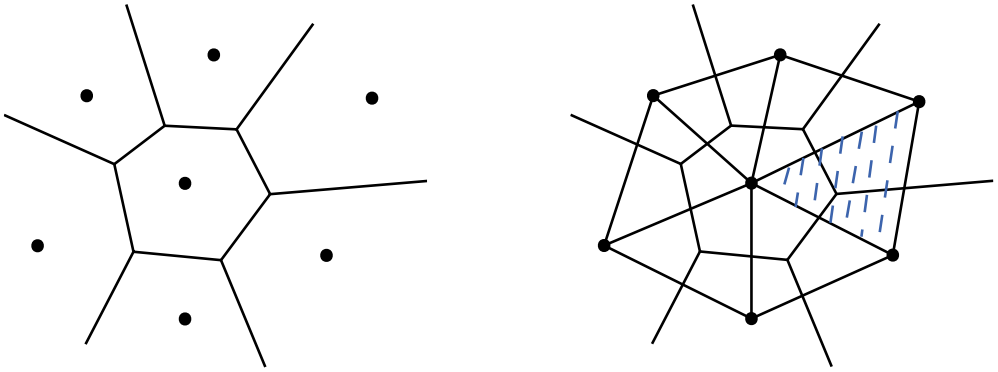

(a) (b)

Figure 5. 8 – (a) Initial Voronoï diagram, (b) Delaunay tessellation (triangulation)

As a result of the tessellation process, the cell is divided into a number of sub-cells equal to the number of neighbour nodes. Thus, the area of the cell, A_v, is equal to the sum of the area of each sub-cell, A_i, expressed by:

$$A_v = \sum_{i=1}^{n} A_i \, , \forall A_i \geq 0 \tag{5. 13}$$

As it was previously seen, the numerical integration of the NNRPIM is based in the Voronoi diagram and Delauny tessellation.

Similar to the RPIM, the numerical integration in the NNRPIM is based on the Gauss-Legendre concept, so the integration points are placed in the centre of each sub-cell. The simplest integration scheme resorts to the placement of only one point in each sub-cell and, in this case, the integration weight is the area of the corresponding sub-cell [78].

Still, more integration points can be added, for which the sub-cells are again divided by crossing the centre point with the middle points of the edges of the considered sub-cells, as depicted in Figure 5. 9. The formed cells are then quadrilateral (for both triangular or quadrilateral initial shapes) and the Gauss-Legendre numerical integration is applied to the resultant sub-quadrilaterals to obtain the integration points [78].

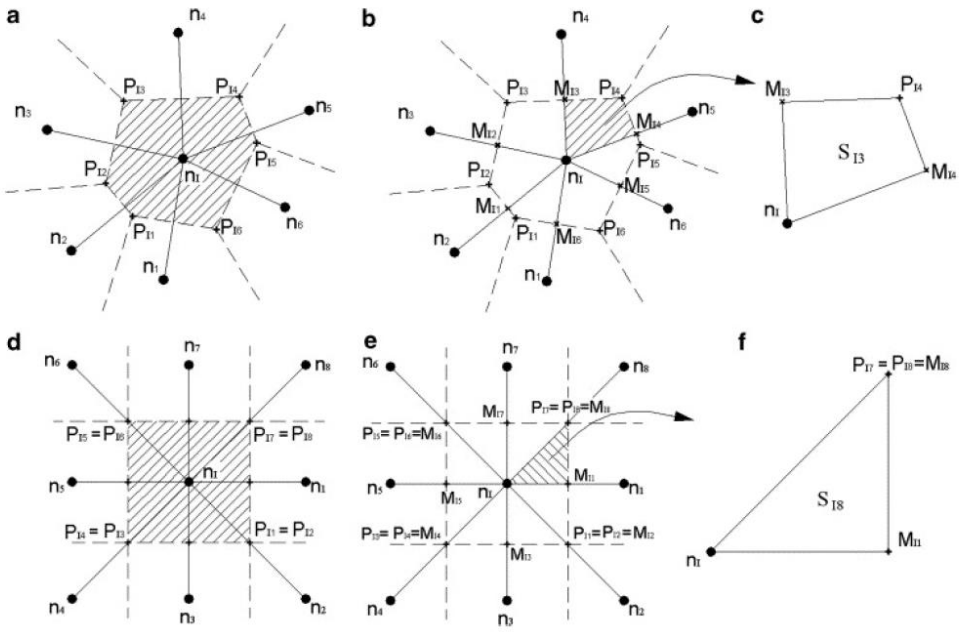

Figure 5. 9 – For an irregular mesh: (a) Voronoï cell and the intersection points, P; (b) middle points, M, and the corresponding generated quadrilaterals; (c) obtained quadrilateral sub-cell. For a regular mesh: (d) Voronoï cell and the intersection points, P; (e) middle points, M, and the corresponding generated triangles; (f) obtained triangular sub-cell.

Interpolation Functions

Since the meshless methods do not have elements, it is necessary to apply an interpolation method based on the nodal domain for the construction of the shape functions. Both RPIM and NNRPIM use the same procedure to construct the shape functions, using the radial point interpolation (RPI) technique combined with an RBF and a polynomial base function [76].

Considering a function, $u(\boldsymbol{x_I})$, defined in the domain Ω that is discretised by a set of n nodes, only the nodes inside the influence-cell of the point of interest, $\boldsymbol{x_I}$, have consequence over $u(\boldsymbol{x_I})$.

The value of $u(\boldsymbol{x_I})$ at the point of interest $\boldsymbol{x}_I$ is then given by:

$$u(\boldsymbol{x_I}) = \sum_{i=1}^{n} R_i(\boldsymbol{x_I}) a_i(\boldsymbol{x_I}) + \sum_{j=1}^{m} p_j(\boldsymbol{x_I}) b_j(\boldsymbol{x_I}) = \{\boldsymbol{R}(\boldsymbol{x_I})^T, \boldsymbol{p}(\boldsymbol{x_I})^T\} \begin{Bmatrix} \boldsymbol{a}(\boldsymbol{x_I}) \\ \boldsymbol{b}(\boldsymbol{x_I}) \end{Bmatrix} \quad (5.\ 14)$$

Where $R_i(\boldsymbol{x_I})$ is the RBF, n is the number of nodes inside the influence-cell of $\boldsymbol{x_I}$, $p_j(\boldsymbol{x_I})$ defines the m monomials of the polynomial basis and $a_i(\boldsymbol{x_I})$ and $b_i(\boldsymbol{x_I})$ are the associated non-constant coefficients. To guarantee a stable function, usually $m < n$.

The equation (5. 14) can be represented in the form of vectors:

$$\boldsymbol{R}(\boldsymbol{x_I}) = \{R_1(\boldsymbol{x_I}), R_2(\boldsymbol{x_I}), \dots R_n(\boldsymbol{x_I})\}^T \quad (5.\ 15)$$

$$\boldsymbol{p}(\boldsymbol{x_I}) = \{p_1(\boldsymbol{x_I}), p_2(\boldsymbol{x_I}), \dots p_m(\boldsymbol{x_I})\}^T \quad (5.\ 16)$$

$$\boldsymbol{a}(\boldsymbol{x_I}) = \{a_1(\boldsymbol{x_I}), a_2(\boldsymbol{x_I}), \dots a_n(\boldsymbol{x_I})\}^T \quad (5.\ 17)$$

$$\boldsymbol{b}(\boldsymbol{x_I}) = \{b_1(\boldsymbol{x_I}), b_2(\boldsymbol{x_I}), \dots b_m(\boldsymbol{x_I})\}^T \quad (5.\ 18)$$

The distance between $\boldsymbol{x_I}$ and the neighbour node $\boldsymbol{x_i}$ is given by $r_{Ii} = \|\boldsymbol{x_i} - \boldsymbol{x_I}\|$, which resembles the variable established in the RBF. In [79], several RBFs were developed, but the most popular is the Multiquadrics functions, that were initially proposed by Hardy [79] and is represented by:

$$R(r_{Ii}) = (r_{Ii}^2 + c^2)^p \quad (5.\ 19)$$

Where c and p are parameters that assume a value close to 0 and 1, respectively, for obtaining accurate results. The $\boldsymbol{a}$ and $\boldsymbol{b}$ (non-constant parameters) need to be determined.

The polynomial basis function is defined as:

$$\boldsymbol{p}(\boldsymbol{x})^{\boldsymbol{T}} = [1, x, y, x^2, xy, y^4, \dots] \quad (5.\ 20)$$

To assure a unique approximation, the polynomial term must be defined by:

$$\sum_{i=1}^{n} p_j(x_i)a_i = 0, \qquad j = 1,2,\dots,m \quad (5.\ 21)$$

Considering the previous equation and the equation (5. 14), it is obtained the following system:

$$\begin{bmatrix} \boldsymbol{R} & \boldsymbol{p} \\ \boldsymbol{p^T} & 0 \end{bmatrix} \begin{Bmatrix} \boldsymbol{a} \\ \boldsymbol{b} \end{Bmatrix} = \begin{Bmatrix} \boldsymbol{u_s} \\ 0 \end{Bmatrix} = \boldsymbol{G} \begin{Bmatrix} \boldsymbol{a} \\ \boldsymbol{b} \end{Bmatrix} \quad (5.\ 22)$$

Where:

$$\boldsymbol{R} = \begin{bmatrix} R(r_{11}) & R(r_{21}) & \cdots & R(r_{1n}) \\ R(r_{21}) & R(r_{22}) & \cdots & R(r_{2n}) \\ \vdots & \vdots & & \vdots \\ R(r_{n1}) & R(r_{n2}) & \cdots & R(r_{nm}) \end{bmatrix} \quad (5.\ 23)$$

$$\boldsymbol{u_s} = \{u_1, u_2, \cdots u_n\}^T \quad (5.\ 24)$$

The polynomial basis is defined as:

$$Constant\ basis: \boldsymbol{p} = \{1\ 1 \cdots 1\}^T \tag{5. 25}$$

$$2D\ problem: \boldsymbol{p} = \begin{bmatrix} 1 & 1 & \cdots & 1 \\ x_1 & x_2 & \cdots & x_n \\ y_1 & y_2 & \cdots & y_n \end{bmatrix}^T \tag{5. 26}$$

$$3D\ problem: \boldsymbol{p} = \begin{bmatrix} 1 & 1 & \cdots & 1 \\ x_1 & x_2 & \cdots & x_n \\ y_1 & y_2 & \cdots & y_n \\ z_1 & z_2 & \cdots & z_n \end{bmatrix}^T \tag{5. 27}$$

Then, the non-constant coefficients can be determined with the following equation:

$$\begin{Bmatrix} \boldsymbol{a} \\ \boldsymbol{b} \end{Bmatrix} = \boldsymbol{G}^{-1} \begin{Bmatrix} \boldsymbol{u}_s \\ 0 \end{Bmatrix} \tag{5. 28}$$

Replacing in equation (5. 14):

$$u(\boldsymbol{x_I}) = \{\boldsymbol{R}(\boldsymbol{x_I})^T, \boldsymbol{p}(\boldsymbol{x_I})^T\}\boldsymbol{G^{-1}} \begin{Bmatrix} \boldsymbol{u_s} \\ 0 \end{Bmatrix} = \{\Phi(\boldsymbol{x_I}), \Psi(\boldsymbol{x_I})\} \begin{Bmatrix} \boldsymbol{u_s} \\ 0 \end{Bmatrix} \tag{5. 29}$$

With $\Phi(\boldsymbol{x_I}) = \{\varphi_1(\boldsymbol{x_I}), \varphi_2(\boldsymbol{x_I}), \cdots, \varphi_n(\boldsymbol{x_I})\}$ representing the shape function and $\Psi(\boldsymbol{x_I}) = \{\psi_1(\boldsymbol{x_I}), \psi_2(\boldsymbol{x_I}), \cdots, \psi_m(\boldsymbol{x_I})\}$ representing a by-product of the equation system (without any physical meaning).

$$\varphi(\boldsymbol{x_I}) = \{\boldsymbol{R}(\boldsymbol{x_I})^T, \boldsymbol{p}(\boldsymbol{x_I})^T\}\boldsymbol{G^{-1}} = \{\Phi(\boldsymbol{x_I}), \Psi(\boldsymbol{x_I})\} = \{\varphi_1(\boldsymbol{x_I}), \varphi_2(\boldsymbol{x_I}), \cdots, \varphi_n(\boldsymbol{x_I}), \psi_1(\boldsymbol{x_I}), \psi_2(\boldsymbol{x_I}), \cdots, \psi_m(\boldsymbol{x_I})\} \tag{5. 30}$$

The RPIM shape function $\Phi(\boldsymbol{x_I})$ respects the delta Kronecker property, allowing the use of direct imposition techniques to apply the essential boundary conditions in the stiffness matrix.

$$\varphi_i(\boldsymbol{x_j}) = \delta_{ij} \tag{5. 31}$$

Where δ_{ij} is the delta Kronecker, for which $\delta_{ij} = 0$ if $i = j$ and $\delta_{ij} = 1$ if $i \neq j$.

Chapter 6

Fluid Mechanics

Fluid mechanics is an area of physics that studies the flow of fluids and the forces exerted upon them. The properties that describe a fluid are, generally, the density, compressibility and the dynamic viscosity, that is characteristic of each fluid and depends on the environment in which it is inserted.

In this chapter, the concepts of velocity and strain rate are described, as well as the discretization process.

6.1 Fundamentals of Flow Formulation

In studies of flow dynamics, it is generally considered that the elastic effects are insignificant, which allows to treat the fluid as viscoplastic. This assumption defines the material under study as unable to sustain deviatoric stress while static.
Another important feature of flow problems is that velocities, $\boldsymbol{v}$, rather than displacements, $\boldsymbol{u}$, are of principal importance and is described by a time integration:

$$\frac{\partial \boldsymbol{u}}{\partial t} = \boldsymbol{v} \tag{6. 1}$$

In this sequence, using the definition of strain and replacing the displacements by the velocities, the strain rate, $\dot{\varepsilon}$, can be defined as

$$\dot{\varepsilon}_{ij} = \frac{1}{2}\left(\frac{\partial v_i}{\partial x_j} + \frac{\partial v_j}{\partial x_i}\right) \tag{6. 2}$$

The rate of deformation (or strain rate) is related to the stress tensor, σ , that considering a flow formulation of incompressible viscoplastic material is described by a sum of two contributors: a deviatoric stress tensor, σ_d, and an average stress tensor, σ_m:

$$\sigma = \sigma_d + \sigma_m \tag{6. 3}$$

$$\sigma_{\boldsymbol{m}} = p\boldsymbol{I} \tag{6. 4}$$

Being p the pressure and $\boldsymbol{I}$ the identify matrix.

Following a similar reason, the strain rate tensor is given by,

$$\dot{\varepsilon} = \dot{\varepsilon}_d + \dot{\varepsilon}_m \tag{6. 5}$$

Where $\dot{\varepsilon}_d$ is the deviatoric strain rate and $\dot{\varepsilon}_m$ an isotropic strain rate defined by

$$\dot{\varepsilon}_m = \dot{\varepsilon}_m \boldsymbol{I} \tag{6. 6}$$

Considering the previous equations and assumptions (that were taken from [80], [81]), the deviatoric stresses and deviatoric strain rates present a proportional relation,

$$\sigma_d = \mu \boldsymbol{I_0} \dot{\varepsilon} \tag{6. 7}$$

Where μ is the material viscosity and $\boldsymbol{I_0}$ is the matrix represented as,

$$\boldsymbol{I_0} = \begin{bmatrix} 4 & -2 & 0 \\ -2 & 4 & 0 \\ 0 & 0 & 3 \end{bmatrix} \tag{6. 8}$$

Since in this work the fluid is considered incompressible, it is necessary to impose a numerical formulation to define it. This formulation is the penalty method, being required the use of a penalty parameter, which can be a function of viscosity,

$$\alpha = 10^{7-8}\mu \tag{6. 9}$$

6.2 Problem Discretization

The flow formulation permits the analysis of the material using the traditional displacement-based methodology. Thus, the nodal displacements that are considered in the regular 2D linear elastic equations are now replaced by velocities. The vector of nodal velocities is then written as equation (6. 10), where the nodal values are represented with a tilde above v.

$$\tilde{\boldsymbol{v}} = [\tilde{v}_{x1} \quad \tilde{v}_{y1} \quad \tilde{v}_{x2} \quad \tilde{v}_{y2} \quad \cdots \quad \tilde{v}_{xn} \quad \tilde{v}_{yn}]^T \tag{6. 10}$$

Therefore, the velocity in a point of interest is given by,

$$\boldsymbol{v} = \boldsymbol{N_v}\tilde{\boldsymbol{v}} \tag{6. 11}$$

Being $\boldsymbol{N_v}$ the velocity shape functions matrix, defined as,

$$\boldsymbol{N_v} = \begin{bmatrix} N_{v1} & 0 & N_{v2} & 0 & \cdots & N_{vn} & 0 \\ 0 & N_{v1} & 0 & N_{v2} & \cdots & 0 & N_{vn} \end{bmatrix} \tag{6. 12}$$

In the same line of thought, the vector of nodal pressures is given by,

$$\tilde{\boldsymbol{p}} = [\tilde{p}_1 \quad \tilde{p}_2 \quad \cdots \quad \tilde{p}_n]^T \tag{6. 13}$$

Which is used to obtain the pressure at any point of interest with the following equation,

$$p = \boldsymbol{N_p}\tilde{\boldsymbol{p}} \tag{6. 14}$$

Where the shape functions matrix of the pressure, $\boldsymbol{N_p}$, is expressed by,

$$\boldsymbol{N_p} = [N_{p1} \quad N_{p2} \quad \cdots \quad N_{pn}] \tag{6. 15}$$

The equation (6. 15) with the strain operator matrix, $\boldsymbol{S}$, allows to write the strain vector as,

$$\dot{\varepsilon} = \boldsymbol{S}\boldsymbol{v} = \boldsymbol{S}\boldsymbol{N_v}\tilde{\boldsymbol{v}} \tag{6. 16}$$

Where,

$$\boldsymbol{S} = \begin{bmatrix} \frac{\partial \varphi_1}{\partial x} & 0 & \frac{\partial \varphi_n}{\partial x} & 0 \\ 0 & \frac{\partial \varphi_1}{\partial y} \ldots & 0 & \frac{\partial \varphi_n}{\partial y} \\ \frac{\partial \varphi_1}{\partial y} & \frac{\partial \varphi_1}{\partial x} & \frac{\partial \varphi_n}{\partial y} & \frac{\partial \varphi_n}{\partial x} \end{bmatrix} \tag{6. 17}$$

Being φ the shape function and n the number of inside the influence-domain of the point of integration $\boldsymbol{x}_i$ or the number of nodes forming the element containing the integration point $\boldsymbol{x}_i$.

Since the pressure is equal to the mean stress, the stress is defined as the following constitutive law,

$$\sigma = \mu \boldsymbol{D_0}\dot{\varepsilon} + \boldsymbol{m}p \tag{6. 18}$$

or,

$$\sigma = 2\mu\left(\dot{\varepsilon}_{ij} - \frac{\delta_{ij}\varepsilon_{kk}}{3}\right) + \delta_{ij}p \tag{6. 19}$$

Where σ is the stress, μ the viscosity, δ_{ij} the delta Kronecker property and $\boldsymbol{m}$ and $\boldsymbol{D_0}$ are matrices defined by, for a 2D problem,

$$\boldsymbol{m} = \{1 \quad 1 \quad 0\} \tag{6. 20}$$

$$\boldsymbol{D_0} = \begin{bmatrix} \frac{4}{3} & -\frac{2}{3} & -\frac{2}{3} & 0 & 0 & 0 \\ -\frac{2}{3} & \frac{4}{3} & -\frac{2}{3} & 0 & 0 & 0 \\ -\frac{2}{3} & -\frac{2}{3} & \frac{4}{3} & 0 & 0 & 0 \\ 0 & 0 & 0 & 1 & 0 & 0 \\ 0 & 0 & 0 & 0 & 1 & 0 \\ 0 & 0 & 0 & 0 & 0 & 1 \end{bmatrix} \tag{6. 21}$$

Despite the nonexistence of the inverse of $\boldsymbol{D_0}$, it can be written as,

$$\dot{\boldsymbol{\varepsilon}} = \frac{1}{\mu}\boldsymbol{D}^{-1}(\boldsymbol{\sigma} - \boldsymbol{m}p) \tag{6. 22}$$

With

$$\boldsymbol{D^{-1}} = \begin{bmatrix} 2 & 0 & 0 & 0 & 0 & 0 \\ 0 & 2 & 0 & 0 & 0 & 0 \\ 0 & 0 & 2 & 0 & 0 & 0 \\ 0 & 0 & 0 & 1 & 0 & 0 \\ 0 & 0 & 0 & 0 & 1 & 0 \\ 0 & 0 & 0 & 0 & 0 & 1 \end{bmatrix} \tag{6. 23}$$

Generally, the viscosity is dependent on the strain rate, following the relation,

$$\mu = (\sigma_y + \gamma \dot{\tilde{\varepsilon}}^m)/3\dot{\tilde{\varepsilon}} \tag{6. 24}$$

Where σ_y is the uniaxial yield stress, which is a function of the second invariant of the strain rate, $\tilde{\varepsilon}$, and temperature, T. The fluidity parameter is γ.

$$\sigma_y = \sigma_y(\tilde{\varepsilon}, T) \tag{6. 25}$$

$$\dot{\tilde{\varepsilon}} = \left(\frac{2}{3}\dot{\varepsilon}_{ij}.\dot{\varepsilon}_{ij}\right)^{1/2} \tag{6. 26}$$

Assuming pure elasticity, $\gamma = 0$, the governing equations of the problem are now the conservation momentum,

$$\boldsymbol{S^T\sigma} + \boldsymbol{b} = 0 \tag{6. 27}$$

Where $\boldsymbol{b}$ is the body force and incompressibility defined as,

$$\boldsymbol{m^T S v} = 0 \tag{6. 28}$$

In equations (6. 12) and (6. 15) it is defined the matrix of velocity and pressure shape functions, respectively. It is important to notice that the former was obtained in the integration points, considering a full integration mesh, while the second was obtained in the reduced integration mesh, considering the points of integration coincident with the nodes. This leads to,

$$\begin{bmatrix} \boldsymbol{K} & \boldsymbol{Q} \\ \boldsymbol{Q^T} & \boldsymbol{0} \end{bmatrix} \begin{bmatrix} \tilde{\boldsymbol{v}} \\ \tilde{\boldsymbol{p}} \end{bmatrix} = \begin{bmatrix} \boldsymbol{f} \\ \boldsymbol{0} \end{bmatrix} \tag{6. 29}$$

Where

$$\boldsymbol{K} = \int_\Omega (\boldsymbol{SN_v})^T \mu \boldsymbol{D_0} (\boldsymbol{SN_v})\, d\Omega \tag{6. 30}$$

$$\boldsymbol{Q} = \int_\Omega (\boldsymbol{SN_v})^T \boldsymbol{m N_p}\, d\Omega \tag{6. 31}$$

$$\boldsymbol{f} = \int_\Omega (\boldsymbol{N_v})^T \boldsymbol{b}\, d\Omega + \int_\Omega (\boldsymbol{N_v})^T \boldsymbol{t}\, d\Omega \tag{6. 32}$$

Where $\boldsymbol{K}$ is the stiffness matrix associated with velocity, $\boldsymbol{Q}$ is the matrix that imposes the incompressible condition and $\boldsymbol{f}$ is the vector of external forces.

In the previous discretization it is required to guarantee that the resulting equations are never singular, so convergence is assured by the following condition,

$$\begin{bmatrix} \boldsymbol{K_e} & \boldsymbol{Q_e} \\ \boldsymbol{Q_e^T} & \dfrac{\boldsymbol{I}}{\boldsymbol{\alpha}} \end{bmatrix} \begin{bmatrix} \widetilde{\boldsymbol{v}}_e \\ \widetilde{\boldsymbol{p}}_e \end{bmatrix} = \begin{bmatrix} \boldsymbol{f_e} \\ \boldsymbol{0} \end{bmatrix} \tag{6. 33}$$

Where α is the penalty number and $\boldsymbol{I}$ is the identity matrix. This result in a single stiffness matrix,

$$\widetilde{\boldsymbol{K}}_e \widetilde{\boldsymbol{v}}_e = (\boldsymbol{K_e} - \boldsymbol{Q_e Q_e^T}) \widetilde{\boldsymbol{v}}_e = \boldsymbol{f_e} \tag{6. 34}$$

And the final assembled non-linear system of equations, described as it follows, are solved iteratively,

$$\widetilde{\boldsymbol{K}} \widetilde{\boldsymbol{v}} = \boldsymbol{f} \tag{6. 35}$$

$$\widetilde{\boldsymbol{K}} = \widetilde{\boldsymbol{K}}(\boldsymbol{v}), \qquad \mu(\dot{\varepsilon}) = \mu(\boldsymbol{v}) \tag{6. 36}$$

Chapter 7

Numerical Methods in Hemodynamics

7.1 Blood Flow Assessment

The first studies of blood flow were performed in tubes with a constant cross-section, which intended to reproduce the blood vessel's geometry. In this sequence, in 1838 it was published the Poisseuille's law, that derived from a study in narrow tubes, in which was described the relationship between flow and pressure gradient [9].

Later, when the influence of blood flow in the arterial disease development started to be questioned, the scientific community focused on the study of flow patterns using several techniques, such as hot film anemometry, laser Doppler anemometry and photochromic methods or dye injections [82]. Regarding the aorta artery, the hot film anemometry technique was applied to determine the velocity profiles inside the vessel. The results showed that flow is highly disturbed in the ascending aorta [83].

In vivo 3D study concerning blood flow was primarily documented at the beginning of the 1990s and it was performed through use of angioscopy. A few years later, Doppler ultrasound emerged, and, when applied in the study of the aorta, 3D spiral flow patterns were detected at several locations of the vessel [84].

Despite the evolution of imaging techniques for assessing blood flow patterns, mathematical and numerical methods have also emerged in parallel. In 1968, Huckaba and Hahn [67] developed a realistic mathematical approach for modelling arterial blood flow, taking as starting point the studies of blood rheology completed by Merrill, Hershey *et al*. and Charm *et al*. [67]. At that point, they assumed that flow through an artery was "almost periodic, unsteady-state flow of a non-Newtonian fluid through a flexible-walled, tapered branching conduit.".

Concerning the hemodynamics in a specific blood vessel - the abdominal aorta-, the majority of studies are taken from two papers: Mills et al., that measured blood velocity in large arteries using catheter tip velocity probe (invasive method) and Olufsen et al., that used MRI to measure the flow along the aorta [3]. Currently, this last imaging technique is widely used for validating results of numerical simulation studies.

7.2 Numerical Analysis Applied to Blood Flow

With the evolution of technology and the rise of more powerful computer systems, blood flow problems started to be simulated using numerical methods. These methods have been applied for almost 30 years, being the most common the Finite Difference (FDM), Finite Volume (FVM) and Finite Element Methods [22], [85]. All these methods rely on a grid to discretise the governing equations. The former method was first utilised by Euler, in 1768, being the oldest method among the three previously enumerated and, for many years, it was the preferred [30], [86]. In modern solvers, FDM is less common because the construction of the finite difference operator is complex for grids that are not structured and uniform which, in their turn, are characteristic of complex 3D geometries.

Posteriorly, the finite element method appeared in the 1950s and it was originally used for discretising geometries of solid mechanics. With the advances in the computational sciences, this method has been successfully applied in the study of complex geometries not only in the solid mechanics field, but also in the fluid mechanics' area, as for example, in the analysis of hemodynamics in aneurysms [33], [76]. Since FEM will be implemented in the present dissertation, a more detailed review of its evolution and applications will be explained in the next subchapter.

Another method that is widely applied for discretising the Navier-Stokes equations is the finite volume method (FVM). This method is characterised by high geometrical flexibility, in other words, it can discretise complex geometries with structured or unstructured grids, maintaining its computational efficiency [87]. Due to this aspect, FVM is especially suitable for the simulation of flows in complex geometries. The first application of this method was carried out by McDonald, in 1971, for the simulation of 2D inviscid flows (without viscosity) [88]. Then, the FVM was also transposed to the analysis of biological fluids, such as blood flow. In the study of Azam and Salam [33], three-dimensional analysis of non-Newtonian blood flow in a 3D model of AAA was performed using the finite volume method. The results showed that recirculating vortices were present in both the systolic and diastolic phases of the cardiac cycle and it increased the blood clot formation inside an aneurysm. Also, the pressure gradient inside the vessel is responsible for thrombus formations and dilation of the aneurysm wall, that can lead to rupture. Recently, Joly *et al*. [49] utilised the concept of Lagrangian-coherent structures, a flow tracer, for characterising blood flow's transport inside a geometrical model of an AAA.

Other FVM studies have been performed concerning the flow inside blood vessels, not only in disease states, but also in zones of disrupted flows, such as in the aortic arch [65] and in the aortic bifurcation [57].

In sum, the 1970s and, in particular, the 1980s were a period of great evolution regarding algorithms and methods applied to the study of 3D flows (vectorisation, domain decomposition, multigrid and methods for specific purposes, such as particle methods) [7], [89].

Although the previously referred methods are widely used, other numerical methods, such as meshless methods, were formulated and successfully applied to solve problems of engineering and biological sciences. In this dissertation, meshless methods will be implemented, so the revision of the state-of-the-art about this subject will be described in more detail in subchapter 7.4.

7.3 FEM

The finite element method has its start in solid mechanics, specifically in the aeronautic field, with pioneering work done by Turner, Clough, Martin and Topp (1956) [90]. Regardless this original publication of the method, the first time that the name "FEM" appeared in literature was in a paper of Clough, published in 1960 [91]. Since its first publication to this day, FEM has been applied in most of the complex physical problems that are impossible to solve using classical analytical approaches. More recently, this method was transposed for the resolution of fluid mechanics problems, including the analysis of biological fluids such as blood flow. Since the aim of this dissertation is the study of blood flow in aortic aneurysms, this subchapter is organised according to three lines of studies: (1) FEM applied to aortic aneurysms; (2) FEM applied to blood flow and (3) FEM applied to blood flow in aortic aneurysms.

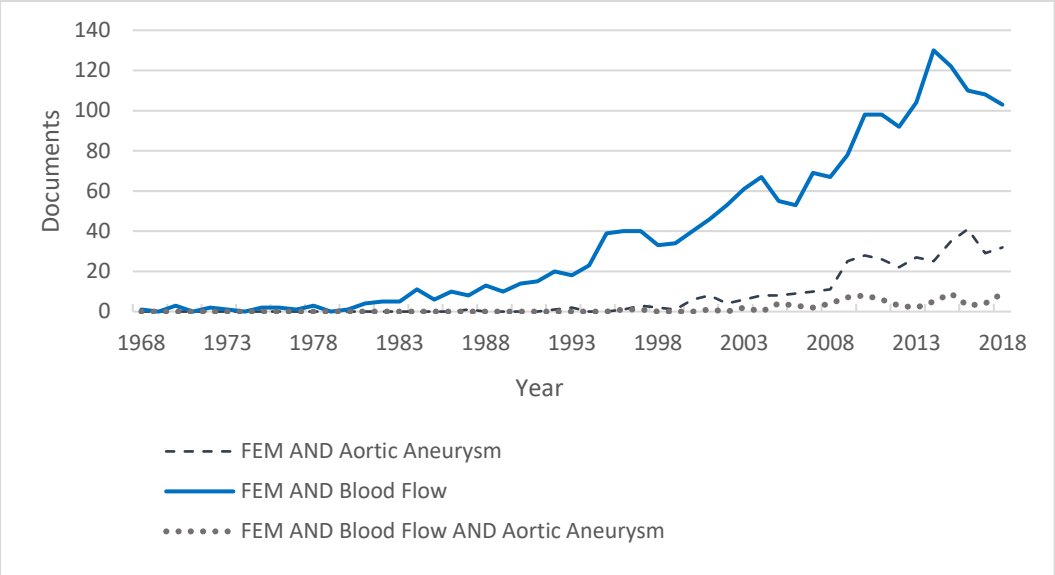

Figure 7. 1 - Number of documents published over the years, in the indicated fields. The data was obtained through a research made on *Scopus* database (www.scopus.com), considering as keywords the subjects designated in the graph.

To understand the evolution of FEM in the blood flow field, a research on *Scopus* database was performed, using different keywords. In the graph depicted in Figure 7. 1, it can be verified that, regardless of the keywords that were used ("FEM AND Blood Flow" or "FEM AND Blood Flow AND Aortic Aneurysm"), the number of papers using FEM on blood flow analysis follows a rising trend over the years, demonstrating that it stills a subject of substantial interest. When the search is narrowed to a more detailed area of hemodynamics ("FEM AND Blood Flow AND Aortic Aneurysms"), the trend is less growing, which can indicate that there are still many questions to be answered and there is a field of opportunities for new researches, specifically in aortic aneurysm's structures.

Concerning the keywords "FEM AND Aortic Aneurysms", the results include not only the hemodynamic studies, but also studies applied to the analysis of the mechanical properties of the vessel wall, that is inherent to the area of solid mechanics. Also, these results comprise the analysis of the interaction between blood flow and the vessel wall, which will not be detailed in this dissertation.

7.3.1 FEM applied to aortic aneurysms

According to Figure 7. 2, the first study of FEM applied to aortic aneurysms was published in 1987. Stringfellow *et al*. [92] were the authors of this pioneer publication, in which it was calculated the influence of the aortic aneurysm geometry in the stress of the aneurysm wall. Since then, several studies were performed in order to comprehend some features such as: the biomechanical factors that lead to aortic aneurysm's rupture [93], the influence of the aortic diameter in the stress fields inside the diseased vessel [94], the effect of ILT on aortic aneurysm's wall stresses [51] and fluid-structure interaction (FSI) approaches to obtain results concerning the influence of the blood flow in the vessel wall expansion and disease formation [21].

As it was previously stated, this sort of studies are not the scope of this thesis however, it is important to mention them for a better comprehension of the approaches that have been made in the study of aortic aneurysms. For a more in-depth knowledge on the field, consult the references [2], [43], [52].

7.3.2 FEM applied to blood flow

The application of finite element methods in problems of fluid mechanics occurred when, near the end of the 1960s and early 1970s, it was realised that this method could be applied to non-symmetric operators. Thenceforward, FEM started to be widely used for solving complex fluid problems, including the resolution of finite models of Navier-Stokes equations, that were first presented in 1969 [7].

No long after the first publication of FEM in fluid problems, the potentialities of this method have led the scientific community to begin to explore problems in the most diverse fields of science, including in the field of bioengineering. Although the first publication on numerical analysis of blood flow with FEM was in 1968, the first relevant study was published in 1970 by Davids [95]. It was developed a precursor study which sought to formulate an efficient and unified procedure for analysing fluid-flow problems. For that purpose, it was performed a numerical analysis of viscous flow in a long tube of constant diameter, under time-varying pressures. The flow rates, the velocity profiles and the wall shearing stresses were obtained as results.

Two decades later, in 1991, the application of finite element methods in blood flow problems was extended to more complex structures. In this sequence, Wong, Jonhston, Ethier and Cobbold [82] studied blood flow in arteries of various geometries in order to understand how the flow patterns are affected by the geometry of the vessel. To achieve that goal, a computer program was developed to simulate steady and pulsatile flow by solving the governing equations with the finite element method. Several models of arterial structures were considered: normal, stenosed and aneurysmal arteries, and bifurcations models. The authors concluded that zones prone to an arterial disease are related to regions of flow recirculation or stagnation. These results are validated and in agreement with the conclusions drawn by Caro *et al*. [96], in a paper published in 1971, concerning the influence of flow patterns in the arterial wall.

In the mid-1990s, the models used for studying blood flow started to be more realistic: imaging techniques, such as MRI and CT, were used to provide accurate replicas of *in vivo* arteries or to obtain computer models for blood flow modelling [97], [98]. Thenceforth, the

number of studies of fluid-flow in biological geometries started to rise, with more complexed features and accurate results.

7.3.3 FEM applied to the study of blood flow in aortic aneurysms

In Chapter 4, on aortic aneurysms, it was explained that this pathology presents unclear and unspecific symptoms, so the early diagnoses become important for disease's evolution, follow-up and intervention. On the other hand, it was also seen in Chapter 3 that blood plays a vital role in the development and progression of arterial pathologies, including in the aorta. In this sequence, the study of the blood influence, resorting to numerical simulations, on such a mortal and asymptomatic disease (such as aortic aneurysms) has intrigued the scientific community since the end of the 20th century.

The first article concerning the application of FEM on aortic aneurysm's hemodynamic problems was published in 1996, by Khraishi *et al.* [8]. The model that was used consisted of an axisymmetric bulge in a tube, which was intended to approximate the geometry of an abdominal aortic aneurysm. The flow equations were solved numerically with the finite element method, and as outcomes it was observed that the geometry of the model (AAA shape) profoundly influences the pressure, shear stresses and flow patterns.

Half a decade later, in 2001, it emerged the first study in which the geometrical model was obtained through an imaging technique (in this case, the multislice CT) [99]. In contrast, nowadays, almost all studies adopt imaging techniques to reproduce with accuracy the anatomical features of the vessels under investigation. This promotes better outcomes in blood flow studies.

It was at the beginning of the 21st century that the approaches on blood flow studies started to incorporate the interaction between the vessel wall and blood in a method called fluid-structure interaction (FSI). However, in this dissertation, the focus is only on blood flow and not in its repercussion in the vessel wall. More information regarding blood flow in arteries, including in aneurysms, can be found in the review made by Lighthill [100] and Lasheras [14].

Another important feature that has been increasingly implemented on aortic aneurysms geometrical models is the intraluminal thrombus (ILT), which plays a significant role in the vessel rupture and is originated due to the hemodynamic behaviour inside the diseased aorta. The studies that are performed with the focus on ILT aim to determine its influence and growing on the aneurysm's wall and not just the blood flow passage through an aneurysm that present ILT [46], [50].

Regardless of the progress and results that have been made all over the years in this field of study using FEM, another type of methods started to attract the attention of the computational fluid mechanics community – the meshless methods.

7.4 Meshless Methods

It is widely known that difficulties are often encountered when discretising models with 3D meshes, such as in the finite element method. Therefore, since the early 1980s, different authors have explored the possibility of developing numerical methods where meshes were not necessary. The first attempts come from finite difference (FD) experts that acquired FD structures in random irregular grids, however, it was only in 1988 that was developed the first meshless approximation method – the Smoothed-Particle Hemodynamics (SPH), which belong to the group of Free-Lagrange methods. The SPH had its roots in computational physics and astrophysics and consisted on a set of arbitrary particles. Later, SPH originated another method, the Reproducing Kernel Particle Method (RKPM) [101].

In 1994, Nayroles *et al*. developed the Diffuse Element Method (DEM), where only a set of nodes and a boundary description is required to formulate the Galerkin equations. Also, the interpolating functions in this method are constructed using the Moving Least-Squares approximants (MLS), that were proposed by Salkauskas and Lancaster. Even though no finite element mesh is required in DEM, there is a need for an "auxiliary grid", so Belytschko et al. extended this method, calling it the Element-Free Galerkin Method (EFGM), that is currently one of the most popular and stable meshless method applied to both solid and fluid mechanics [102], [103].

Since the previous approximation methods do not present the delta Kronecker property, they are limited in the imposition of natural and essential boundary conditions, so several interpolation methods have been developed, as for example the Natural Element Method (NEM) [104], the Point Interpolation Method (PIM) [105], the Radial Point Interpolation Method (RPIM) [106], the Meshless Finite Element Method (MFEM) [107], and the Natural Neighbour Finite Element Method (NNFEM) [78].

The PIM originated the RPIM by combining the (original) polynomial basis function with a Gaussian Radial Basis Function (RBF). The combination of the NEM and the RPIM originated an improved meshless method, the Natural Neighbour Radial Point Interpolation Method (NNRPIM). This method constructs the interpolation functions similarly to the RPIM and uses the natural neighbour concept to describe nodal connectivity and generate a background integration mesh. Since the integration mesh is entirely dependent on the nodes, the NNRPIM in considered a "truly" meshless method [76].

In this thesis, the meshless methods used were the RPIM and the NNRPIM, therefore, a brief survey of the published work concerning the study of blood flow using these methods will be presented.

Meshless methods have been extended, through the years, to other fields such as flow dynamics, which includes blood flow's studies in human anatomic models. For understanding the application of meshless methods on the scope of the dissertation, a survey was performed in Scopus database, where it was obtained the graph depicted in Figure 7. 2.

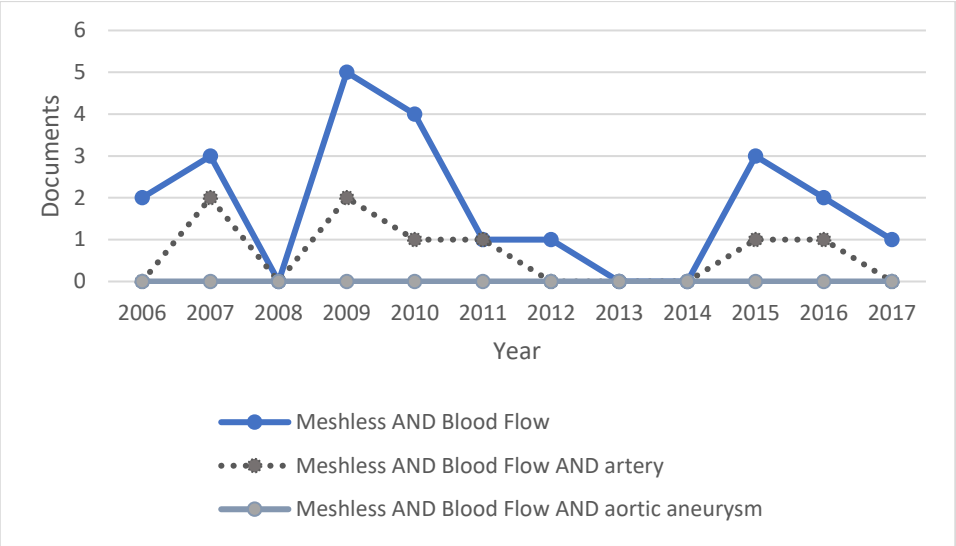

Figure 7. 2 - Number of documents published over the years, in the indicated fields. The data was obtained through a research made on *Scopus* database (www.scopus.com), considering as keywords the topics designated in the graph.

As seen in Figure 7. 2, this advanced method has not been widely used in the study of blood flow. One of the first reports of a meshless method applied in fluid mechanics problems was published in 1996, with the implementation of a stabilised finite point method for solving convection-diffusion and convective transport problems [101], [103].

Regarding the blood flow, the first work was published just in 2006. It consisted of a two-dimensional analysis of the blood flow in arterial anastomoses and the results were then compared to the ones provided by a finite volume method commercial software, showing a significant agreement [108]. Several papers were published over the years and it was revealed a tendency for the application of the smoothed particle hydrodynamics formulation. This particular method is widely used in flow problems since it is suited for simulating problems with complex boundary dynamics and it possesses a low computational cost. For instance, applications of these methods can be found in a report published in 2010, where it was implemented the smoothed particle hydrodynamics formulation for a non-Newtonian flow in a study of blood-vessel interaction [109]. Later, in 2016, the same formulation was used to understand the characteristics of blood flow and the formation of thrombus in a blood vessel [110]. Concerning the methods that will be used in the dissertation (RPIM and NNRPIM), no published papers were found in the literature. Specifying the search for the study of blood flow in aortic aneurysms, there is no register in the literature concerning the application of meshless methods in this field.

Chapter 8

Preliminary Work

In this chapter, it will be presented the preliminary work concerning aortic artery's fluid flow analysis. This chapter begins with the study of blood flow in simple 2D and 3D geometries, which comprises a convergence analysis and the calibration of the parameters of simulation. Then, 2D and 3D models of an abdominal aortic aneurysm are introduced, and a static fluid flow analysis is carried out in order to comprehend the influence of the variation of the aneurysm's diameter in the blood flow patterns.

To perform the numerical simulations not only in this chapter, but also in the upcoming chapter, it was used FEMAS® (Finite Element Meshless Method Analysis Software – cmech.webs.com), a meshless computational framework developed by Prof. Jorge Belinha. The software is implemented in the commercial software Matlab® and uses the meshless formulations previously explained in Chapter 5 for analysing 2D and 3D geometrical models using several discretization techniques. Regarding the numerical analysis, FEMAS® enables the use of FEM, RPIM and NNRPIM not only for fluid flow analysis, but also for linear elasto-static analysis, bone tissue remodelling analysis, etc.

8.1 Blood Flow Analysis in Simple Models

Before analysing 2D and 3D models of the blood flow in human aortic aneurysm geometries, a preliminary study was performed using simpler geometries. The main objective of this phase was to analyse the convergence of the FEM with triangular elements with 3 nodes (first order polynomial elements), RPIM, NNRPIM and FEM with triangular elements with 6 nodes (second order polynomial elements) and acquire the level of discretization that enables more accurate results, for 2D geometrical models. After the convergence study in two-dimensional geometries, the second main goal of this subchapter was to calibrate the blood flow simulation parameters both in 2D and 3D geometries. In this case, 4 node tetrahedral elements were used for the FEM (first order polynomial elements).

To carry out the objectives outlined above, this subchapter follows the subsequent pipeline:

- Analysis of two 2D geometrical models of a branched aorta
    - Convergence study
    - Analysis of the velocity profiles in various regions of the aortic models

- Calibration of the parameters of simulation considering the results of the previous step

- Analysis of a 3D geometrical model of a branched aorta
  - Analysis of the velocity profiles in various regions of the aortic model
  - Calibration of the parameters of simulation considering the results of the previous step

8.1.1 Two-dimensional Branched Models

To accomplish the preliminary tests, two 2D models of a healthy abdominal aorta (segment of the aorta that comprehends the renal arteries) were developed in FEMAP®. The geometries are schematized in Figure 8. 1, with the correspondent dimensions of the real human aortic artery obtained from the literature [12], [33], [111].

As it is observed, both models are very similar: the geometry and dimensions are the same however, one does not have any divisions (Figure 8. 1 (a)) and the other one has segmented regions (Figure 8. 1 (b)). The main purpose of constructing these differences between the models was to comprehend the differences of blood flow results in an irregular mesh (obtained from the geometry represented in the left) and in a semi-structured mesh (obtained from the geometry represented in the right). This last geometry will enable a more precise analysis of the blood flow in the inlet and outlet regions of the blood vessel, since those regions are constricted to an area that will posteriorly generate a regular mesh. The discrepancies between both models will also contribute to understanding blood flow's behaviour in regular and irregular meshes and conclude about which scenario provides better results.

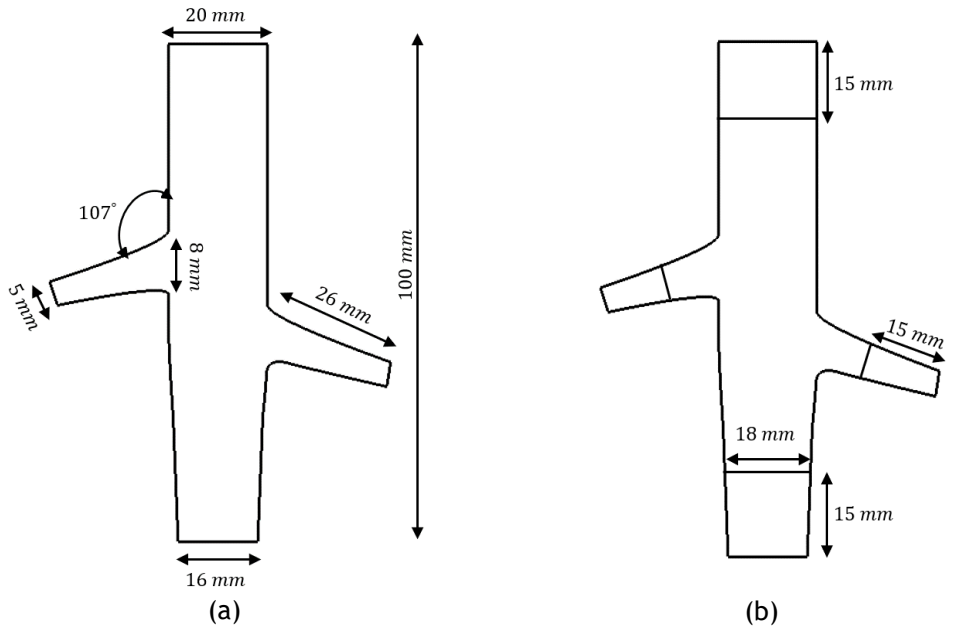

Figure 8. 1 – Representation of the two-dimensional geometrical models of the abdominal aorta and renal arteries: (a) first case study: model without segments; (b) second case study: model segmented in the inlet and outlet regions. The dimensions that are not represented in the model (b) are equal to the ones represented in the model (a).

For the analysis of the two-dimensional geometrical models, the blood was considered a Bingham fluid, with a density of $1{,}05\ kg/mm^3$ and a viscosity of $3{,}5 \times 10^{-6}\ N.ms/mm^3$. The

velocity in the inlet of the blood vessel was considered laminar, described by a parabolic profile and with a maximum of 0.15 mm/ms, as it is represented in Figure 8. 2. The value of the velocity was taken from the data presented in Table 3. 2 of Chapter 3.

For imposing the velocity in the geometrical models, it was used the equation of the parabola:

$$u(R) = a_0(R)^2 + a_1 R + a_2 \tag{8. 1}$$

Assuming that the value of the velocity in the walls is null and in the centreline of the blood vessel is maximum, the equation was solved, and the non-constant parameters were obtained:

$$\begin{cases} a_0(R)^2 + a_1 R + a_2 = 0 \\ a_0(0)^2 + a_1 \times 0 = 0 \\ a_0\left(\frac{R}{2}\right)^2 + a_1 \times \frac{R}{2} = V_{max} \end{cases} \Leftrightarrow \begin{cases} a_0 = -0{,}0015 \\ a_1 = 0{,}03 \\ a_2 = 0 \end{cases} \tag{8. 2}$$

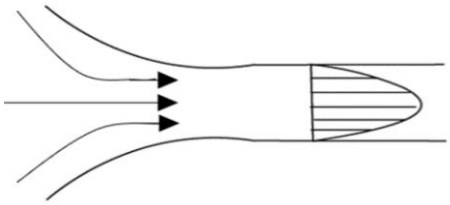

Figure 8. 2 – Schematization of the blood's velocity parabolic profile.

In Figure 8. 3 it is represented the imposition of the velocity profile in the geometrical model, as well as the essential boundary conditions that contours the vessel. The nodes marked in grey represent the inlet velocity and the nodes marked in yellow are constrained in all directions, i.e., in Ox and Oy. The extremities of the branched model were left with no constraints to allow the blood flow to come out.

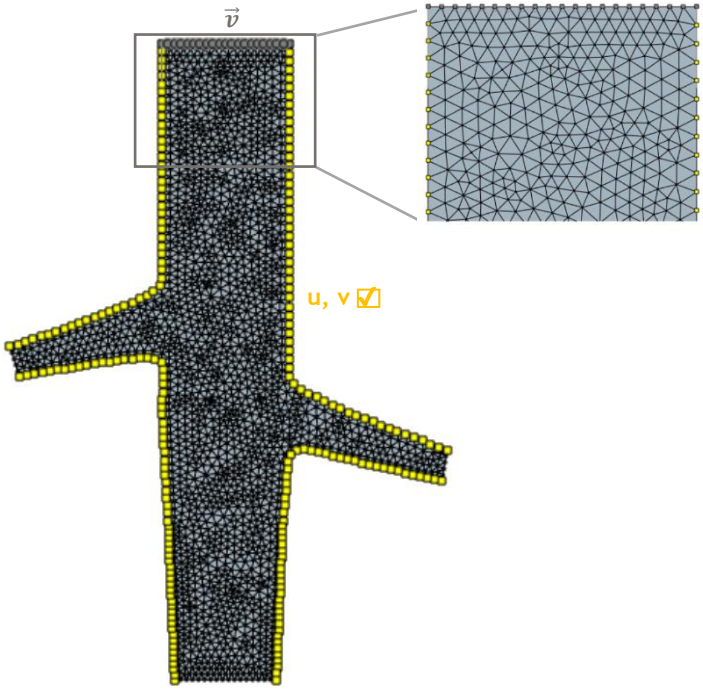

Figure 8. 3 - Representation of the inlet velocity and essential boundary conditions that were applied in both 2D models under study.

For the fluid flow analysis, it was used the standard parameters presented in Table 8. 1. Posteriorly, these values may undergo some changes for obtaining better results, which will be mentioned in the models in which these parameters were altered.

Table 8. 1 – RPIM and NNRPIM parameters.

RPIM	NNRPIM
Nodes in the influence-domain: **16**	c = **0.0001**
c = **1.42**	p = **0.9999**
p = **1.03**	Influence-cell: **Second Order**
Polynomial Basis: **Constant**	Polynomial Basis: **Constant**
Integration Points: **1 per triangle**	Integration Points: **1 per sub-cell**

8.1.1.1 First Case Study: non-structured mesh

In order to understand the convergence of the numerical methods, several meshes were constructed with a successively refinement of triangular elements with 3 nodes following a quadratic growth ratio. Therefore, the model was discretized with 247, 499, 1009, 2013, 4009 and 6003 nodes, that corresponds to, approximately, 250, 500, 1000, 2000, 4000 and 6000 nodes, as it can be seen in Figure 8. 4. The same models were also discretized with triangular elements with 6 nodes, which resulted in meshes of 892, 1868 and 3836 nodes, respectively. The meshes with 2013, 4009 and 6003 were not constructed with 6 nodes' elements because the resulting mesh would be composed by a high number of nodes, increasing significantly the computational cost.

It is noticed that, instead of having a model with 6000 nodes, it should be represented a model with 8000 nodes. However, because of the high computational cost that a model with 8000 nodes would entail, it could not be created, so an intermediary model of 6000 nodes was built alternately.

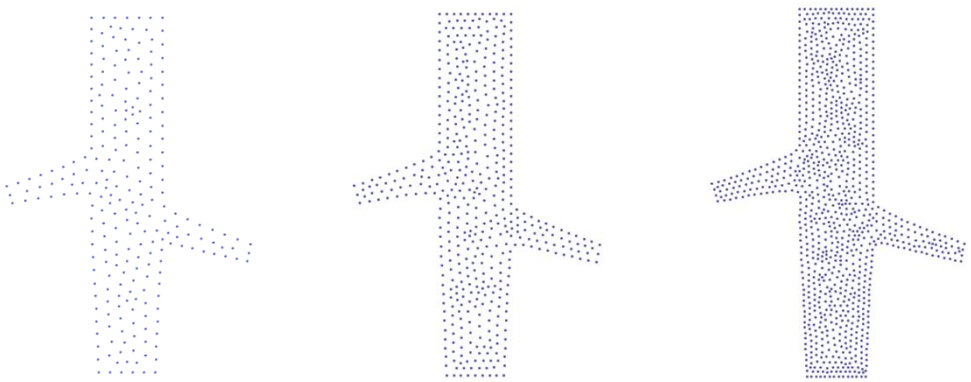

(a) 247 (b) 499 (c) 1009

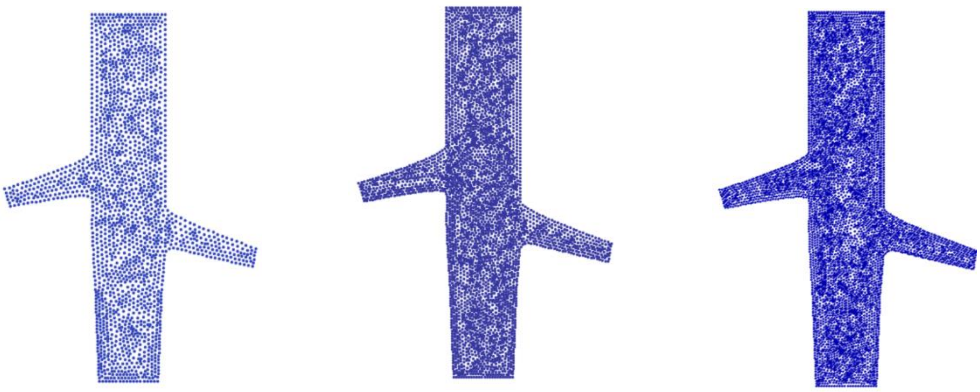

(d) 2013 (e) 4009 (f) 6038

Figure 8. 4 – Geometrical models with an increasing number of nodes for the convergence study.

The graphs of the convergence study are depicted in Figure 8. 6 and they display the velocities registered in the points A, B, C and D, in function of each of the six models illustrated above. The points by which the velocities were obtained are represented in Figure 8. 5.

After de convergence analysis, graphs of the blood flow's velocity profile were constructed for each of the six models. For this step of the analysis, 4 sections were defined in the geometrical models for extracting the values of the velocity in the comprised nodes. These sections are also represented in Figure 8. 5.

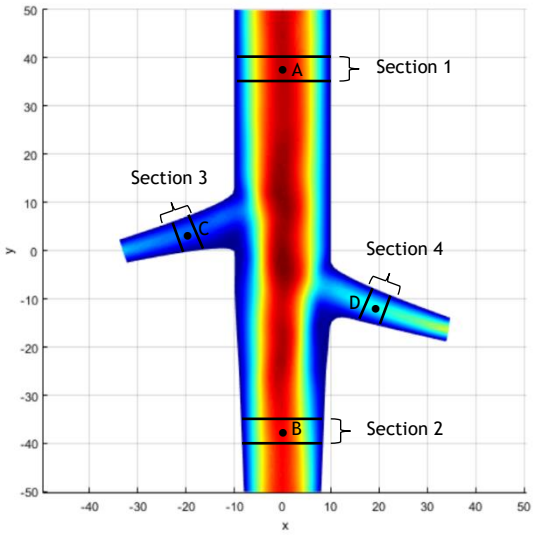

Figure 8. 5 – Representation of the points and sections for the analysis of the blood flow velocity.

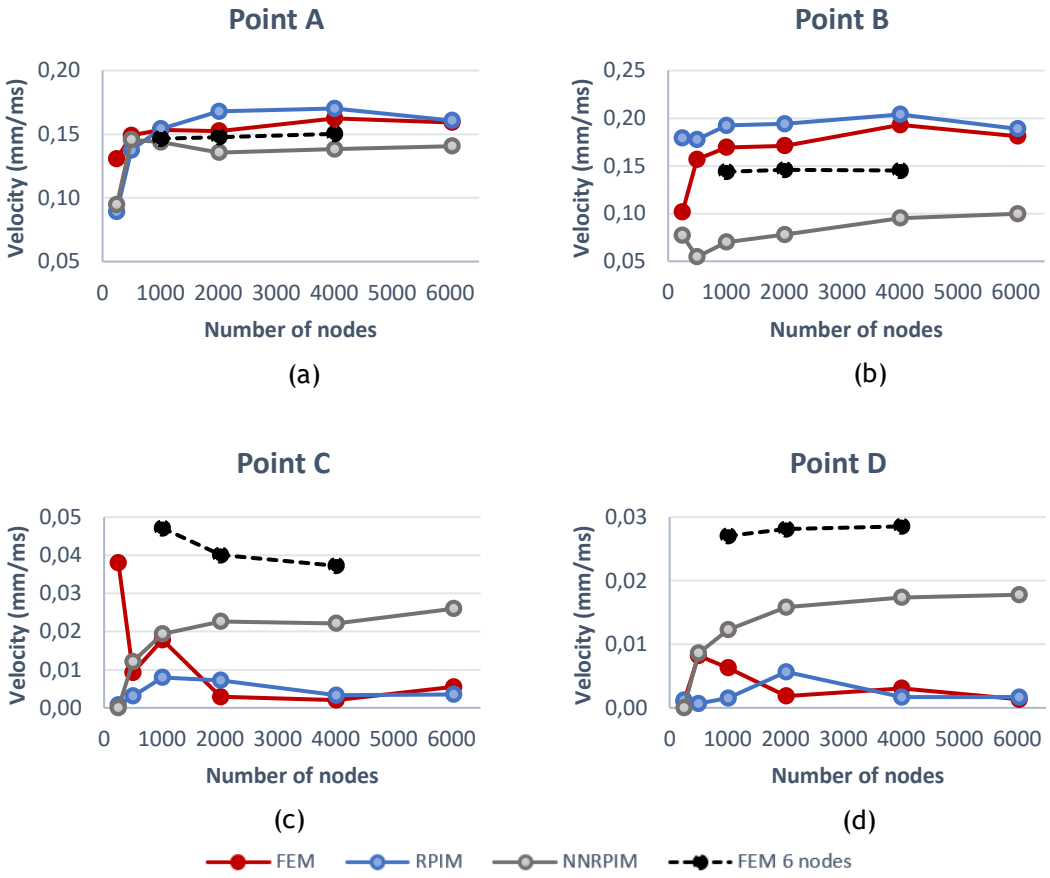

Figure 8. 6 – Convergence graphs: velocities in points A, B, C and D with the increase of the number of nodes in the models with a non-structured mesh.

In the graph of Figure 8. 6 (a) it is observed that the velocity solution stabilizes from the model with 1000 nodes. This behaviour is similar for FEM, RPIM, NNRPIM and FEM with elements with 6 nodes, which means that all numerical methods provided an analogous result. In point B, the four methods under study also stabilize their solution after 1000 nodes. However, the numerical results of the velocity are not as similar as in the first graph, with the NNRPIM registering a higher difference. From the first graph it is concluded that, in the beginning of the geometrical model, the velocity does not vary significantly compared to the inlet velocity (0,15 mm/ms). In the second graph, it is observed a slight increase of the velocity, excepting from the NNRPIM results.

In Figure 8. 6 (c) and (d), that correspond to point C and D, respectively, the lines in the graphs are not as constant as the previously analysed graphs, namely the ones from FEM and RPIM. This is because these points are placed in the branches of the model, which are regions in which the velocity is very slow and instable. This is also correlated to the discontinuity of the blood vessel in that region, which induces a disruption in the blood flow. The results of the four numerical methods present some differences: the velocity in the NNRPIM increased gradually with the increase of the number of nodes; in the results from FEM with 6 nodes, the line is already stabilized since there is no data from models with a mesh less than 1000 nodes and above 4000 nodes; lastly, it is observed that the FEM and RPIM are the lines with the closest results. With the observation of the graphs of points C and D, it can be concluded that the velocity is similar in both branches of the geometrical model, with a higher difference registered in the results from the FEM with 6 nodes.

After the previous analysis of the four graphs, and taking into consideration the variations of graphs (c) and (d), the convergence was considered achieved from the model with 2000 nodes. This means that the results obtained in this model are very similar to the results of the models with a higher number of nodes, allowing simulations with less computational cost and with equivalent results.

In order to observe the velocity profiles in several regions of the geometrical models, it was constructed graphs that describe the velocity in each node comprised in the sections of Figure 8. 5. In Figure 8. 7 it is represented the graphs for the model with less nodes (247 nodes) and in Figure 8. 9 it is pictured the graphs for the model with 2013 nodes (which is the model in which the convergence is achieved). The results of the remaining geometrical models are presented in the Appendix.

After the figures of the graphs, it is depicted the corresponding colour dispersion maps of the blood's velocity, allowing a better understanding of the flow behaviour inside the branched model.

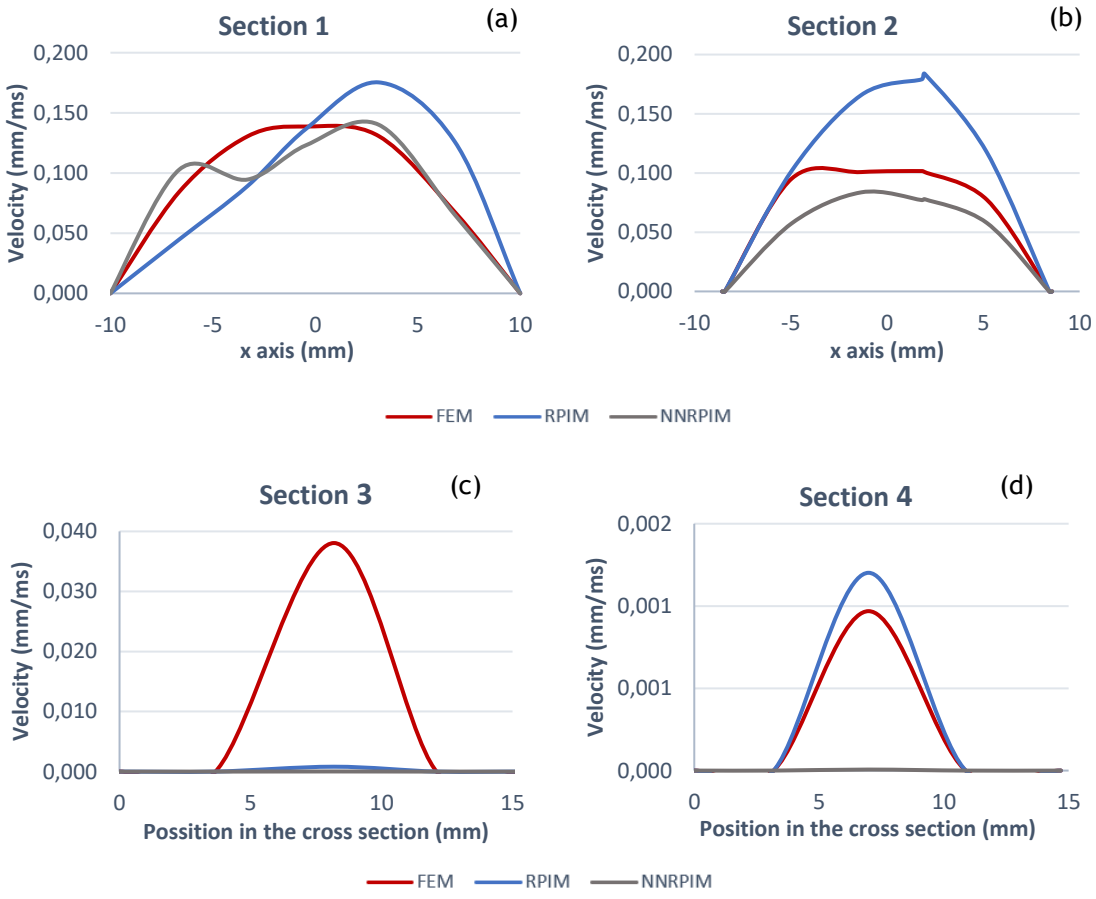

Figure 8. 7 - Velocity profiles of the blood flow in: (a) section 1; (b) section 2; (c) section 3 and (d) section 4. These results were obtained from the geometrical model with 247 nodes, using FEM, RPIM and NNRPIM.

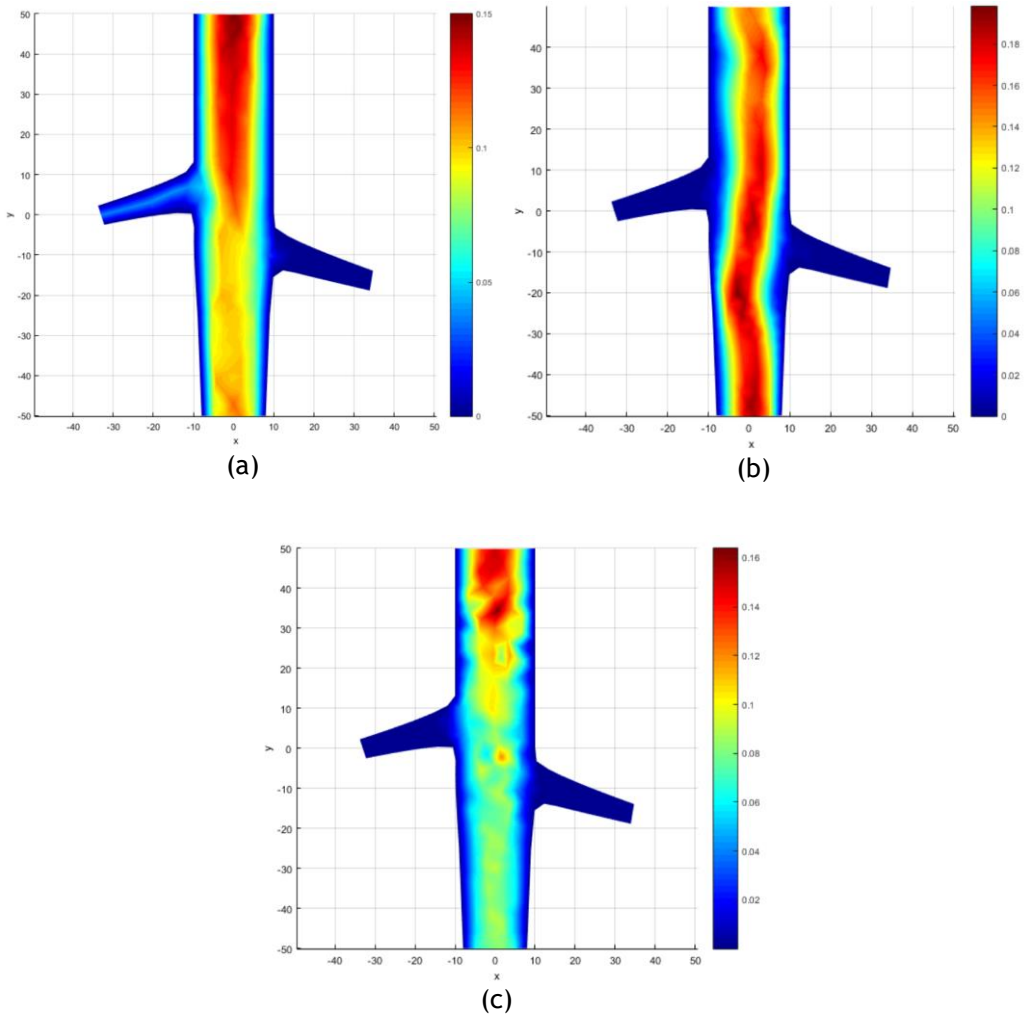

Figure 8. 8 – Colour dispersion maps of the blood velocity in the branched model with 247 nodes using: (a) FEM (colour bar up to 0.15 mm/ms), (b) RPIM (colour bar up to 0.1981 mm/ms) and (c) NNRPIM (colour bar up to 0.1639 mm/ms).

In the graphs of Figure 8. 7, it is observed that, in all sections of the geometrical model, the velocity profile is approximately parabolic for all the numerical methods. The main difference that is noticed are in the results from sections 3 and 4, where the velocity obtained with the NNRPIM was almost zero. It should be noticed that the scale of the velocity axis in the graph from section 3 is 10 times higher than the graph from section 4. Taking this observation into account, the velocity obtained in the RPIM was similar for both sections. The main difference is the results from FEM, which were almost 40 times higher in the section 3 compared to the section 4.

The interpretation of the graphs can be validated by the isomaps depicted in Figure 8. 8. In the first figure, corresponding to the results of FEM analysis, it is observed that the blood flow velocity decreases along the extension of the vessel and a small velocity is detected in the right branch. On the other hand, the blood flow in the left branch is vestigial. These patterns can be also observed in the graphs from Figure 8. 7, where it is detected the discrepancies between the curves from the sections 3 and 4. In Figure 8. 8 (b), the velocity maintained almost constant along the vessel, with a register of a very low blood velocity in the branches. In the

last figure, corresponding to the results from NNRPIM, the velocity decreased along the extension of the model and no blood flowed to the branches.

Lastly, it can be concluded that all the numerical methods provided irregular blood flow patterns, which is related to the scarcity of nodes in the mesh and with the fact that the mesh itself is irregular. To improve the results, the mesh was refined, so the next figures illustrate the results of the model with 2013 nodes.

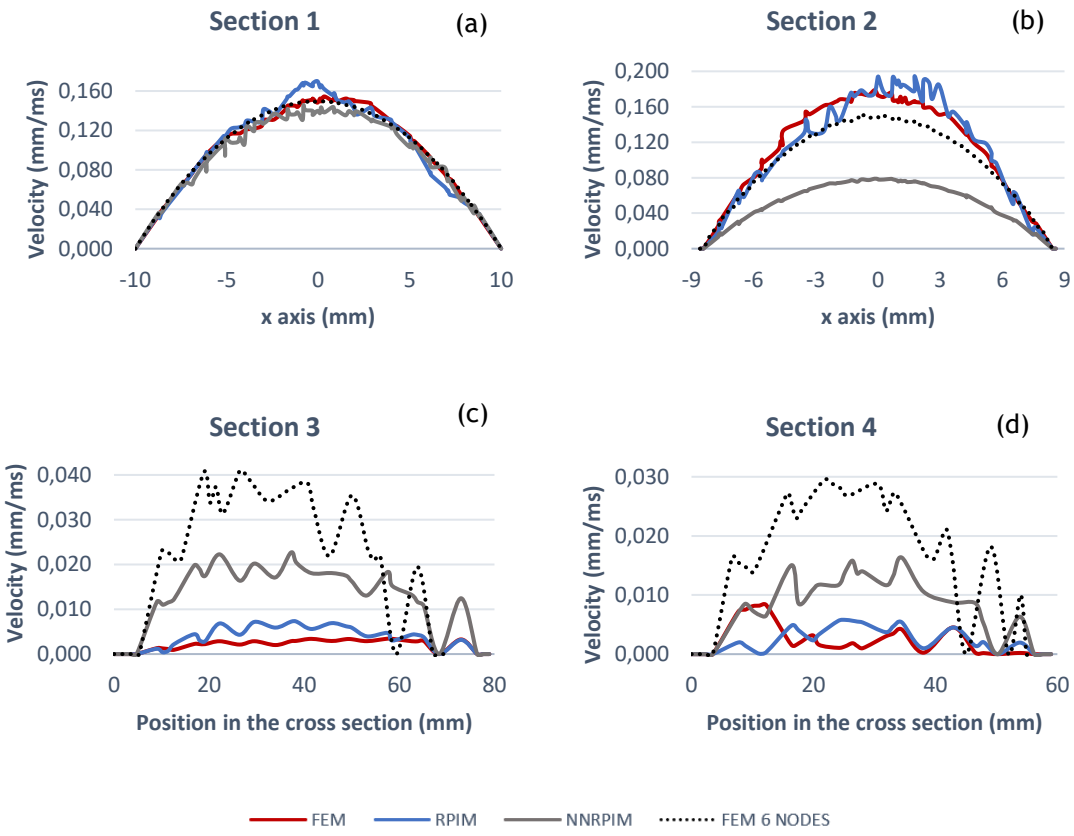

Figure 8. 9 - Velocity profiles of the blood flow in: (a) section 1; (b) section 2; (c) section 3 and (d) section 4. These results were obtained from the geometrical model with 2013 nodes, using FEM (triangular elements with 3 nodes), RPIM, NNRPIM and FEM (triangular elements with 6 nodes).

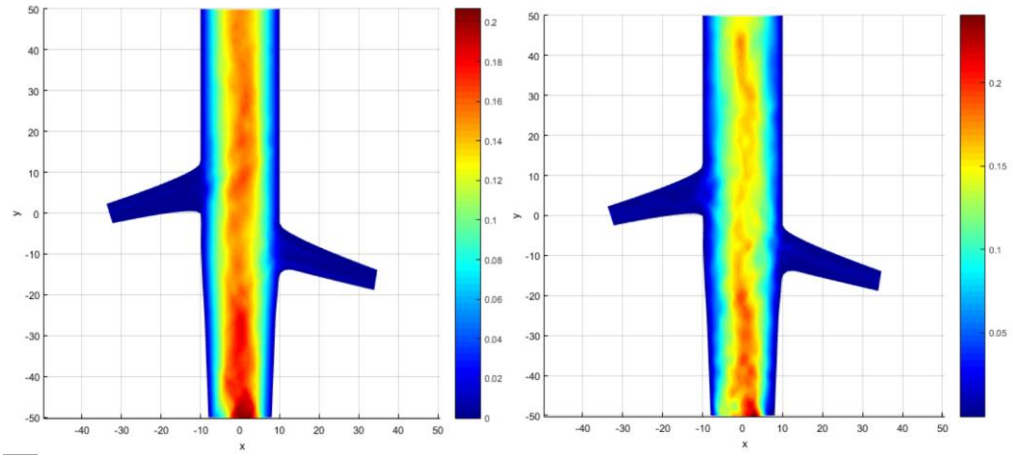

(a) (b)

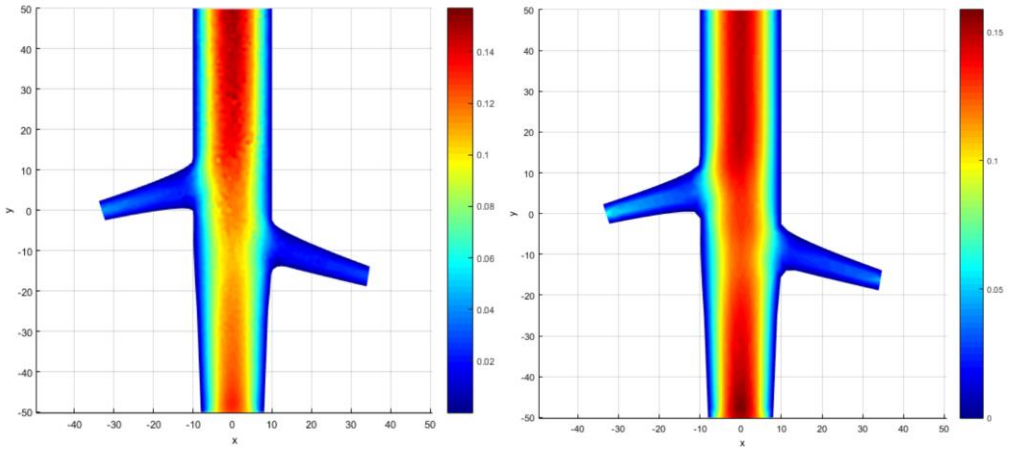

Figure 8. 10 - Colour dispersion maps of the blood velocity in the branched model with 2013 nodes with: (a) FEM (colour bar up to 0.2066 mm/ms), (b) RPIM (colour bar up to 0.2402 mm/ms), (c) NNRPIM (colour bar up to 0.1567 mm/ms) and (d) FEM with triangular elements with 6 nodes (colour bar up to 0.1587 mm/ms).

The graphs of Figure 8. 9 indicate that the velocity profiles of the blood flow in all sections were approximately parabolic, for all the numerical methods. In section 1, it is observed a high correspondence between the curves of every methods, which means that, in the beginning of the vessel, the blood flow behaviour was very similar. In section 2 the same behaviour is observed, with the NNRPIM registering a slight difference compared to the other methods. Also, it is detected that the blood's velocity in section 2 registered an increase compared to the values from section 1. In sections 3 and 4, the numerical methods that enabled some significant results of blood flow in the branches of the model were the NNRPIM and the FEM with 6 nodes elements. This can be also observed in the Figure 8. 10 (c) and (d), where there is an evident blood flow velocity in both branches, contrary to what is observed in Figure 8. 10 (a) and (b). Giving an overview of the results from the isomaps, it can be stated that the numerical method that provided the best results was the FEM with triangular elements with 6 nodes, since the colour is mainly uniform along the entire vessel, including in the branches.

Comparing the isomaps of Figure 8. 8 and Figure 8. 10 it is concluded that a refinement of the mesh didn't improve significantly the results, with exception for the NNRPIM, where it was obtained a more continuous flow in the mesh with a higher number of nodes.

8.2.1.2. Second Case Study: semi-structured mesh

For the second case study, the geometrical model represented in the Figure 8. 1 (b) was also meshed with a continuously increased number of nodes following a quadratic ratio. Thus, it was obtained 6 discretized models with 251, 510, 1010, 2017, 4026 and 5986 nodes, that correspond to, approximately, 250, 500, 1000, 2000, 4000 and 6000 nodes (see Figure 8. 11). It is noticed that, instead of having a model with 6000 nodes, it should be represented a model with 8000 nodes instead. However, because of the high computational cost that a model with 8000 nodes would entail, it could not be created. Thus, an intermediary model of 6000 nodes was built alternately.

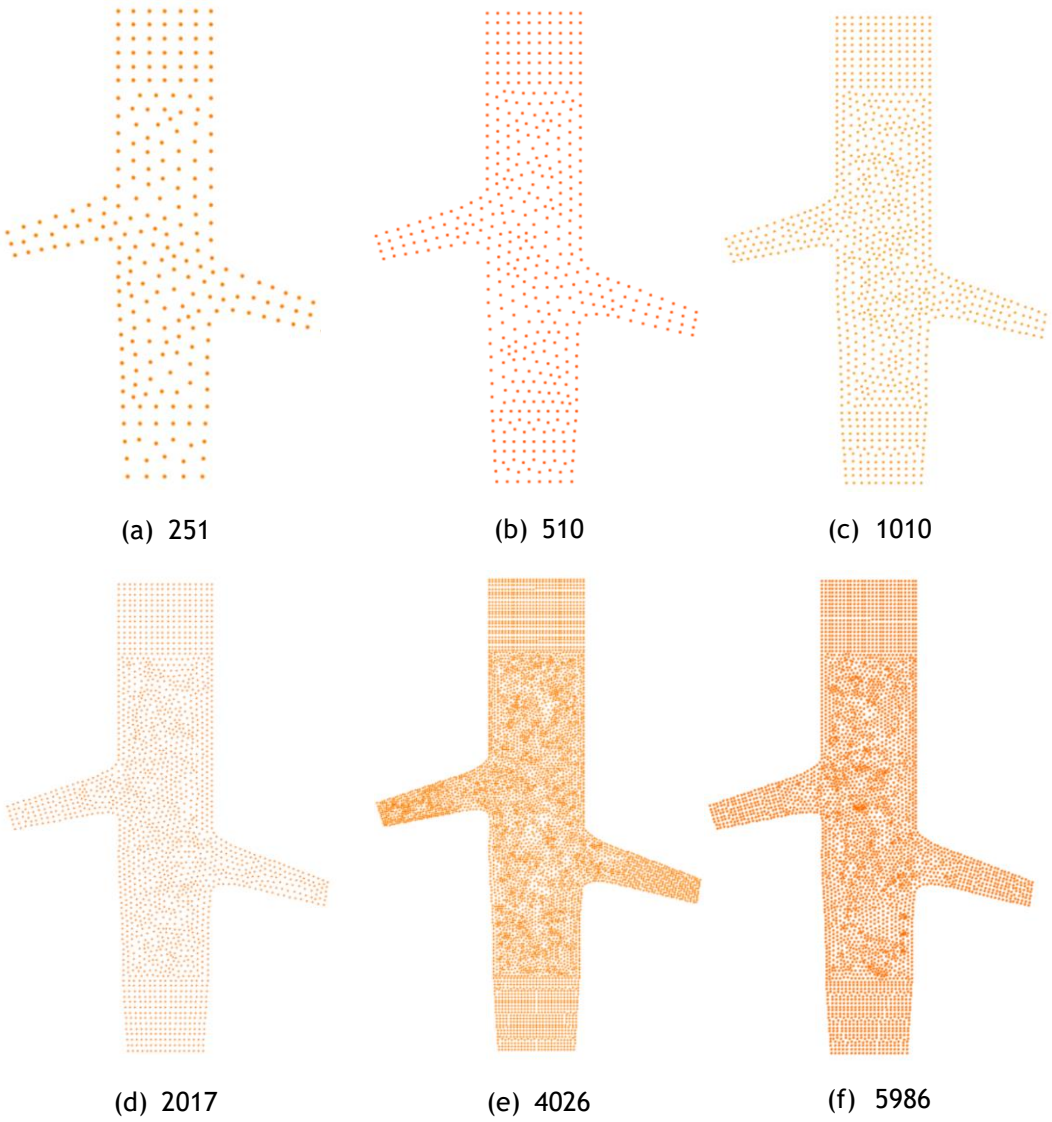

Figure 8. 11 - Geometrical models with an increasing discretization for the convergence study.

After the discretization process, each model was analysed separately. The first part of the analysis consisted in a convergence study, as in the prevous case-study, where 4 points were selected from the geometrical models (see Figure 8. 12). After the selection of the points, a fluid flow analysis was performed using FEM (with triangular elements with 3 nodes), RPIM, NNRPIM and FEM (with triangular elements with 6 nodes) and the results obtained for the convergence are represented in graphs of Figure 8. 13.

The blood flow velocity profile was then represented in graphs for each of the six models. For this phase, 4 segments (lines) were defined in the geometrical model and the values of the velocity were obtained for each node of the segment. These segments are represented in the Figure 8. 12.

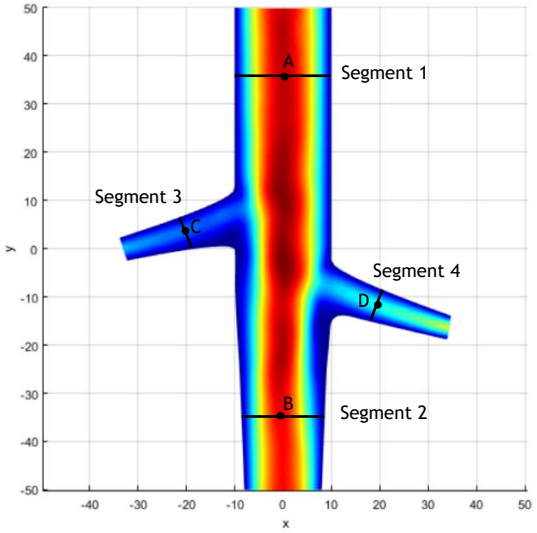

Figure 8. 12 - Representation of the points and segments for the analysis of the blood flow velocity.

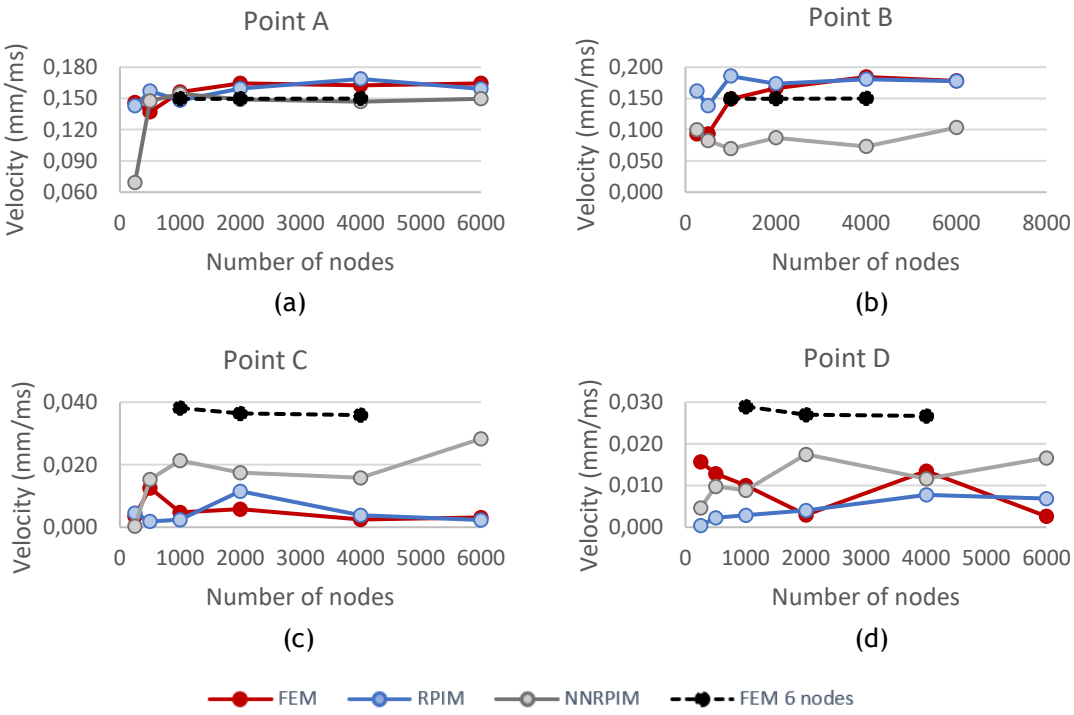

Figure 8. 13 - Convergence graphs: velocities in points A, B, C and D with the increase of the number of nodes in the models with a semi-structured mesh.

As it was verified in the results of the first case-study, in Figure 8. 13 (a) the convergence is achieved from the model with approximately 1000 nodes. The results of the blood velocity in point A, for the four numerical methods under analysis, did not differ significantly, which means that all models provided similar results. In point B, the four methods stabilized from the model with 2000 nodes, however, the NNRPIM results are the most discordant. From the observation of the graphs of points A and B, it can be concluded that, in the former, the velocity did not vary significantly compared to the inlet velocity (0.15 mm/ms), meaning that there were few perturbations. In point B, is observed an increase in the velocity (compared to the

inlet velocity) for the FEM and RPIM. On the other hand, the FEM with 6 nodes maintained a constant velocity and, for the NNRPIM, the results were significantly lower.

In Figure 8. 13 (c) and (d), corresponding to points C and D, respectively, the lines in the graphs are not as constant as in the previously analysed graphs. This is because these points are placed in the branches of the model, that are regions in which the velocity is very slow and instable due to the discontinuity of the blood vessel. The results of the four numerical methods present some differences: the velocity in the NNRPIM increased gradually with the increase of the number of nodes; in FEM with 6 nodes, the line is already stabilized since there is no data from models with a mesh less than 1000 nodes and above 4000 nodes; lastly, it is verified that the FEM and RPIM are the lines with the closest results. With the observation of the graphs of points C and D, it can be concluded that the velocity is similar in both branches of the geometrical model, with a difference of approximately 0,001 mm/ms between each branch.

Considering the previous analysis of the four graphs, the convergence was considered achieved from the model with 2000 nodes, as it occurred in the first case study.

After de convergence study, it was constructed graphs of the velocity profiles of specific segments in order to access the blood's velocity in the beginning, ending and ramifications of each geometrical model. For this purpose, it was obtained the velocity of each node comprised in the segments represented in Figure 8. 12 and created the graphs that are represented in Figure 8. 14 and Figure 8. 16, which corresponds to the results of the model with 251 nodes and 2017 nodes, respectively. The results of the remaining geometrical models are presented in the Appendix. After the figures of the graphs, it is depicted the corresponding colour dispersion maps of the blood's velocity.

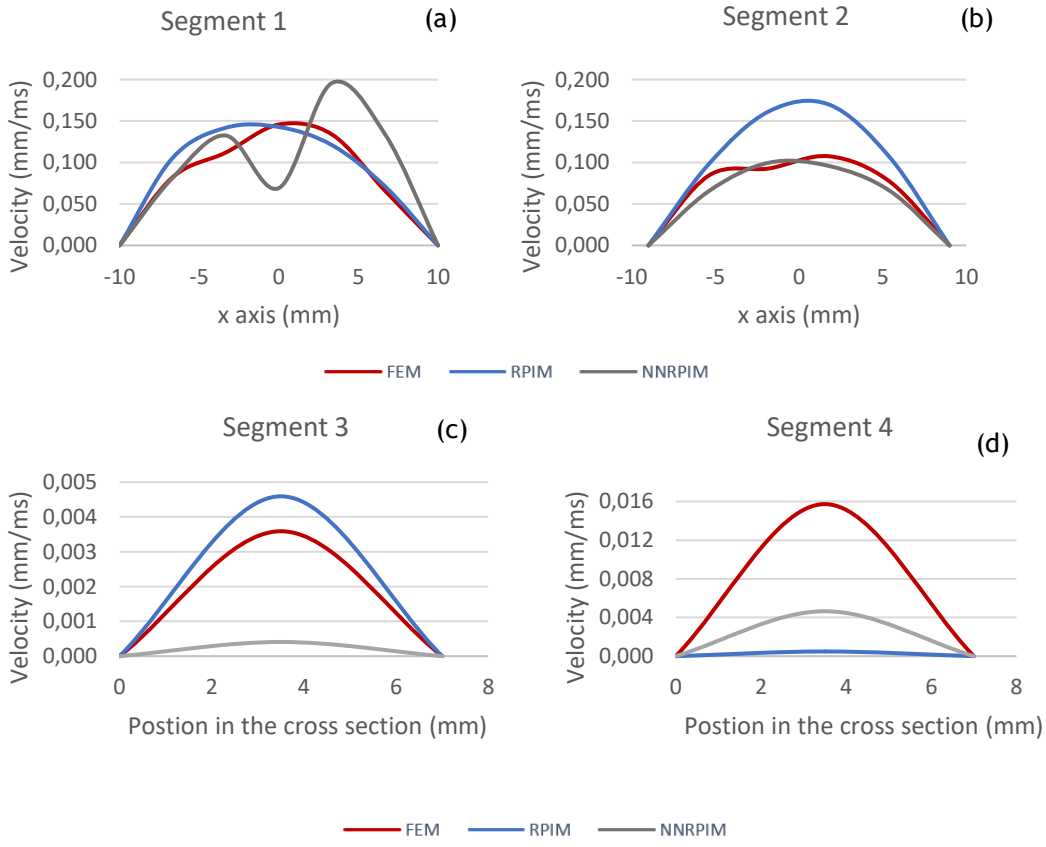

Figure 8. 14 - Velocity profiles of the blood flow in: (a) segment 1; (b) segment 2; (c) segment 3 and (d) segment 4. These results were obtained from the geometrical model with 251 nodes, using FEM, RPIM and NNRPIM.

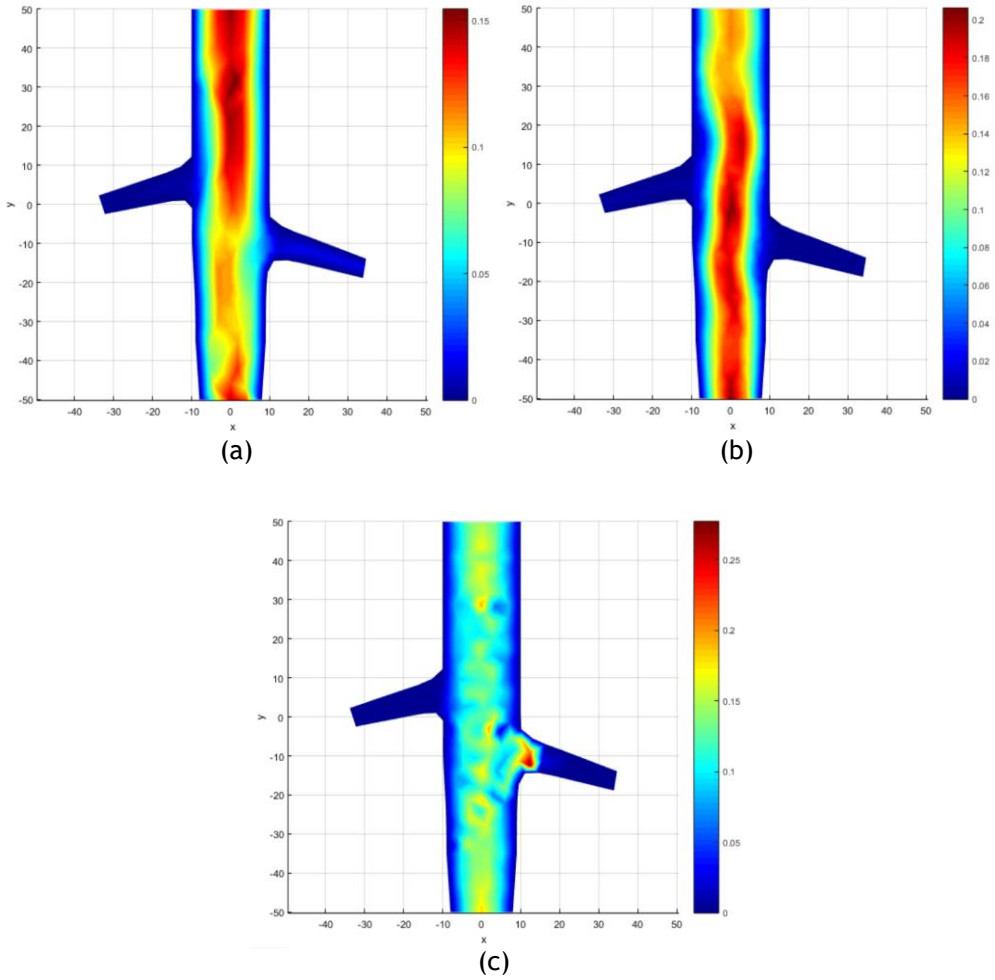

Figure 8. 15 - Colour dispersion maps of the blood velocity in the branched model with 251 nodes with: (a) FEM (colour bar up to 0.1545 mm/ms), (b) RPIM (colour bar up to 0.2062 mm/ms) and (c) NNRPIM (colour bar up to 0.2768 mm/ms).

Analysing the graphs of Figure 8. 14, it is observed an approximate parabolic profile of the velocity in the four segments, for all the numerical methods. In the graph (a) and (b) the peak of the velocity did not differ significantly from the inlet velocity, meaning that few perturbations occurred. The main characteristic on the velocities between these two graphs is that in graph (b) there is a slight decrease of the value of the velocity, for FEM and NNRPIM, which denotes to losses along the vessel extension, mainly caused by the branches. On the other hand, the RPIM results present an increase in the section 2.

In the segments 3 and 4, the velocities decreased significantly, especially in the former, where the maximum velocity is approximately 0,005 mm/ms, resulting from RPIM. In the segment 4, the peak is in 0,016 mm/ms (approximately), obtained with FEM.

Observing the maps of colours for this study (see Figure 8. 15), it is noticed that they resemble those obtained in the first case study for the model with nearly 250 nodes (see Figure 8. 8 and Figure 8. 7). This means that the different meshes enabled similar results, for this number of nodes. Posteriorly, the same procedure was performed for the model with 2013 nodes to observe the alterations in the blood flow pattern in a more refined mesh. The results are presented in Figure 8. 16 and Figure 8. 17.

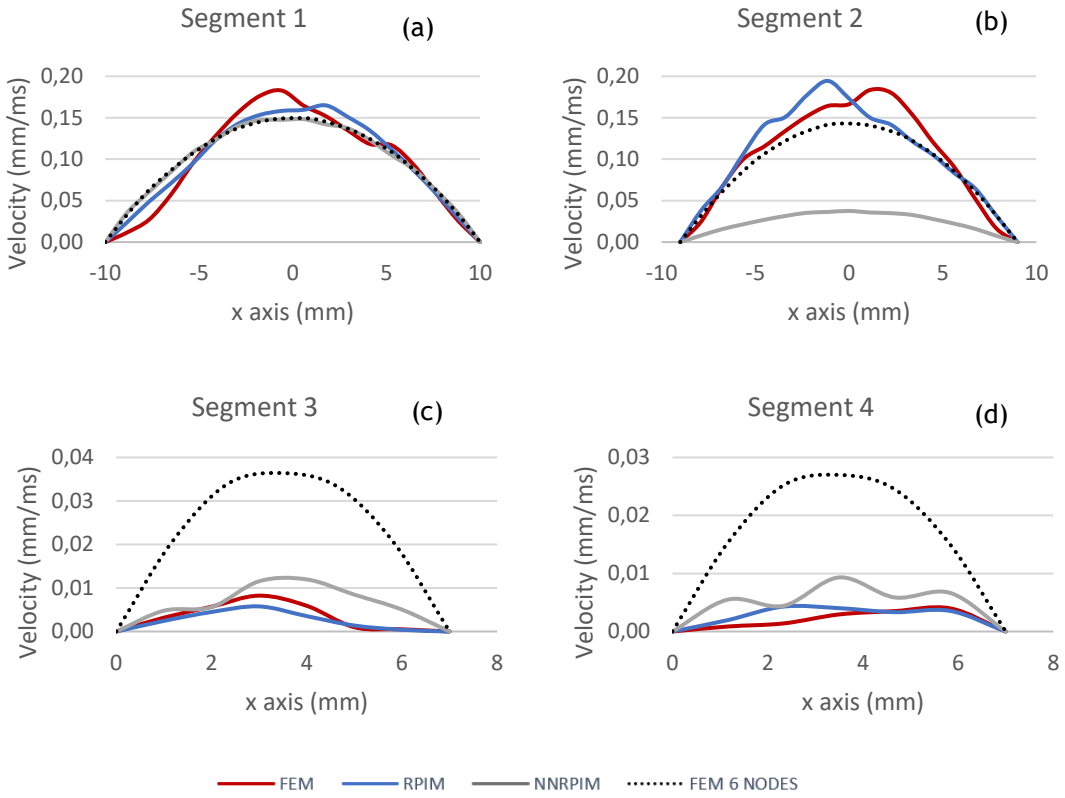

Figure 8. 16 - Velocity profiles of the blood flow in: (a) section 1; (b) section 2; (c) section 3 and (d) section 4. These results were obtained from the geometrical model with 2017 nodes, using FEM, RPIM, NNRPIM and FEM with 6 nodes elements.

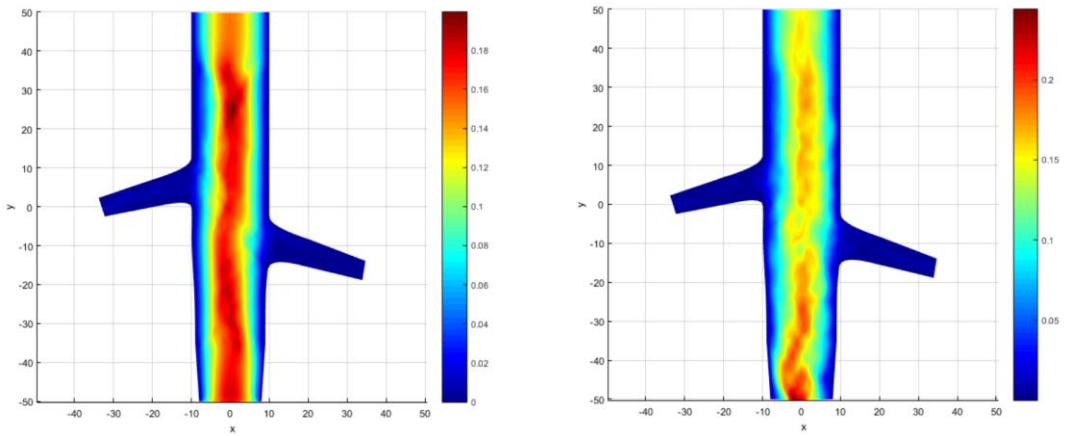

(a) (b)

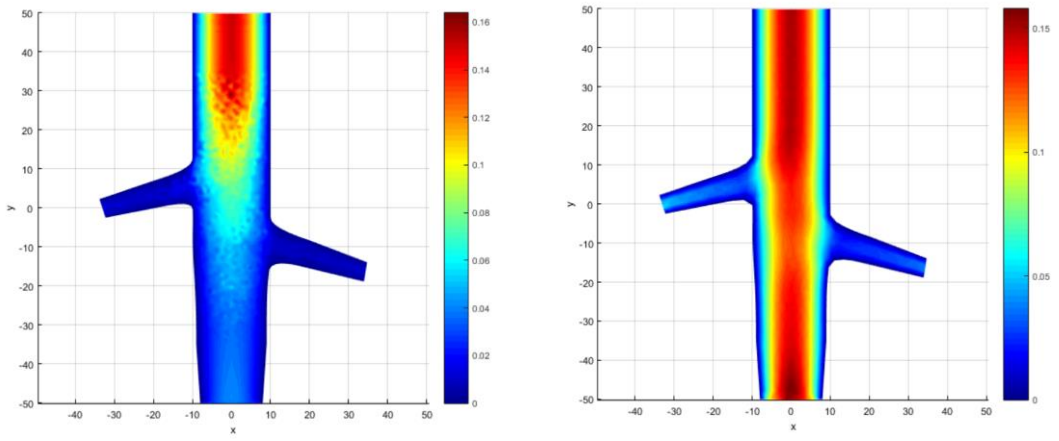

Figure 8. 17 - Colour dispersion maps of the blood velocity in the branched model with 2017 nodes with: (a) FEM with triangular elements with 3 nodes (colour bar up to 0.1994 mm/ms), (b) RPIM (colour bar up to 0.2439 mm/ms), (c) NNRPIM (colour bar up to 0.1638 mm/ms) and (d) FEM with triangular elements with 6 nodes (colour bar up to 0.1580 mm/ms).

The conclusions withdrawn from the observation of Figure 8. 16 follow the same reasoning of the previously analysed graphs: the blood flow velocity in every section was described by a parabolic profile, for all the numerical methods, and it was verified a relevant decrease of the velocity in the sections 3 and 4. From the observation of all graphs, the method that provided the best results was the FEM with triangular elements with 6 nodes. Also, this can be observed by the colour map of Figure 8. 17 (d), where the blood flow is almost constant along the entire extension of the blood vessel.

Comparing the results obtained in this study with the results from the first case study (for the model with approximately 2000 nodes) it is concluded that, although they are very similar, the results from FEM and NNRPIM of the first case study was slightly better, specially the colour dispersion maps.

After the analysis of the two case studies explained before, it was concluded the following remarks:

- For both case studies, the convergence was considered achieved from the geometrical model with 2000 nodes. Taking this to account, the forthcoming two-dimensional models to be studied will have 2000 nodes;
- The differences in the results between the first and second case studies were not significantly dissimilar, which means that a total irregular mesh and a semi-structured mesh do not provide different results. In order to study the regularity of the mesh and its consequence in the results, the two-dimensional models of abdominal aortic aneurysms that will follow this first study will have a regular mesh;
- In all the maps of colours, it was verified that the blood flow was not constant and well demarcated in the entire extension of the model, registering oscillations and large dispersions. For assessing this problem, the parameters of simulation will be altered.

8.2.1.3. Definition of the parameters of simulation

For this phase, it was only considered the model with approximately 2000 nodes of the first case study, which resemble to the geometry with no segments. The choice of the model was based in the irregularity of the mesh: the parameters of simulation need to be calibrated in accordance to the results provided by an irregular mesh, which is the scenario that will be expected in a mesh of a real aortic aneurysm geometry. Also, the results of both case studies were identical, meaning that the calibration of the parameters of simulations would follow the same reasoning.

Since the results of the two-dimensional simulations were characterized by dispersed flows, two approaches were defined in attempt to obtain a constant flow for all the numerical methods:

1. First it was imposed an outlet velocity in the end of the blood model to force the flow to come out of the blood vessel;
2. Then, it was imposed two additional outlet velocities in both branches of the model, resulting in a total of 3 outlet velocities.

The results were then compared, and it was concluded which scenario (no outlet velocity, one outlet velocity or three outlet velocities) provide the best blood flow pattern.

As outlet conditions, the velocity of the blood was considered lower than the inlet velocity, which is based in the knowledge that the blood flow velocity decreases with the distance from the heart (that was explained in detail in Chapter 3). Since there are two branches in the geometrical model under study, it was considered a velocity reduction of 1 mm/ms, so the imposed outlet velocity was 0.14 mm/ms (data obtained from Table 3. 2, considering the abdominal segment of the aorta).

Knowing the inlet and outlet velocities, it was necessary to estimate the velocities that would come out of the branches. For that, it was used the expression of the volumetric flow rate [87]:

$$Q = \iint_A v \times dA \tag{8. 3}$$

Where v is the blood flow velocity and A is the cross-sectional vector area.

For approaching the problem in study, the scheme of Figure 8. 18 was constructed.

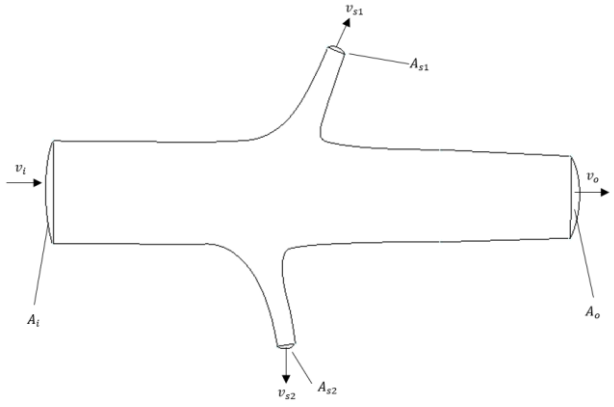

Figure 8. 18 – Schematization of the velocities and section areas of the geometrical model in study.

Assuming that the volumetric flow rate that enters the blood vessel is equal to the volumetric flow rate that comes out and considering that the outlet velocity in both branches are equal, the following calculation was performed:

$$Q_{inlet} = Q_{oulet}$$

$$Q_i = Q_o + Q_{s1} + Q_{s2} \Leftrightarrow v_i A_i = v_o A_0 + v_{s1} A_{s1} + v_{s2} A_{s2} \quad (8.\ 4)$$

And $v_{s1} = v_{s2}$, the volumetric flow rate is given by:

$$v_i A_i = v_o A_0 + 2 v_s A_s \quad (8.\ 5)$$

Thus, it can be stated that:

$$Q_i = Q_0 + 2Q_s \Leftrightarrow Q_s = \frac{Q_i - Q_0}{2} \quad (8.\ 6)$$

The calculation of each volumetric flow rate was then performed:

$$Q_i = \left[\int_0^{L_i} v_i \, dx\right] \times 1mm \Leftrightarrow [0.15x]_0^{20} = 3\ m^3/s \quad (8.\ 7)$$

$$Q_o = \left[\int_0^{L_0} v_0 \, dx\right] \times 1mm \Leftrightarrow [0.14x]_0^{16} = 2.24\ m^3/s \quad (8.\ 8)$$

$$Q_s = \frac{3 - 2.24}{2} = 0.38\ m^3/s \quad (8.\ 9)$$

After obtaining the volumetric flow rate of the branches, it was necessary to calculate the blood flow velocity:

$$0.38 = \left[\int_0^{L_s} v_s(x) \, dx\right] \times 1mm \quad (8.\ 10)$$

Where,

$$v_s(x) = ax^2 + bx + c \quad (8.\ 11)$$

$$0.38 = \left[\frac{ax^3}{3} + \frac{bx^2}{2} + cx\right]_0^5 \quad (8.\ 12)$$

And $x = L_s = 5\ mm$.

From the resolution of the Equation (8. 12) and considering the Equation (8. 1) it was obtained:

$$x = 0 \Rightarrow v_s(x) = 0$$

$$x = L_s \Rightarrow v_s(x) = \frac{ax^3}{3} + \frac{bx^2}{2} + cx = 0 \qquad (8.\ 13)$$

$$x = \frac{L_s}{2} \Rightarrow v_s(x) = \frac{bx^2}{2} + cx = max$$

By solving the previous conditions, the value of the velocity in the branches is obtained and given by 0.114 mm/ms.

In Table 8. 2 and Table 8. 3 it is displayed the results of the blood flow velocity obtained with the four numerical methods, and assuming the imposition of one and three outlet velocities.

Table 8. 2 - Colour dispersion maps of the branched aortic model with one and three outlet velocities, with four numerical methods: FEM with triangular elements with 3 nodes, RPIM, NNRPIM and FEM with triangular elements with 6 nodes.

	1 Outlet Velocity	**3 Outlet Velocities**
FEM	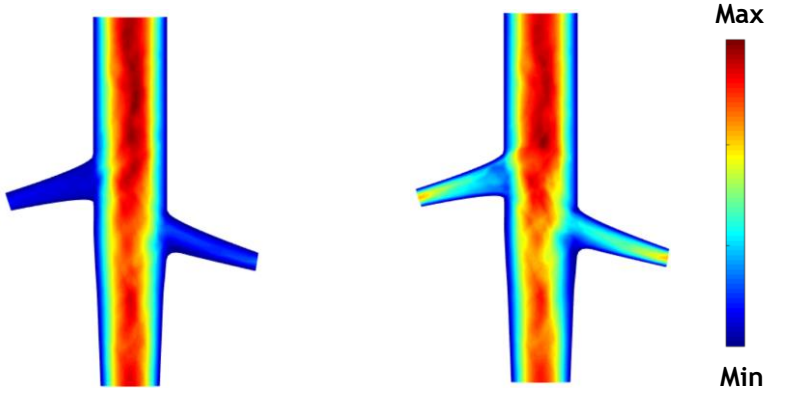	
	Max = 0.1571 / Min = 0.0	Max = 0.1649 / Min = 0.0
RPIM	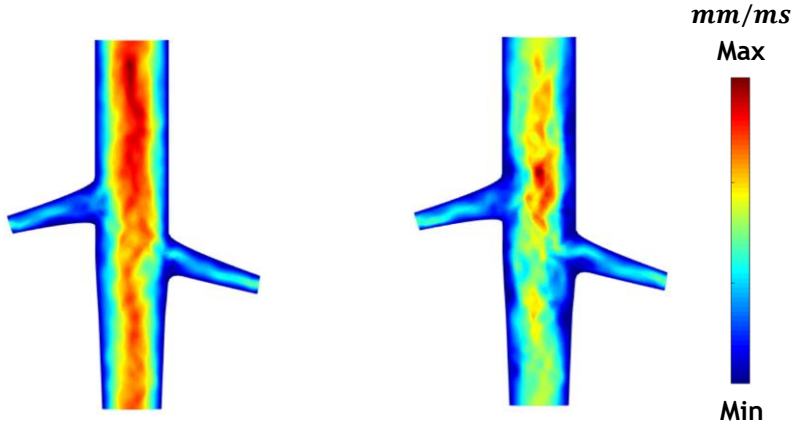	
	Max = 0.1781 / Min = 0.0	Max = 0.2510 / Min = 0.0

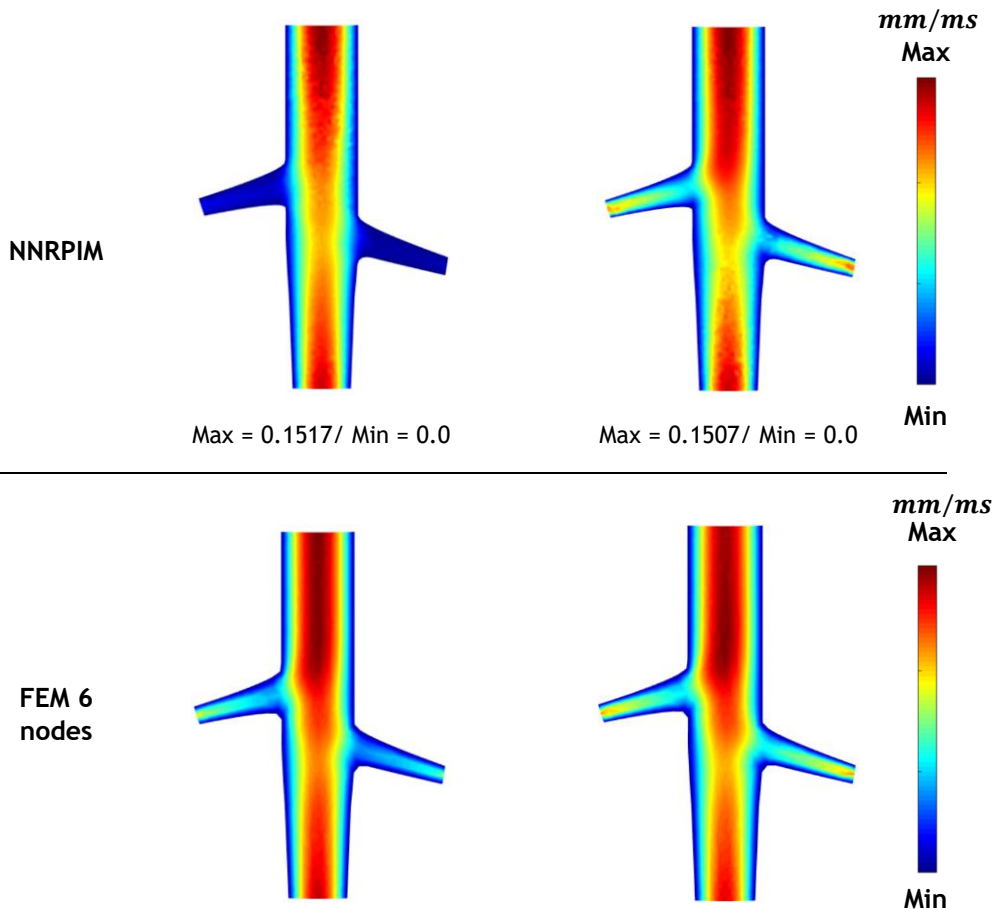
NNRPIM
mm/ms
Max
Min
Max = 0.1517/ Min = 0.0
Max = 0.1507/ Min = 0.0
FEM 6 nodes
mm/ms
Max
Min
Max = 0.1506/ Min = 0.0
Max = 0.1555/Min = 0.0

Table 8. 3 - Graphs of the blood flow velocity profiles in each section, considering one and three outlet velocities.

	1 Outlet Velocity	3 Outlet Velocities
Section 1	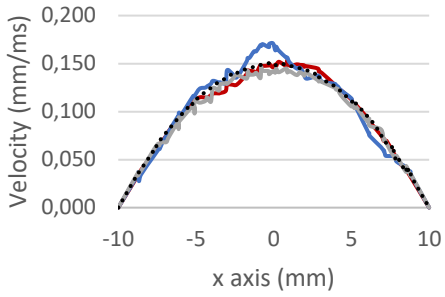	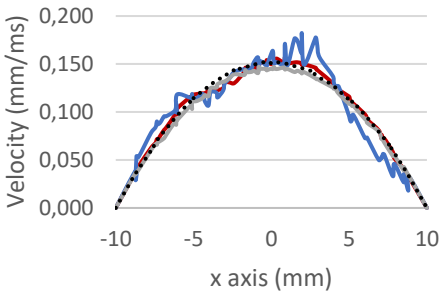
Section 2	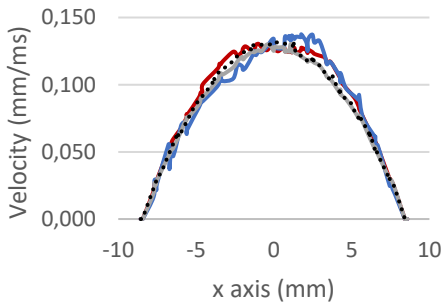	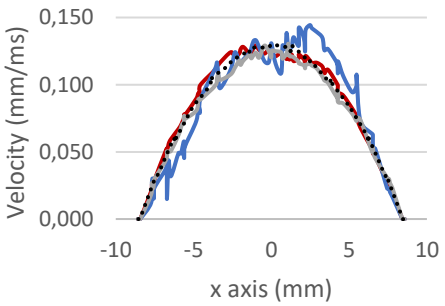
Section 3	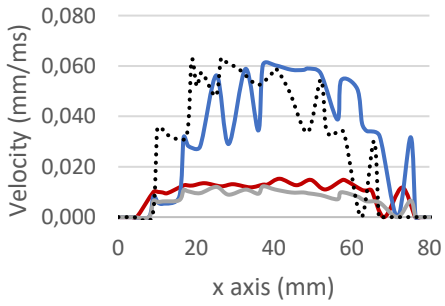	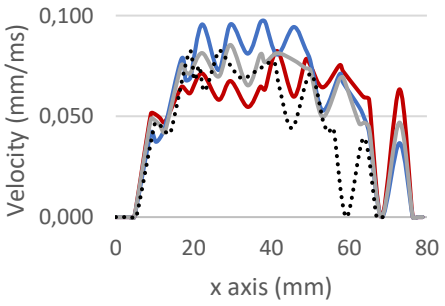
Section 4	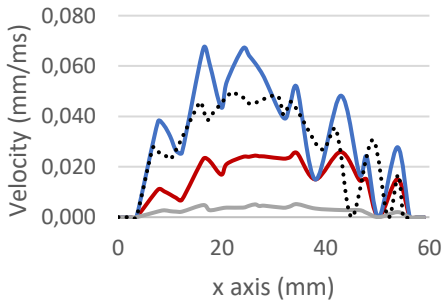	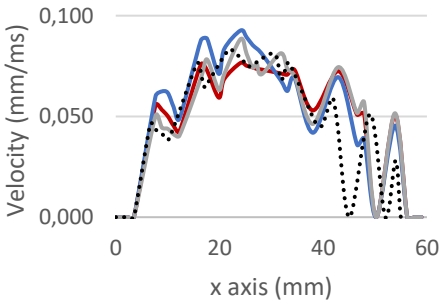

In the isomaps from Table 8. 2 it is observed that the colours of the blood flow dispersion were more defined compared to the results provided in the case studies analysed previously, which means that the blood flowed in a laminar and constant regime, with few perturbations.

Comparing the results between the simulations with 1 outlet velocity and with 3 outlet velocities it was verified that the last one enabled flow patterns with more irregularities than the former. The explanation for this result is the fact that the blood flow was forced to diverge to the branches, causing disruptions and irregularities in the stream. In the first scenario, where it was only imposed an outlet velocity in the end of the model, it is detected a notable blood velocity in the branches, especially in the RPIM and FEM with 6 nodes results (see graphs from Table 8. 3). This means that, despite not being imposed any outlet velocity in the branches, the flow diverged to them in a natural mode.

From the results of Table 8. 2 and Table 8. 3, it is concluded that (1) the imposition of 1 outlet velocity has better outcomes in the blood flow pattern; (2) in both scenarios, the method that verified inferior results was the RPIM, because the flow presents several irregularities along the extension of the model; (3) the method with better outcomes was the FEM with triangular elements with 6 nodes.

Since the method that enabled inferior results was RPIM, the parameters of simulation for this method were altered (see Table 8. 4). The implementation of these parameters was completed in three situations: no outlet velocity, one outlet velocity and three outlet velocities. The results can be observed in Figure 8. 19.

Table 8. 4 – RPIM parameters

RPIM
Nodes in the influence-domain: **27**
c = **1.42**
p = **1.03**
Polynomial Basis: **Constant**
Integration Points: **3 per triangle**

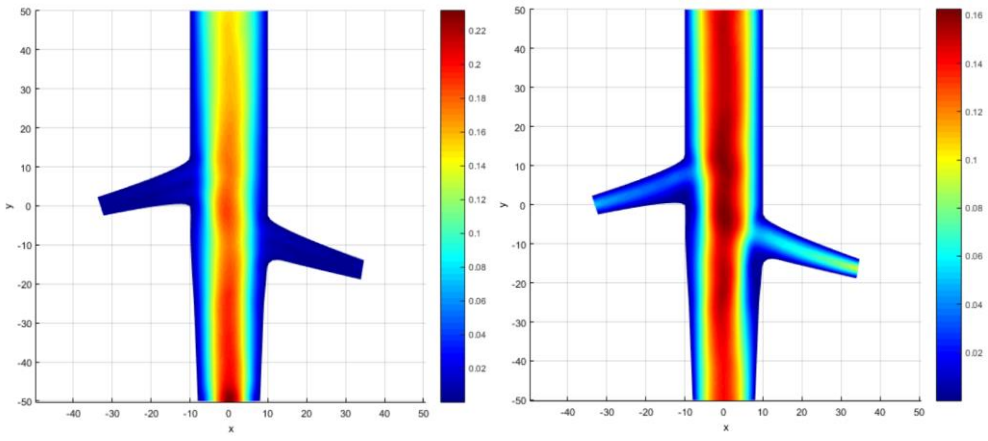

(a) (b)

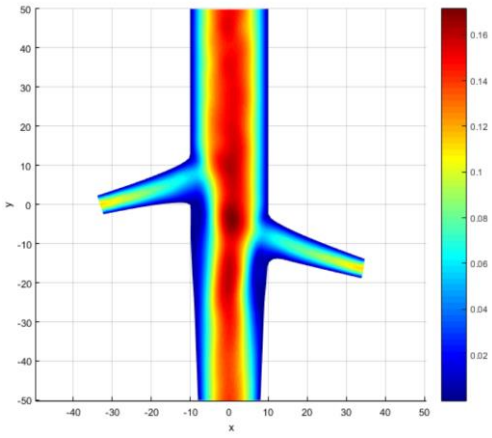

(c)

Figure 8. 19 – Blood flow velocity isomaps of the RPIM simulation with altered parameters: (a) model with no outlet velocity (colour bar up to 0.2316 mm/ms); (b) model with one outlet velocity in the end of the blood vessel (colour bar up to 0. 0.1624 mm/ms); (c) model with three outlet velocities (colour bar up to 0.1714 mm/ms).

The colour dispersion maps from Figure 8. 19 reveal a significant improvement in the results after the change of the RPIM parameters. The colours of the geometrical models are much well defined compared to the ones of Figure 8. 17 (b) and Table 8. 2 .

It is observed in Figure 8. 19 (a) that the maximum velocity was approximately 0,23 mm/ms, causing a higher concentration of dark red colour in the end of the model. When the outlet velocity was imposed, the results improve, and it is verified already some velocity in the branches of the model. Finally, when the three outlet velocities are imposed, the results are equally satisfactory, with the detail of a higher evidence of blood flow velocity in the branches.

By analysing all the previous outcomes, it can be withdrawn the following conclusions:

- The results of the simulation of blood flow in non-structured and semi-structured meshes did not differ significantly;
- Irregular meshes resulted in disruptions and oscillations in the colour maps for all the numerical methods, so it was necessary to implement additional outlet velocities;
- The study of the blood flow and the calibration of the parameters of simulation in irregular meshes are important in this particular study, since the real geometries of the aortic aneurysms will have an irregular mesh, being important the definition of the parameters that will be implemented in order to obtain better results;
- The results of the blood flow when imposed the outlet velocities enhanced significantly, being the greatest discrepancy observed in the RPIM results;
- To solve the anterior problem, the RPIM parameters were altered, enabling improved results.

After this phase of the blood flow study, it is also necessary to calibrate the parameters of simulation in three-dimensional geometries and obtain the features that will allow better outcomes.

8.1.2 Three-dimensional Branched Model

For the analysis of the blood flow in a three-dimensional geometry, the model represented in Figure 8. 20 (a) was constructed, using the same dimensions of the 2D model (see Figure 8. 1). The geometry, that represents half of a branched infra-aorta, was designed and meshed in SolidWorks® and, posteriorly, imported to FEMAS®, where a static fluid flow analysis was completed. It is noticed that, in Figure 8. 20 (a), it is represented two points, A and B, which will be used for obtaining the blood flow velocities for a posterior analysis.

The properties of the blood for this study were considered the same as in the previous analysis, i.e., the blood was assumed a Bingham fluid, with a density of $1{,}05\ kg/mm^3$ and a viscosity of $3{,}5 \times 10^{-6}\ N.ms/mm^3$.

In Figure 8. 20 (b) it is represented the essential boundary conditions in the curved surface of the model, where the nodes marked in grey are constrained in all directions, i.e, Ox, Oy and Oz. In Figure 8. 20 (c) it is observed the essential boundary conditions in the frontal surface of the model, in which the green nodes are constrained in the Ox direction. Also, in the last representation, it is possible to verify the imposition of the blood flow velocity in the superior surface of the blood vessel.

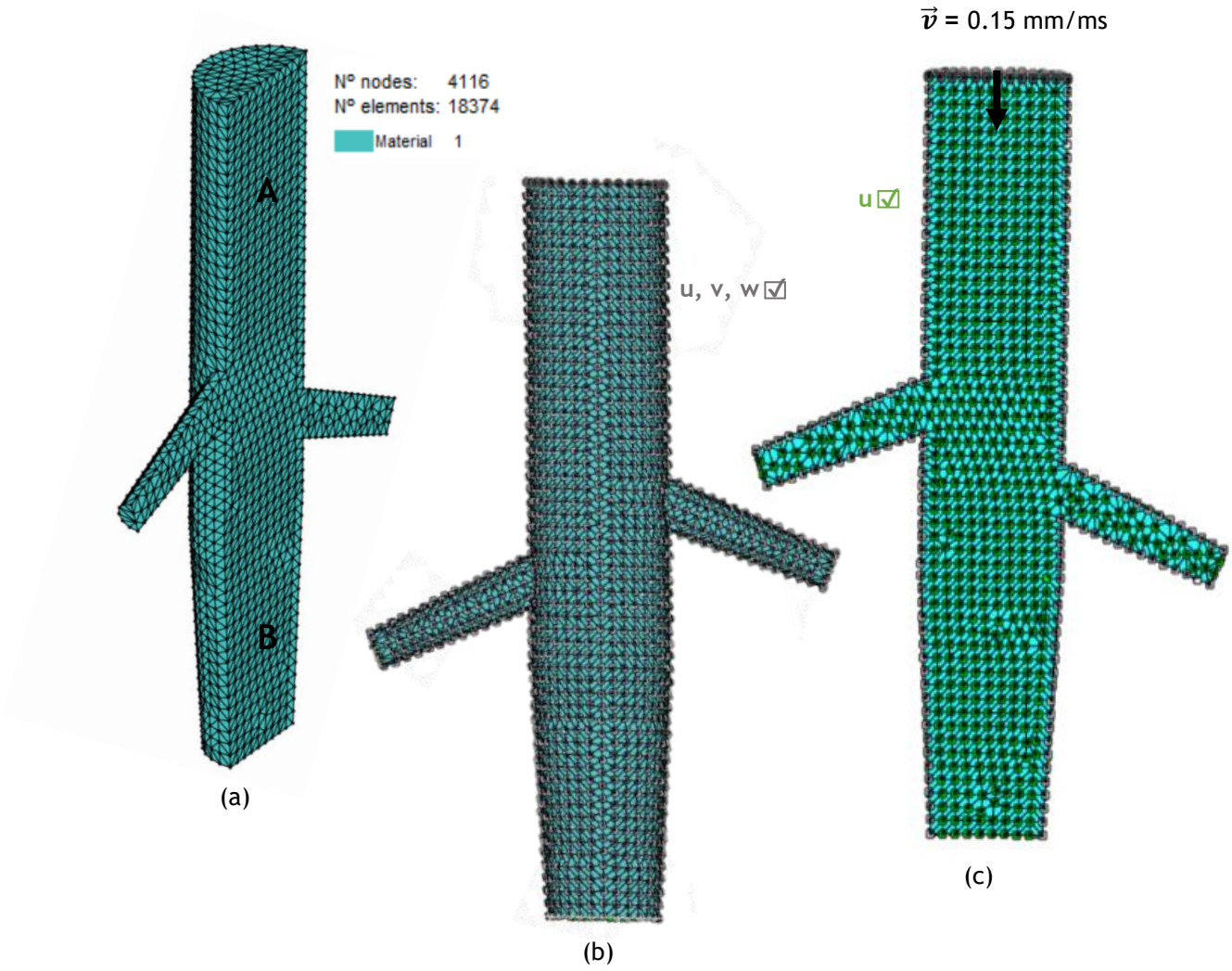

Figure 8. 20 - Representation of the global 3D geometric model: (a) element mesh; (b) and (c) boundary conditions and imposition of the blood's velocity.

The velocity was imposed in the superior plane of the geometrical model following a uniform distribution, which does not agree with the real velocity distribution in pipes. However, as observed in stress distributions in solids in which a stress concentration, due to the application of a concentrated load, tends to gradually distribute along the extension (Saint Venant's principle), in fluid flows inside pipes, the initial imposed velocity tends to adjust to a parabolic distribution. Thus, after a short distance from the velocity imposition, it is visible that the velocity profile follows a parabolic pattern [112].

The parameters of the RPIM and NNRPIM for three-dimensional simulations are described in Table 8. 5.

Table 8. 5 – RPIM and NNRPIM parameters

RPIM	NNRPIM
Nodes in the influence-domain: **27**	c = **0.0001**
c = **1.42**	p = **0.9999**
p = **1.03**	Influence-cell: **Second Order**
Polynomial Basis: **Constant**	Polynomial Basis: **Constant**
Integration Points: **1 per triangle**	Integration Points: **1 per sub-cell**

After the definition of the essential constraints and parameters for the simulation, a static fluid flow analysis was performed using FEM, RPIM and NNRPIM in three different scenarios:

- Analysis of the blood flow with no imposed outlet velocity;
- Analysis of the blood flow with one imposed outlet velocity, in the end of the blood vessel;
- Analysis of the blood flow with three imposed outlet velocities, in the end and branches of the model.

The results of the simulations are depicted from Figure 8. 21 to Figure 8. 29.

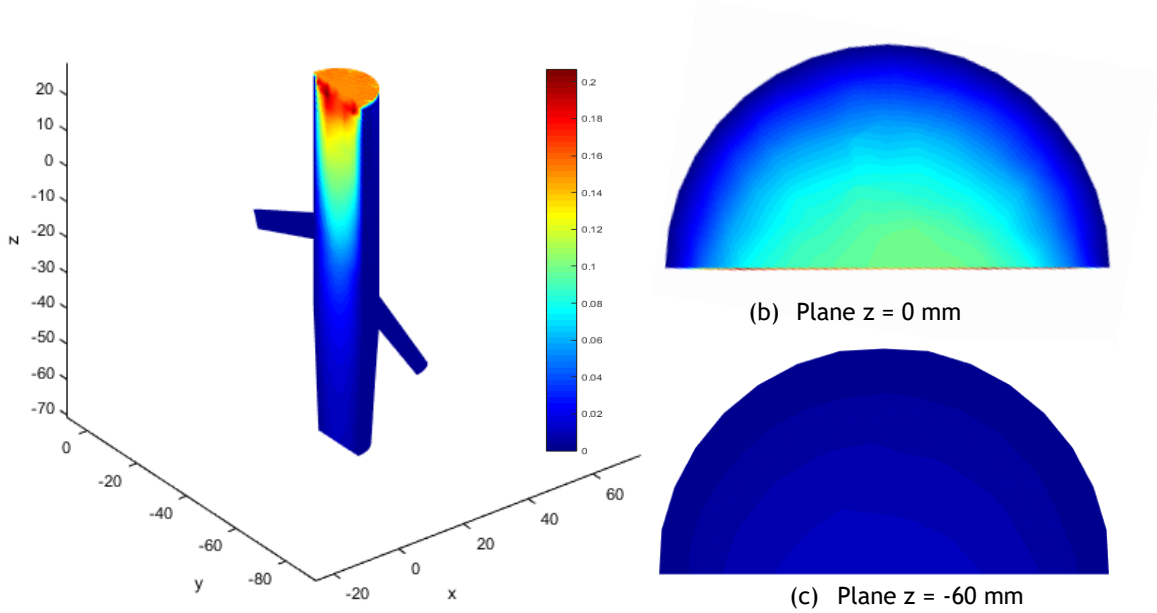

(a) Global three-dimensional model (colour bar up to 0.2051 mm/ms)

(b) Plane z = 0 mm

(c) Plane z = -60 mm

Figure 8. 21 – Colour dispersion maps of the blood flow velocity with FEM analysis. For this simulation it was only considered the inlet velocity and no outlet velocities.

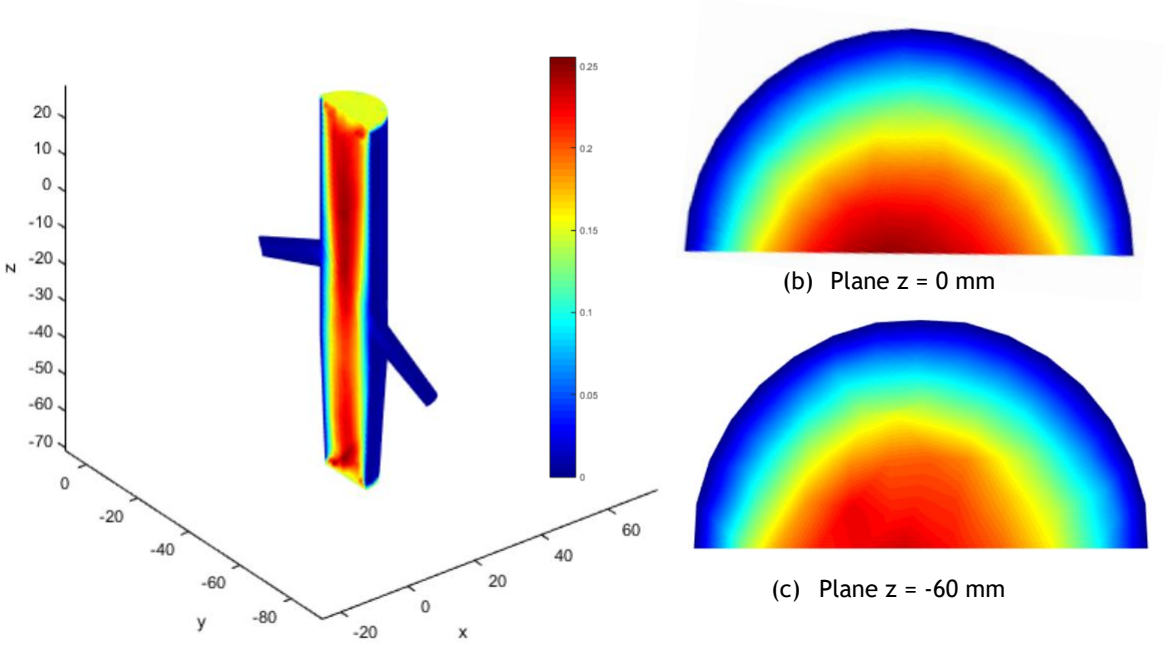

(a) Global three-dimensional model (colour bar up to 0.2550 mm/ms)

(b) Plane z = 0 mm

(c) Plane z = -60 mm

Figure 8. 22 - Colour dispersion maps of the blood flow velocity with FEM analysis. For this simulation it was considered one outlet velocity (in the end of the geometrical model).

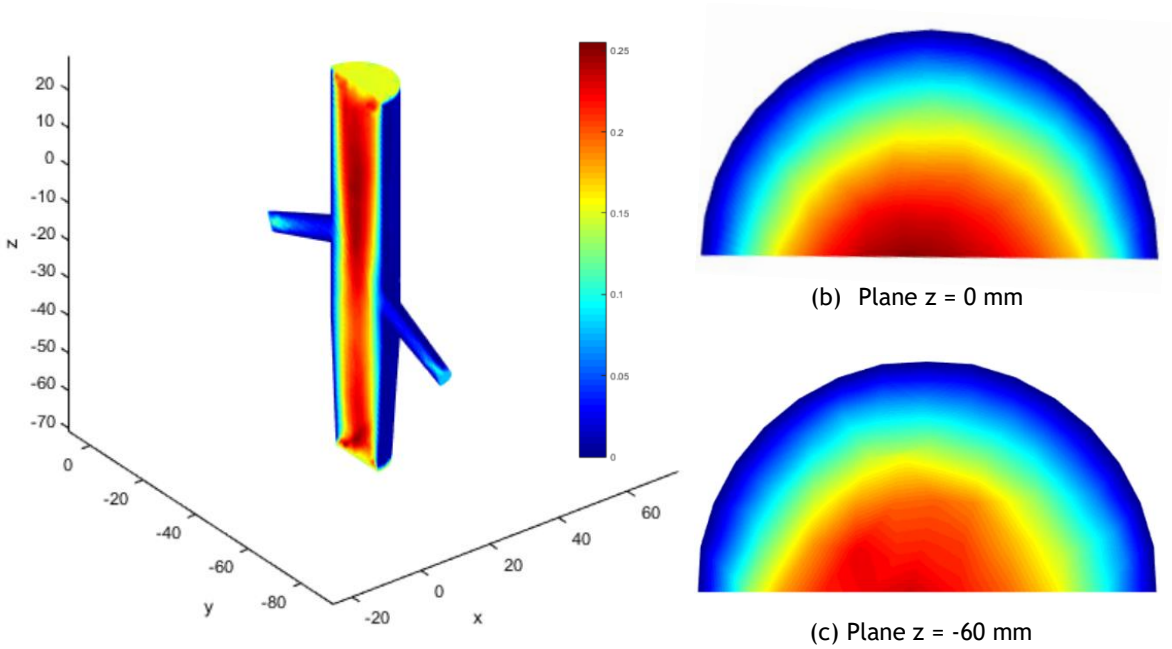

(a) Global three-dimensional model (colour bar up to 0.2550 mm/ms)

(b) Plane z = 0 mm

(c) Plane z = -60 mm

Figure 8. 23 - Colour dispersion maps of the blood flow velocity with FEM analysis. For the simulation it was considered three outlet velocities (in the end and in both ramifications of the geometrical model).

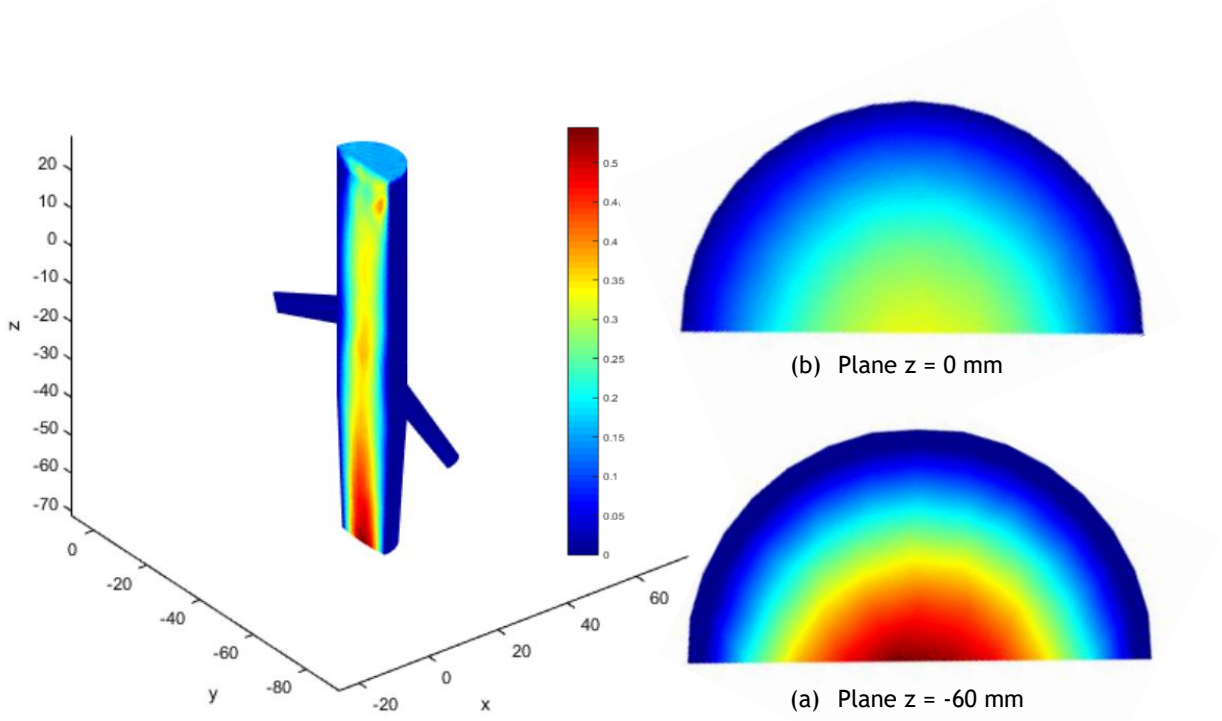

(a) Global three-dimensional model (colour bar up to 0.5441 mm/ms)

Figure 8. 24 - Colour dispersion maps of the blood flow velocity with RPIM analysis. For this simulation it was only considered the inlet velocity and no outlet velocity.

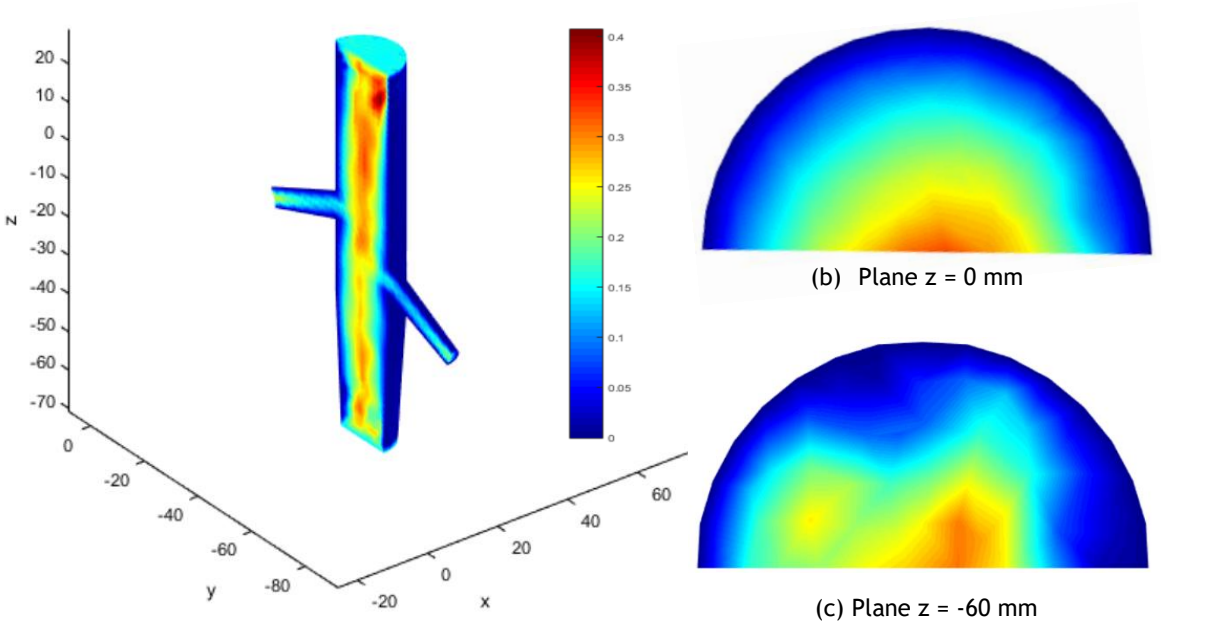

(a) Global three-dimensional model (colour bar up to 0.4067 mm/ms)

Figure 8. 25 - Colour dispersion maps of the blood flow velocity with RPIM analysis. For this simulation it was considered one outlet velocity (in the end of the geometrical model).

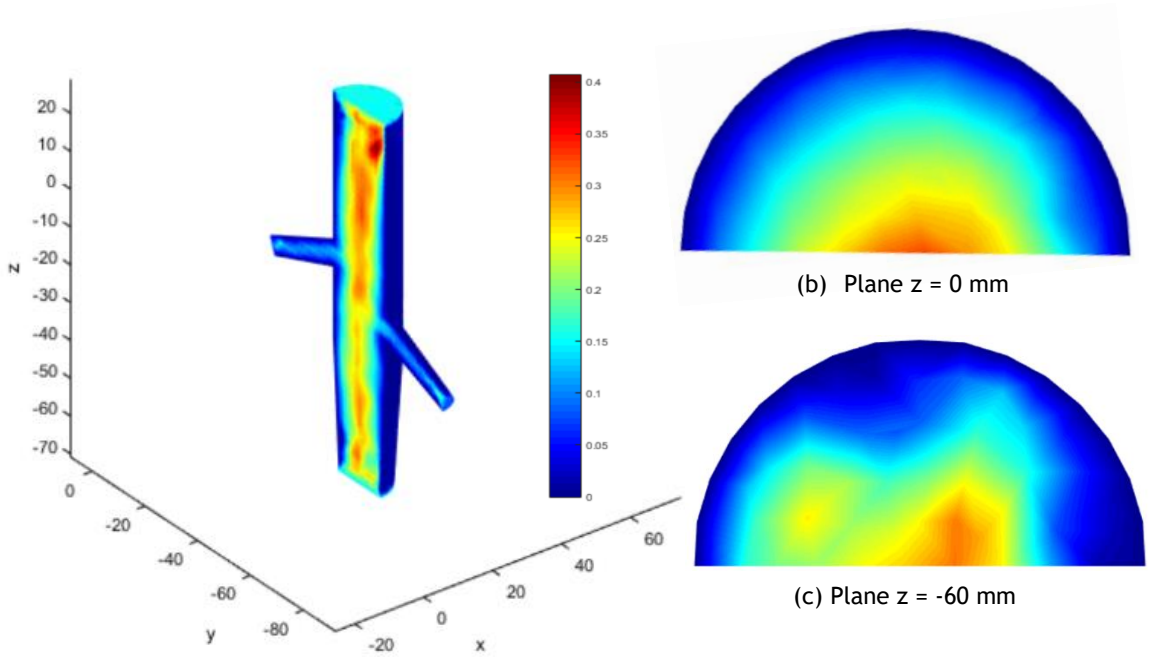

(a) Global three-dimensional model (colour bar up to 0.4071 mm/ms)

(b) Plane z = 0 mm

(c) Plane z = -60 mm

Figure 8. 26 - Colour dispersion maps of the blood flow velocity with RPIM analysis. For the simulation it was considered three outlet velocities (in the end and in both ramifications of the geometrical model).

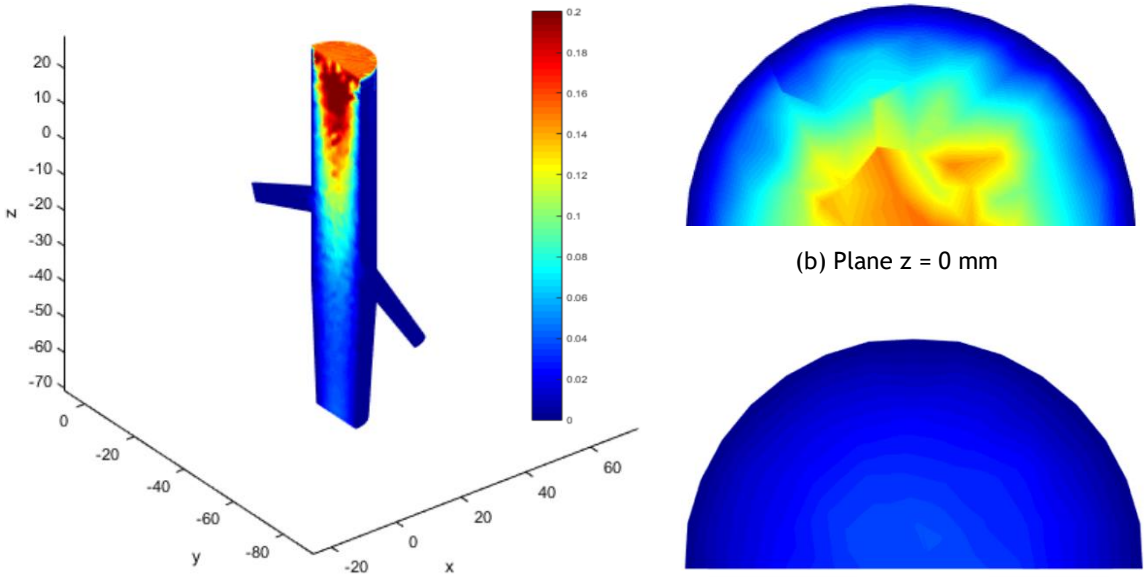

(a) Global three-dimensional model (colour bar saturated at 0.2 mm/ms)

(b) Plane z = 0 mm

(c) Plane z = -60 mm

Figure 8. 27 - Colour dispersion maps of the blood flow velocity with NNRPIM analysis. For this simulation it was only considered the inlet velocity and no outlet velocity.

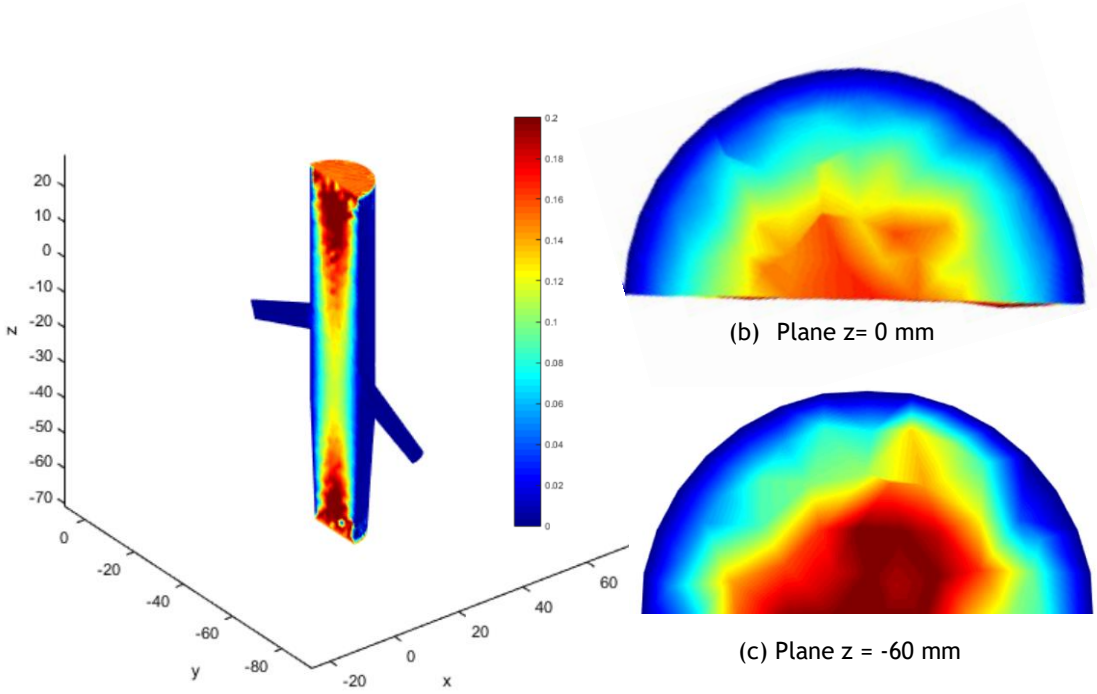

(a) Global three-dimensional model (colour bar saturated at 0.2 mm/ms)

Figure 8. 28 - Colour dispersion maps of the blood flow velocity with NNRPIM analysis. For this simulation it was considered one outlet velocity (in the end of the geometrical model).

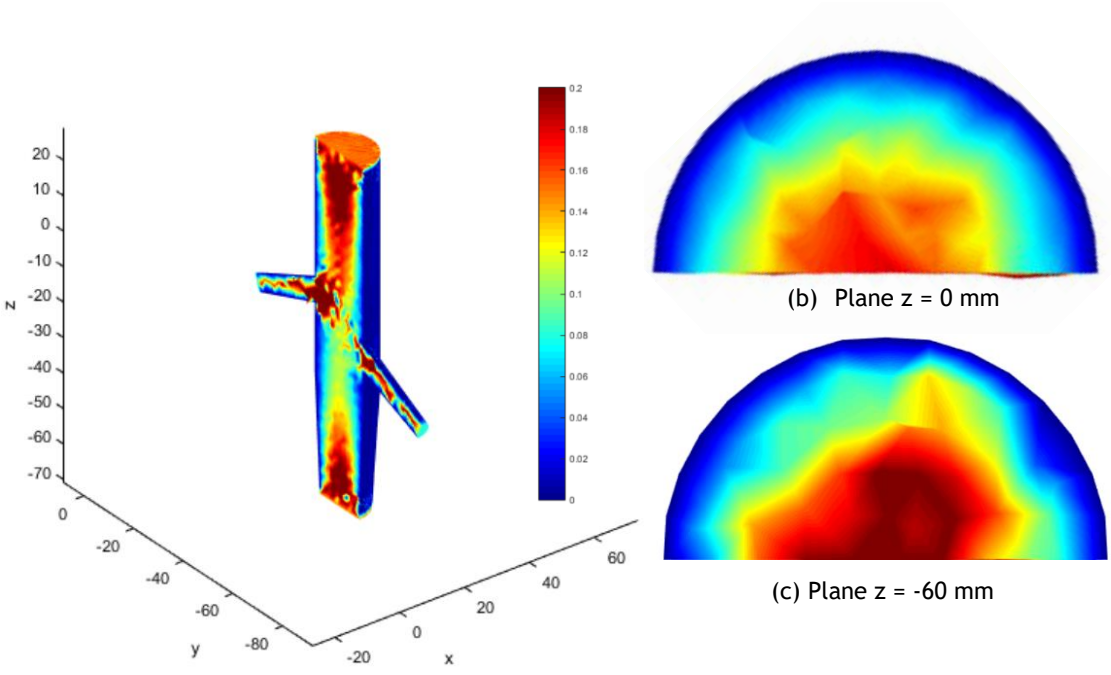

(a) Global three-dimensional model (colour saturated at 0.2 mm/ms)

Figure 8. 29 - Colour dispersion maps of the blood flow velocity with NNRPIM analysis. For the simulation it was considered three outlet velocities (in the end and in both ramifications of the geometrical model).

In the previous figures it is demonstrated the patterns of colours of the blood flow velocity for FEM, RPIM and NNRPIM. In the first approach, were it was not imposed an exit velocity in any of the extremities of the geometry, it is observed that the isomaps present several irregularities for all the numerical methods. In these cases, the velocity dispersed and did not follow a laminar and constant profile in the entire extension of the branched artery, achieving a maximum in the terminal portion of the model, for the RPIM (see Figure 8. 24). In the result of FEM and NNRPIM, the opposite was observed, i.e., a decrease in the blood velocity in the inferior region of the model.

Posteriorly, when one outlet velocity was imposed, the results of FEM and NNRPIM improved significantly, revealing a more regular and defined map of colour (see Figure 8. 22 and Figure 8. 28, respectively). On the other hand, the results from RPIM did not improve, being verified disruptions in the blood flow velocity.

Lastly, when the three outlet velocities were imposed, the FEM results were very similar to the previous scenario (one outlet velocity), with some significant velocity being registered in the branches of the model, as it was expected. The RPIM results follow the same reasoning of the FEM results, i.e., it is verified little changes between the application of one or three outlet velocities. For the NNRPIM, if we contrast the results up to a maximum value of 0.2 mm/ms, it is observed a high concentration of blood velocity in specific zones, that correspond to the inlet, outlet and beginning of the branches of the geometrical model.

To conclude about the differences between the numerical methods in this three-dimensional study, the graphs of Figure 8. 30 were constructed. The points A and B that are presented in the graphs have the following coordinates: $[x_{A,}\ y_{A,}\ z_{A,}] = [-41.26,\ 19.77,\ 0.5468]$ and $[x_{B,}\ y_{B,}\ z_{B,}] = [-42.77,\ 19.77, -60.21]$, respectively (see Figure 8. 20).

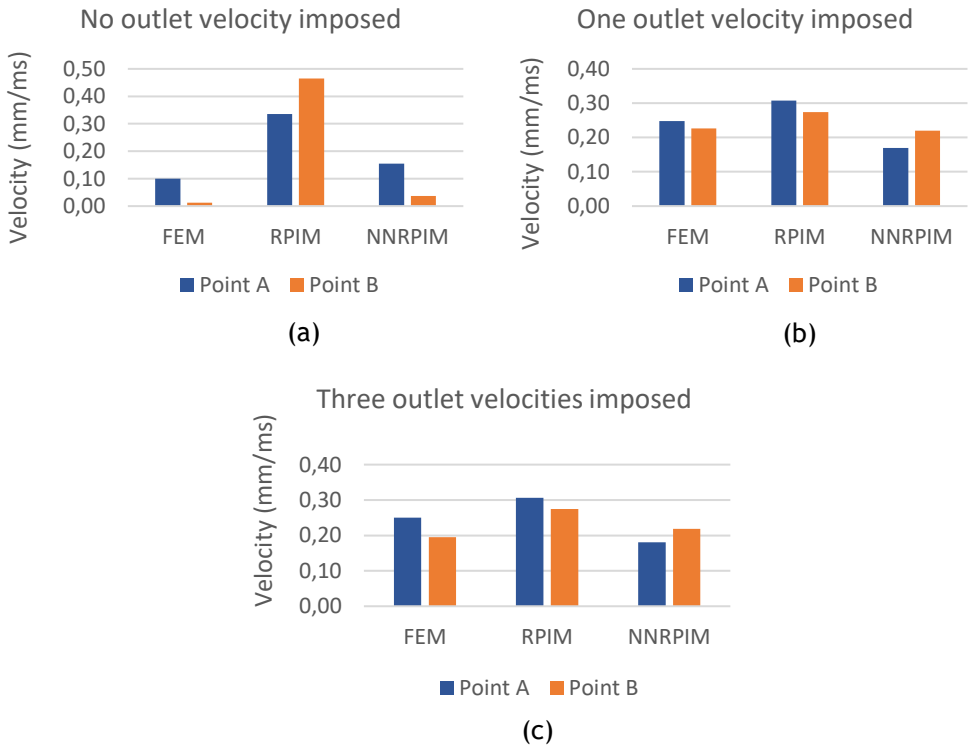

Figure 8. 30 – Comparison between the numerical methods used in the three-dimensional study, in three scenarios: imposition of none, one or three outlet velocities.

Observing Figure 8. 30 it is verified that the graphs (b) and (c) are highly similar. This was already expected, since in the colour maps it was observed few differences between the scenarios where one and three outlet velocities are imposed. In these cases, the main change in blood velocity occurs in the branches, not affecting significantly the entire geometrical model. On the other hand, the graph (a) presents more discrepancies when compared to the graphs (b) and (c).

Focusing on the numerical methods it is observed that:

- In the graph (a) the method that registered a higher difference in the velocity was the RPIM, being almost three and four times higher in points A and B, respectively, compared to the other methods. Also, it is observed that the results from RPIM provided a higher velocity in point B, and the other methods resulted in the opposite (the point A with higher velocity);
- In the graphs (b) and (c) the results between the numerical methods were more similar, due to the imposition of an outlet velocity in the final portion of the geometrical model. Also, the differences between the velocities in both points were not so abrupt as in the first graph, which is associated to a laminar and constant blood flow behaviour.

From this study on blood flow in a three-dimensional branched structure it is possible to conclude that:

1. The FEM is the method that provides better results among the three numerical methods that were studied;
2. Even with the calibration of the parameters of simulation in the RPIM, the results did not follow the expected, registering disruptions and irregular patterns along the geometrical model;
3. The NNRPIM is the method that provide less optimal results, which can be related to the Galerkin weak form integration problems, scarce smoothness of the mesh or with the fluid formulation that was used.

8.2 Blood Flow Analysis in a Fusiform Aortic Aneurysm

In this subchapter it will be studied the blood flow in two and three-dimensional aortic aneurysm models, using FEM, RPIM and NNRPIM. As a variation factor, the maximum diameter of the aneurysm was gradually increased to study how it influences the behaviour of the blood flow inside the diseased blood vessel.

The 2D and the 3D models of the fusiform aneurysm were constructed and meshed in FEMAP® and then imported to FEMAS®, where a fluid flow analysis was performed following the parameters defined in the previous section.

8.3.1. Two-dimensional Analysis

In Figure 8. 31 it is observed the two-dimensional models of the fusiform aneurysms with an increasing diameter. As in the branched model, these models are 100 mm length and the neck has a 20 mm distance. It is noticed that all the models have approximately 2000 nodes, regarding to the number of nodes achieved in the convergence study. The boundary conditions that were defined are the same as in the previous study, i.e., the curved segments of the model are constrained in all directions (Ox and Oy). Since the geometrical models present a regular mesh, only the inlet parabolic velocity was considered in this study.

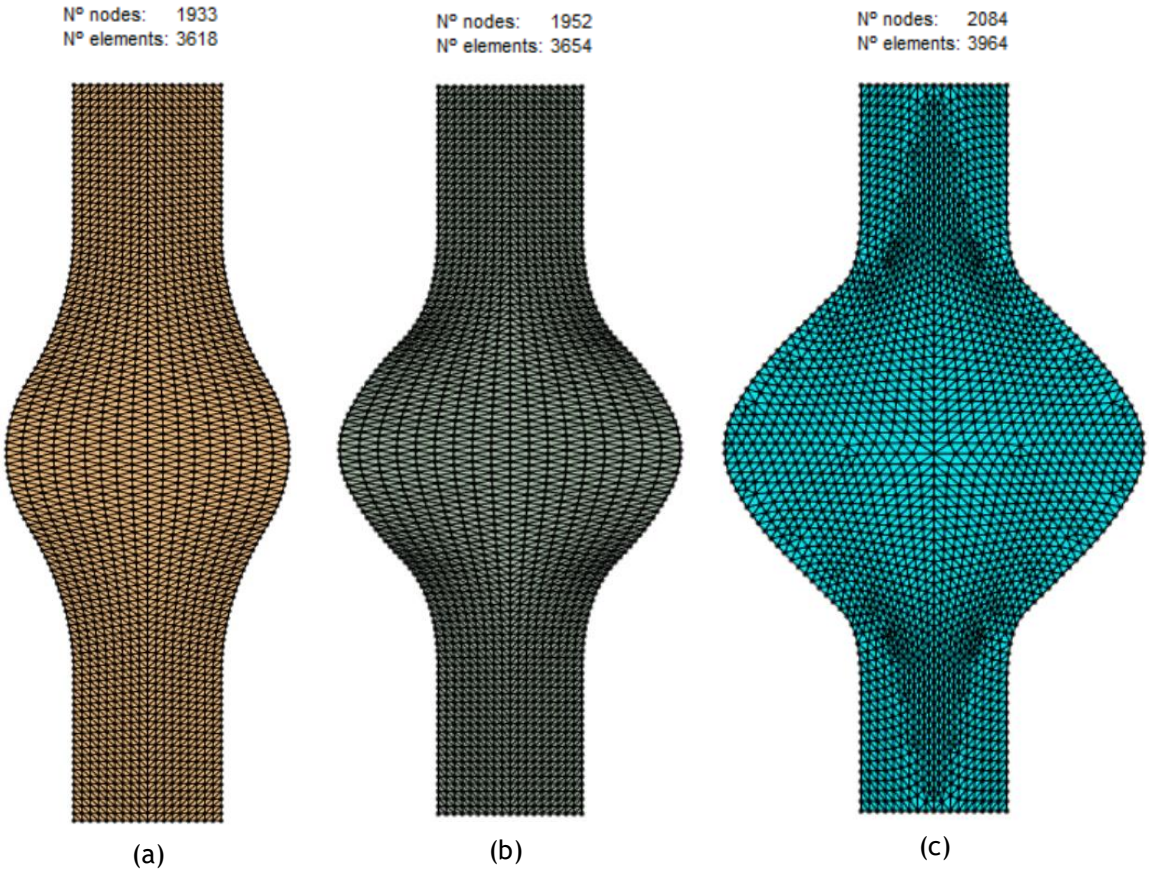

Figure 8. 31 – Global geometrical models of the fusiform aortic aneurysms with a maximum diameter of: (a) 40 mm; (b) 50 mm and (c) 60 mm.

Table 8. 6 – Colour dispersion maps of the velocity in the aortic aneurysms' models, with the variation of the maximum diameter. The diameters of 40 mm, 50 mm and 60 mm correspond to the Aneurysm 1, 2 and 3, respectively.

	FEM	RPIM	NNRPIM	
Aneurysm 1	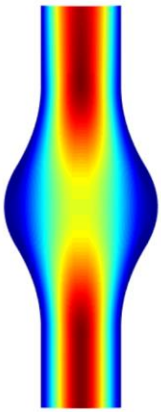	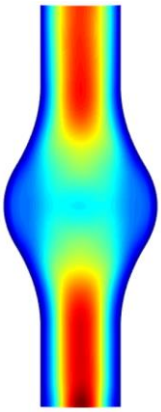	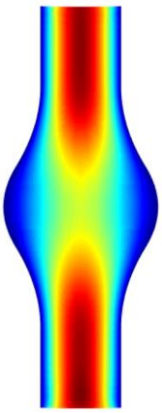	mm/ms Max  Min
	Max: 0.1568 Min: 0.0	Max: 0.1825 Min: 0.0	Max: 0.1541 Min: 0.0	
Aneurysm 2	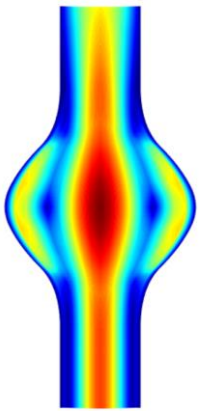	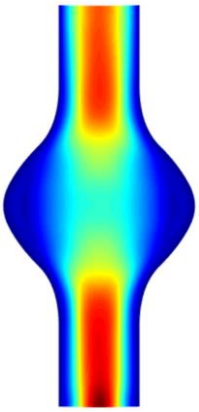	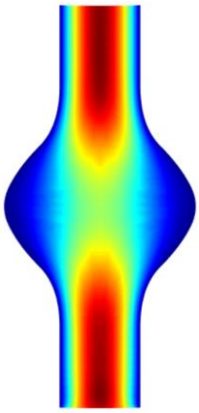	mm/ms Max 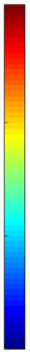 Min
	Max: 0.2393 Min: 0.0	Max: 0.1902 Min: 0.0	Max: 0.1522 Min: 0.0	
Aneurysm 3	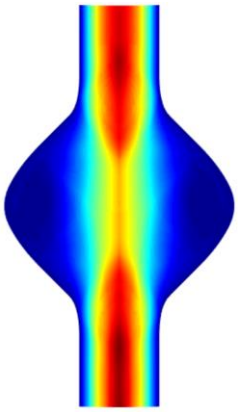	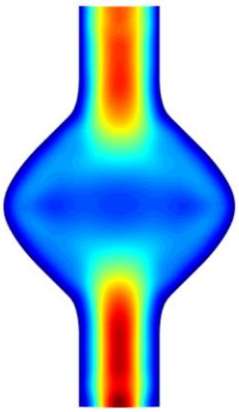	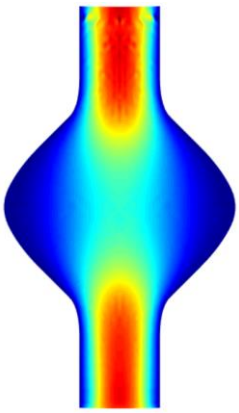	mm/ms Max  Min
	Max: 0.1664 Min: 0.0	Max: 0.1904 Min: 0.0	Max: 0.1633 Min: 0.0	

After obtaining the maps of colours, three regions were delimited in the geometrical models, as it is depicted in Figure 8. 32. The blood's velocity of the nodes that are comprised in each section were obtained and the results can be observed from Figure 8. 33 to Figure 8. 35.

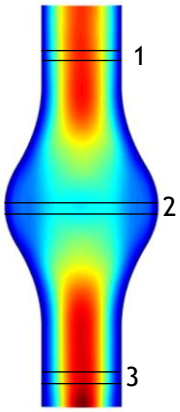

Figure 8. 32 – Schematization of the sections demarked for analysis.

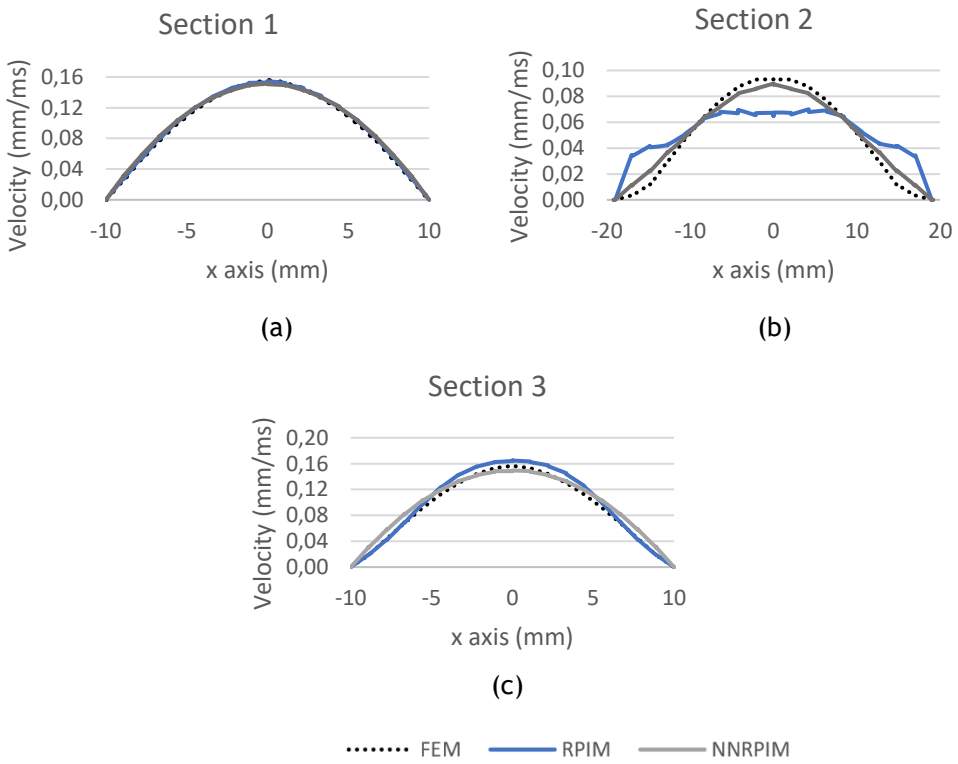

Figure 8. 33 – Velocity profiles of the blood flow in the Aneurysm 1, taken from: (a) section 1; (b) section 2; (c) section 3.

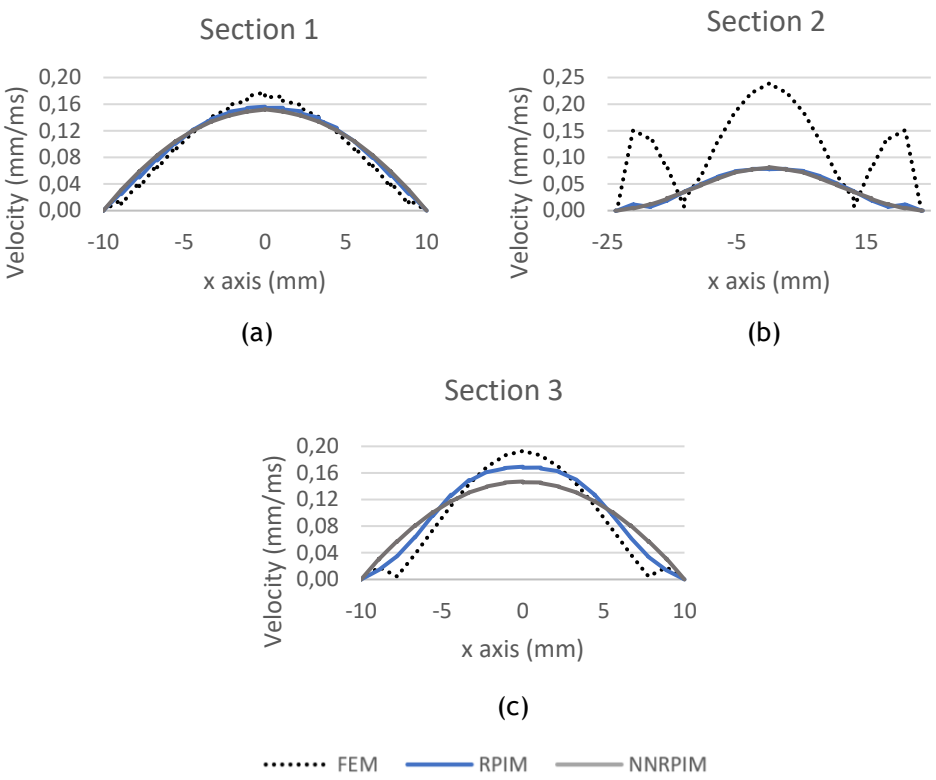

Figure 8. 34 - Velocity profiles of the blood flow in the Aneurysm 2, taken from: (a) section 1; (b) section 2; (c) section 3.

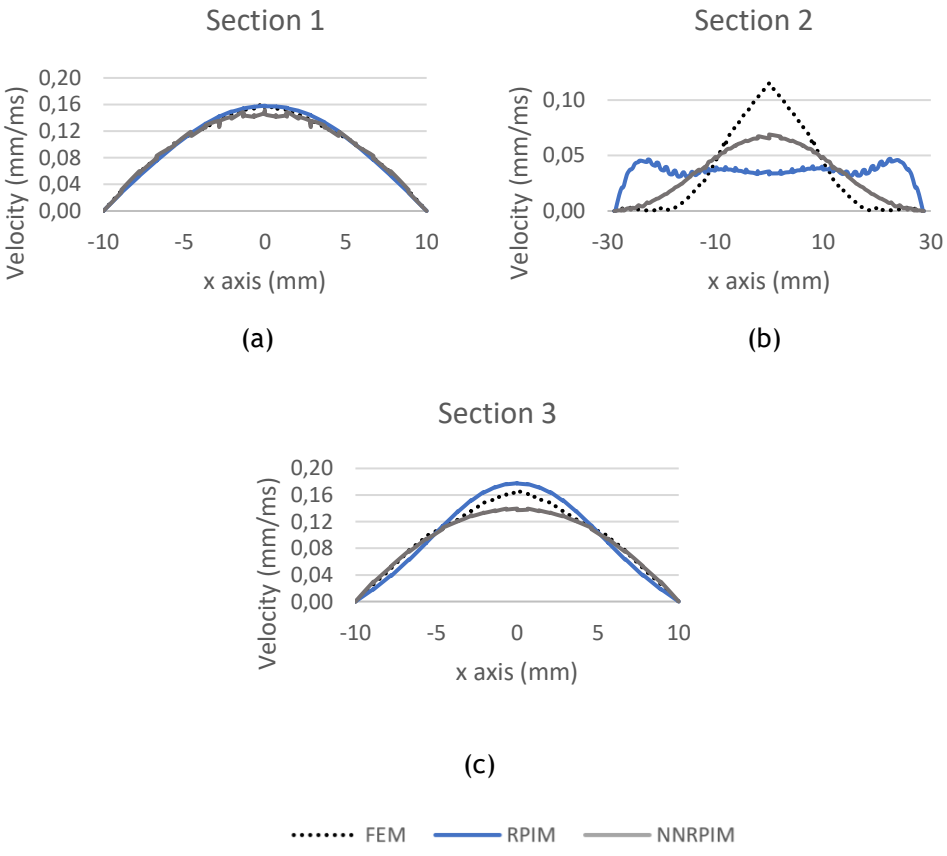

Figure 8. 35 - Velocity profiles of the blood flow in the Aneurysm 3, taken from: (a) section 1; (b) section 2; (c) section 3.

In the isomaps of Table 8. 6 it is observed the behaviour of the blood's velocity in the three aneurysms, using different numerical methods: FEM, RPIM and NNRPIM. The common feature that is observed in all the results is the steadiness of the isomaps colours: since the meshes are regular, it enabled a better-defined blood velocity pattern when compared to the irregular meshes previously analysed.

Focusing on the aneurysm 1, the blood flow enters and exits the model with a laminar and well-defined parabolic velocity, which can be verified by the symmetry of the colours. The dispersion of the flow occurs in the dilated zone, where the velocity decreases significantly. This analysis is transversal to all the numerical methods, however, in RPIM and NNRPIM there is a slight difference in the velocity obtained near the aneurysm walls: while in FEM the velocity was almost zero near the dilated wall, in RPIM and NNRPIM it is verified the passage of blood flow in those regions. Another data that can be stated by the observation of the results is the maximum velocity that was obtained for all methods. The values of the outlet velocity did not differ significantly from the inlet velocity or either from each other, being the most evident difference verified in the velocity of RPIM, that was approximately 0,03 mm/ms higher than the other methods.

The results of the aneurysm 2 follow the same reasoning as the anterior, however, in this case, the results from FEM are higher than the other methods, inclusively near the dilated wall. Also, in RPIM and NNRPIM results, it is observed low velocity near the dilated wall, which did not occur in the first aneurysm. Comparing the values of the velocities between the first and second aneurysms, it is verified an increase of the velocity in the dilated area in FEM; in RPIM the velocities were similar, with a maximum observed in the outlet of the geometry and, in NNRPIM, the results did not present significant discrepancies.

Finally, in the aneurysm 3 it is observed a slight decrease in the velocity for FEM results. The results for RPIM maintained similar and the velocity for NNRPIM increased lightly.

What can be concluded from the observation of the Table 8. 6 and from the graphs of Figure 8. 33, Figure 8. 34 and Figure 8. 35 is that the increasing of the maximum diameter of an aortic aneurysm do not alter significantly the maximum velocities. What changes are the blood flow patterns inside the geometrical models, which become turbulent and low-defined in the enlarged area when compared to the healthy portions of the blood vessel.

8.3.2. Three-dimensional Analysis

After the analysis of the blood flow in aortic aneurysms of two dimensions, a three-dimensional fluid flow study was performed. The constructed 3D geometrical models represent a quarter of an abdominal aneurysm and were built in FEMAP® following the same dimensions of the 2D model.

The properties of the blood flow were the same as in the previous studies as well as the parameters of simulation, which are described in Table 8. 5.

In Figure 8. 36 it is represented the essential boundary conditions applied in one of the geometrical models. For the remaining two models (with a higher diameter) the same boundary conditions were considered. Besides the boundary conditions, it is also represented, in Figure 8. 36 (b), three points – A, B and C -, from which the values of the blood's velocity will be analysed.

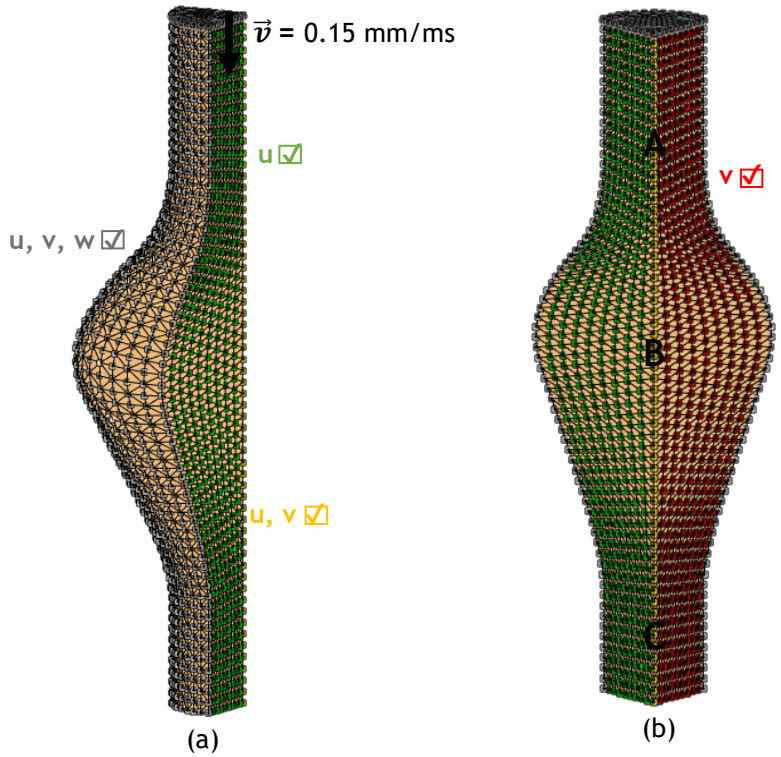

Figure 8. 36 – Essential Boundary Conditions applied in the three-dimensional fusiform aortic aneurysm.

As it can be observed, the nodes marked in grey are constrained in all directions, i.e, Ox, Oy and Oz and the nodes marked in green and red are constrained in the Ox and Oy directions, respectively. Also, there are nodes marked in yellow, which are constrained in both directions Ox and Oy. The blood flow velocity was imposed in the superior surface of the geometrical models and are represented by the nodes marked in grey (in the top of the model). The principle of application of the velocity followed the same reasoning as in the previous 3D study, in which the velocity was applied uniformly. Then, following Saint Venant's principle, the profile becomes naturally parabolic.

The results of the blood flow's study in this three-dimensional model are displayed from Figure 8. 37 to Figure 8. 45.

8.3.2.1 Aneurysm 1

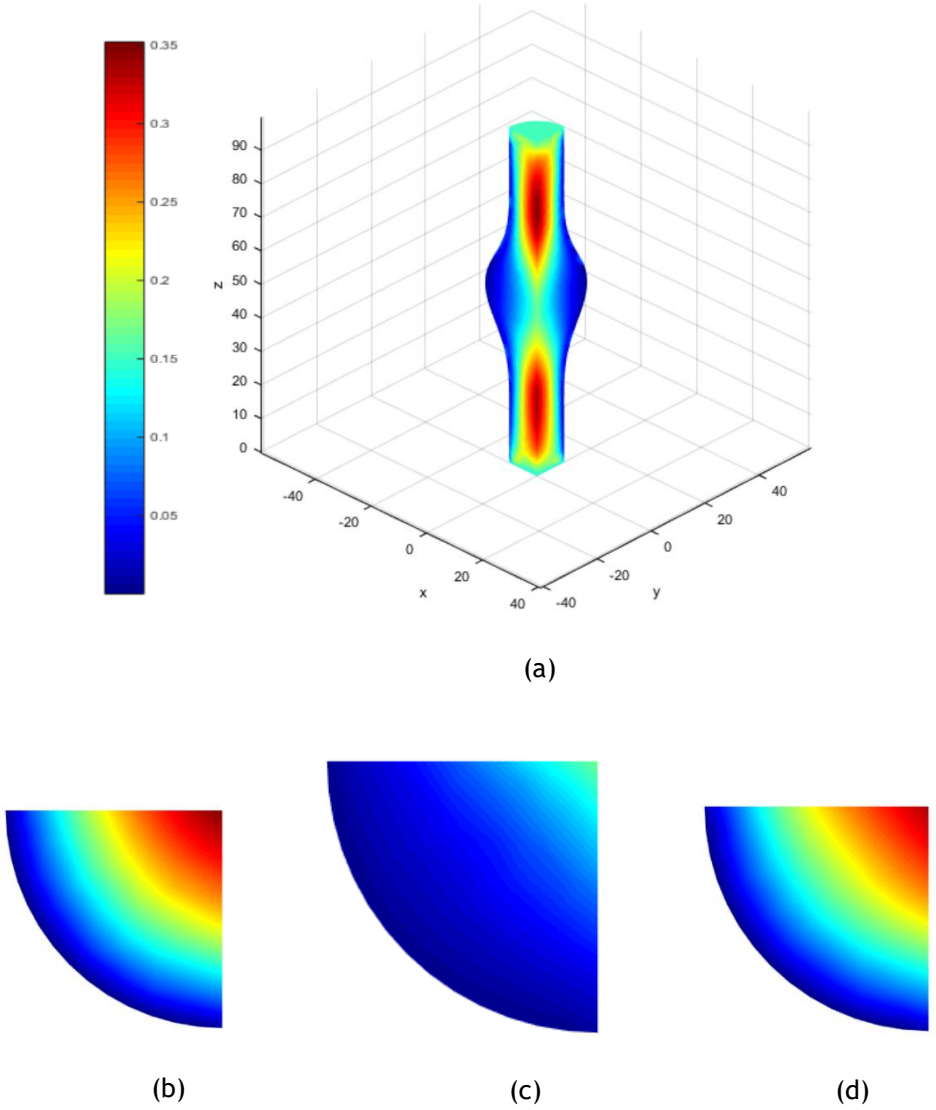

Figure 8. 37 – Colour dispersion map of the Aneurysm 1, using FEM: (a) global geometrical model (colour bar up to 0.3516 mm/ms); (b) plane z = 80 mm; (c) plane z = 50 mm; (d) plane z = 20 mm.

The results of Figure 8. 37 present a pattern similar to the 2D results, i.e., in the beginning of the blood vessel, the blood flows laminarly and with a parabolic profile, with a maximum velocity in the centreline. In the dilated portion of the aorta, it is verified a dispersion and a significant reduction of the blood flow, returning to a parabolic profile after the dilation. Observing the cross sections depicted in the figures (b), (c) and (d) it is detected that the maximum velocity occurs in the vertex, corresponding to the centreline of the geometrical model. Also, few differences are presented between figures (b) and (d), revealing that in the beginning and in the end of the vessel, the blood flow profile is similar.

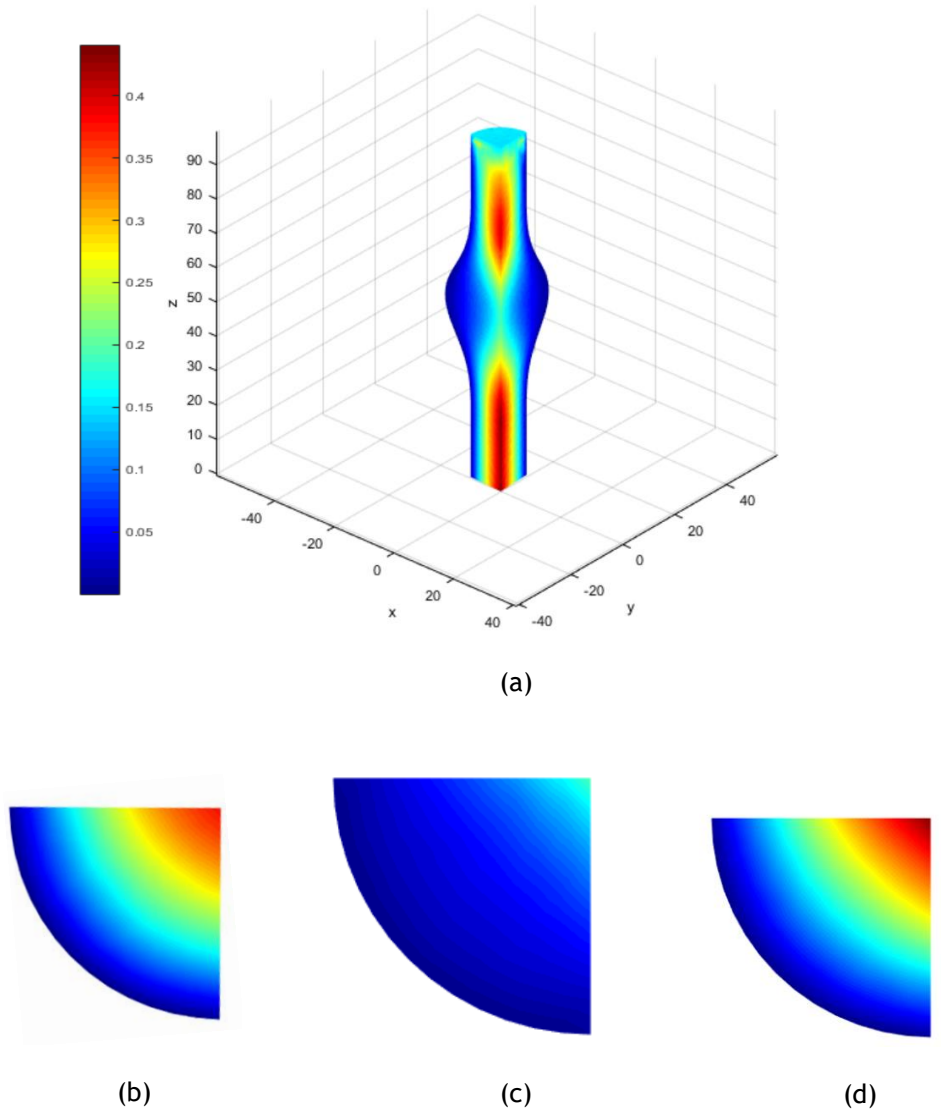

Figure 8. 38 - Colour dispersion map of the Aneurysm 1, using RPIM: (a) global geometrical model (colour bar up to 0.44 mm/ms); (b) plane z = 80 mm; (c) plane z = 50 mm; (d) plane z = 20 mm.

The results of Figure 8. 38 are very similar to the results obtained in FEM. The main difference that is observed is that, in this case, the maximum velocity occurs after the dilated portion of the vessel and the maximum velocity is approximately 0.1 mm/ms higher relatively to the previous result. The blood flow patterns follow the same reasoning, with a decrease of the velocity in the enlarged portion, maintaining the centreline with higher velocity.

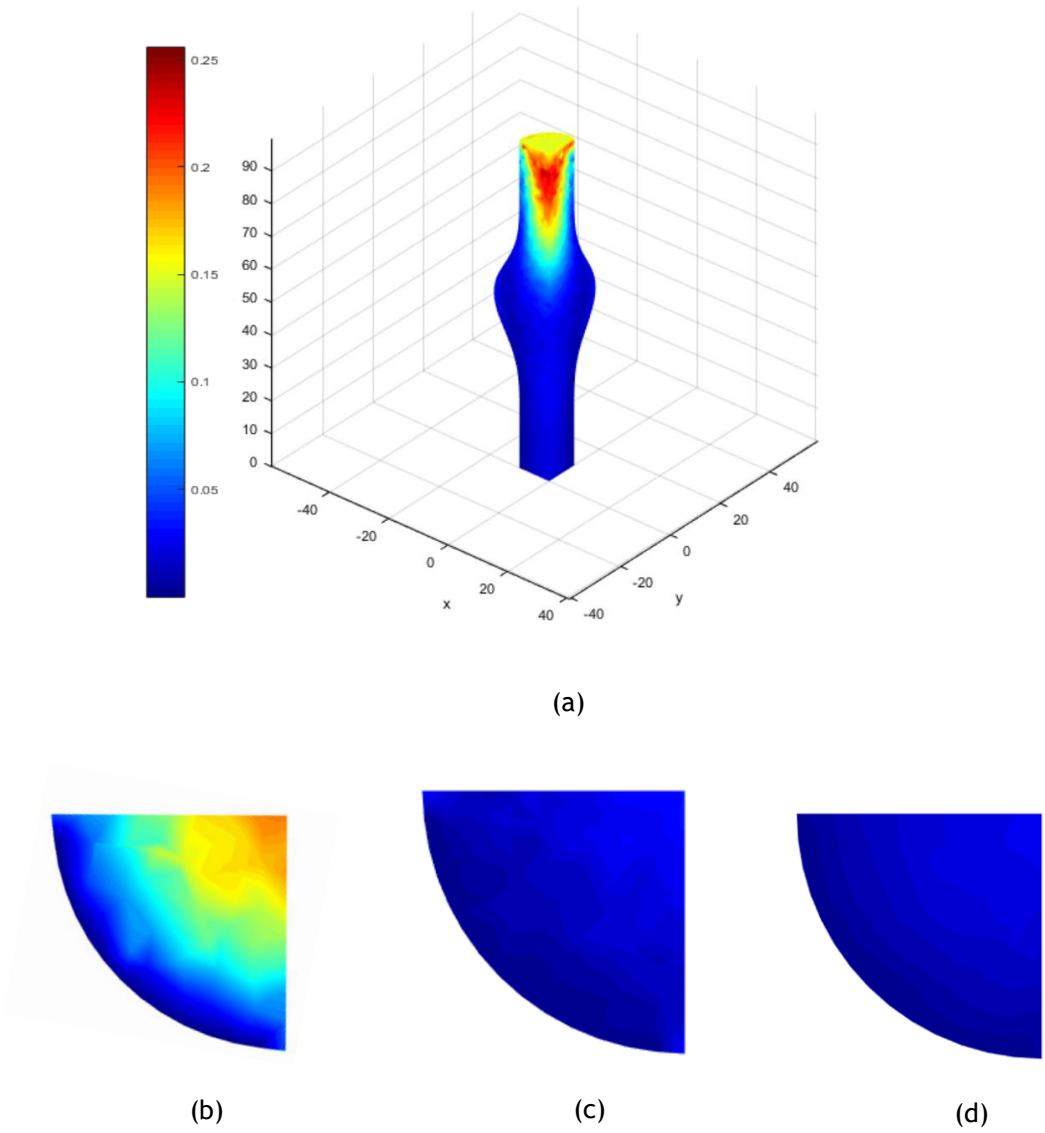

Figure 8. 39 - Colour dispersion map of the Aneurysm 1, using NNRPIM: (a) global geometrical model (colour bar up to 0.2555 mm/ms); (b) plane z = 80 mm; (c) plane z = 50 mm; (d) plane z = 20 mm.

The results obtained in NNRPIM are the most despair. The blood did not flow uniformly as in the previous results, standing only in the inlet portion of the geometrical model. What is verified is that when the blood flow reaches the dilated portion, it disperses and loses velocity and is not able to return to the initial pattern. As it is observed in figure (b), the velocity pattern in not well defined, which means that the flow was not stabilized in that region. In figure (c) it is also observed dispersion in the flow in the centreline.

8.3.2.2. Aneurysm 2

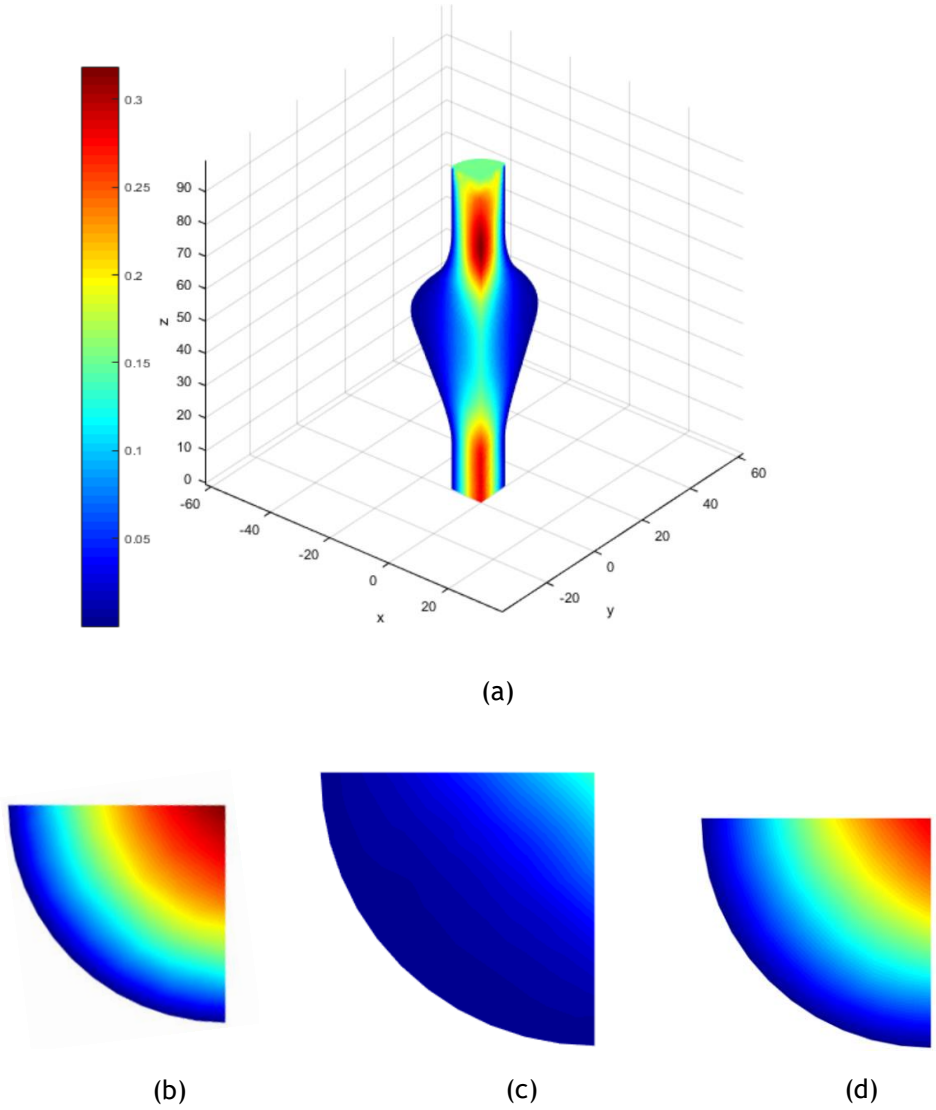

Figure 8. 40 - Colour dispersion map of the Aneurysm 2, using FEM: (a) global geometrical model (colour bar up to 0.3180 mm/ms); (b) plane z = 80 mm; (c) plane z = 50 mm; (d) plane z = 20 mm.

In the Figure 8. 40 it is verified a blood flow pattern similar to the observed in the Aneurysm 1. The maximum velocity occurred in the superior portion of the aneurysm, while in the inferior part, it was registered a small decrease. In the dilated part of the model, the velocity decreased to, approximately, 0.1 mm/ ms, which means that it reduced 0.05 mm/ms compared to the inlet velocity.

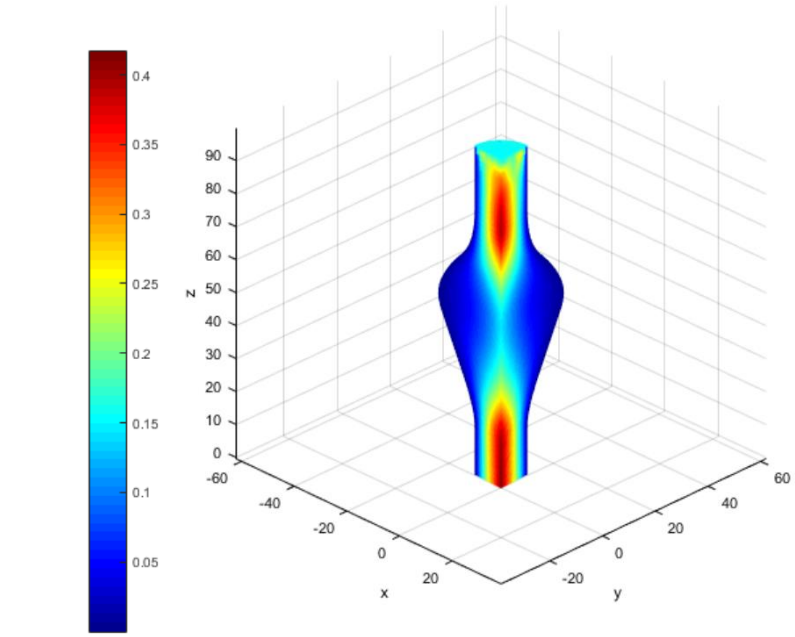

(a)

(b) (c) (d)

Figure 8. 41 - Colour dispersion map of the Aneurysm 2, using RPIM: (a) global geometrical model (colour bar up to 0.4166 mm/ms); (b) plane z = 80 mm; (c) plane z = 50 mm; (d) plane z = 20 mm.

The results from the RPIM were also very similar to the results of the Aneurysm 1. The maximum velocity was 0.4166 mm/ms, meaning that it increased almost 2.8 times compared to the inlet velocity. The blood flow patterns are well defined in the figures (b) and (d), showing an almost null velocity near the vessel wall and a gradually crescent velocity as it approaches the centreline.

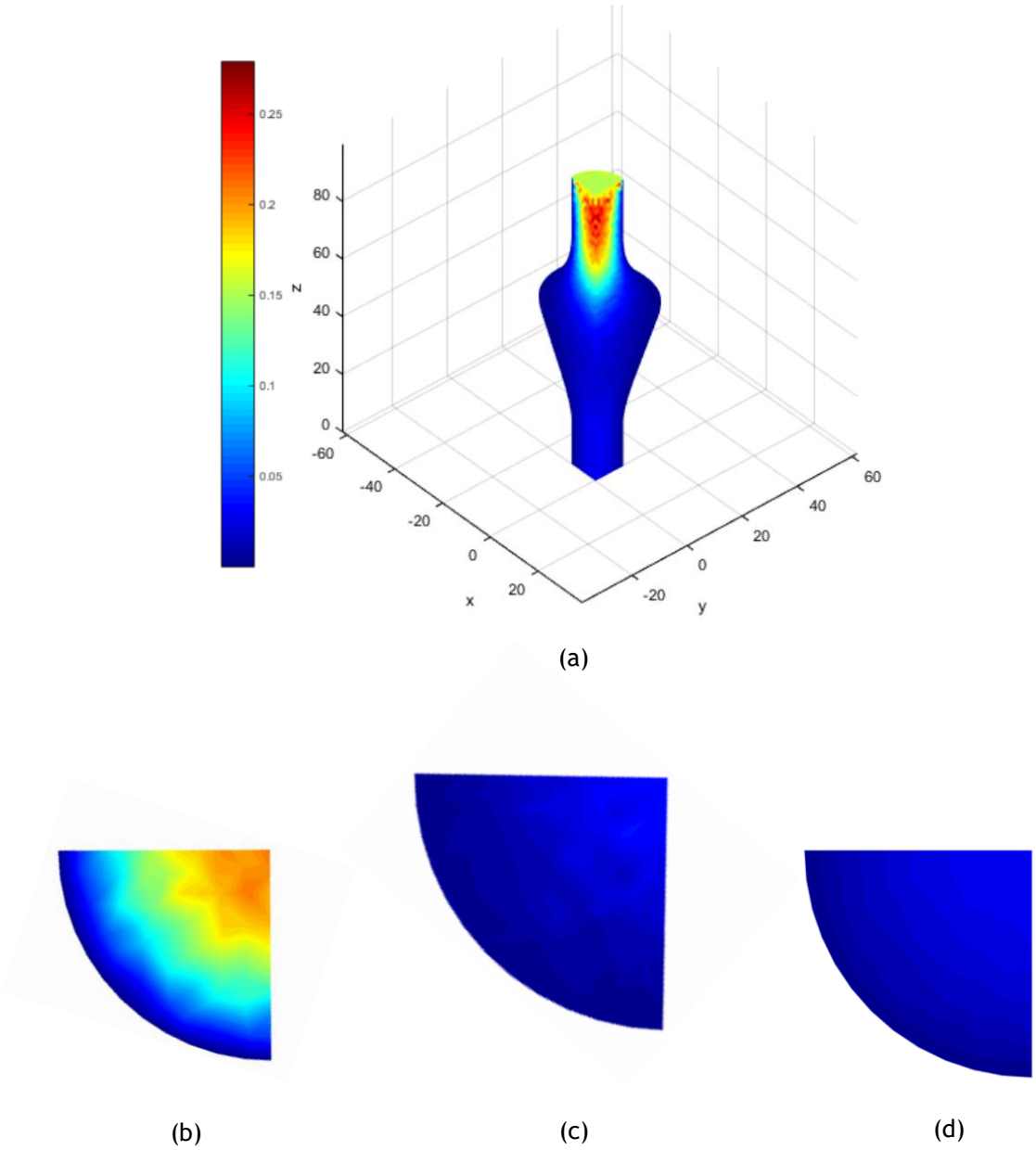

Figure 8. 42 - Colour dispersion map of the Aneurysm 2, using NNRPIM: (a) global geometrical model (colour bar up to 0.2787 mm/ms); (b) plane z = 80 mm; (c) plane z = 50 mm; (d) plane z = 20 mm.

As it was observed in the results from the NNRPIM in the Aneurysm 1, the blood did not flow uniformly along the geometrical model. There are irregularities in the velocity patterns, namely in the figures (b) and (c).

8.3.2.3. Aneurysm 3

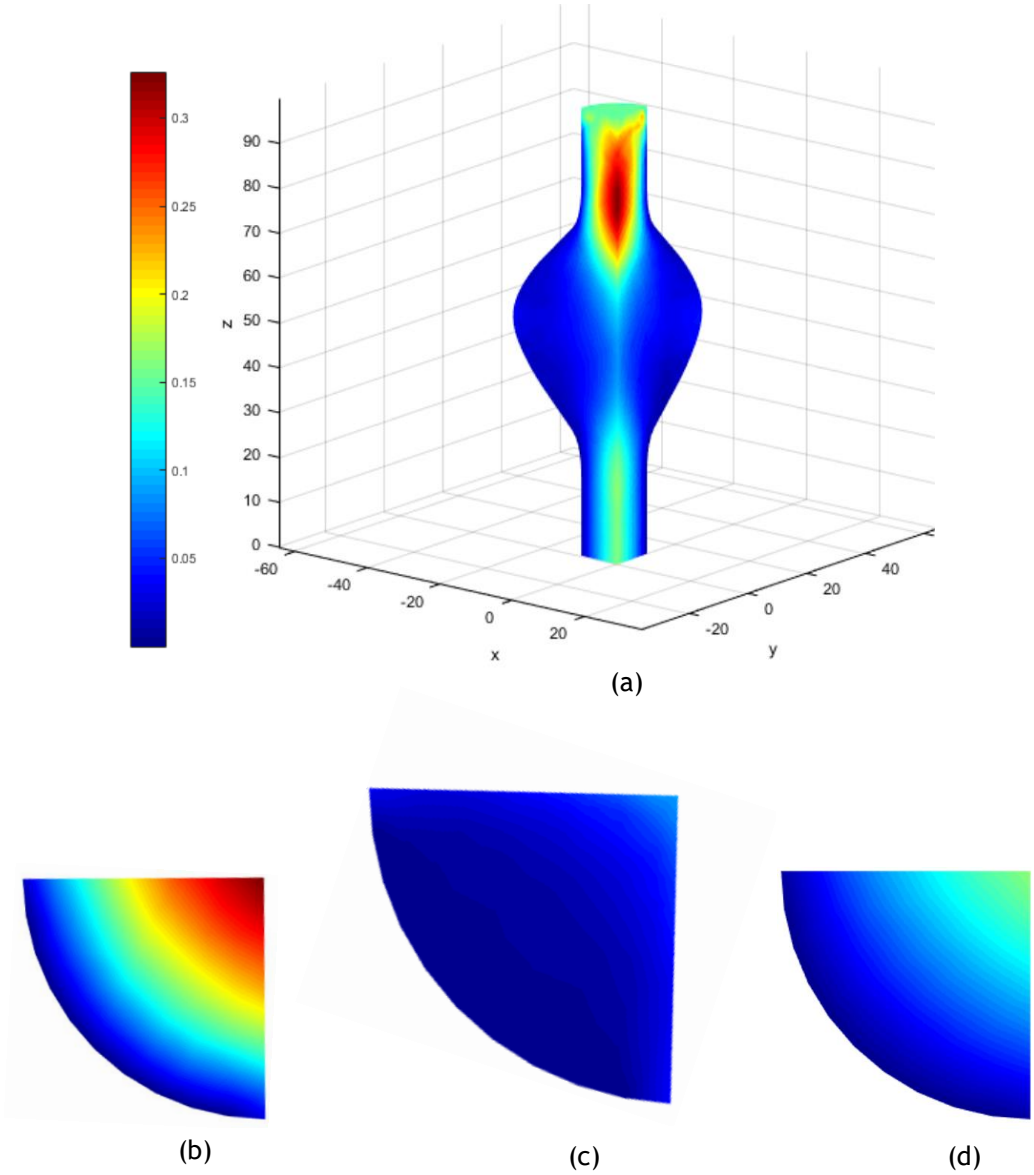

Figure 8. 43 - Colour dispersion map of the Aneurysm 3, using FEM: (a) global geometrical model (colour bar up to 0.3255 mm/ms); (b) plane z = 80 mm; (c) plane z = 50 mm; (d) plane z = 20 mm.

In the Figure 8. 43 it is verified that the colour dispersion map is different from the previous results, for the FEM. In this case, the blood started to describe a parabolic profile, registering a maximum velocity of 0.3255 mm/ms before reaching the dilated area. When the geometrical model returned to the normal diameter, the velocity continued lower than in the beginning, which means that after the dispersion of the blood flow, the velocity did not reach the same behaviour as in the superior portion.

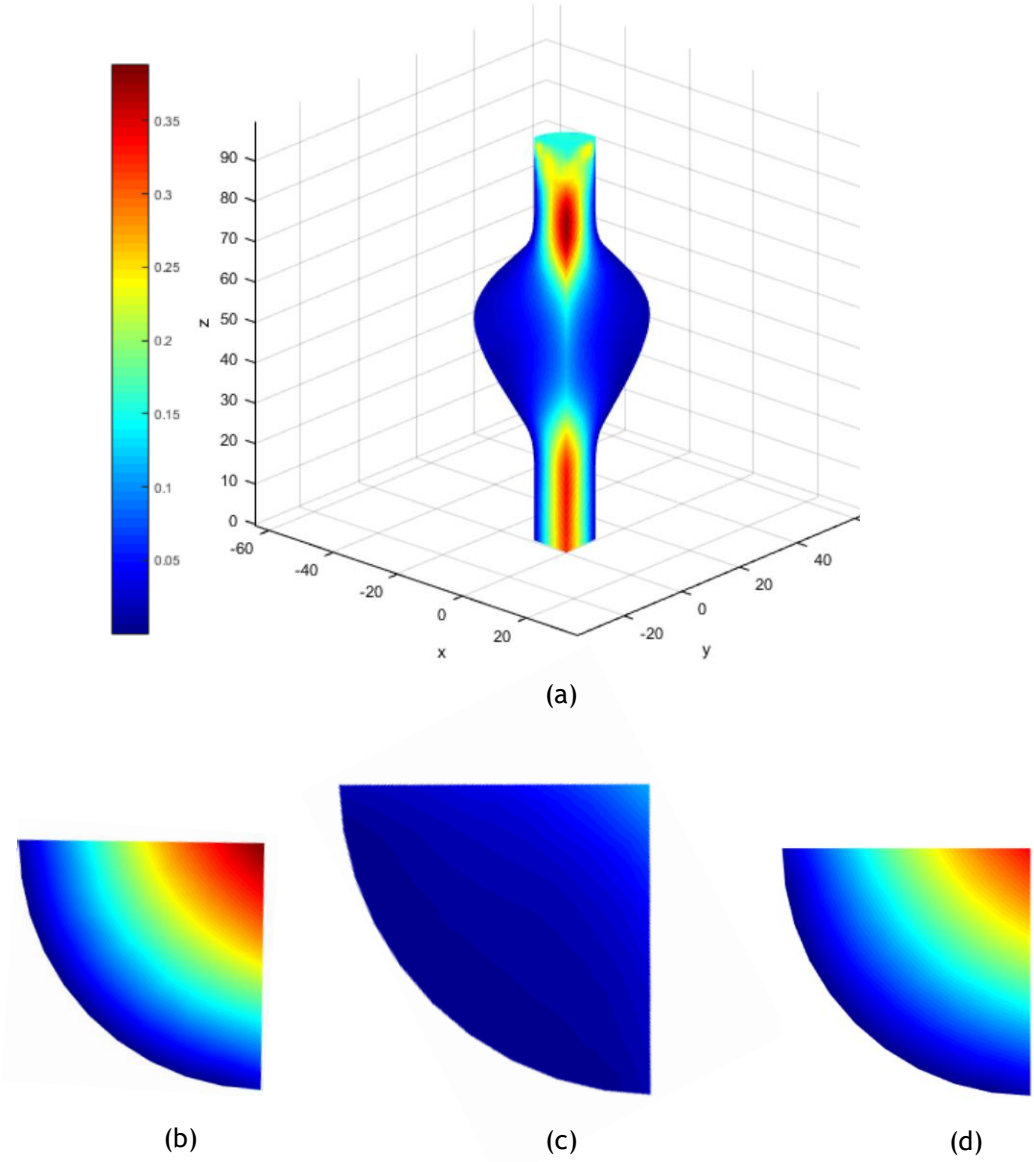

Figure 8. 44 - Colour dispersion map of the Aneurysm 3, using RPIM: (a) global geometrical model (colour bar up to 0.3877 mm/ms); (b) plane z = 80 mm; (c) plane z = 50 mm; (d) plane z = 20 mm.

The results of Figure 8. 44 are better than the results with FEM because the blood flow in the begging and end of the blood vessel present a similar behaviour. The maximum velocity was obtained before the dilated portion, with a value of 0.3877 mm/ms.

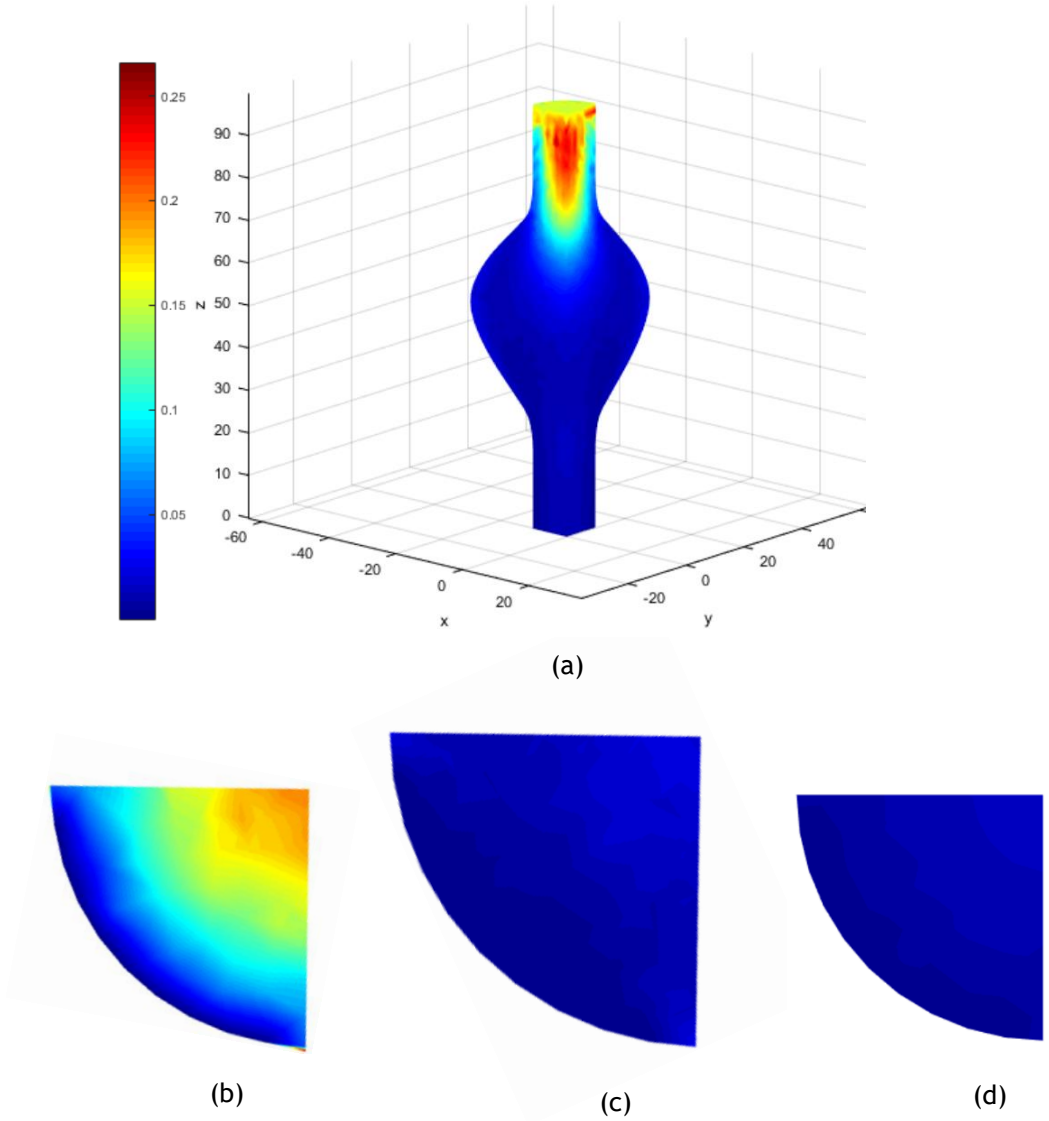

Figure 8. 45 - Colour dispersion map of the Aneurysm 3, using NNRPIM: (a) global geometrical model (colour bar up to 0.2654 mm/ms); (b) plane z = 80 mm; (c) plane z = 50 mm; (d) plane z = 20 mm.

In Figure 8. 45 it is observed that the blood flow patterns are similar to the previous NNRPIM results, with the maximum velocity being registered right near the inlet.

In order to conclude about the differences between the numerical methods, three points of the vertex of each plane were selected: point A (z = 80 mm), point B (z = 50 mm) and point C (z = 20 mm), previously represented in Figure 8. 36. Then, the graphs from Figure 8. 46 were obtained, enabling a more direct comparison of the numerical methods.

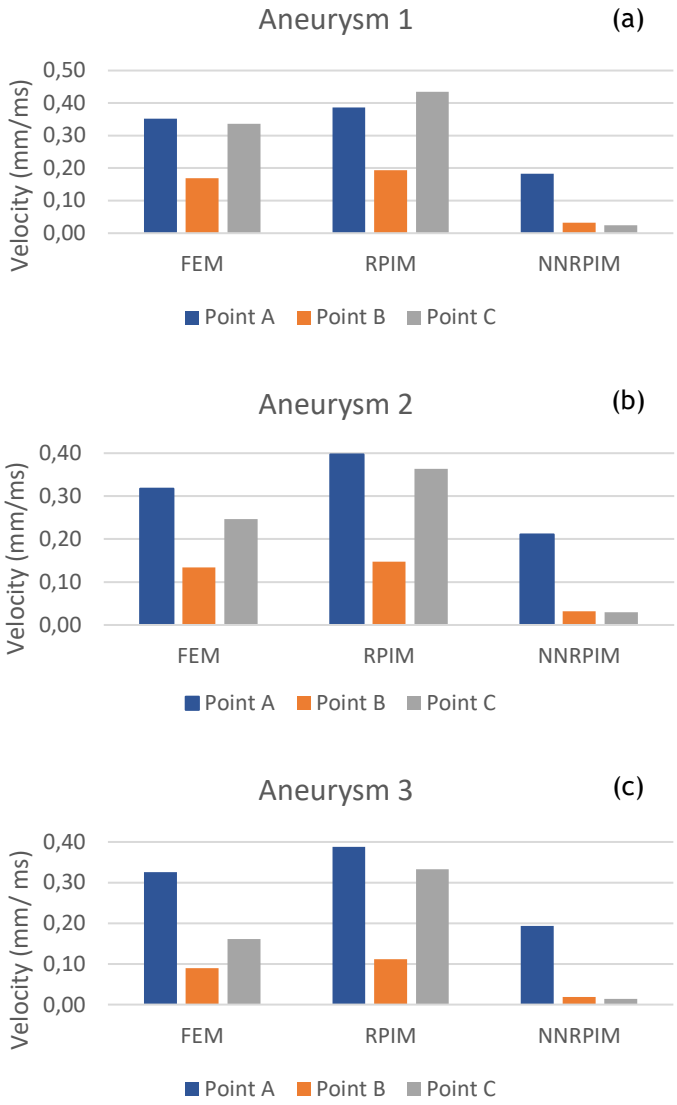

Figure 8. 46 - Velocities registered in points A, B and C, using FEM, RPIM and NNRPIM, in the: (a) Aneurysm 1; (b) Aneurysm 2 and (c) Aneurism 3.

The graphs of Figure 8. 46 demonstrate the differences, for each numerical method, of the velocities in the selected points. In all the graphs it is possible to verify that the NNRPIM is the method that provided the most distinct results, especially in points B and C, where the velocities were almost null.

Comparing the results of the finite element method for the three aneurysms, it is noticed that the last aneurysm is the more distinct. For the RPIM and NNRPIM, the results obtained for the three aneurysms were similar.

Observing the isomaps and graphs, it is concluded that the value of the velocities does not change significantly when the maximum diameter increases (for the same numerical method). What changes is the blood flow patterns for each one, especially in the dilated zone.

Also, it is important no notice that, near the arterial wall the velocity is almost null. In addition, the dilated zone has not only low velocity near the wall but also in the total area comprised by the aneurysm, which correlates to the fact that, in the aneurysmal walls, is very common the formation of intraluminal thrombus. This process was explained in detail in the Chapter 4 and is in accordance with the obtained results.

Chapter 9

Abdominal Aortic Aneurysms - Clinical Cases

In the previous chapter, the parameters of simulation of blood flow in geometries with irregular and regular meshes were studied, and withdrawn conclusions about the flow patterns inside the blood vessels. After the experimental study, the main objective is to simulate the blood flow in real aneurysmal geometries, according to the knowledge acquired by the interpretation of the preliminary results.

Thus, this chapter aims to present two clinical cases of abdominal aortic aneurysms – one saccular and other fusiform – and obtain the results of the blood flow velocities. Then, the results will be compared between the numerical methods and with the clinical values, for concluding about the efficiency of the numerical methods that were implemented.

To fulfil the objectives mentioned above, this chapter begins with a brief demonstration of the construction of the two and three-dimensional geometrical models from DICOM images. Formerly, the imposition of the boundary conditions and applied velocities are presented, as well as the obtained outcomes for the 2D and 3D simulations.

9.1. Saccular Abdominal Aortic Aneurysm

In this subchapter, it is presented the study of a saccular abdominal aortic aneurysm. For this phase of the dissertation, it was very important the collaboration between our research group and the vascular surgery department of Hospital of São João of Porto, which provided the geometry, dimensions and blood flow velocities in several regions of the diseased aorta. Additionally, the research team of Hospital of São João of Porto have contributed with relevant insights related with the expected results and clinical observations, valuable comments that allowed to improve significantly the simulations.

The present case study refers to an infrarenal abdominal aortic aneurysm, with a skull-caudal extension of 97 mm and a maximum antero-posterior diameter of 62 mm. To obtain the medical image, the patient, female and aged 90 years old, was submitted to a Computed Tomography Angiography (CTA), after the administration of an intravenous contrast. The image obtained from this exam is presented in the Figure 9. 1 (a) and was acquired from 3D Slicer®, after calibrating the DICOM image provided by the hospital.

After loading the image, it was necessary to identify the anatomical structure required for this study (in this case, the abdominal aortic aneurysm) and initiate the process of segmentation for obtaining the geometrical model. Thus, a region of interest, which is represented in the white square of Figure 9. 1 (a), was delimited and the abdominal aortic aneurysm became more evident, as it can be seen in Figure 9. 1 (b). After identifying the aneurysm, it was segmented and obtained the mask represented in red in the Figure 9. 1 (c).

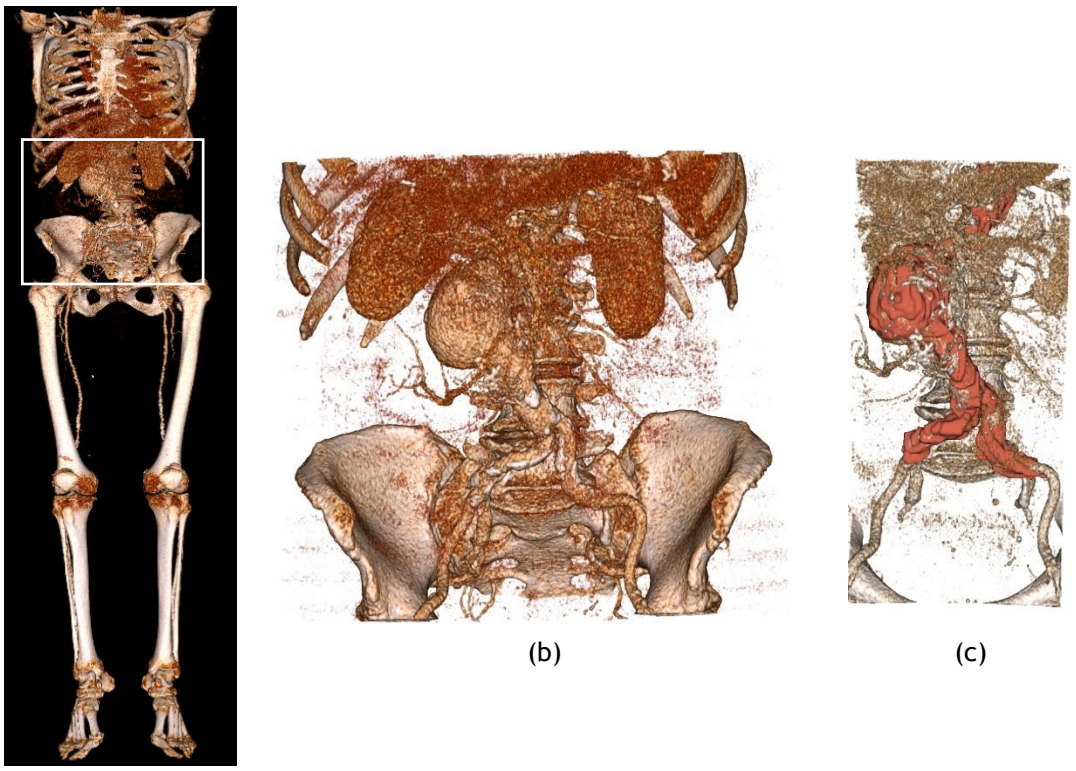

(a) (b) (c)

Figure 9. 1 – Process of segmentation of the abdominal aortic aneurysm in a DICOM image: (a) Global CT scan, with definition of the ROI; (b) augmented view of the ROI; (c) mask obtained from the segmentation of the anatomical region of interest.

Succeeding the segmentation process, the model was exported to a .stl file and opened in MeshMixer®, where it was smoothened and meshed in the superficial surface. Then, the geometrical model was exported to FEMAP®, allowing to refine and remesh the 3D domain with tetrahedral elements. After this process, the model is ready to be exported to an .inp file and loaded in FEMAS® to perform the static fluid flow analysis.

In the Figure 9. 2 (a) and (b), respectively, it is observed the three and two-dimensional models of the saccular aneurysms. The three-dimensional model is constituted by a tetrahedral mesh with 3015 nodes and 14443 elements (linear polynomial elements) and the two-dimensional model is discretized with 4530 triangular elements and 2417 nodes (linear polynomial elements).

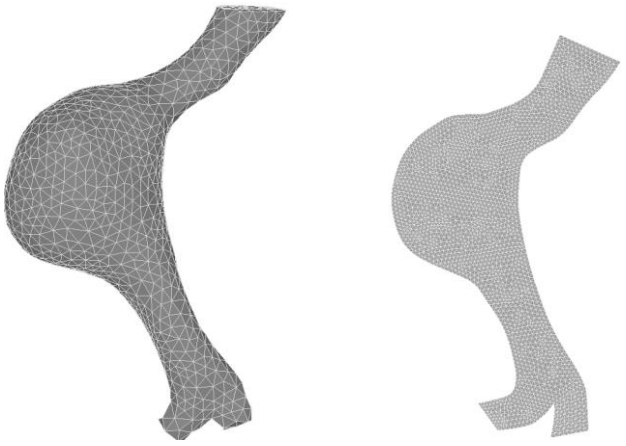

(a) (b)

Figure 9. 2 – Anterior view of the geometrical models: (a) 3D and (b) 2D.

As it was previously mentioned, this study was subdivided into a two and three-dimensional analysis. After the achievement of conclusions in both approaches, the results will be compared between the different numerical methods that were implemented. In addition, they will also be compared to the ones provided by the hospital, which are described in Table 9. 1, and were obtained from an Abdominal Ultrasound with Doppler Exam.

Table 9. 1 – Blood Flow Velocities in several segments of the infrarenal aortic aneurysm obtained in clinical environment.

	Diastolic Velocity (cm/s)	***Tele diastolic Velocity (cm/s)***
Healthy segment before the aneurysm	35.4	6.4
Healthy segment after the aneurysm	15.7	4.29
Right Iliac Artery	44.7	5.0
Left Iliac Artery	50.1	4.0

In the previous table, the velocities are subdivided in two: the diastolic and tele diastolic velocities. These numbers were provided in real-time by ultrasound with doppler exam and correspond to the velocities in two distinct phases of the cardiac cycle. The diastolic velocity concerns the velocity of the flow in the blood vessels in the stage where the blood enters the heart; the tele diastolic velocity is related to the velocity in the blood vessels in the end of the diastole (or pre-systole), in which the heart is close to pump out the blood.

For the simulation of the blood flow in the 2D and 3D models, both diastolic and tele diastolic velocities were considered, enabling the study of two different phases of the cardiac cycle.

9.1.1. 2D Analysis

The 2D geometrical model previously observed in Figure 9. 2 (b) was imported to FEMAS® to be analysed with FEM, RPIM and NNRPIM. Before the static fluid flow analysis, the boundary conditions were imposed, as it is depicted in Figure 9. 3. The nodes marked in yellow are constrained in Ox and Oy directions. The iliac arteries extremities were left with no constraints to allow the blood flow to come out. The nodes marked in grey represent the imposition of the blood's velocity according to the data of the "Healthy segment before the aneurysm" presented in the Table 9. 1.

The parameters of simulation for this study are described in Table 9. 2.

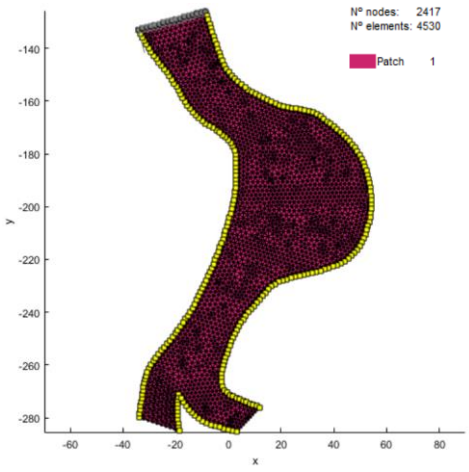

Figure 9. 3 – Imposed Boundary Conditions.

Table 9. 2 – RPIM and NNRPIM parameters.

RPIM	NNRPIM
Nodes in the influence-domain: **27**	c = **0.0001**
c = **1.42**	p = **0.9999**
p = **1.03**	Influence-cell: **Second Order**
Polynomial Basis: **Constant**	Polynomial Basis: **Constant**
Integration Points: **3 per triangle**	Integration Points: **1 per sub-cell**

In Figure 9. 4 it is observed the results of the fluid flow analysis for FEM, RPIM and NNRPIM, with the imposition of the diastolic velocity in the inlet of the blood vessel.

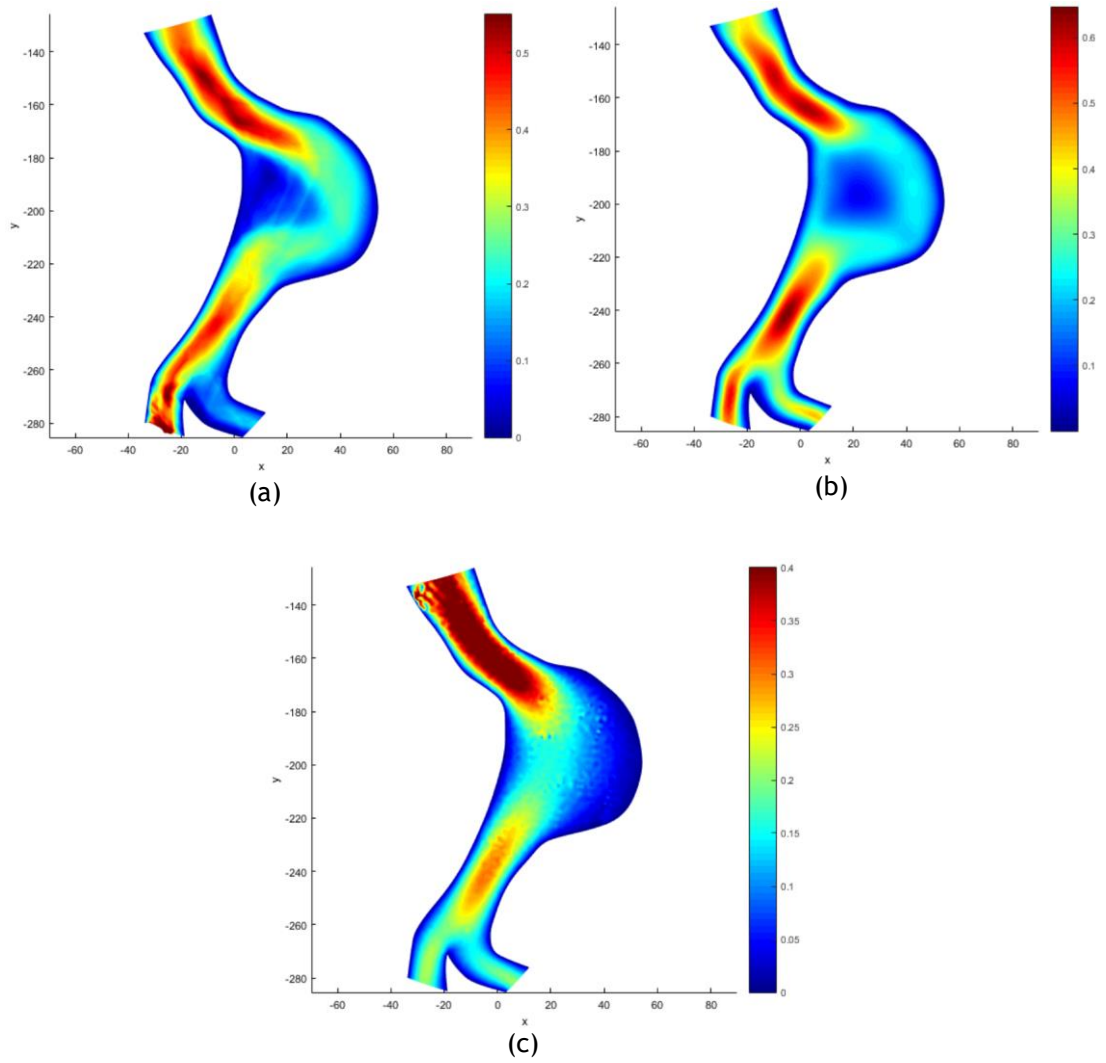

Figure 9. 4 - Colour dispersion map of the saccular aneurysm, using: (a) FEM (colour bar saturated at 0.55 mm/ms); (b) RPIM (colour bar up to 0.6460 mm/ms); (c) NNRPIM (colour bar saturated at 0.4 mm/ms)

In the Figure 9. 4 it is verified that the blood flow patterns were similar for FEM and RPIM, i.e., the blood flowed with an almost constant and laminar profile in the healthy segments, with the verification of a dispersion in the diseased portion, as it was expected. For FEM, in the dilated zone of the blood vessel, the velocity is more evident near the dilated wall, leaving the portion with no dilation with a significant small velocity. On the other hand, in the RPIM results it is verified a similar velocity near the walls of the entire aneurysm, with a significant decrease of the velocity in the centreline. The NNRPIM provided the most different results, with the dilated wall of the aneurysm being left with almost no velocity (contrary to the other methods).

After the observation of the isomaps, it was collected the blood's velocities in the sections schematized in Figure 9. 5. Also, for comparing the results with the ones provided by the hospital (see Table 9. 1) it was defined four points – A, B, C and D, in which the value of the velocity was obtained.

The graphs with the velocities of the three sections were constructed and are represented in Figure 9. 6.

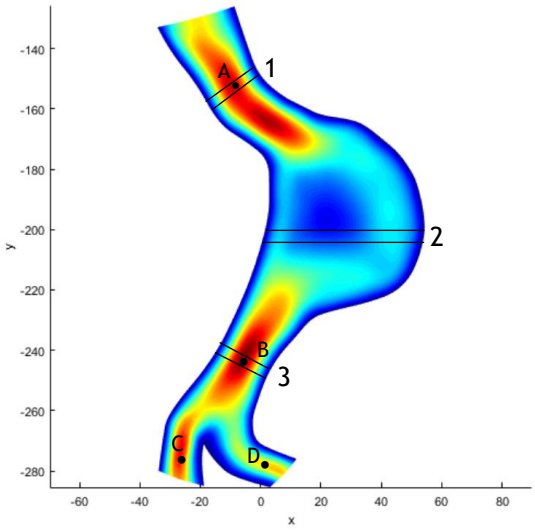

Figure 9. 5 – Delimitation of sections and points for obtaining the blood flow velocity.

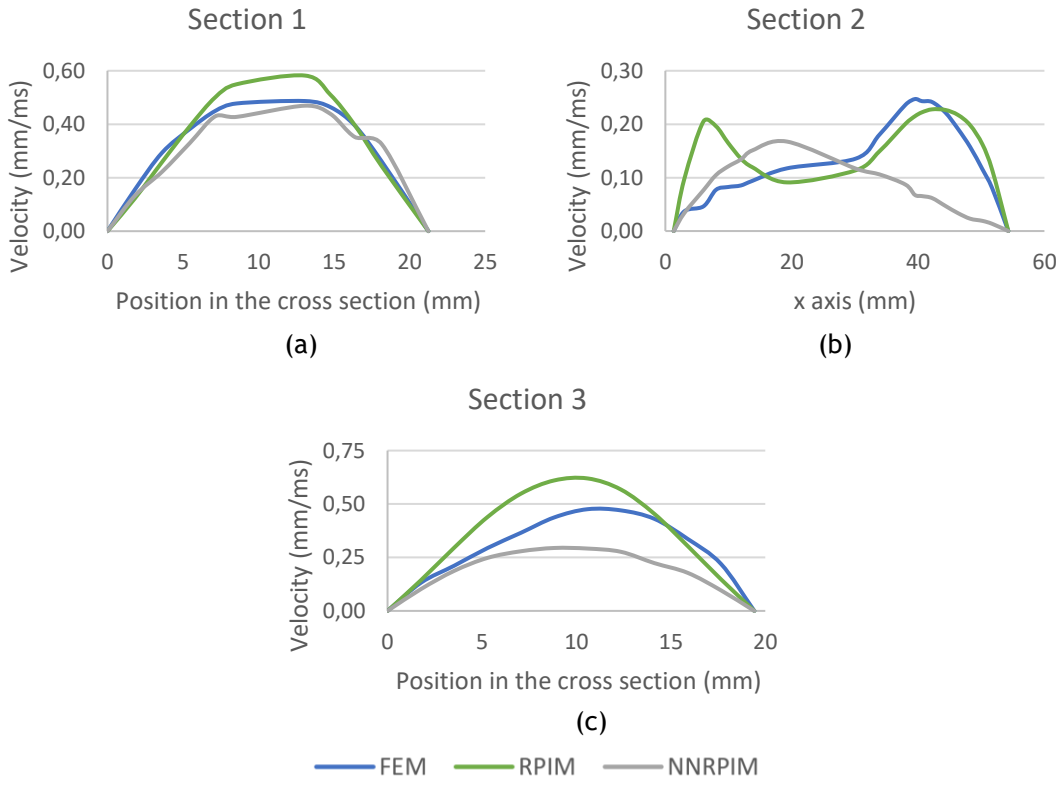

Figure 9. 6 – Comparison between the velocity profiles obtained by FEM, RPIM and NNRPIM in: (a) section 1; (b) section 2; (c) section 3.

The results of the graphs indicate that the velocity profiles in sections 1 and 3 were similar for the three methods. The major differences are observed in the aneurysm, where the three methods provided rather different velocity patterns.

From section 1 to section 3, it is verified a slight increase in the velocity for RPIM, a decrease for NNRPIM and the velocity from FEM maintained similar in the beginning and end of the blood vessel.

Table 9. 3 – Velocities, in mm/ms, obtained from points A, B, C and D in the diastolic phase.

	FEM	*RPIM*	*NNRPIM*
Point A	0.478	0.55	0.43
Point B	0.44	0.61	0.29
Point C	0.43	0.52	0.20
Point D	0.18	0.42	0.19

In order to verify the similarity of the clinical and experimental results, the values of the velocities from Table 9. 1 were compared to the velocities presented in Table 9. 3. The following conclusions were withdrawn:

- The velocity in the "Healthy segment before the aneurysm" is 0.354 mm/ms and the results of the simulations varied between 0.43 and 0.55 mm/ms. The difference between the clinical and the experimental results did not differ significantly, and the discrepancies are justified by the fact that it was imposed 0.354 mm/ms as inlet velocity in the model, so it is normal (as it was observed in all the previous results) an increase of the velocity along the vessel as it forms and stabilizes in a parabolic profile;
- The velocity in the "Healthy segment after the aneurysm" was 0.157 mm/ms, which present a high discrepancy from the results obtained in the simulations. However, it is seen that the closer result is 0.29 mm/ms, obtained from NNRPIM;
- Lastly, the right and left iliac arteries velocities, which have a velocity of 0.447 mm/ms and 0.501 mm/ms, respectively, present a high resemblance to the results obtained from RPIM.

Since not all the methods provided close results to the clinics, another approach was completed: the imposition of the outlet velocities in the right and left iliac arteries. The results obtained in this step are presented in the Figure 9. 7 and Figure 9. 8.

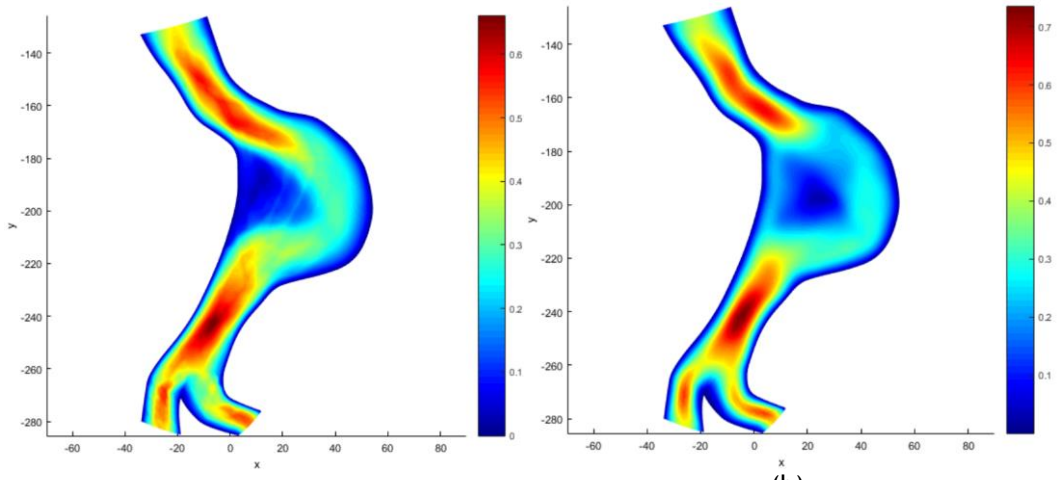

(a) (b)

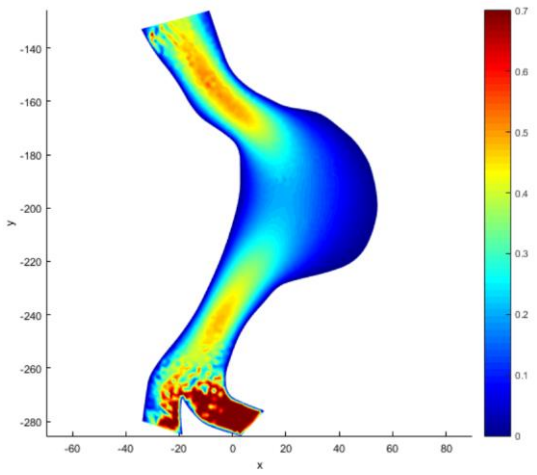

(c)

Figure 9. 7 - Colour dispersion map of the saccular aneurysm, with the imposition of the outlet velocities, using: (a) FEM (colour bar up to 0.6597 mm/ms); (b) RPIM (colour bar up to 0.7344 mm/ms) (c) NNRPIM (colour bar saturated at 0.7 mm/ms).

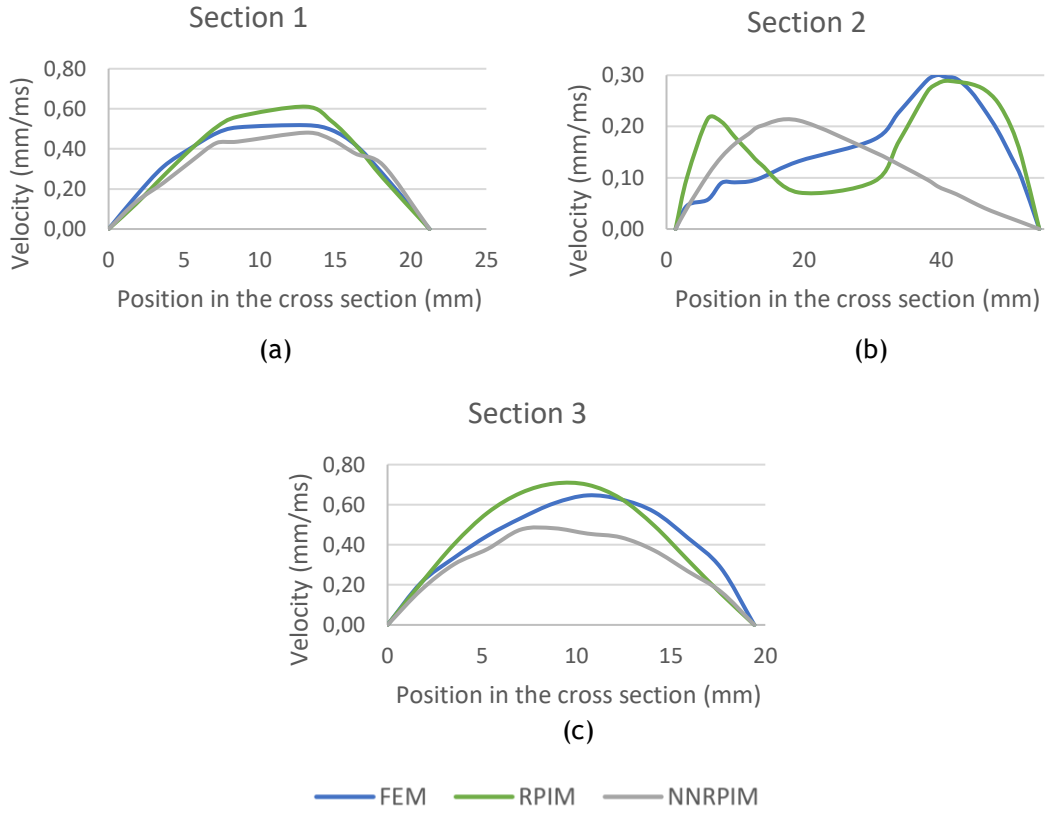

Figure 9. 8 - Comparison between the velocity profiles obtained by FEM, RPIM and NNRPIM in: (a) section 1; (b) section 2; (c) section 3. In this case, the outlet velocities were imposed.

After imposing the outlet velocities, it is seen that the results did not alter substantially. The main discrepancies are observed in the velocity profiles of the iliac arteries in FEM: in the Figure 9. 4 (a) the velocity in the left iliac artery was considerably higher than in the right iliac artery, due to a restraint in the mesh, that caused a specific group of nodes to enable higher results than it was expected. When the outlet velocity was imposed, this problem was not verified. Also, the results of NNRPIM did not followed the expected, since there is a high

concentration of blood flow in the iliac arteries, probably caused by some mesh inconsistency or failures in the numerical integration of the numerical method itself (it would be required more integration points in each subcell).

Comparing the graphs from Figure 9. 6 and Figure 9. 8, the main difference is observed in the results from section 3. The velocity in the section 3 after the imposition of the outlet velocities were approximately 0,1 mm/ms higher than the results were no outlet velocities were imposed.

After the analysis of the blood flow in the diastolic phase of the cardiac cycle, the study continued with the analysis of the tele diastolic stage. As before, the inlet velocity considered is in the "Healthy segment before the aneurysm" from Table 9. 1. The results are depicted in Figure 9. 9 and in the graphs of Figure 9. 10.

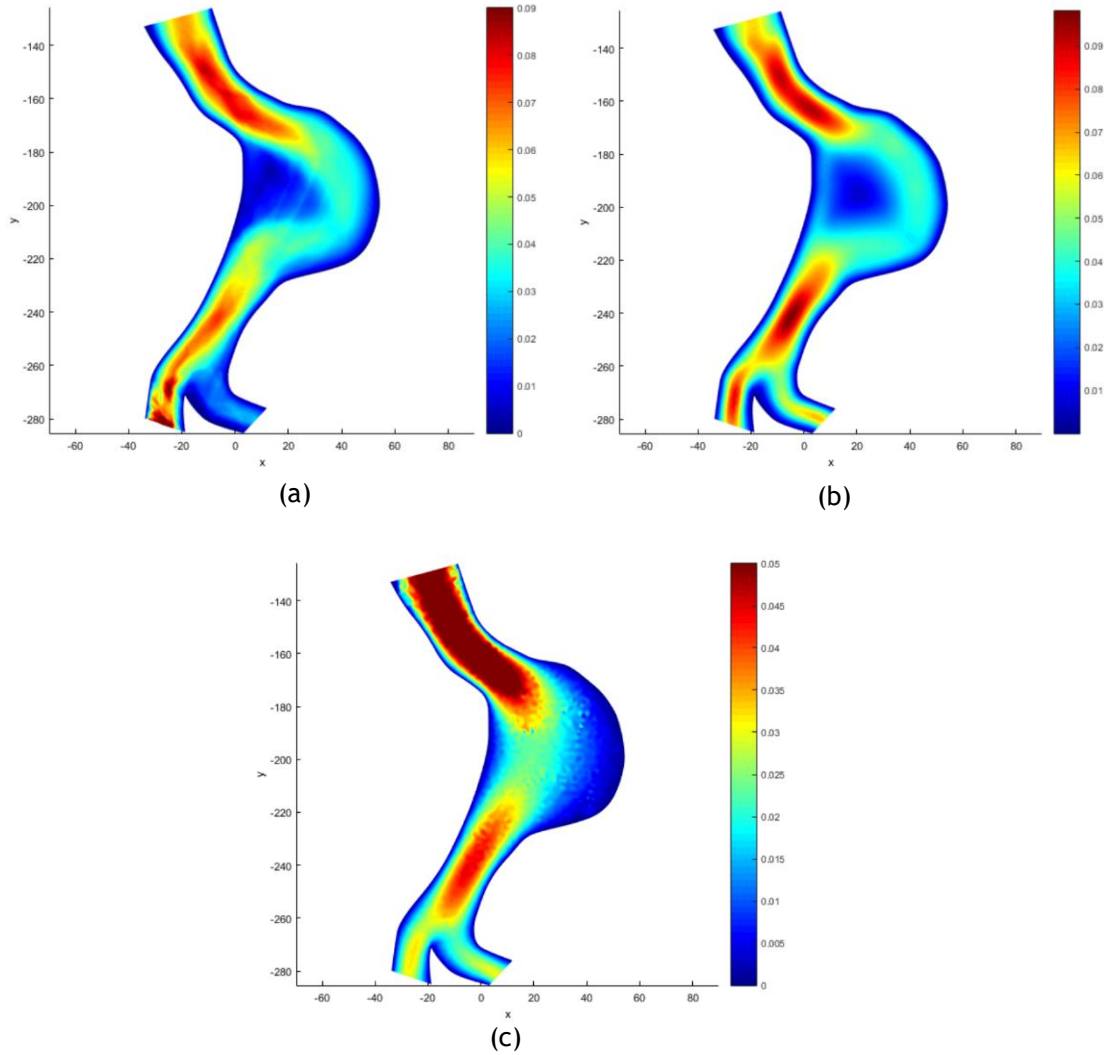

Figure 9. 9 - Colour dispersion map of the saccular aneurysm in the tele diastolic phase, using: (a) FEM (colour bar up saturated at 0.09 mm/ms); (b) RPIM (colour bar saturated at 0.0981 mm/ms); (c) NNRPIM (colour bar saturated at 0.05 mm/ms).

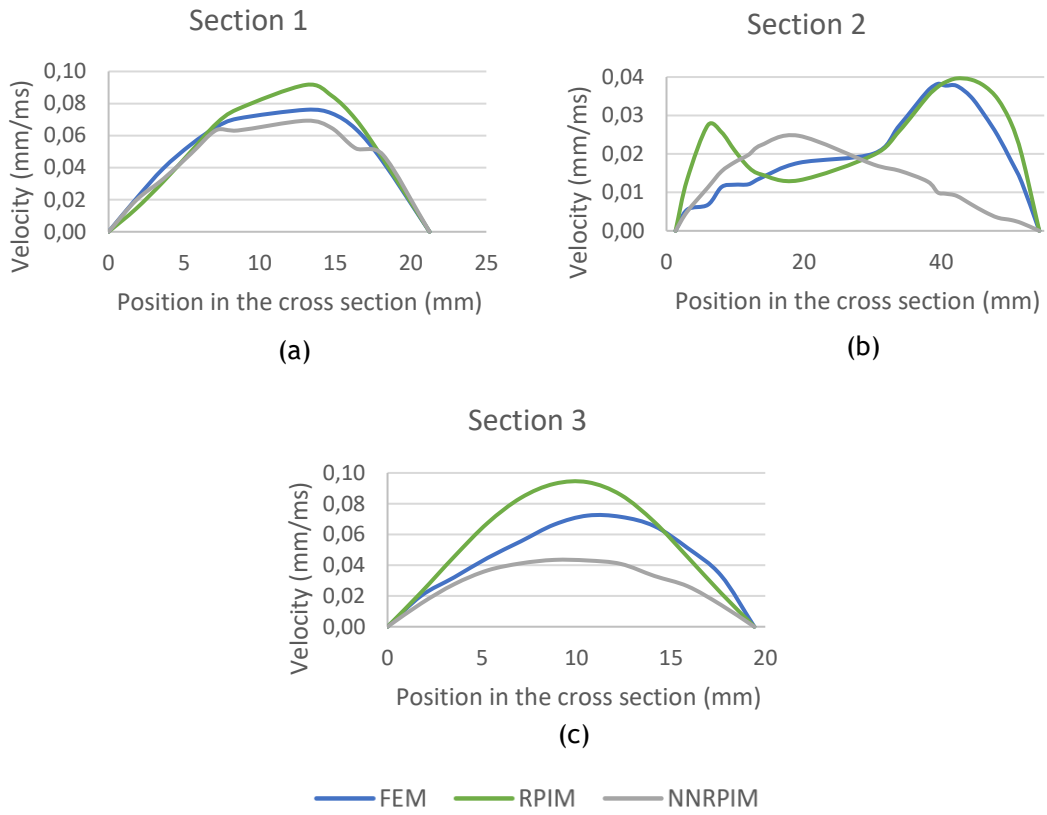

Figure 9. 10 - Comparison between the velocity profiles obtained by FEM, RPIM and NNRPIM in: (a) section 1; (b) section 2; (c) section 3.

From Figure 9. 9 and graphs of Figure 9. 10 it is concluded that, although the phase of the cardiac cycle is different, the velocity profiles and the patterns that appear in the blood vessel are similar, i.e., the tele diastolic and the diastolic results are analogous, differing only in the values of the velocity. To compare the results with the velocities provided by the Hospital of São João, four points were selected as schematized in Figure 9. 5. In the Table 9. 4 it is described the velocities in those points, obtained with FEM, RPIM and NNRPIM.

Table 9. 4 - Velocities, in mm/ms, obtained from points A, B, C and D in the tele diastolic phase.

	FEM	***RPIM***	***NNRPIM***
Point A	0.07	0.08	0.06
Point B	0.07	0.09	0.04
Point C	0.06	0.08	0.03
Point D	0.03	0.06	0.03

In the healthy segment before the aneurysm the value of the velocity is 0.064 m/ms, which present a high resemblance to the velocities obtained in Point A. In the healthy segment after the aneurysm, the velocity did not change significantly in the experimental results compared to the velocity in Point A. The velocity for this zone is 0.0429 mm/ms, which is close to the NNRPIM result. Lastly, the velocities in the right and left iliac arteries are 0.05 mm/ms and 0.04 mm/ms, respectively. By observing the values of Point C (left iliac artery) and Point D (right iliac artery) it can be concluded that the FEM results are the most approximated, however, the results from the other numerical methods were also identical.

As it was proceeded in the analysis of the diastole, for this case the outlet velocities were also imposed, and the results can be observed in Figure 9. 11 and Figure 9. 12.

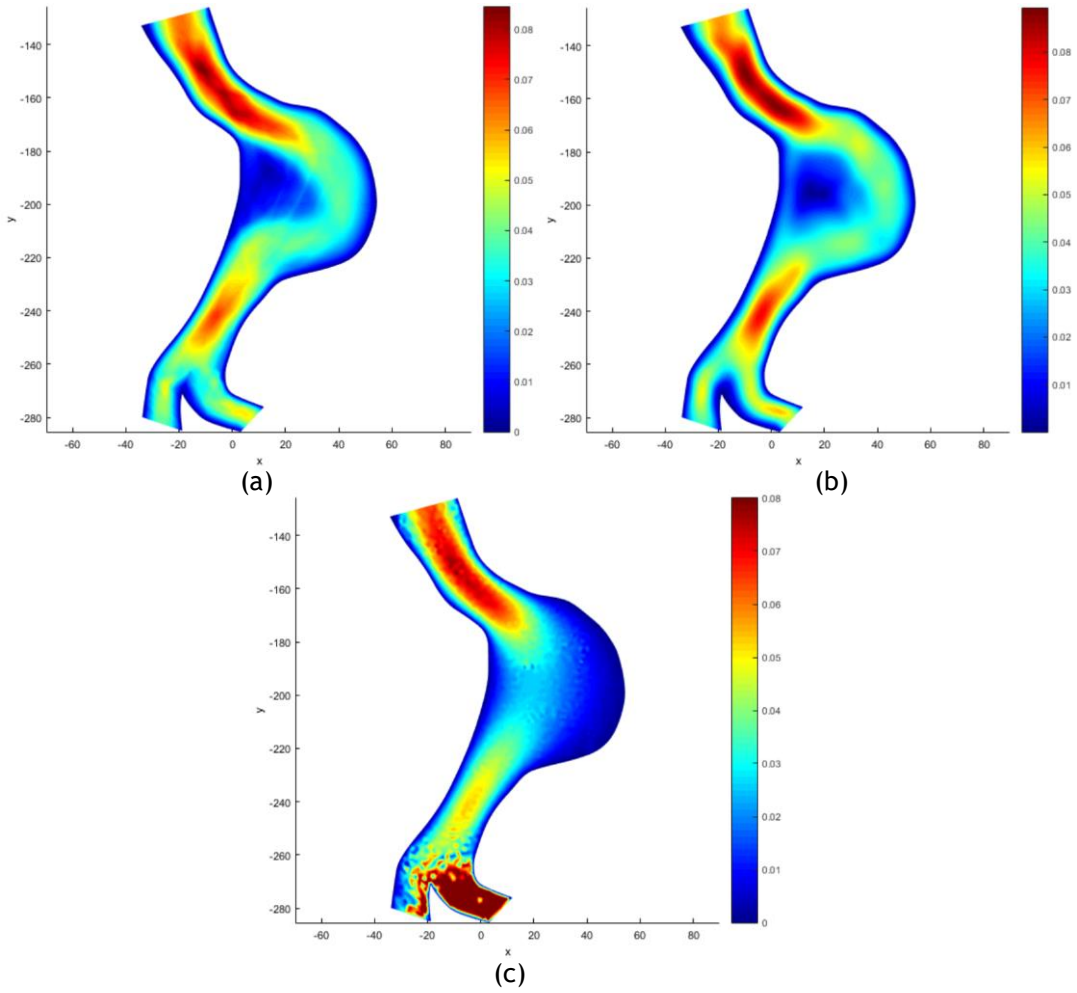

Figure 9. 11 - Colour dispersion map of the saccular aneurysm in the tele diastolic phase, with the imposition of the outlet velocities, using: (a) FEM (colour bar up to 0.0844 mm/ms); (b) RPIM (colour bar up to 0.0892 mm/ms); (c) NNRPIM (colour bar saturated at 0.08 mm/ms).

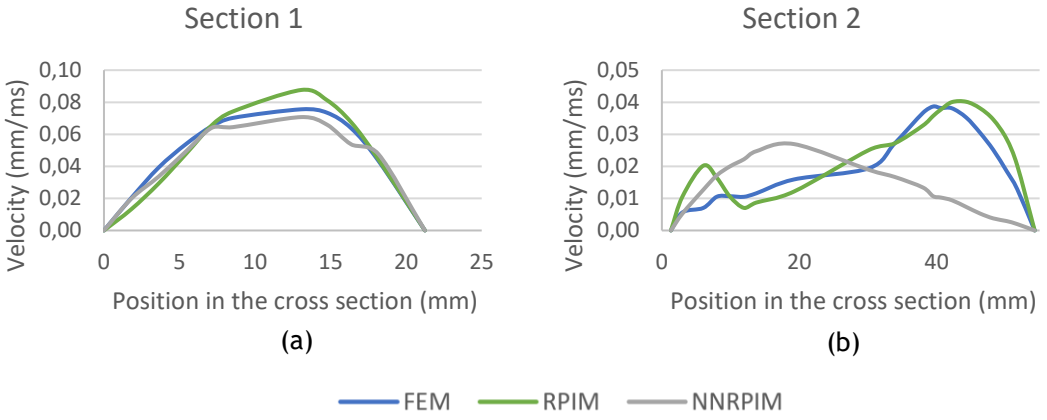

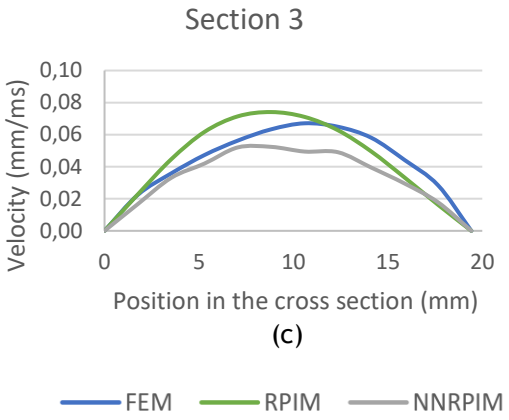

Figure 9. 12 - Comparison between the velocity profiles obtained by FEM, RPIM and NNRPIM in: (a) section 1; (b) section 2; (c) section 3. In this case, the outlet velocities were imposed.

The results demonstrate that the velocity profiles in the iliac arteries are smoothened and in the rest of the blood vessel maintained similar to the results with no outlet velocities, with exception for the NNRPIM's results.

After this study we arrive at the following conclusions:

- The blood flow patterns in two distinct phases of the cardiac cycle were similar, differing only in the velocity, that was greater for the diastolic phase and smaller for the tele diastolic phase;
- There was no particular numerical method that provided the best results, for every point of the aneurysm, when compared to the clinical values. Regarding the approximation of values between the experimental results and the clinical values, it can be concluded that the numerical methods are, in global, efficient for studying the blood flow in 2D anatomical geometries, although it is still necessary some calibration of the flow formulation;
- The intervariability analysis of the results (i.e., between the different numerical methods) demonstrates that the method that provides most discrepant results is the NNRPIM, subsequently, the FEM and RPIM provide identical values, proving that meshless methods are an alternative efficient technique for blood flow analysis.

9.1.2. 3D Analysis

For the three-dimensional study of the blood flow in the saccular aneurysm, the essential boundary conditions represented in the Figure 9. 13 were applied. The nodes marked in grey are constrained in all directions, i.e., in Ox, Oy and Oz. The blood flow velocity was imposed regarding the values of the "Healthy segment before the aneurysm", described in the Table 9. 1. As in the preliminary studies, the blood was uniformly applied in the upper surface of the model, leading to a subsequent parabolic profile as it distances from the inlet. The blood properties that were considered are the same as in the preliminary study and the parameters of simulation can be seen in the Table 9. 5.

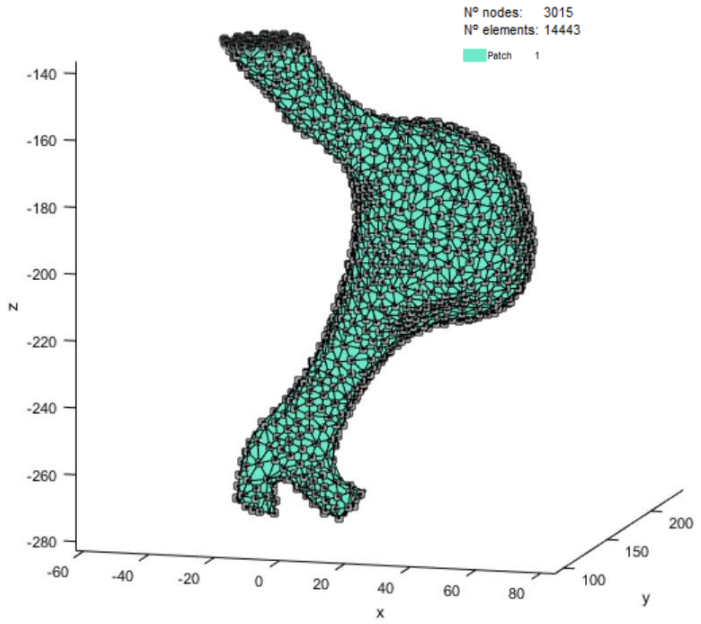

Figure 9. 13 – Essential Boundary Conditions imposed in the 3D geometrical model.

Table 9. 5 – RPIM and NNRPIM parameters for the 3D study.

RPIM	NNRPIM
Nodes in the influence-domain: **27**	c = **0.0001**
c = **1.42**	p = **0.9999**
p = **1.03**	Influence-cell: **Second Order**
Polynomial Basis: **Constant**	Polynomial Basis: **Constant**
Integration Points: **1 per triangle**	Integration Points: **1 per sub-cell**

The results of the fluid flow analysis are represented in several perspectives in the Figure 9. 14 and Figure 9. 15, which correspond to the results obtained from FEM and RPIM, respectively. Regarding the NNRPIM results, these were not obtained due to numerical difficulties related with the nodal mesh. There were some parts of the domain in which the natural neighbour concept (automatically applied by FEMAS® software, regardless the nodal mesh) only identified one neighbour node. Such single node natural neighbour, in a 3D analysis, does not allows to construct a 3D shape function, hindering the complete process of analysis.

The phase of the cardiac cycle that was considered, in this first analysis, is the diastole, thus the diastolic velocity was imposed in the inlet.

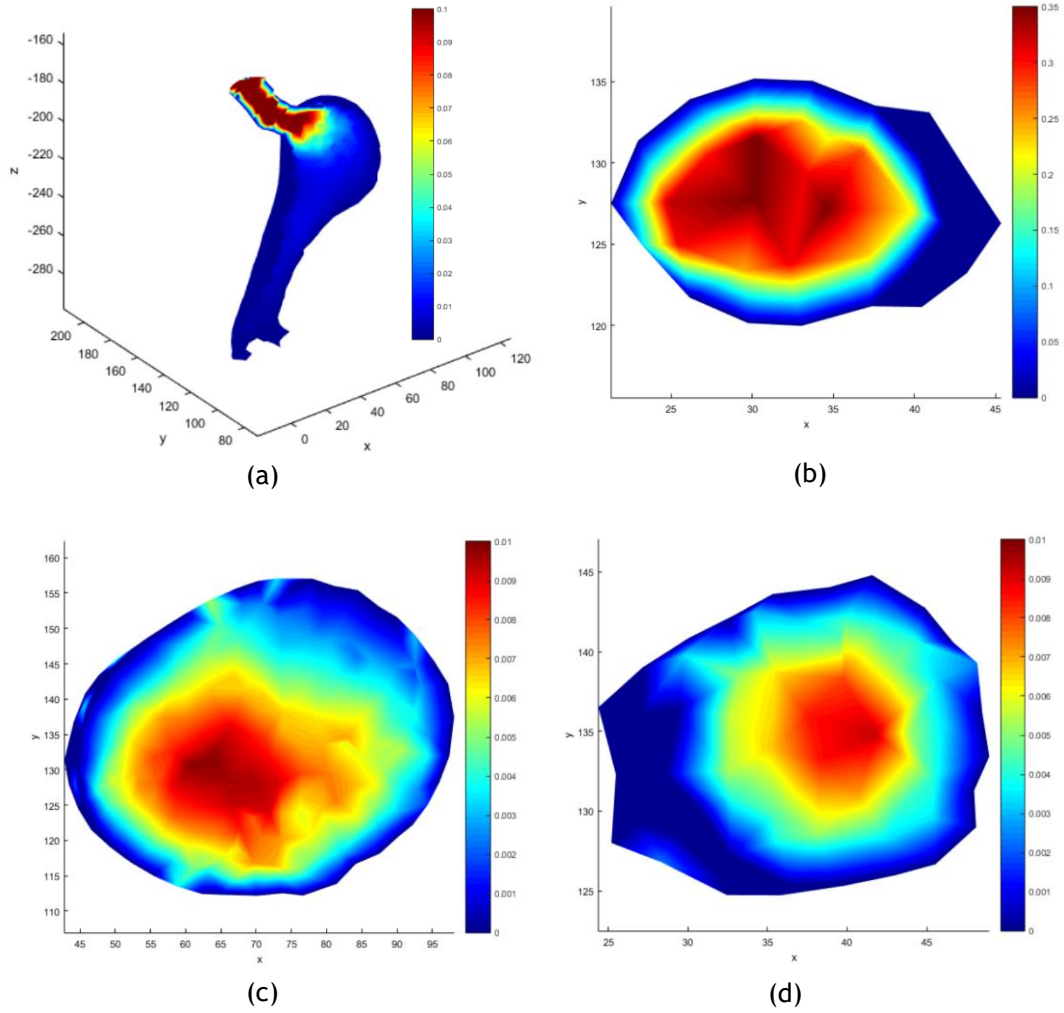

Figure 9. 14 - Colour dispersion map of the 3D saccular aneurysm, using FEM: (a) sagittal plane cut y = 127 mm (colour bar saturated at 0.1 mm/ms); (b) transverse plane cut between z = -170 mm and z = -175 mm (colour bar saturated at 0.35 mm/ms) ; (c) transverse plane cut between z = -220 mm and z = -230 mm (colour bar saturated at 0.01 mm/ms); (d) transverse plane cut between z = -260 mm and z = -270 mm (colour bar saturated at 0.01 mm/ms).

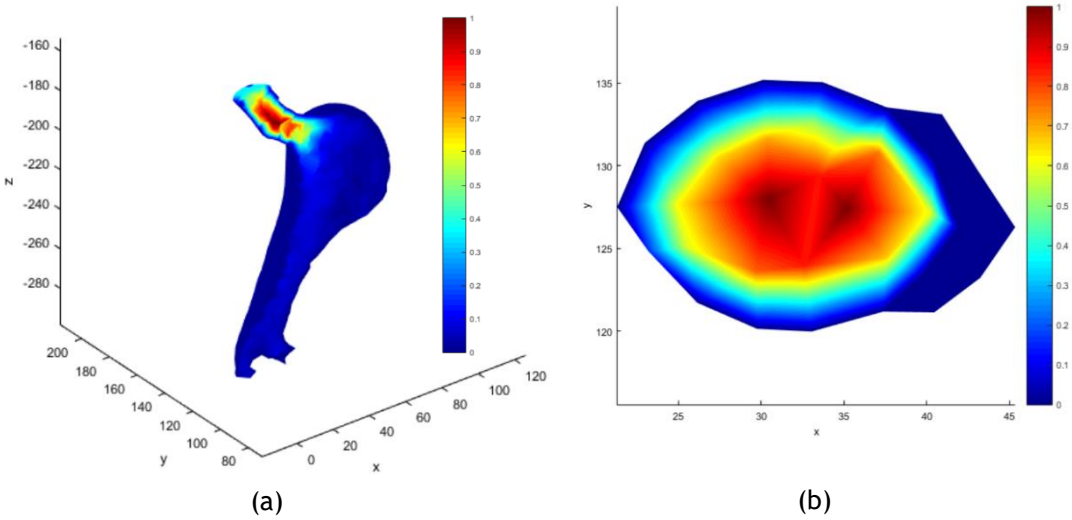

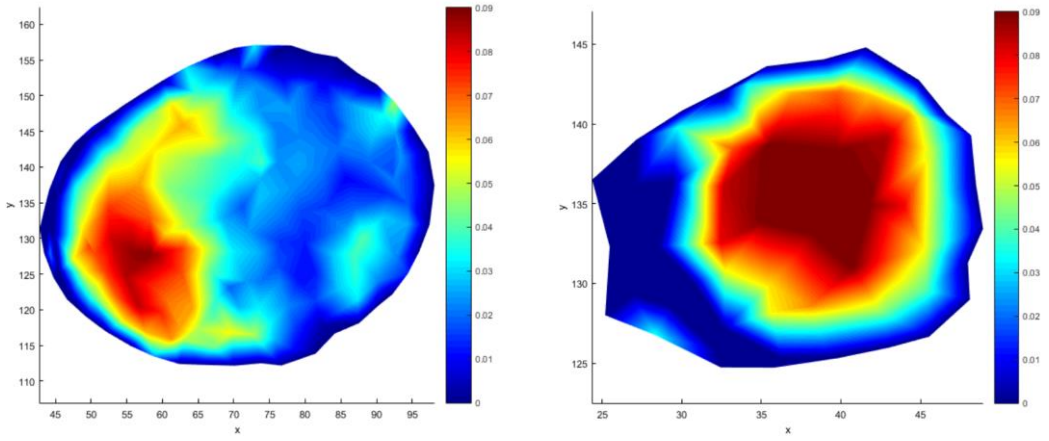

(c) (d)

Figure 9. 15 - Colour dispersion map of the 3D saccular aneurysm, using RPIM: (a) sagittal plane cut y = 127 mm (colour bar saturated at 1 mm/ms); (b) transverse plane cut between z = -170 mm and z = -175 mm (colour bar saturated at 1 mm/ms) ; (c) transverse plane cut between z = -220 mm and z = -230 mm (colour bar saturated at 0.09 mm/ms); (d) transverse plane cut between z = -260 mm and z = -270 mm (colour bar saturated at 0.09 mm/ms).

As it is observed in Figure 9. 14 and Figure 9. 15 it is possible to identify a high reduction of the blood flow velocity not only when the blood reaches the dilated zone, but also afterwards. To quantify with more detail this reduction of velocity, five points were selected from the geometrical model and the results are presented in Table 9. 6. The regions of the selected points are schematized in Figure 9. 16.

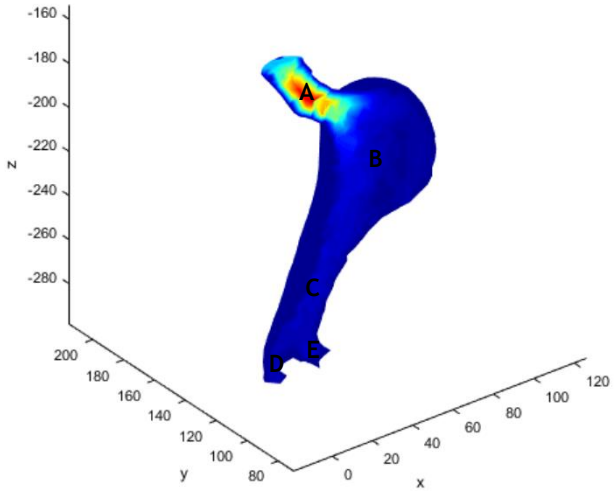

Figure 9. 16 – Schematization of the selected points for obtaining blood's velocity.

Table 9. 6 – Blood flow velocity (in mm/ms) obtained in the selected points of the geometrical model.

	A	B	C	D	E
FEM	0.322	0.016	0.008	0.001	0.002
RPIM	1.105	0.054	0.127	0.053	0.092

In Table 9. 6 it is verified a direct comparison between the blood's velocities obtained from FEM and RPIM in several zones of the aneurysm. Firstly, the higher velocity is verified in point A for both methods, which corresponds to the red patterns observed in Figure 9. 15 and Figure 9. 16. As the blood flows along the aorta, the flow patterns are maintained constant and acquire a stabilized and parabolic profile until it reaches the saccular aneurysm (see Figure 9. 15 (b) and Figure 9. 16 (b)), where the flow dispersion occurs. In this scenario, it is perceptible a radical decrease in the blood's velocity, which is represented in the isomaps by the diffusion of the colours, evident in the figures (c) of both FEM and RPIM results. Also, the patterns of the blood flow in this section are more concentrated in one side of the aneurysm, especially in RPIM, leaving the dilated zone with lower velocities, which are often associated to thrombus formation (as it was explained in the pathogenesis process in Chapter 4). In the Table 9. 6, this behaviour corresponds to point B, which was slightly higher in RPIM than in FEM.

After passing through the dilated zone, the blood flow, in this three-dimensional model, failed to re-stabilize the velocity, however, despite being very small, the velocity has a parabolic profile, that is evident by the transverse cut represented in Figure 9. 14 (d) and Figure 9. 15 (d). Once again, it is verified that the results from FEM are lower than the RPIM's.

To conclude, the points D and E were selected from the left and right iliac arteries, respectively. From the data of Table 9. 6, the value of the velocity in the right iliac artery was almost 1.8 times higher than the velocity registered in the left iliac artery and the discrepancy between RPIM is of almost 60 times higher than FEM.

After reaching these conclusions, and as it was performed in the 2D study, the blood velocities were compared to the results from the Hospital of São João. The following table schematizes the differences between the experimental and the real results.

Table 9. 7 – Comparison between the experimental and clinical values of the blood's velocity.

	Diastolic Velocity (mm/ms)		
	Hospital Results	***Experimental Results with FEM***	***Experimental Results with RPIM***
Healthy segment before the aneurysm	0.354	0.322	1.105
Healthy segment after the aneurysm	0.157	0.008	0.127
Right Iliac Artery	0.447	0.002	0.092
Left Iliac Artery	0.501	0.001	0.053

Observing the previous table, it is evident that the most discrepant results are the ones obtained in the iliac arteries, which are significantly smaller than the clinical values. Furthermore, it is verified that FEM provided the closest results to the clinics in the healthy segment before the aneurysm, decreasing continuously in the next sections. What is stated from this observation is that FEM could not process and re-stabilize the blood flow after the dilated part of the geometry. On the other hand, despite the high value observed in the initial

segment (probably caused by integration problems), the RPIM's velocity was identical to the clinics in the healthy segment before the aneurysm, presenting a better re-stabilization of the flow.

As it was previously mentioned, the greatest discrepancies occur in the iliac arteries, in both methods, that correspond to curvatures and branched zones, that are already known to present some constraints in the results, as it was already concluded in the preliminary studies. In this sequence, the clinical outlet velocities were imposed in the geometrical model and another fluid flow analysis was performed.

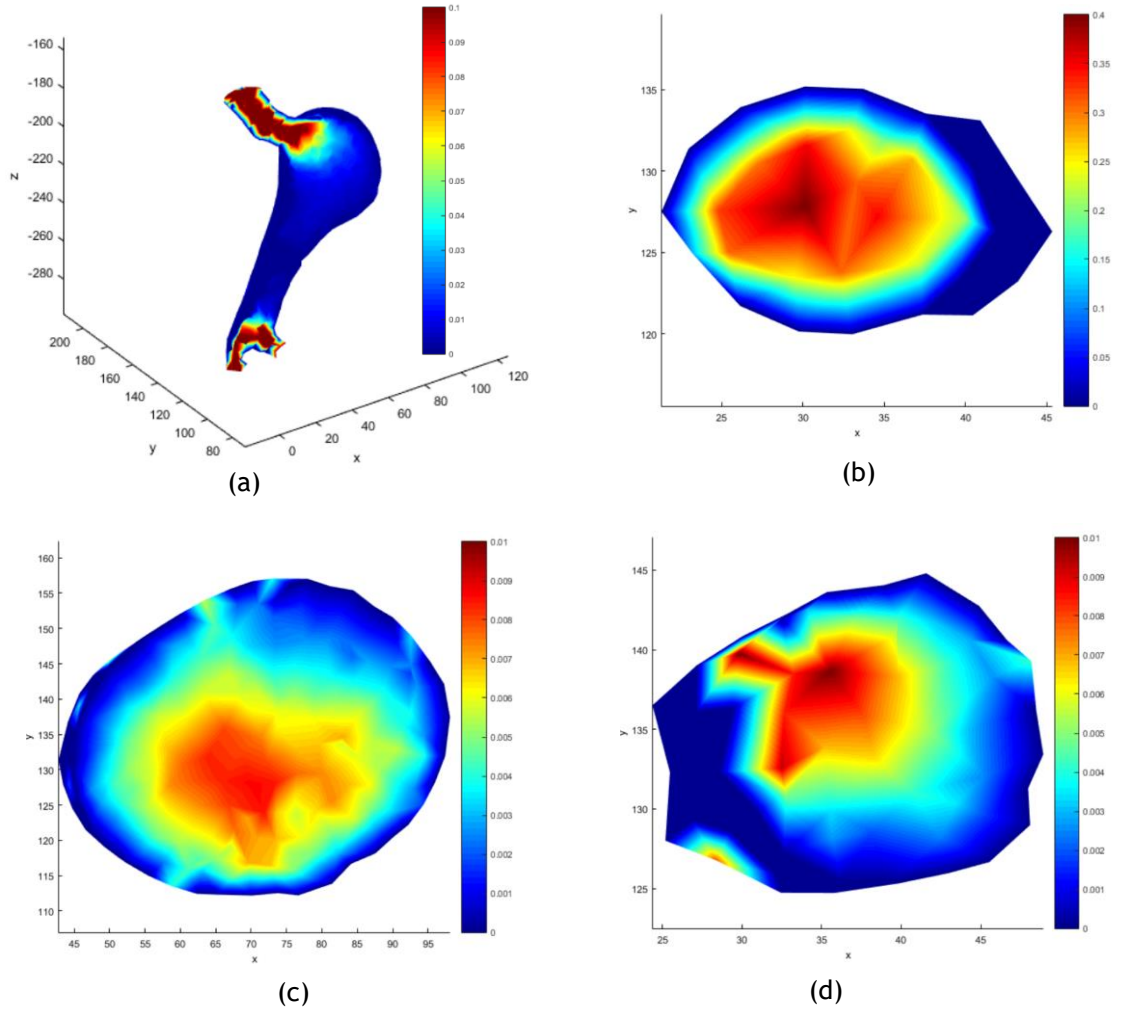

Figure 9. 17 - Colour dispersion map of the 3D saccular aneurysm, using FEM: (a) sagittal plane cut y = 127 mm (colour bar saturated at 0.1 mm/ms); (b) transverse plane cut between z = -170 mm and z = -175 mm (colour bar saturated at 0.4 mm/ms) ; (c) transverse plane cut between z = -220 mm and z = -230 mm (colour bar saturated at 0.01 mm/ms); (d) transverse plane cut between z = -260 mm and z = -270 mm (colour bar saturated at 0.01 mm/ms). The outlet velocities were imposed in the iliac arteries.

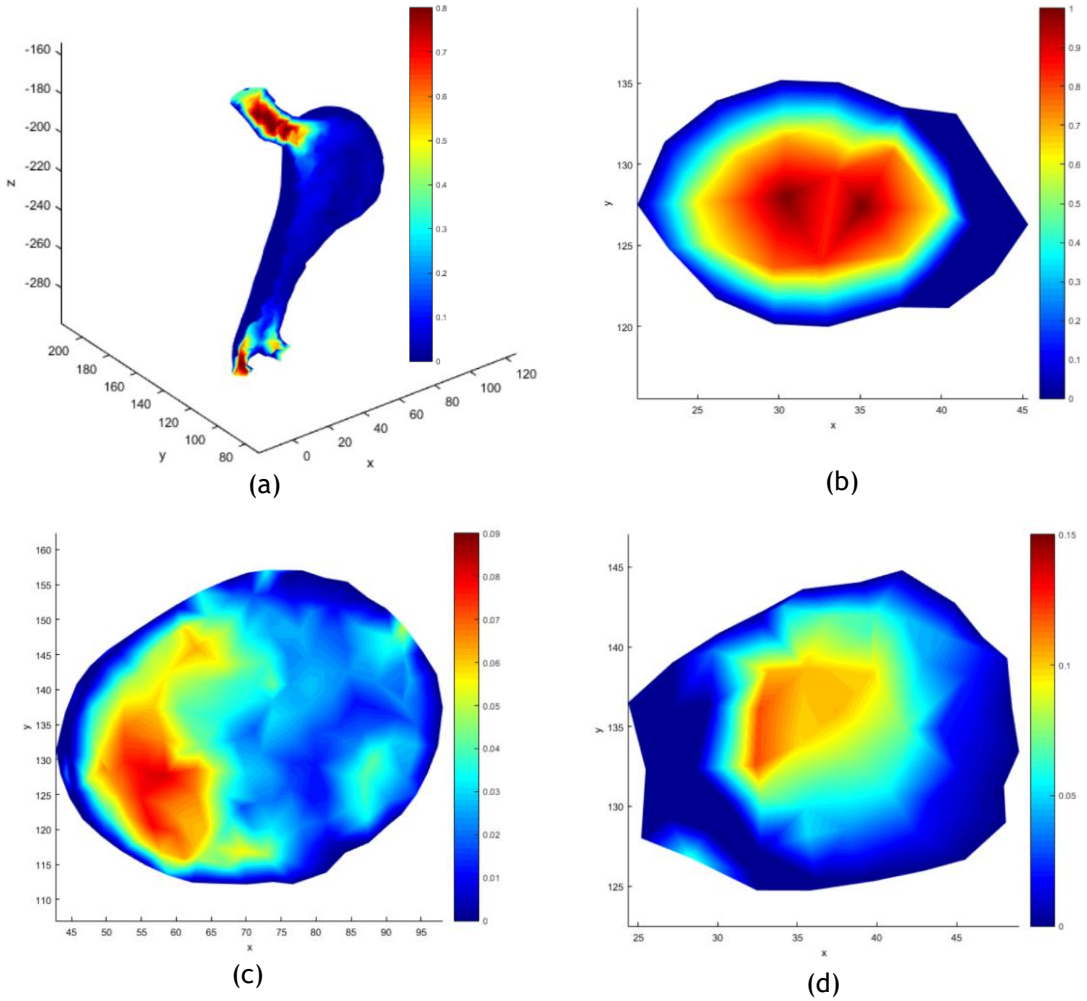

Figure 9. 18 - Colour dispersion map of the 3D saccular aneurysm, using RPIM: (a) sagittal plane cut y = 127 mm (colour bar saturated at 0.08 mm/ms); (b) transverse plane cut between z = -170 mm and z = -175 mm (colour bar saturated at 1 mm/ms) ; (c) transverse plane cut between z = -220 mm and z = -230 mm (colour bar saturated at 0.09 mm/ms); (d) transverse plane cut between z = -260 mm and z = -270 mm (colour bar saturated at 0.015 mm/ms). The outlet velocities were imposed in the iliac arteries.

After imposing the outlet velocities, the major alteration in the colour maps is observed in the iliac arteries, as it was predictable. In the rest of the aneurysm, the blood flow patterns maintained identical to the results of Figure 9. 14 and Figure 9. 15, with exception for the section represented in figures (d). When the outlet velocities were not imposed, the colour dispersion map of figures (d), both for FEM and RPIM, was uniformly distributed along the cross section, with the higher velocity being registered in the centreline. When the outlet velocities were imposed, it was observed a slight concentration of the higher velocities in one side of the cross section, which correspond to the side of the iliac artery with greater blood velocity.

For a more precise comparison between the results of FEM and RPIM after imposing the outlet velocities, the following table was constructed:

Table 9. 8 - Blood flow velocity (in mm/ms) obtained in the selected points of the geometrical model, after imposing the outlet velocities.

	A	B	C	D	E
FEM	0.349	0.012	0.007	0.745	0.445
RPIM	1.101	0.053	0.098	1.324	0.548

From Table 9. 8 it is concluded that the blood flow velocities followed the same behaviour as in the first approach, were no outlet velocities were imposed, however the main alteration are in points D and E, placed in the iliac arteries. Likewise the previous analysis, the RPIM provided higher results than FEM, however, in points B and D, the RPIM values were very high, what can be related to the already mentioned numerical integration difficulty.

After the analysis of the blood flow in the diastolic phase of the cardiac cycle, the tele diastolic phase was also studied and the results of the geometrical model concerning only the imposition of the inlet velocity are depicted in Figure 9. 19 and Figure 9. 20.

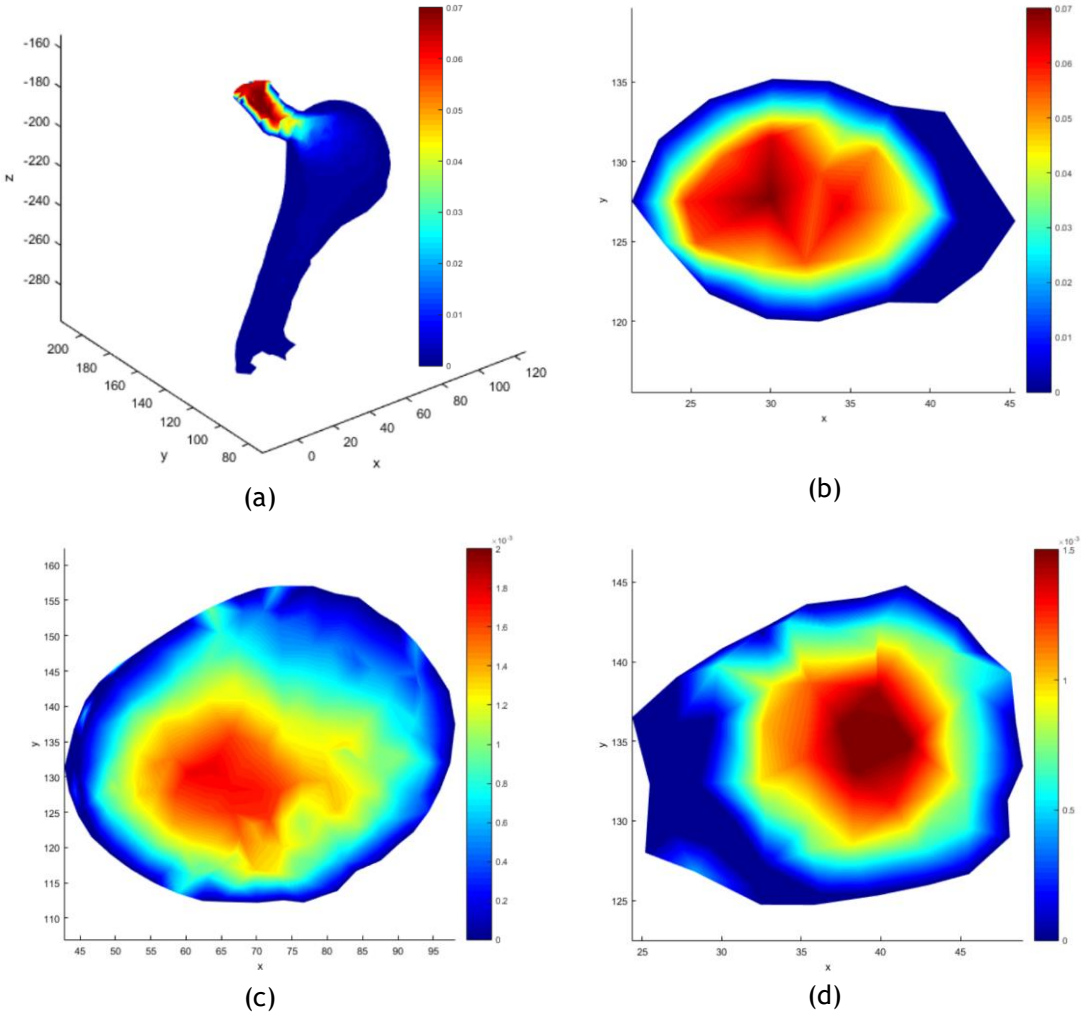

Figure 9. 19 - Colour dispersion map of the 3D saccular aneurysm in the tele diastolic phase, using FEM: (a) sagittal plane cut y = 127 mm (colour bar saturated at 0.07 mm/ms); (b) transverse plane cut between z = -170 mm and z = -175 mm (colour bar saturated at 0.07 mm/ms) ; (c) transverse plane cut between z = -220 mm and z = -230 mm (colour bar saturated at 0.002 mm/ms); (d) transverse plane cut between z = -260 mm and z = -270 mm (colour bar saturated at 0.0015mm/ms).

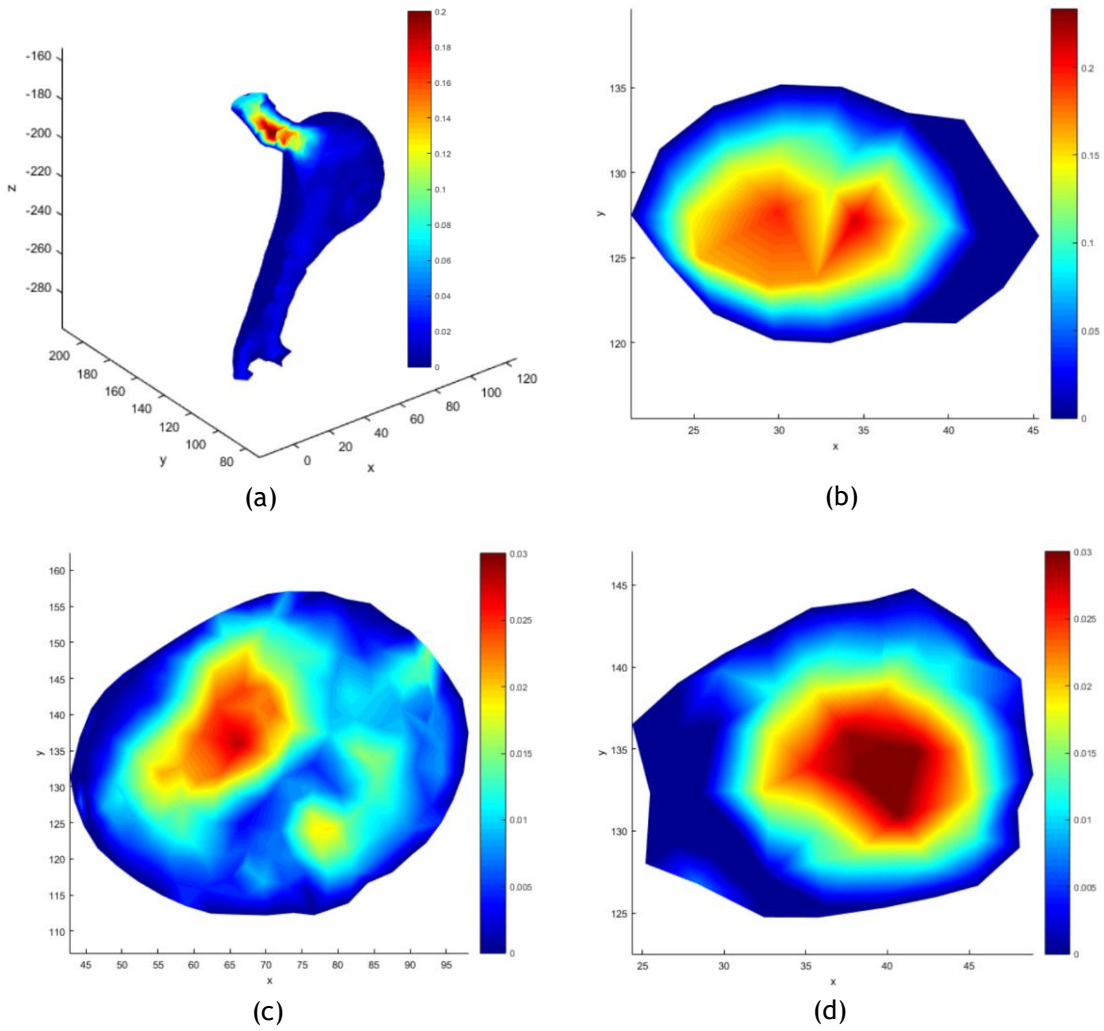

Figure 9. 20 - Colour dispersion map of the 3D saccular aneurysm in the tele diastolic phase, using RPIM: (a) sagittal plane cut y = 127 mm (colour bar saturated at 0.2 mm/ms); (b) transverse plane cut between z = -170 mm and z = -175 mm (colour bar saturated at 0.25 mm/ms) ; (c) transverse plane cut between z = -220 mm and z = -230 mm (colour bar saturated at 0.003 mm/ms); (d) transverse plane cut between z = -260 mm and z = -270 mm (colour bar saturated at 0.003 mm/ms).

Table 9. 9 - Blood flow velocity (in mm/ms) obtained in the selected points of the geometrical model, for the tele diastolic phase of the cardiac cycle.

	A	B	C	D	E
FEM	0.0631	0.0023	0.0005	0.0002	0.0003
RPIM	0.2148	0.0057	0.0157	0.0204	0.0276

Comparing both numerical methods, the results follow the same reasoning as the ones obtained in the diastolic phase, but with the difference that the velocities observed in Figure 9. 19, Figure 9. 20 and Table 9. 9 are smaller, which is inherent to the phase of the cardiac cycle under study. As previously seen, the RPIM led to higher results than FEM, namely in points A, B, D and E. Once again, it is concluded that FEM present some difficulties in re-stabilizing the blood flow after the vessel dilation.

In order to compare the results from Table 9. 9 with the velocities taken from clinical data, the Table 9. 10 was created.

Table 9. 10 - Comparison between the experimental and clinical values of the blood's velocity.

	Tele Diastolic Velocity (mm/ms)		
	Hospital Results	***Experimental Results with FEM***	***Experimental Results with RPIM***
Healthy segment before the aneurysm	0.064	0.0631	0.2148
Healthy segment after the aneurysm	0.0429	0.0005	0.0157
Right Iliac Artery	0.050	0.0002	0.0204
Left Iliac Artery	0.040	0.0003	0.0276

The RPIM was the method that enabled the closest results to the hospital's, with exception for the velocity from the healthy segment before the aneurysm, that presents a larger value when compared to the other sections.

As in the previous analysis, the velocity maintains the same patterns in the several plane cuts, differing only in the magnitude of the obtained results.

After this analysis, and since the iliac arteries are the regions where the blood presents some irregularities, the outlet velocities were imposed, and the results are given by Figure 9. 21 and Figure 9. 22.

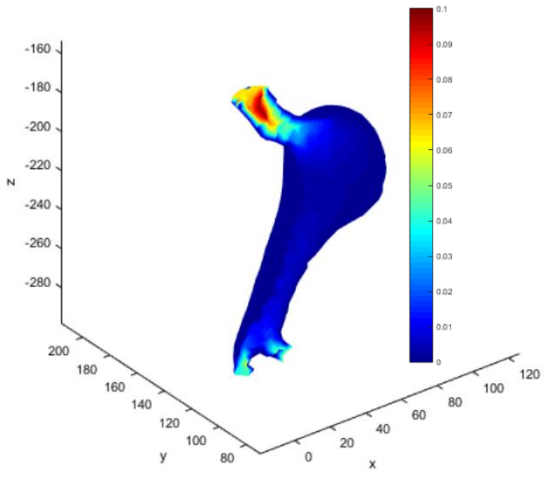

(a)

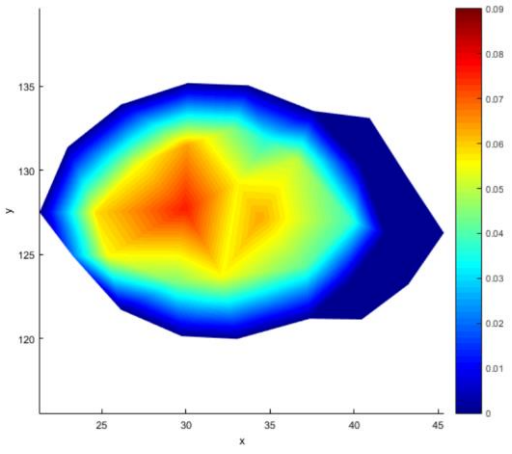

(b)

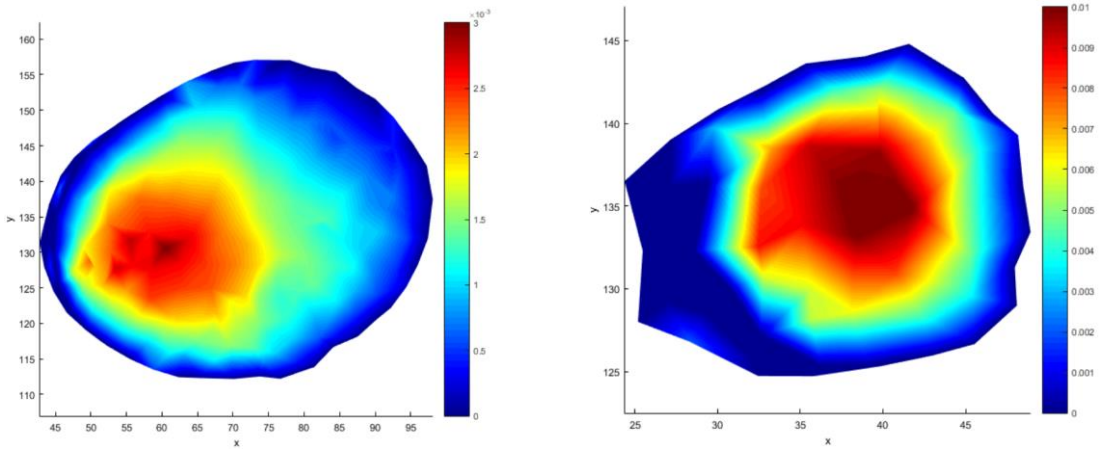

Figure 9. 21 - Colour dispersion map of the 3D saccular aneurysm in the tele diastolic phase, using FEM: (a) sagittal plane cut y = 127 mm (colour bar saturated at 0.1 mm/ms); (b) transverse plane cut between z = -170 mm and z = -175 mm (colour bar saturated at 0.09 mm/ms) ; (c) transverse plane cut between z = -220 mm and z = -230 mm (colour bar saturated at 0.003 mm/ms); (d) transverse plane cut between z = -260 mm and z = -270 mm (colour bar saturated at 0.01 mm/ms). The outlet velocities were imposed in the iliac arteries.

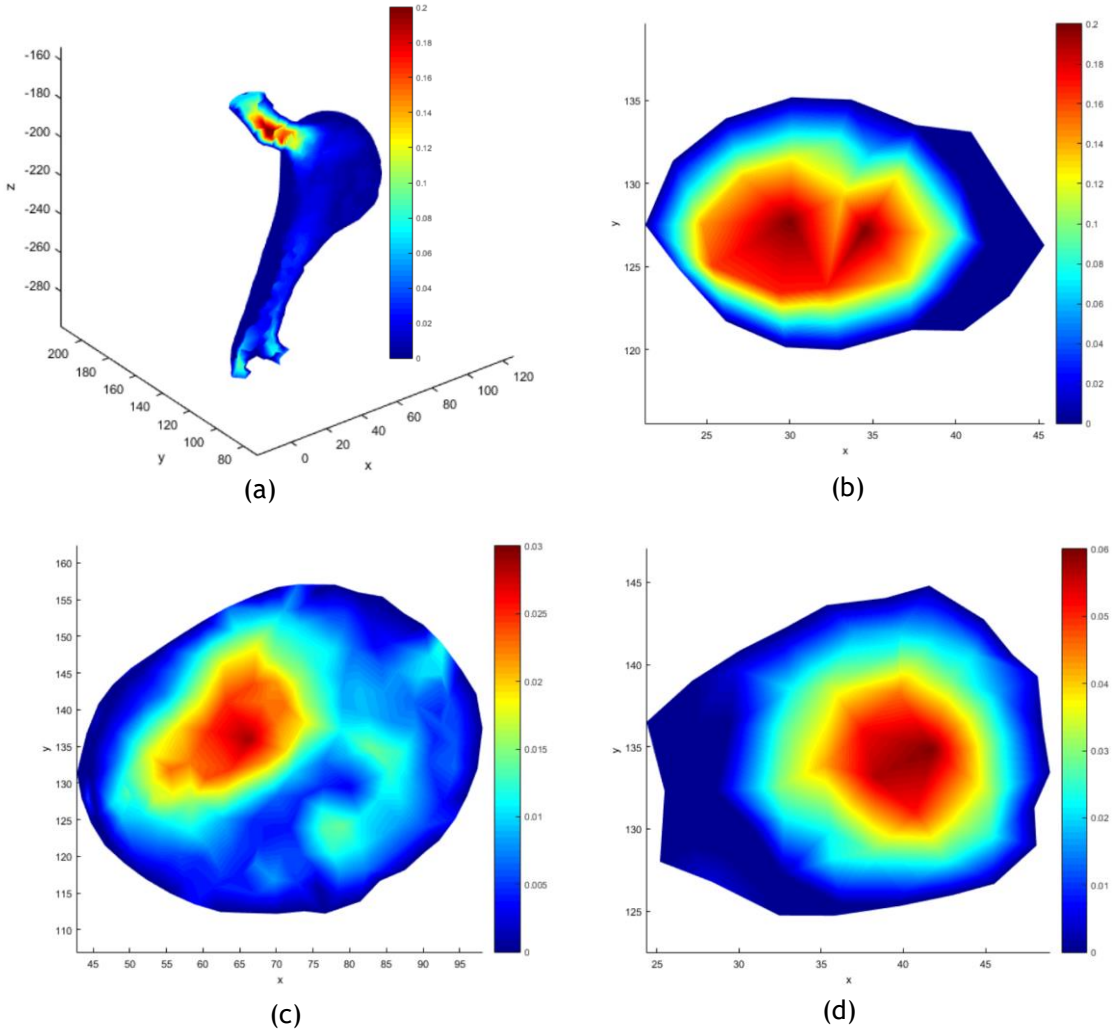

Figure 9. 22 - Colour dispersion map of the 3D saccular aneurysm in the tele diastolic phase, using RPIM: (a) sagittal plane cut y = 127 mm (colour bar saturated at 0.2 mm/ms); (b) transverse plane cut between z = -170 mm and z = -175 mm (colour bar saturated at 0.2 mm/ms) ; (c) transverse plane cut between z = -220 mm and z = -230 mm (colour bar saturated at 0.003 mm/ms); (d) transverse plane cut between z = -260 mm and z = -270 mm (colour bar saturated at 0.06 mm/ms). The outlet velocities were imposed in the iliac arteries.

Table 9. 11 – Blood flow velocity (in mm/ms) obtained in the selected points of the geometrical model, for the tele diastolic phase of the cardiac cycle, after imposing the outlet velocities.

	A	B	C	D	E
FEM	0.0632	0.0027	0.0061	0.0594	0.0503
RPIM	0.2181	0.0196	0.0454	0.0821	0.0764

Similarly to what was obtained before, the RPIM still provides the major results and the most closer to the clinics.

After the complete analysis of the blood flow in the three-dimensional saccular aortic aneurysm, the following conclusions are withdrawn:

- The numerical method that provided the preferred results was the RPIM. In FEM, the blood did not stabilize after the dilation of the aorta, which did not occur with RPIM;
- The blood flow patterns, for both methods, were identical, differing mainly in the dilated portion, where FEM presented a diffused but distributed velocity pattern, while in RPIM the velocity was concentrated in one specific side of the bulge;
- The results were less favoured in the iliac arteries, which correspond to a branched zone, where (theoretically) blood disruptions and irregularities occurs. In practice, and using the numerical methods applied in this study, it was observed that the velocities and blood flow patterns in these regions are not well processed. This can be related to the flow formulation that was applied, with integration problems in the weak form of Galerkin or with the own model's mesh;
- In the different phases of the cardiac cycle, the results of the blood flow patterns were identical, meaning that it is the geometry that has a major role in the blood's results and not so significantly the imposed velocities.

9.2. Fusiform Abdominal Aortic Aneurysm

In order to understand the differences that occur in the blood flow in aneurysms of various geometries, the fusiform aneurysm represented in Figure 9. 23 was constructed, following the same reasoning described for the saccular aneurysm.

Considering the conclusions remarked from the study of the saccular aortic aneurysm, for this analysis it was promptly imposed both inlet and outlet velocities, since the results obtained in these conditions are preferred than the ones where only the inlet velocity is considered.

It is noticed that, in this model, the iliac arteries are not represented, because the accentuated curvature (that is observed in Figure 9. 23) of the iliac arteries would lead to inaccurate results, characteristic of zones with branches and curvatures, as it was concluded in the analysis of the previous aneurysm.

Since this anatomical image was not obtained from the Hospital of São João (due to logistic constraints in the acquisition of the images), the numerical results of this aneurysm (which was obtained from an online database www.embodi3d.com) will not be compared with clinical results. The diastolic inlet and outlet velocities were both considered 0.325 mm/ms. The inlet and outlet tele diastolic velocities were 0.05 mm/ms and 0.039 mm/ms, respectively. These values were confirmed by the medical doctors that collaborated in this study.

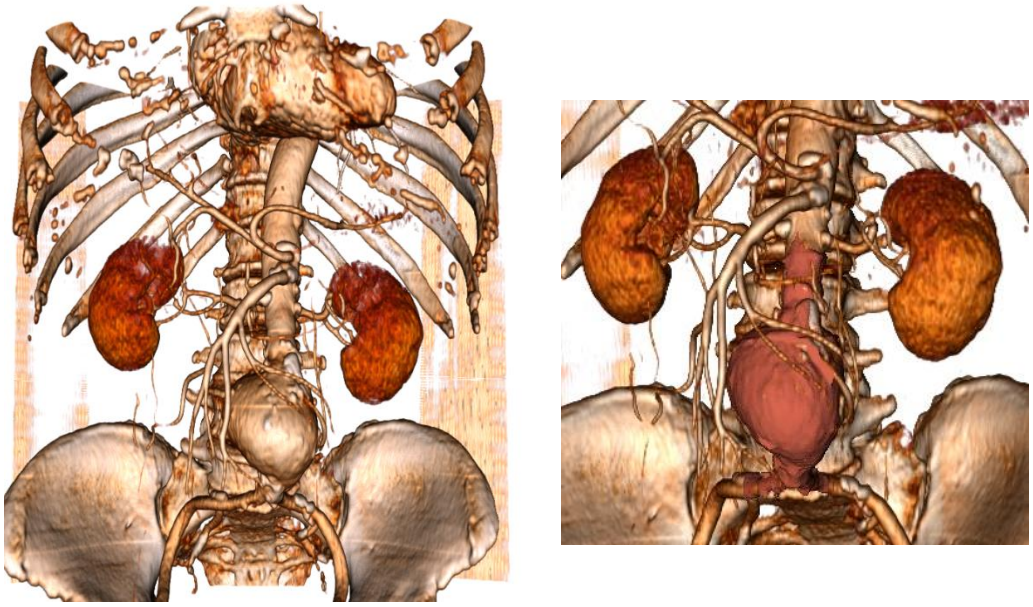

(a) (b)

Figure 9. 23 – Abdominal Aortic Aneurysm: (a) DICOM image obtained from CTA and (b) aneurysmal mask.

After the segmentation of the DICOM image, and taking into consideration the steps for constructing the geometrical model already described in the subchapter 9.1, the fusiform aortic aneurysm models were obtained, as it can be observed in Figure 9. 24. The 3D model is composed by a tetrahedral mesh of 3084 nodes and 15551 elements (linear polynomial elements) and the 2D model is discretized with 4035 triangular elements (linear polynomial elements) and 2116 nodes. The boundary conditions that were imposed in the fusiform aneurysm are the same as the ones applied in the saccular aneurysm.

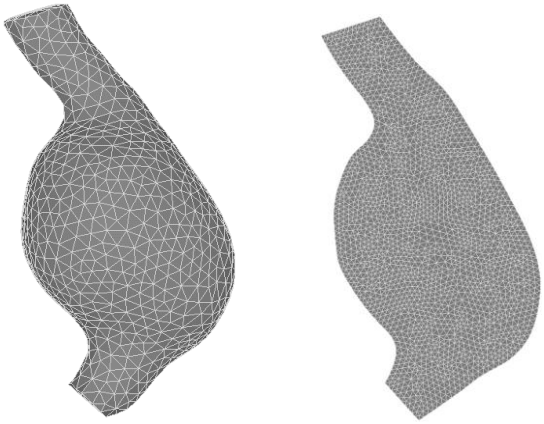

(a) (b)

Figure 9. 24 - Lateral view of the geometrical models: (a) 3D and (b) 2D.

9.2.1. 2D Analysis

In Figure 9. 25 and Figure 9. 26, it is represented, respectively, the results of the static fluid flow analysis for the diastolic and tele diastolic phases of the cardiac cycle.

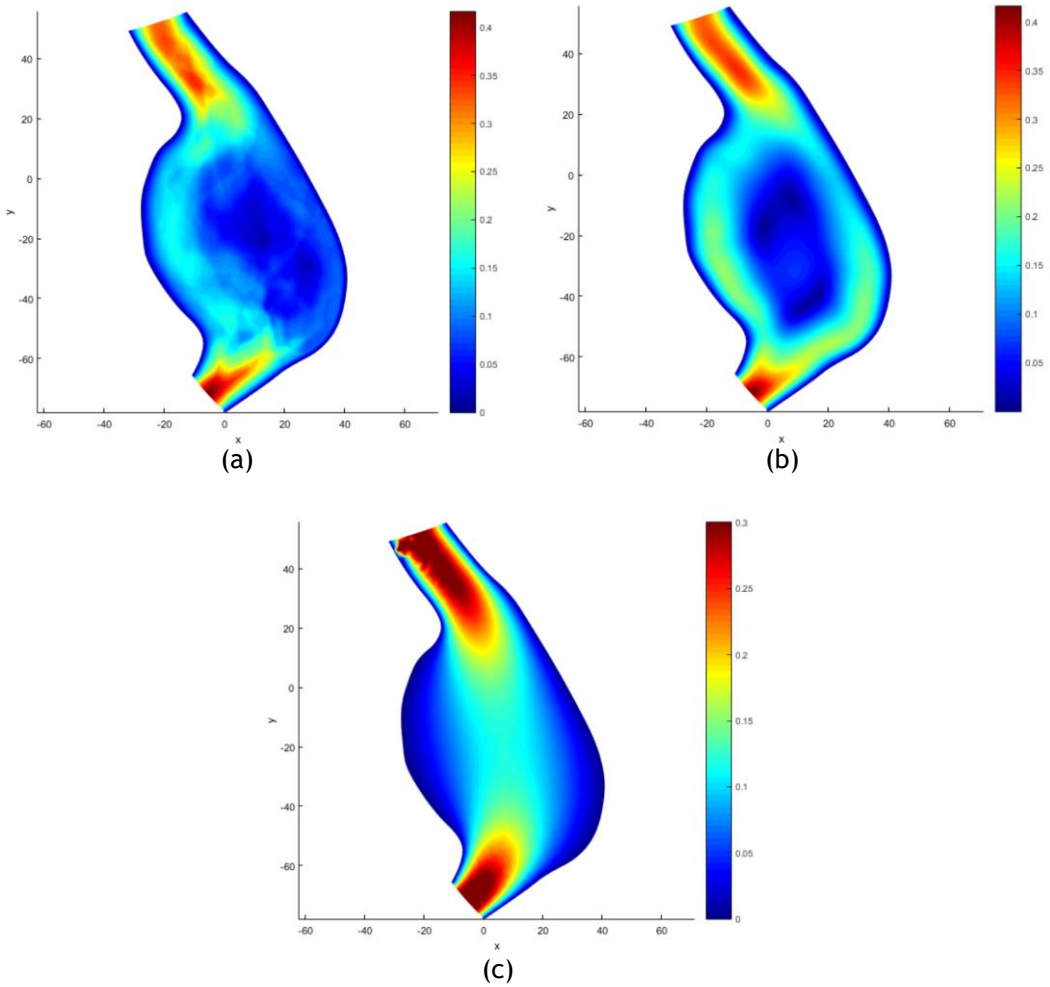

Figure 9. 25 - Colour dispersion map of the fusiform aneurysm, in the diastolic phase of the cardiac cycle: (a) FEM (colour bar up to 0.4158 mm/ms); (b) RPIM (colour bar up to 0.4158 mm/ms); (c) NNRPIM (colour bar saturated at 0.3 mm/ms).

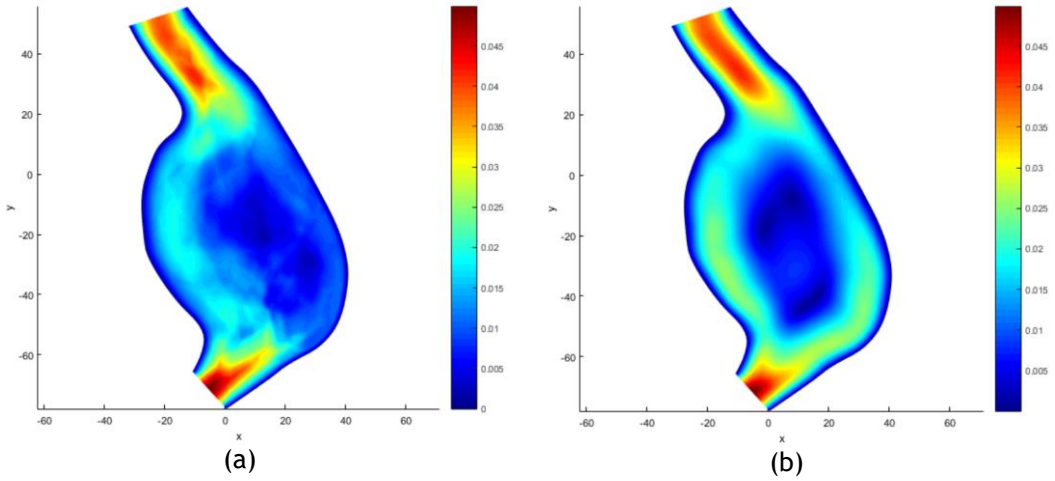

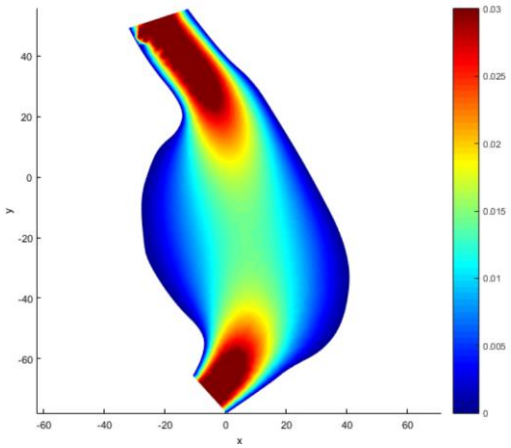

(c)

Figure 9. 26 - Colour dispersion map of the fusiform aneurysm, in the tele diastolic phase of the cardiac cycle: (a) FEM (colour bar up to 0.0498 mm/ms); (b) RPIM (colour bar up to 0.0.0498 mm/ms); (c) NNRPIM (colour bar saturated at 0.03 mm/ms).

The results presented in Figure 9. 25 and Figure 9. 26 demonstrate that, independently of the cardiac cycle phase in which the blood is simulated, the results of the flow patterns are identical. In Figure 9. 25 (a) and Figure 9. 26 (a), which regards the FEM analysis, the blood entered the vessel with a parabolic profile, dispersing when reaching the dilated area. It is noticed that the velocity, in the aneurysm, was more concentrated in the left side, which is the side where the bulge has a more accentuated curvature. Since there are no iliac arteries, the blood flow in the outlet portion of the blood vessel re-stabilized, forming a well-defined parabolic profile. In the RPIM analysis, for both diastolic and tele diastolic phases, the blood flow patterns are more accurate than in FEM's and are well defined near the walls, leaving the centre of the aneurysm with a low velocity. Despite the differences in the blood flow patterns, it is noticed that the maximum velocity obtained for FEM and RPIM are the same, i.e., 0.4158 mm/ms and 0.0498 mm/ms for the diastolic and tele diastolic phases, respectively.

The most unexpected, but superior, result is from NNRPIM, which provided a continuous blood flow pattern along the centreline of the blood vessel, as theoretically expected. Near the wall of the aneurysm, the velocity is low, potentiating the formation of ILT.

After the analysis of the isomaps, three points were selected in the geometrical model, in order to quantify the velocity in specific regions. In Figure 9. 27 it is depicted the schematization of the selected points in the fusiform aortic aneurysm and the results that were obtained are presented in Table 9. 12.

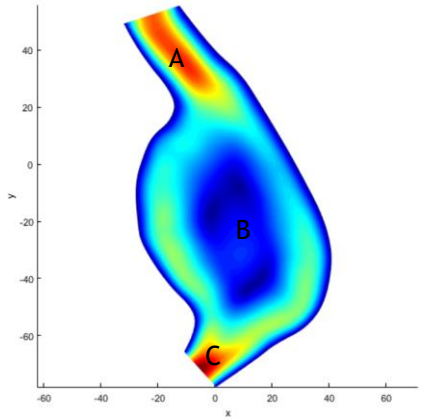

Figure 9. 27 – Selected points in the 2D model for obtaining blood's velocity.

Table 9. 12 – Blood's diastolic velocity (mm/ms) in specific points of the two-dimensional fusiform aneurysm model.

	A	B	C
FEM	0.34	0.03	0.37
RPIM	0.35	0.04	0.35
NNRPIM	0.30	0.12	0.35

Table 9. 13 - Blood's tele diastolic velocity (mm/ms) in specific points of the two-dimensional fusiform aneurysm model.

	A	B	C
FEM	0.040	0.004	0.044
RPIM	0.042	0.005	0.042
NNRPIM	0.036	0.014	0.042

Observing the Table 9. 12 and Table 9. 13 it is verified that, in all numerical methods, the velocity decreased in point B, as it was already detected in the dispersion colour maps. Regarding the points A and C, the velocities were identical for the three numerical methods, which not only indicates that the flow re-stabilized after the bulge, but also that the different numerical methods provided close results. Thus, with this study, it is possible to verify that the blood flow simulations with the advanced discretization meshless methods that were used are efficient in 2D fusiform aneurysmal geometries. In order to understand if this conclusion is analogous to 3D structures, a 3D analysis was performed.

9.2.2. 3D Analysis

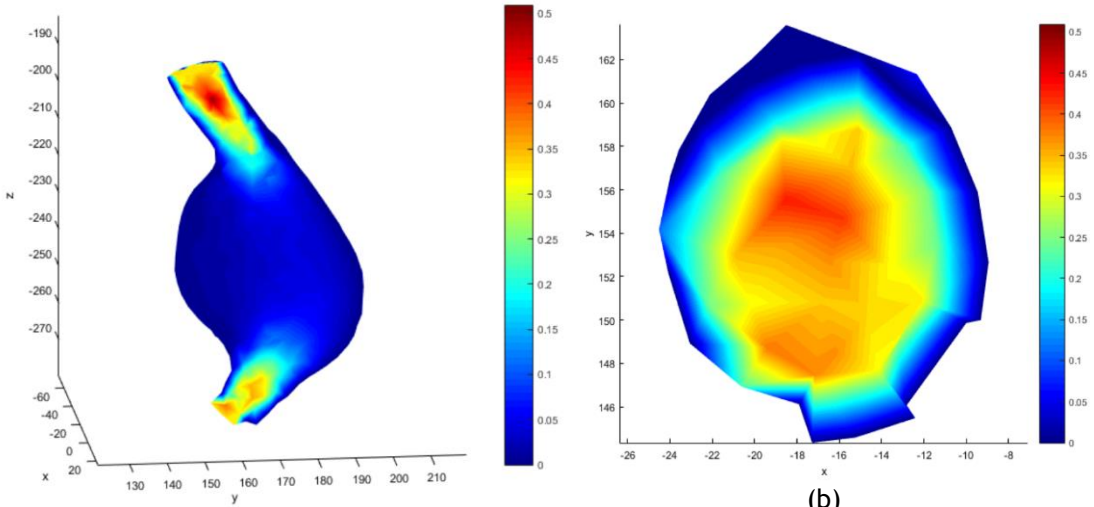

(a) (b)

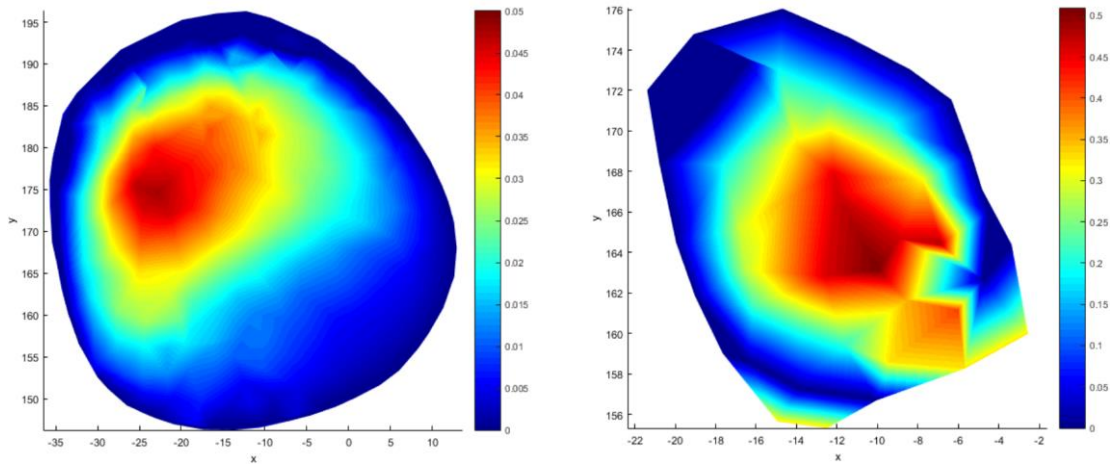

(c) (d)

Figure 9. 28 - Colour dispersion map of the 3D fusiform aneurysm, in the diastolic phase, using FEM: (a) sagittal plane cut x = -14 mm (colour bar up to 0.5085 mm/ms); (b) transverse plane cut between z = -190 mm and z = -185 mm (colour bar up to 0.5085 mm/ms) ; (c) transverse plane cut between z = -230 mm and z = -240 mm (colour bar saturated at 0.05 mm/ms); (d) transverse plane cut between z = -270 mm and z = -275 mm (colour bar up to 0.5085 mm/ms).

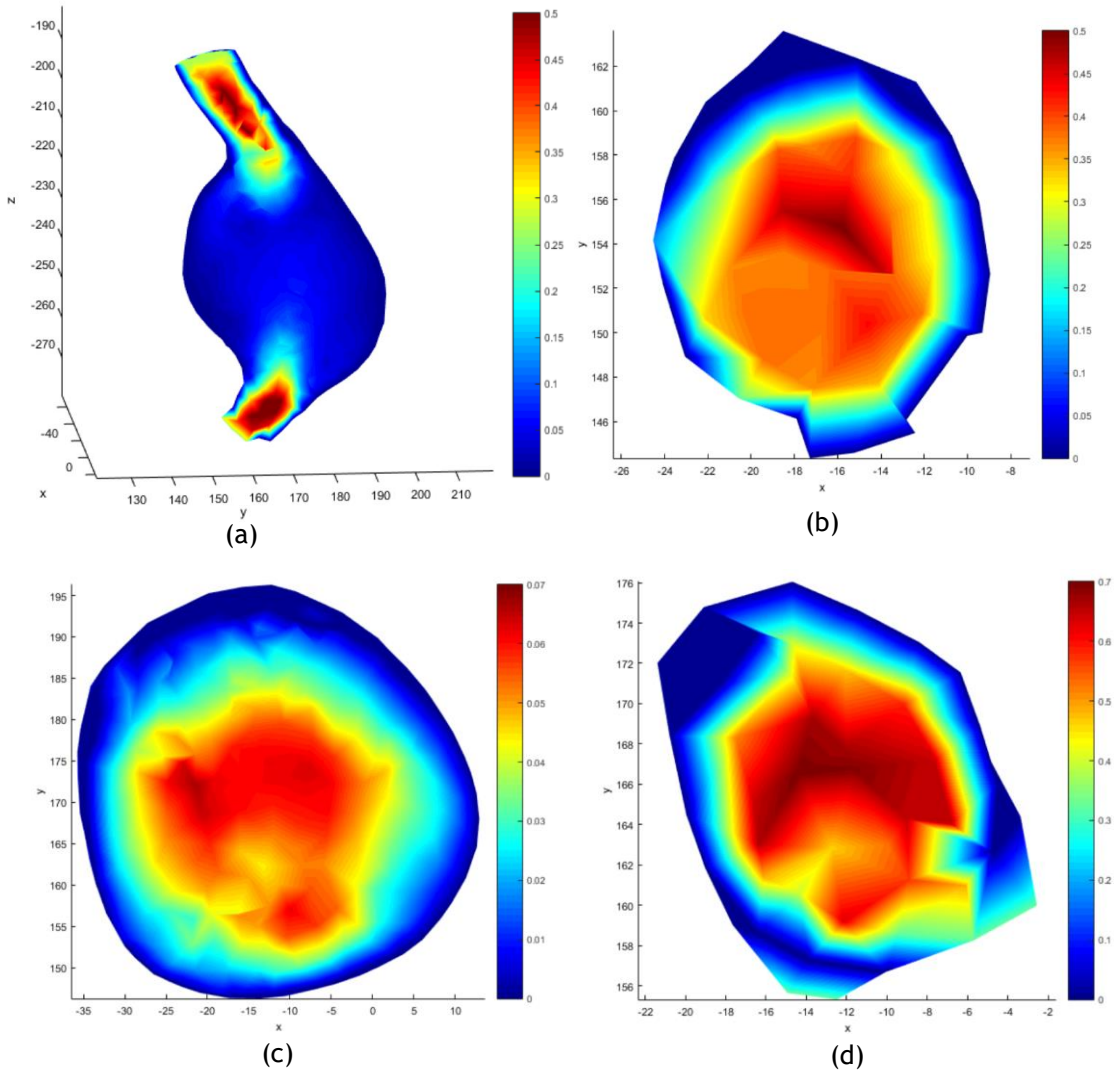

(a) (b)

(c) (d)

Figure 9. 29 - Colour dispersion map of the 3D fusiform aneurysm, in the diastolic phase, using RPIM: (a) sagittal plane cut x = -14 mm (colour bar saturated at 0.5 mm/ms); (b) transverse plane cut between z = -190 mm and z = -185 mm (colour bar saturated at 0.5 mm/ms) ; (c) transverse plane cut

between z = -230 mm and z = -240 mm (colour bar saturated at 0.07 mm/ms); (d) transverse plane cut between z = -270 mm and z = -275 mm (colour bar saturated at 0.7 mm/ms).

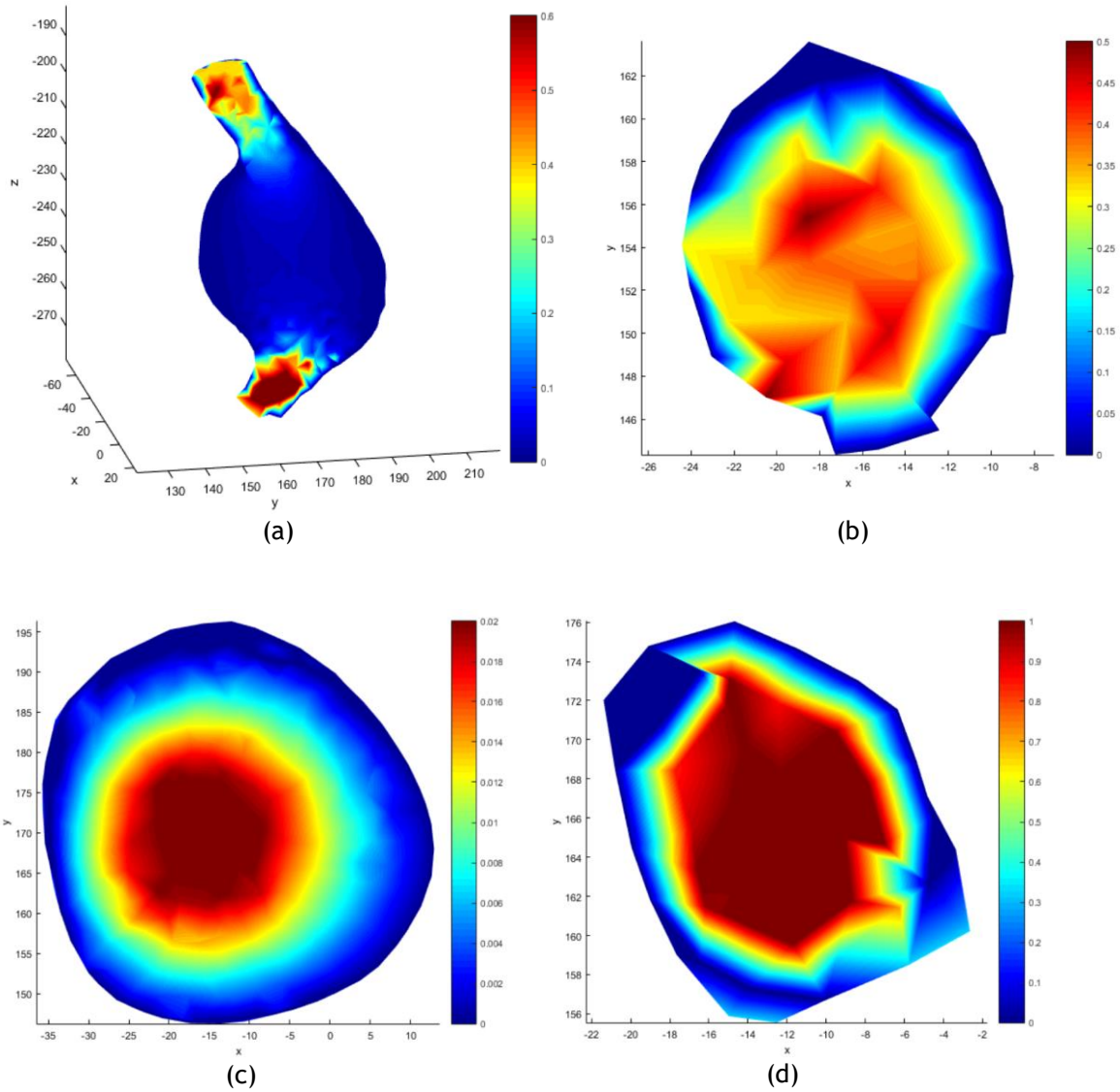

Figure 9. 30 - Colour dispersion map of the 3D fusiform aneurysm, in the diastolic phase, using NNRPIM: (a) sagittal plane cut x = -14 mm (colour bar saturated at 0.6 mm/ms); (b) transverse plane cut between z = -190 mm and z = -185 mm (colour bar saturated at 0.5 mm/ms) ; (c) transverse plane cut between z = -230 mm and z = -240 mm (colour bar saturated at 0.02 mm/ms); (d) transverse plane cut between z = -270 mm and z = -275 mm (colour bar saturated at 1 mm/ms).

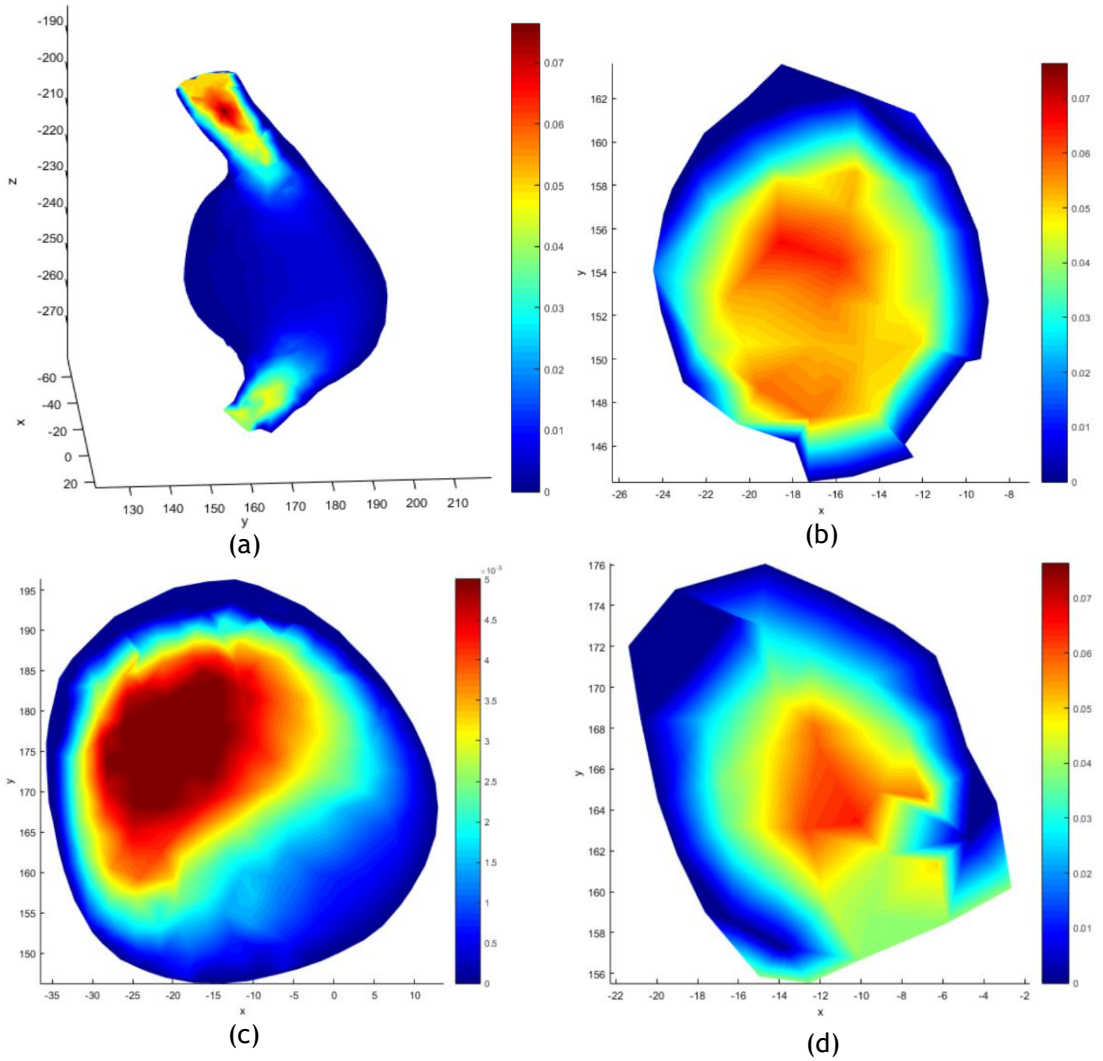

Figure 9. 31 - Colour dispersion map of the 3D fusiform aneurysm, in the tele diastolic phase, using FEM: (a) sagittal plane cut x = -14 mm (colour bar up to 0.0763 mm/ms); (b) transverse plane cut between z = -190 mm and z = -185 mm (colour bar up to 0.0763 mm/ms) ; (c) transverse plane cut between z = -230 mm and z = -240 mm (colour bar saturated at 0.005 mm/ms); (d) transverse plane cut between z = -270 mm and z = -275 mm (colour bar up to 0.0763 mm/ms).

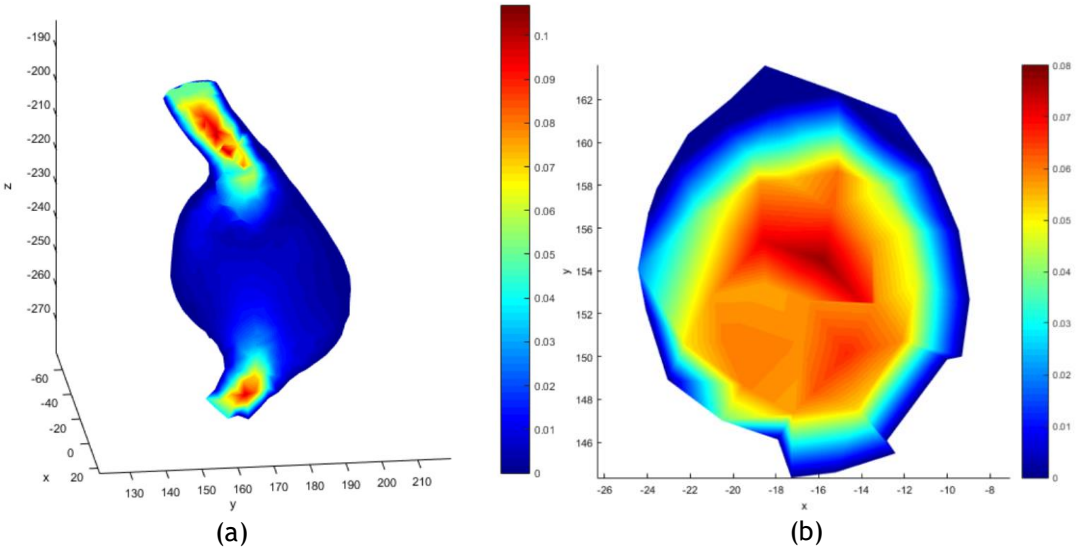

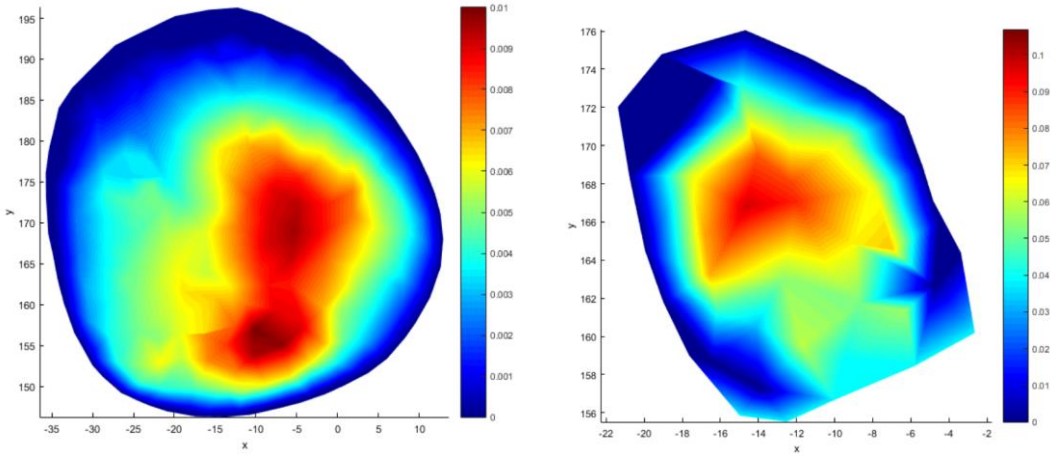

Figure 9. 32 - Colour dispersion map of the 3D fusiform aneurysm, in the tele diastolic phase, using RPIM: (a) sagittal plane cut x = -14 mm (colour bar up to 0.1068 mm/ms); (b) transverse plane cut between z = -190 mm and z = -185 mm (colour bar saturated at 0.08 mm/ms) ; (c) transverse plane cut between z = -230 mm and z = -240 mm (colour bar saturated at 0.01 mm/ms); (d) transverse plane cut between z = -270 mm and z = -275 mm (colour bar saturated at 0.2 mm/ms).

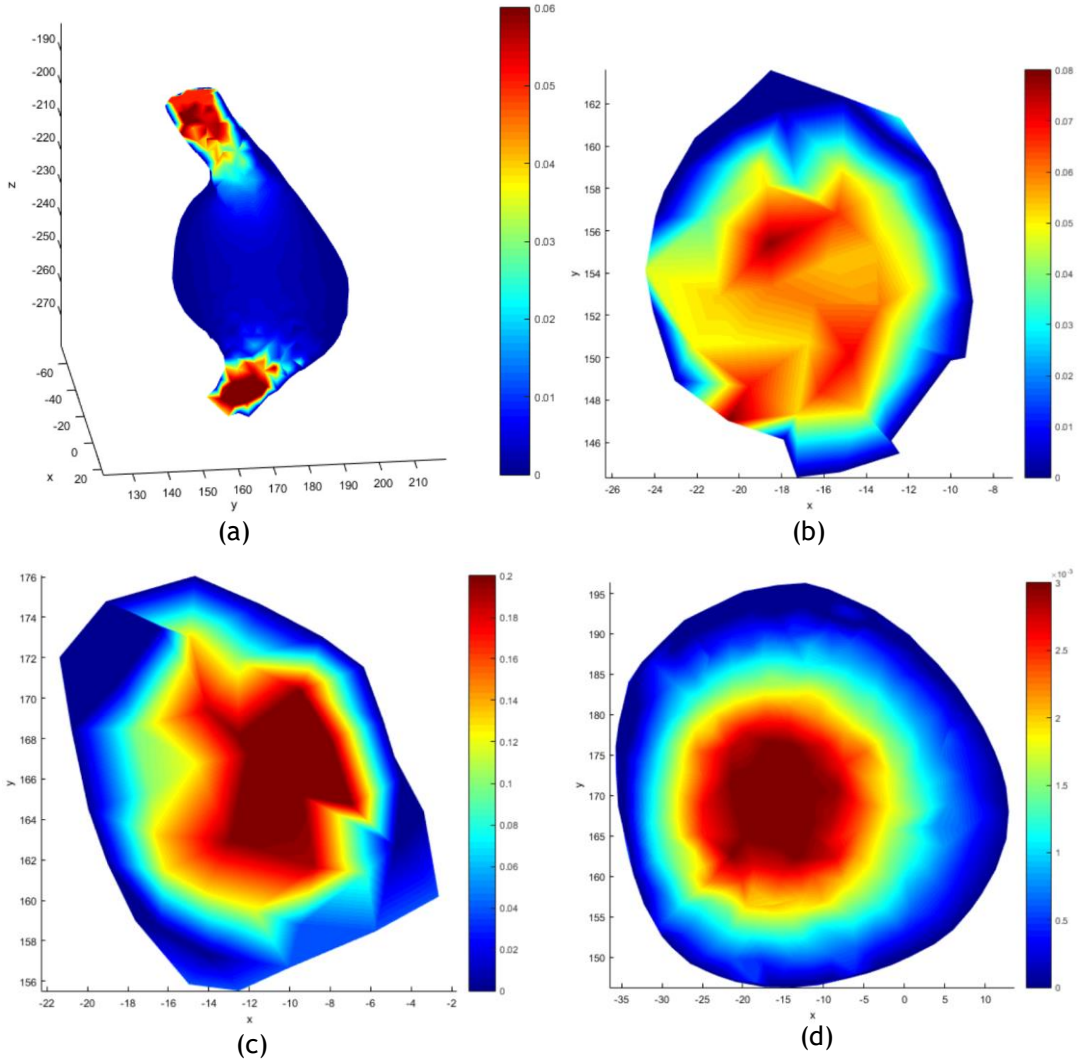

Figure 9. 33 - Colour dispersion map of the 3D fusiform aneurysm, in the tele diastolic phase, using NNRPIM: (a) sagittal plane cut x = -14 mm (colour bar saturated at 0.06 mm/ms); (b) transverse plane cut between z = -190 mm and z = -185 mm (colour bar saturated at 0.08 mm/ms) ; (c) transverse plane cut between z = -230 mm and z = -240 mm (colour bar saturated at 0.03 mm/ms); (d) transverse plane cut between z = -270 mm and z = -275 mm (colour bar saturated at 0.2 mm/ms).

From Figure 9. 28 to Figure 9. 30 it is observed the isomaps of the blood flow in the diastolic phase of the cardiac cycle. In the results from FEM (see Figure 9. 28), it is verified that the inlet and outlet portions of the aortic aneurysm present higher velocities and the blood flow profile is distributed along the entire diameter of the blood vessel. On the other hand, the dilation portion not only present lower velocities, but also a concentration of the velocity in a specific side of the aorta, which can be seen in the transverse plane cut represented in Figure 9. 28 (c). Regarding the results of RPIM and NNRPIM, the healthy segments of the aorta present similar blood flow patterns to FEM's, differing in the aneurysmal portion: in RPIM, the blood's velocity was not concentrated in one side of the bulge, but distributed in all its diameter, with a diffused pattern (see Figure 9. 29 (c)); in NNRPIM, the fluid velocity was also distributed, but with a more precise pattern, being superior in the centreline and decreasing as it approaches the aneurysmal wall (see Figure 9. 30 (c)).

Analysing all the three-dimensional results of the different numerical methods, it is verified that, in NNRPIM, the flow is less accurate, especially in the inlet and outlet regions, possibly due to a limitation of the flow formulation used in this work.

As it was performed for the 2D geometrical model, three points were selected, and the velocities obtained in order to quantify the blood flow in specific regions of the aortic aneurysm. The selection of points is schematized in Figure 9. 34.

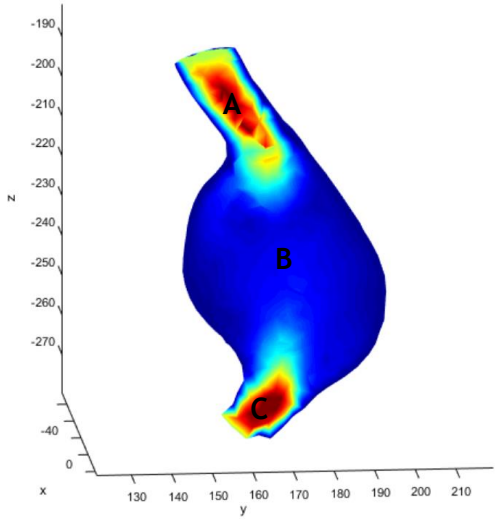

Figure 9. 34 - Selected points in the 3D model for obtaining blood's velocity.

Table 9. 14 - Blood's diastolic velocity (mm/ms) in specific points of the three-dimensional fusiform aneurysm model.

	A	B	C
FEM	0.42	0.03	0.36
RPIM	0.52	0.06	0.76
NNRPIM	0.35	0.02	1.03

Table 9. 15 - Blood's tele diastolic velocity (mm/ms) in specific points of the three-dimensional fusiform aneurysm model.

	A	B	C
FEM	0.064	0.004	0.046
RPIM	0.078	0.008	0.097
NNRPIM	0.054	0.003	0.123

In Table 9. 14 and Table 9. 15 it is represented the blood flow velocity in three points of the aortic aneurysm, both in the diastolic and tele diastolic phase, respectively. As it was observed in the previous 2D analysis, the velocity in the dilated portion of the aorta decreases significantly for all the numerical methods that were studied. It is also verified that, in point A and for both diastolic and tele diastolic results, the velocity was similar for the three numerical methods, differing mostly in point C. The main difference between the results in the healthy segment of the aorta after the aneurysm is in NNRPIM, which is verified a significant increase of the blood's velocity, possibly due to an integration problem or to the flow formulation that was used in this study.

With the static fluid flow analysis performed in a two and three-dimensional real geometry of a fusiform aortic aneurysm, it is possible to conclude that:

- The 2D results were identical for FEM and RPIM analysis, however, the NNRPIM's provided superior blood flow patterns, which is verified by the continuity of the colours along the vessel;
- The 3D results were less accurate than the 2D, but they were superior than the outcomes of the previous aneurysm (the saccular aneurysm). Since there is no branches and accentuated curvatures in the termination of the fusiform aneurysm, the blood flow re-stabilized more efficiently than in the scenario where the outlet is composed by branches, so the velocity profiles, both in 2D and 3D, were preferred in this aneurysm, namely in the outlet region;
- Comparing the blood velocity patterns between the diastolic and tele diastolic phases, it is verified that there is no substantial alteration among both scenarios;
- Taking into consideration the results that were obtained, it is concluded that meshless methods are efficient for analysing blood flow problems in complex anatomical geometries.

Chapter 10

Conclusions and Future Work

Aortic aneurysms are a silent disease, caused by multifactorial processes that lead to pathophysiological remodelling of the aorta. One of the main triggers for the disease's onset and evolution is hemodynamics, that has already been proven to play a crucial role in aneurysm's rupture. In this context, blood flow simulations are important to support the medical community to comprehend better the disease's evolution. In my best knowledge, there are no documents concerning the study of blood flow in aortic aneurysms using meshless methods, which leaves a branch of new research opportunities in this field. Therefore, in this thesis, the use of advanced discretization meshless methods – RPIM and NNRPIM – was extended for the analysis of blood flow in two and three-dimensional models, being the first-time meshless methods are applied in this context.

The main objective of this thesis was to perform a static fluid flow analysis of blood in aortic aneurysm's geometries using FEM and meshless methods and demonstrate that meshless methods are an efficient alternative numerical technique. Another goal of this work was to study the variation of the results in 2D and 3D models, using regular and irregular meshes and calibrate the parameters of simulation that provide the best results. Lastly, the blood flow simulation in realistic geometries and the comparison of the results with the clinics were another major objective of this work.

After reaching the results of various blood flow simulations, relevant conclusions were obtained. It was confirmed that the blood flow patterns are improved in models with regular meshes, both in two and three-dimensional structures. Irregular meshes strongly disturb the blood flow, implying the need for the calibration of the parameters of simulation. However, the calibration was not sufficient for obtaining results as accurate and as smooth as the ones obtained with regular meshes.

In the simulations with simpler geometries, it was observed that the blood flow results are not as stable in branched zones as in the rest of the blood vessel, being necessary the imposition of outlet velocities to linearize the flow. In this first study, it was concluded that (1) the convergence is achieved from models with 2000 nodes; (2) the blood flow results were preferred in FEM with elements with 6 nodes and (3) the imposition of outlet velocities improve the results significantly. In the 3D branched model, it was also observed that the imposition of the outlet velocities provides a well-defined blood pattern along the entire extension of the vessel, being the FEM the method that reproduces better results.

In the study of the fusiform aortic aneurysm, it was observed that, regardless the increase of the diameter, the blood flow velocities maintain similar, with exception for the NNRPIM, where the results were not as proper as in FEM and RPIM, which can due to limitations in the integration scheme.

Lastly, in the study of the real geometry of a saccular aneurysm, the meshless methods were able to produce good results in the 2D geometry, however, in 3D the flow presented some

irregularities and diffusions, not being as defined as in 2D. In the other hand, the 2D and 3D results of the real geometry of a fusiform aortic aneurysm were apparently more accurate than the previous aneurysm's results, and the 3D velocity profiles were not as diffused, being identical to the 2D results. With these outcomes, it can be concluded that, for 3D and very irregular geometries with branches and accentuated curvatures, the software used was not effective in predicting the blood flow, which can be due to the fluid formulation that was applied in this work.

Taking into consideration all the results achieved in the several studies, it is proved that the use of meshless methods in fluid flow problems are adequate, more precisely for 2D studies. For 3D geometries, the meshless results are satisfactory when the mesh is regular, which means that 3D models with irregular meshes are at disadvantage. Also, it can be stated that the FEM and the meshless methods, namely RPIM, are well prepared for the study of anatomical geometries. Due to some limitations of the software that was used, the NNRPIM was not able to reproduce as good results as the RPIM.

Another important remark of this thesis is the practical knowledge acquired in several basic numerical tools that were necessary for developing the geometrical models:

- 3D-Slicer® – which is a freeware capable to produce STL files from CT medical images;
- FEMAP® (Siemens PLM Software, student version) – which allows the construction of meshes from STL files and provides drawing tools to produce models and their respective meshes;
- SolidWorks® - which is a solid modeling computer-aided design (CAD) and computer-aided engineering software that allows the design and simulation of three-dimensional models;
- FEMAS® (Finite Element and Meshless Analysis Software - cmech.webs.com) - which is a freeware academic software that allows the analysis of models using either the FEM or meshless methods combined with several linear and non-linear formulations, such as the fluid flow proposed for the dissertation, and allows the user to import an input file (INP file) such as the ones created in FEMAP.

While this work reached all the planned objectives, it also had various limitations. Firstly, the results, especially in 3D, are not coherent to the results obtained in the 2D, for the saccular geometry. Also, in the 2D saccular aneurysm, the NNRPIM presented some unexpected results in the iliac arteries, which can be related to the integration scheme, the non-smoothness of the mesh or with the flow formulation that was applied. Secondly, the realistic models had to be smoothed to be used in FEMAS®, which removed some surface irregularities characteristic of the anatomical structure under study. This smoothing was performed due to the demanding task of implementation of the boundary conditions inherent to the software that was used.

As future work, and taking into consideration the limitations and results that were achieved in the several blood flow studies, it would be valuable to implement other fluid formulations, as the Mixed Method and the Mixed Dual Method, to analyse blood, especially in three-dimensional structures. Additionally, it could be analysed in more detail the calibration of RPIM and NNRPIM parameters for fluid flow analysis. The consideration of other rheological properties, such as non-Newtonian fluids, would be advantageous when combined with realistic geometries, which approach a more accurate scenario. Lastly, the vessel wall in this thesis was considered rigid, while in reality it is hyper elastic. Taking into consideration that the blood flow affects directly the vessel wall, it would be interesting to study their interaction,

especially in aortic aneurysm scenarios, where it is proved that blood flow potentiates the aggravation of the disease.

References

[1] Y. T. Zhang, Y. L. Zheng, W. H. Lin, H. Y. Zhang, and X. L. Zhou, "Challenges and opportunities in cardiovascular health informatics," *IEEE Trans. Biomed. Eng.*, vol. 60, no. 3, pp. 633–642, 2013.

[2] N. Kontopodis, K. Tzirakis, and C. V Ioannou, "The Obsolete Maximum Diameter Criterion , the Evident Role of Biomechanical (Pressure) Indices , the New Role of Hemodynamic (Flow) Indices , and the Multi-Modal Approach to the Rupture Risk Assessment of Abdominal Aortic Aneurysms," *Ann. Vasc. Dis.*, vol. 11, no. 1, pp. 78–83, 2018.

[3] K. H. Fraser, M. Siobhan, J. R. Blake, W. J. Easson, and P. R. Hoskins, "Characterization of an abdominal aortic velocity waveform in patients with abdominal aortic aneurysm," *Ultrasound Med. Biol.*, vol. 34, no. 1, pp. 73–80, 2008.

[4] S. Shadden and C. Taylor, "Characterization of Coherent Structures in the Cardiovascular System," *Ann. Biomed. Eng.*, vol. 36, no. 7, pp. 1152–1162, 2008.

[5] R. Machado, "Contribuição para o tratamento do aneurisma da aorta abdominal. Impacto das tecnologias endovasculares," Instituto the Ciências Biomédicas Abel Salazar - Universidade do Porto, 2016.

[6] W. C. Sternbergh and S. R. Money, "Hospital cost of endovascular versus open repair of abdominal aortic aneurysms: A multicenter study," *J. Vasc. Surg.*, vol. 31, no. 2, pp. 237–244, 2000.

[7] J. T. Oden, "Historical Comments on Finite Elements," Austin, 2011.

[8] T. A. Khraishi, D. F. Elger, R. S. Budwig, and K. H. Johansen, "The effects of modeling parameters on the hemodynamics of an abdominal aortic aneurysm (AAA)," *Am. Soc. Mech. Eng.*, vol. 237, pp. 349–354, 1996.

[9] R. Baxter, N. Hastings, A. Law, and E. J. . Glass, *Applied Biofluid Mechanics*. McGraw-Hill, 2009.

[10] S. Brown, "Computational Fluid Dynamic Modeling of Aortic Blood Flow," McMaster Univerity, 2013.

[11] C. A. Taylor and J. D. Humphrey, "Open Problems in Computational Vascular Biomechanics: Hemodynamics and Arterial Wall Mechanics," *Comput. Methods Appl. to Mech. Eng.*, vol. 64, no. 12, pp. 2391–2404, 2009.

[12] L. Formaggia and A. Veneziani, *Cardiovascular Mathematics: Modeling and simulation of the circulatory system*, vol. 11, no. 3. Springer Science & Business Media, 2010.

[13] K. B. Chandran, A. P. Yoganathan, and S. E. Rittgers, *Biofluid Mechanics: The Human Circulation*. 2007.

[14] J. C. Lasheras, "The Biomechanics of Arterial Aneurysms," *Annu. Rev. Fluid Mech.*, vol. 39, no. 1, pp. 293–319, 2007.

[15] C. Caro, T. Pedley, R. Schroter, and W. Seed, *The Mechanics of the Circulation*. Cambridge University Press, 2012.

[16] P. A. Iaizzo, *Handbook of Cardiac Anatomy, Physiology, and Devices*. Humana Press, 2005.

[17] T. Poutanen, T. Tikanoja, H. Sairanen, and E. Jokinen, "Normal aortic dimensions and flow in 168 children and young adults," *Clin. Physiol. Funct. Imaging*, vol. 23, no. 4, pp. 224–229, 2003.

[18] M. K. Halushka, *Genetic Diseases of the Aorta (Including Aneurysms)*. Elsevier, 2014.

[19] J. D. Humphrey and C. A. Taylor, "Intracranial and Abdominal Aortic Aneurysms : Similarities , Differences , and Need for a New Class of Computational Models," *Annu. Rev. Biomed. Eng.*, vol. 10, pp. 221–248, 2008.

[20] A. Fortier, V. Gullapalli, and R. A. Mirshams, "Review of Biomechanical Studies of Arteries and Their Effect on Stent Performance," *Int. J. Cardiol.*, 2014.

[21] C. M. Scotti, A. D. Shkolnik, S. C. Muluk, and E. A. Finol, "Fluid-structure interaction in abdominal aortic aneurysms : effects of asymmetry and wall thickness," *BioMecial Eng. Online*, vol. 22, pp. 1–22, 2005.

[22] F. Ene, P. Delassus, and L. Morris, "The influence of computational assumptions on analysing abdominal aortic aneurysm haemodynamics," *J. Eng. Med.*, vol. 228, no. 8, pp. 768–780, 2014.

[23] F. Gao, Z. Guo, M. Watanabe, and T. Matsuzawa, “Loosely Coupled Simulation for Aortic Arch Model under Steady and Pulsatile Flow,” *J. Biomech. Sci. Eng.*, vol. 1, no. 2, pp. 327–341, 2006.
[24] Z. Domagala *et al.*, “Biomechanical factors in finite element analysis of abdominal aortic aneurysms,” *Acta Angiol.*, vol. 22, no. 4, pp. 164–171, 2016.
[25] Y. C. Fung, *Biomechanics: Mechanical Properties of Living Tissues*, Second Edi. Springer Science & Business Media, 1993.
[26] A. Javadzadegan, A. Simmons, M. Behnia, and T. Barber, “Computational modelling of abdominal aortic aneurysms: Effect of suprarenal vs infrarenal positions,” *Eur. J. Mech. B/Fluids*, vol. 61, pp. 112–124, 2017.
[27] C. Poelma, P. N. Watton, and Y. Ventikos, “Transitional flow in aneurysms and the computation of haemodynamic parameters,” 2015.
[28] T. Sochi, “Non-Newtonian Rheology in Blood Circulation,” 2013.
[29] D. A. Rubenstein, Y. Wei, and M. D. Frame, *Biofluid mechanics*, vol. 43, no. 4. Academic Press, 2012.
[30] T. V. How, *Advances in Hemodynamics and Hemorheology*, vol. 136, no. 1. Jai Press INC., 1996.
[31] P. Vasava, P. Jalali, M. Dabagh, and P. J. Kolari, “Finite Element Modelling of Pulsatile Blood Flow in Idealized Model of Human Aortic Arch : Study of Hypotension and Hypertension,” vol. 2012, 2012.
[32] J. C. Weddell, J. Kwack, P. I. Imoukhuede, and A. Masud, “Hemodynamic Analysis in an Idealized Artery Tree : Differences in Wall Shear Stress between Newtonian and Non-Newtonian Blood Models,” *Biol. Relev. Non-Newtonian Blood Model.*, pp. 1–23, 2015.
[33] M. A. Azam and S. A. A. Salam, “Three Dimensional Analysis of the Blood Flow Regime within Abdominal Aortic Aneurysm,” *IACSIT Int. J. Eng. Technol.*, vol. 3, 2011.
[34] V. L. Marrero, J. A. Tichy, O. Sahni, and K. E. Jansen, “Numerical Study of Purely Viscous Non-Newtonian Flow in an Abdominal Aortic Aneurysm,” *J. Biomech. Eng.*, vol. 136, no. 10, p. 101001, 2014.
[35] C. A. Taylor, T. J. R. Hughes, and K. Zarinsb, “Finite element modeling of blood flow in arteries,” *Comput. Methods Appl. to Mech. Eng.*, vol. 7825, no. 97, 1998.
[36] C. Kleinstreuer, *Biofluid Dynamics - Principles and Selected Applications*. Taylor & Francis Group, 2006.
[37] D. Liepsch, *Biofluid Mechanics: Blood Flow in Large Vessels*. Springer-Verlarg Berlin Heidelberg GmbH, 1990.
[38] N. Sakalihasan, R. Limet, and O. Defawe, “Abdominal aortic aneurysm,” *Lancet*, vol. 365, no. 9470, pp. 1577–1589, 2005.
[39] Z. Domagala *et al.*, “Biomechanical factors in finite element analysis of abdominal aortic aneurysms,” *Acta Angiol.*, vol. 22, no. 4, pp. 164–171, 2016.
[40] O. Tanweer, T. A. Wilson, E. Metaxa, H. A. Riina, and H. Meng, “A Comparative Review of the Hemodynamics and Pathogenesis of Cerebral and Abdominal Aortic Aneurysms : Lessons to Learn From Each Other,” *J. Cerebrovasc. Endovasc. Neurosurg.*, vol. 16, no. 4, pp. 335–349, 2014.
[41] D. Farotto, P. Segers, B. Meuris, J. Vander Sloten, and N. Famaey, “The role of biomechanics in aortic aneurysm management: requirements, open problems and future prospects,” *J. Mech. Behav. Biomed. Mater.*, vol. 77, no. April 2017, pp. 295–307, 2018.
[42] A. Task *et al.*, “2014 ESC Guidelines on the diagnosis and treatment of aortic diseases,” *Eur. Heart J.*, vol. 35, no. 41, pp. 2873–2926, 2014.
[43] E. Choke *et al.*, “A review of biological factors implicated in abdominal aortic aneurysm rupture,” *Eur. J. Vasc. Endovasc. Surg.*, vol. 30, no. 3, pp. 227–244, 2005.
[44] I. M. Nordon, R. J. Hinchliffe, I. M. Loftus, and M. M. Thompson, “Pathophysiology and epidemiology of abdominal aortic aneurysms,” *Nat. Publ. Gr.*, vol. 8, no. 2, pp. 92–102, 2010.
[45] C. M. He and M. R. Roach, “The composition and mechanical properties of abdominal aortic aneurysms,” *J. Vasc. Surg.*, vol. 20, no. 1, pp. 6–13, Jul. 1994.
[46] P. Di Achille, G. Tellides, C. A. Figueroa, and J. D. Humphrey, “A haemodynamic predictor of intraluminal thrombus formation in abdominal aortic aneurysms,” *Proc. R. Soc. A Math. Phys. Eng. Sci.*, vol. 470, no. 2172, 2014.
[47] P. D. A. G. Tellides and J. D. Humphrey, “Hemodynamics - driven deposition of intraluminal thrombus in abdominal aortic aneurysms,” *Int. J. Numer. Methods Biomed. Eng.*, no. August, pp. 1–17, 2016.

[48] E. Metaxa, K. Tzirakis, N. Kontopodis, C. V. Ioannou, and Y. Papaharilaou, “Correlation of Intraluminal Thrombus Deposition, Biomechanics, and Hemodynamics with Surface Growth and Rupture in Abdominal Aortic Aneurysm—Application in a Clinical Paradigm,” *Ann. Vasc. Surg.*, vol. 46, no. September 2017, pp. 357–366, 2018.
[49] F. Joly, G. Soulez, D. Garcia, S. Lessard, and C. Kauffmann, “Flow stagnation volume and abdominal aortic aneurysm growth : Insights from patient-speci fi c computational fl ow dynamics of Lagrangian-coherent structures,” *Comput. Biol. Med.*, vol. 92, no. May 2017, pp. 98–109, 2018.
[50] W. R. Mower, Q. W. J., and S. S. Gambhir, “Effect of Intraluminal Thrombus on Local Abdominal Aortic Aneurysm Wall Strength,” *Proc. first Jt. BMES/EMBS Conf.*, vol. 27, no. 4, p. 244, 1997.
[51] S. J. Haller *et al.*, “Intraluminal thrombus is associated with early rupture of abdominal aortic aneurysm,” *J. Vasc. Surg.*, vol. 67, no. 4, p. 1051–1058.e1, 2017.
[52] M. Lindquist Liljeqvist, R. Hultgren, A. Siika, T. C. Gasser, and J. Roy, “Gender, smoking, body size, and aneurysm geometry influence the biomechanical rupture risk of abdominal aortic aneurysms as estimated by finite element analysis,” *J. Vasc. Surg.*, vol. 65, no. 4, pp. 1014–1021, 2017.
[53] SNS, “Rede De Referenciação Hospitalar - Angiologia e Cirurgia Vascular,” 2017.
[54] F. A. Lederle, “Ultrasonographic Screening for Abdominal Aortic Aneurysms,” *Ann. Intern. Med.*, vol. 139, no. 6, 2003.
[55] J. A. Spittell, “Hypertension and arterial aneurysm,” *J. Am. Coll. Cardiol.*, vol. 1, no. 2, pp. 533–540, 1983.
[56] S. Glagov, C. Zarins, D. Giddens, and D. Ku, “Hemodynamics and Atherosclerosis,” *Arch. Pathol. Lab. Med.*, vol. 112, pp. 1018–1031, 1988.
[57] F. Carneiro, V. G. Ribeiro, and J. C. F. Teixeira, “Numerical study of blood fluid rheology in the abdominal aorta,” *WIT Trans. Ecol. Environ.*, vol. 114, pp. 169–178, 2008.
[58] A. J. Boyd, D. C. S. Kuhn, R. J. Lozowy, and G. P. Kulbisky, “Low wall shear stress predominates at sites of abdominal aortic aneurysm rupture,” *J. Vasc. Surg.*, vol. 63, no. 6, pp. 1613–1619, 2016.
[59] C. J. Drewe, L. P. Parker, L. J. Kelsey, P. E. Norman, J. T. Powell, and B. J. Doyle, “Haemodynamics and stresses in abdominal aortic aneurysms: A fluid-structure interaction study into the effect of proximal neck and iliac bifurcation angle,” *J. Biomech.*, vol. 60, pp. 150–156, 2017.
[60] D. Hardman, S. I. Semple, J. M. J. Richards, and P. R. Hoskins, “Comparison of patient-specific inlet boundary conditions in the numerical modelling of blood flow in abdominal aortic aneurysm disease,” *Int. j. numer. method. biomed. eng.*, vol. 29, no. December 2012, pp. 165–178, 2013.
[61] R. Castro-Ferreira, M. Neiva-Sousa, S. Sampaio, P. Gonçalves Dias, A. da Costa-Pereira, and A. Freitas, “Dez anos de tratamento de aneurismas da aorta abdominal – exclusão endovascular vs. cirurgia aberta nas diferentes regiões portuguesas,” *Angiol. e Cir. Vasc.*, vol. 11, no. 2, pp. 51–60, 2015.
[62] T. Carrel, “Composite Graft Replacement of the Aortic Root, Ascending Aorta, and Proximal Aortic Arch,” *CTS net*, 2015. [Online]. Available: https://www.ctsnet.org/article/composite-graft-replacement-aortic-root-ascending-aorta-and-proximal-aortic-arch. [Accessed: 10-Dec-2018].
[63] “Dartmouth-Hitchcock,” 2018. [Online]. Available: https://www.dartmouth-hitchcock.org/stories/article/33150. [Accessed: 10-Dec-2018].
[64] U. Benedetto, X. Jin, E. Hill, T. Treasure, and M. Petrou, “An Option for Concomitant Management of Moderate Marfan Root Aneurysm at the Time of Mitral Valve Repair: A Role for Personalized External Aortic Root Support,” *Ann. Thorac. Surg.*, vol. 102, pp. 499–501, 2016.
[65] S. Karimi, M. Dabagh, P. Vasava, M. Dadvar, B. Dabir, and P. Jalali, “Effect of rheological models on the hemodynamics within human aorta : CFD study on CT image-based geometry,” *J. Nonnewton. Fluid Mech.*, vol. 207, pp. 42–52, 2014.
[66] Y. I. Cho and K. R. Kensey, “Effects of the non-Newtonian viscosity of blood on flows in a diseased arterial vessel. Part 1: Steady flows,” *Biorheology*, vol. 28, no. 3–4, pp. 241–262, 1991.
[67] C. E. Huckaba and A. W. Hahn, “A Generalized Approach to the Modelinf of Arterial Blood Flow,” *Bull. Math. Biophys.*, vol. 30, 1968.
[68] K. Perktold and G. Rappitsch, “Computer simulation of local blood flow and vessel

mechanics in a compliant carotid artery bifurcation model," *J. Biomech.*, vol. 28, no. 7, pp. 845–856, 1995.
[69] S. Shibeshi and W. Collins, "The rheology of blood flow in a branched arterial system," *Appl. Rheol.*, vol. 15, no. 6, pp. 398–405, 2005.
[70] B. J. B. M. Wolters, M. C. M. Rutten, G. W. H. Schurink, U. Kose, J. De Hart, and F. N. Van De Vosse, "A patient-specific computational model of fluid – structure interaction in abdominal aortic aneurysms," *Med. Eng. Phys.*, vol. 27, pp. 871–883, 2005.
[71] T. Guerra, C. Catarino, T. Mestre, S. Santos, J. Tiago, and A. Sequeira, "A data assimilation approach for non-Newtonian blood flow simulations in 3D geometries," *Appl. Mathemtics Comput.*, vol. 321, pp. 176–194, 2018.
[72] A. D. Caballero and S. Laín, "Computer Methods in Biomechanics and Biomedical Engineering Numerical simulation of non-Newtonian blood flow dynamics in human thoracic aorta," *Computer Methods in Biomechanics and Biomedical Engineering*, vol. 18, no. 11. Taylor & Francis, p. 11, 2015.
[73] J. J. Connor and C. A. Brebbia, *Finite Element Techniques for Fluid Flow*. Newnes-Butterworths, 1976.
[74] A. Huerta and J. Donea, *Finite Element Methods for Flow Problems*. Wiley & Sons, 2003.
[75] G. R. Liu, G. Y. Zhang, Y. T. Gu, and Y. Y. Wang, "A meshfree radial point interpolation method (RPIM) for three-dimensional solids," *Comput. Mech.*, vol. 36, no. 6, pp. 421–430, 2005.
[76] J. Belinha, *Meshless Methods in Biomechanics - Bone Tissue Remodelling Analysis*. Springer, 2012.
[77] J. Belinha, L. M. J. S. Dinis, and R. M. Natal Jorge, "The analysis of the bone remodelling around femoral stems: A meshless approach," *Math. Comput. Simul.*, vol. 121, pp. 64–94, 2016.
[78] L. M. J. S. Dinis, R. M. Natal Jorge, and J. Belinha, "Analysis of 3D solids using the natural neighbour radial point interpolation method," *Comput. Methods Appl. Mech. Eng.*, vol. 196, no. 13–16, pp. 2009–2028, 2007.
[79] R. L. Hardy, "Multiquadric equations of topography and other irregular surfaces," *J. Geophys. Res.*, vol. 76, no. 8, pp. 1905–1915, 1971.
[80] O. C. Zienkiewicz, E. Oñae, and J. C. Heinrich, "A general formulation for coupled thermal flow of metals using finite elements," *Int. J. Numer. Methods Eng.*, vol. 17, no. 10, pp. 1497–1514, 1981.
[81] O. C. Zienkiewicz, Y. C. Liu, and G. C. Huang, "Error estimation and adaptivity in formulation for forming problems," *Int. J. Numer. Methods Eng.*, vol. 25, pp. 23–42, 1988.
[82] P. K. C. Wong, K. Wayne Johnston, C. Ross Ethier, and R. S. C. Cobbold, "Computer simulation of blood flow patterns in arteries of various geometries," *J. Vasc. Surg.*, vol. 14, no. 5, pp. 658–667, 1991.
[83] P. D. Stein and H. N. Sabbah, "Turbulent blood-flow in the ascending aorta of humans with normal and diseased aortic valves," *Circ. Res.*, pp. 58–65, 1976.
[84] P. A. Stonebridge and C. M. Brophy, "Spiral laminar-flow in arteries.," *Lancet*, vol. 338, pp. 1360–1361, 1991.
[85] V. Thomée, "From finite differences to finite elements," *J. Comput. Appl. Math.*, vol. 128, no. 1–2, pp. 1–54, 2001.
[86] J. Blazek, "Principles of Solution of the Governing Equations," in *Computational Fluid Dynamics: Principles and Applications*, 2005, pp. 29–75.
[87] H. K. . Versteeg and W. . Malalasekera, *An Introduction to Computational Fluid Dynamics - The Finite Volume Method*. 2007.
[88] P. W. McDonald, "The Computation of Transonic Flow Through Two-Dimensional Gas Turbine Cascades," *ASME 1971 Int. Gas Turbine Conf. Prod. Show*, p. V001T01A089, 1971.
[89] O. Pironneau, *Finite Element Methods for Fluids*. Wiley, 1988.
[90] M. J. Turner, R. W. Clough, H. C. Martin, and L. J. Topp, "Stiffness and Deflection Analysis of Complex Structures," *J. Aeronaut. Sci.*, vol. 23, pp. 805–824, 1956.
[91] R. W. Clough, "The finite element method in plane stress analysis," *Proc. Second ASCE Conf. Electron. Comput.*, vol. 8, pp. 345–378, 1960.
[92] M. M. Stringfellow, P. F. Lawrence, and R. G. Stringfellow, "The influence of aorta-aneurysm geometry upon stress in the aneurysm wall," *J. Surg. Res.*, vol. 42, no. 4, pp. 425–433, 1987.

[93] F. Inzoli, F. Boschetti, M. Zappa, T. Longo, and R. Fumero, “Biomechanical factors in abdominal aortic aneurysm rupture,” *Eur. J. Vasc. Surg.*, vol. 7, no. 6, pp. 667–674, Nov. 1993.
[94] M. van ’t Veer *et al.*, “Biomechanical properties of abdominal aortic aneurysms assessed by simultaneously measured pressure and volume changes in humans,” *J. Vasc. Surg.*, vol. 48, no. 6, pp. 1401–1407, 2008.
[95] N. Davids, “A unified numerical analysis method for calculating dynamic wall-stress effects in pulsatile flow,” *Comput. Biol. Med.*, vol. 1, no. 1, pp. 51–58, 1970.
[96] C. G. Caro, J. M. Fitz-Gerald, and R. C. Schroter, “Atheroma and Arterial Wall Shear Observation, Correlation and Proposal of a Shear Dependent Mass Transfer Mechanism for Atherogenesis: Appendix,” *Proc. R. Soc. B Biol. Sci.*, vol. 177, no. 1046, pp. 133–159, 1971.
[97] C. A. Taylor, T. J. R. Hughes, and C. K. Zarins, “Computational Investigations in Vascular Disease,” *Comput. Phys.*, vol. 10, no. 3, p. 224, 1996.
[98] J. A. Moore, D. A. Steinman, and C. R. Ethier, “Computational blood flow modelling: Errors associated with reconstructing finite element models from magnetic resonance images,” *J. Biomech.*, vol. 31, no. 2, pp. 179–184, 1997.
[99] D. Pless, D. T. Boll, T. R. Fleiter, R. Scharrer-Pamler, and H.-J. Brambs, “Multislice CT and Computational Fluid Dynamics: a new technique to visualize, analyze and simulate hemodynamics in aortic aneurysms and stentgrafts,” *Stud. Health Technol. Inform.*, vol. 81, pp. 393–395, 2001.
[100] B. M. J. Lighthill, “Physiological fluid dynamics : a survey,” *J. Fluid Mech.*, vol. 52, pp. 475–497, 1972.
[101] E. Oñate, O. C. Zienkiewics, S. Idelsohnl, and C. Sacco, “A finite point method in computational mechanics applications to convective transport and fluid flow,” *Int. J. Numer. Methods Eng.*, vol. 39, no. 1995, pp. 3839–3866, 1996.
[102] S. D. Daxini and J. M. Prajapati, “A review on recent contribution of meshfree methods to structure and fracture mechanics applications,” *Sci. World J.*, vol. 2014, 2014.
[103] E. Oñate, O. C. Zienkiewics, S. Idelsohnl, and C. Sacco, “A stabilized finite point method for analysis of fluid mechanics problems,” *Comput. Methods Appl. to Mech. Eng.*, vol. 139, pp. 315–346, 1996.
[104] N. Sukumar, B. Moran, and T. Belytschko, “The natural element method in solid mechanics,” *Int. J. Numer. Methods Eng.*, vol. 43, no. 5, pp. 839–887, 1998.
[105] G. Wang and G. R. Liu, “A point interpolation method for two dimensional solids,” *Int. J. Numer. Methods Eng.*, vol. 50, no. 4, pp. 937–951, 2001.
[106] J. G. Wang and G. R. Liu, “A point interpolation meshless method based on radial basis functions,” *Int. J. Numer. Methods Eng.*, vol. 54, no. 11, pp. 1623–1648, 2002.
[107] N. Calvo, F. Del Pin, S. R. Idelsohn, and O. Eugenio, “The meshless finite element method,” *Int. J. Numer. Methods Eng.*, vol. 58, pp. 893–912, 2003.
[108] Z. El Zahab, E. A. Divo, A. J. Kassab, and E. A. Mitteff, “Two-Dimensional Meshless Numerical Modeling of the Blood Flow Within Arterial End-to-Side Distal Anastomoses,” *ASME IEMCE2006*, pp. 1–9, 2006.
[109] Y.-P. Chui and P.-A. Heng, “A meshless rheological model for blood-vessel interaction in endovascular simulation,” *Veterinarian*, vol. 103, pp. 252–261, 2010.
[110] M. Al-Saad, S. Kulasegaram, and S. P. A. Bordas, “Blood Flow Simulation Using Smoothed Particle Hydrodynamics,” *Proc. VII Eur. Congr. Comput. Methods Appl. Sci. Eng. (ECCOMAS Congr. 2016)*, no. June, pp. 8241–8246, 2016.
[111] H. Kahraman *et al.*, “The Diameters of the Aorta and Its Major Branches in Patients with Isolated Coronary Artery Ectasia,” pp. 463–468, 2006.
[112] W. Johnson, “Recent developments concerning Saint-Venant ’ s principle : A second update,” *Appl. Mech. Rev.*, vol. 49, no. 10, pp. 101–111, 1996.

Appendix

1. Non-structured mesh

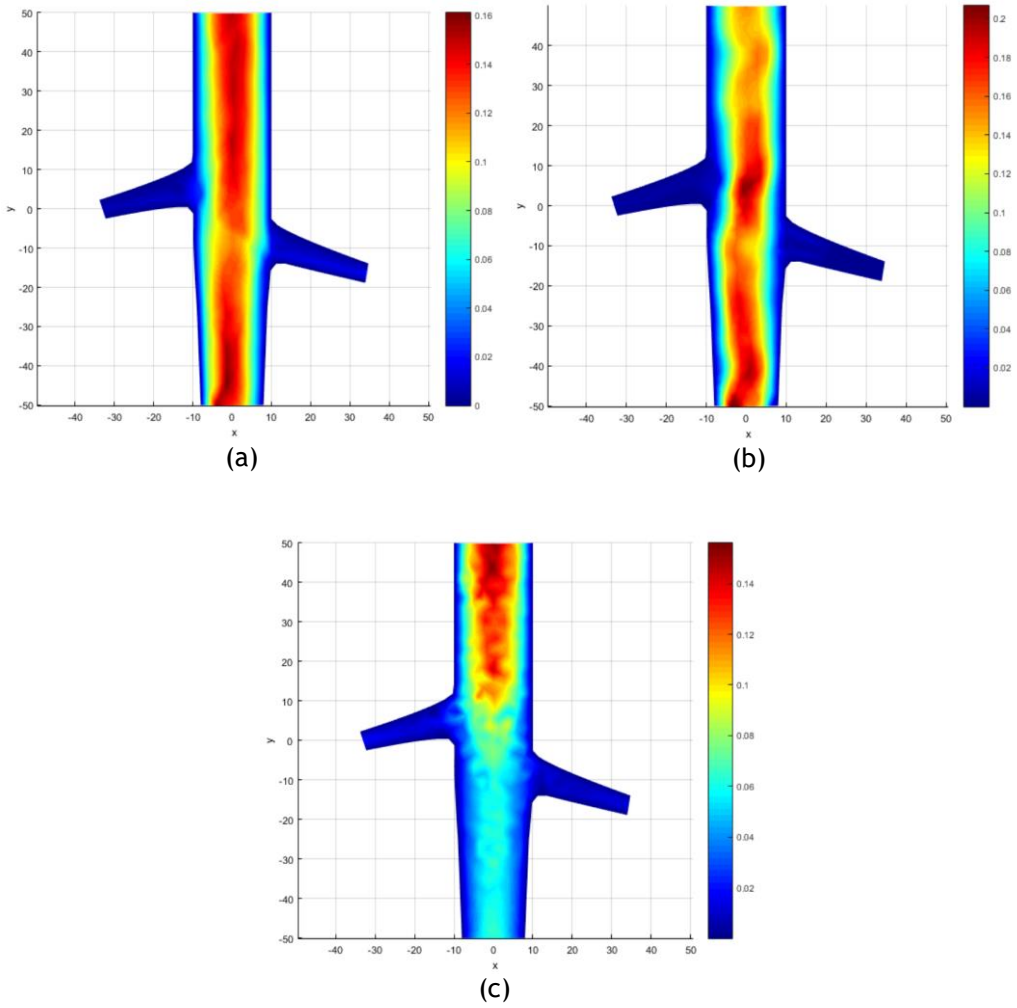

Figure A. 1 - Colour dispersion maps of the blood velocity in the branched model with 499 nodes using: (a) FEM (colour bar up to 0.1611 mm/ms), (b) RPIM (colour bar up to 0.2066 mm/ms) and (c) NNRPIM (colour bar up to 0.1560 mm/ms).

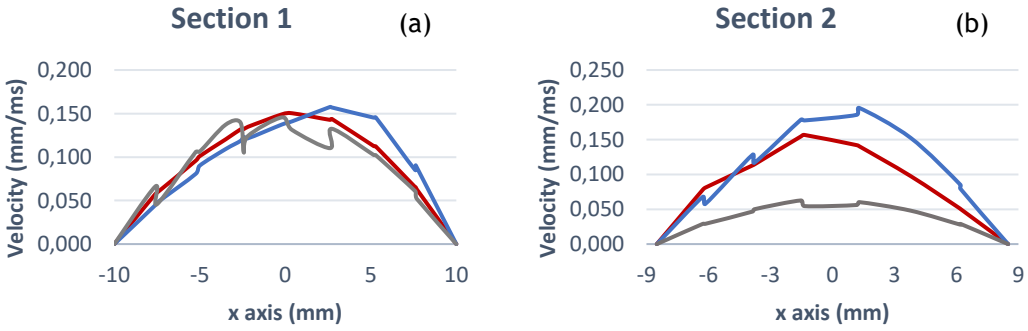

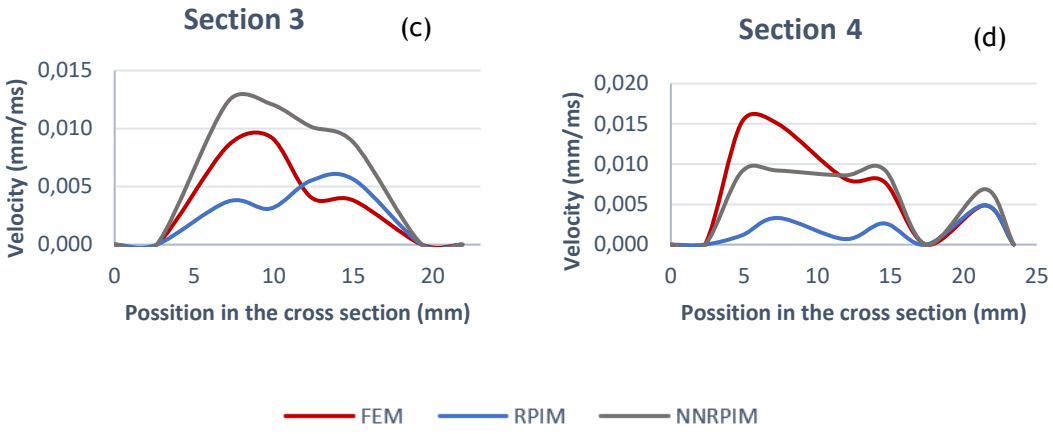

Figure A. 2 - Velocity profiles of the blood flow in: (a) section 1; (b) section 2; (c) section 3 and (d) section 4. These results were obtained from the geometrical model with 599 nodes, using FEM, RPIM and NNRPIM.

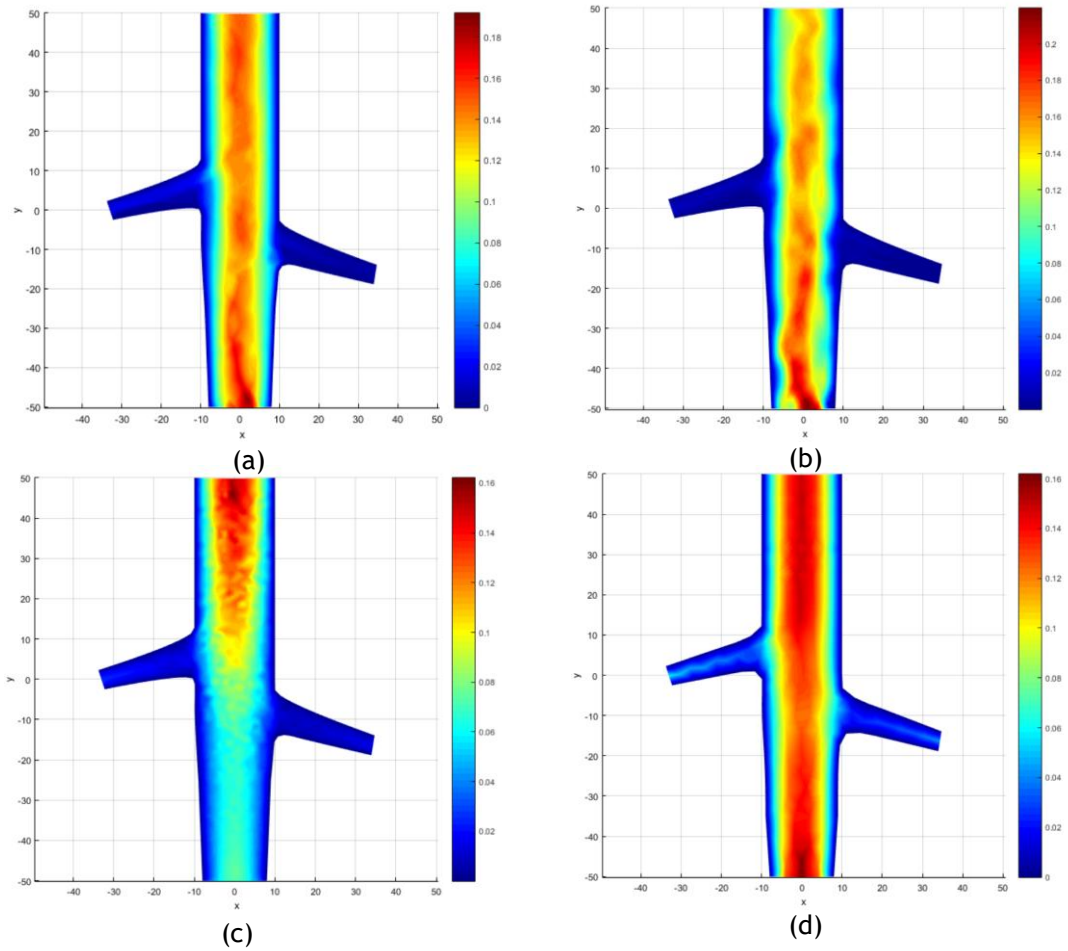

Figure A. 3 - Colour dispersion maps of the blood velocity in the branched model with 1013 nodes using: (a) FEM (colour bar up to 0.1916 mm/ms), (b) RPIM (colour bar up to 0.2194 mm/ms), (c) NNRPIM (colour bar up to 0.1618 mm/ms) and (d) FEM 6 nodes (colour bar up to 0.1618 mm/ms).

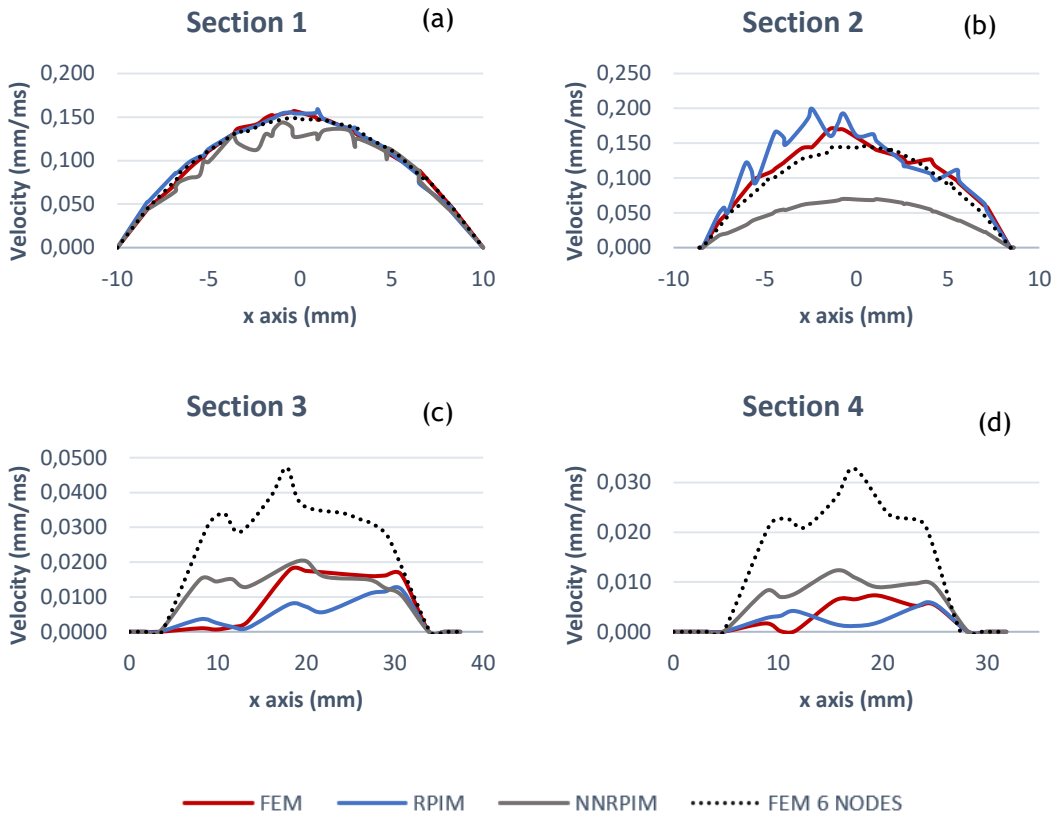

Figure A. 4 - Velocity profiles of the blood flow in: (a) section 1; (b) section 2; (c) section 3 and (d) section 4. These results were obtained from the geometrical model with 1013 nodes, using FEM, RPIM, NNRPIM and FEM 6 nodes.

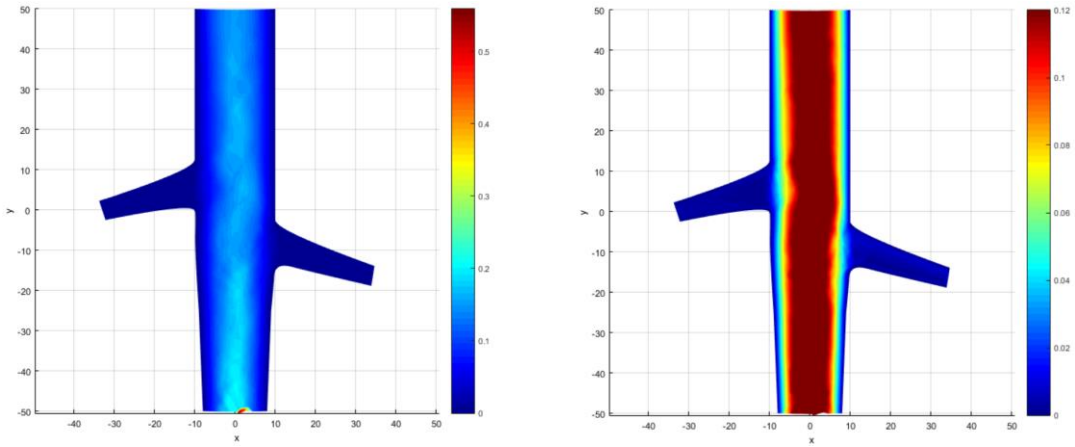

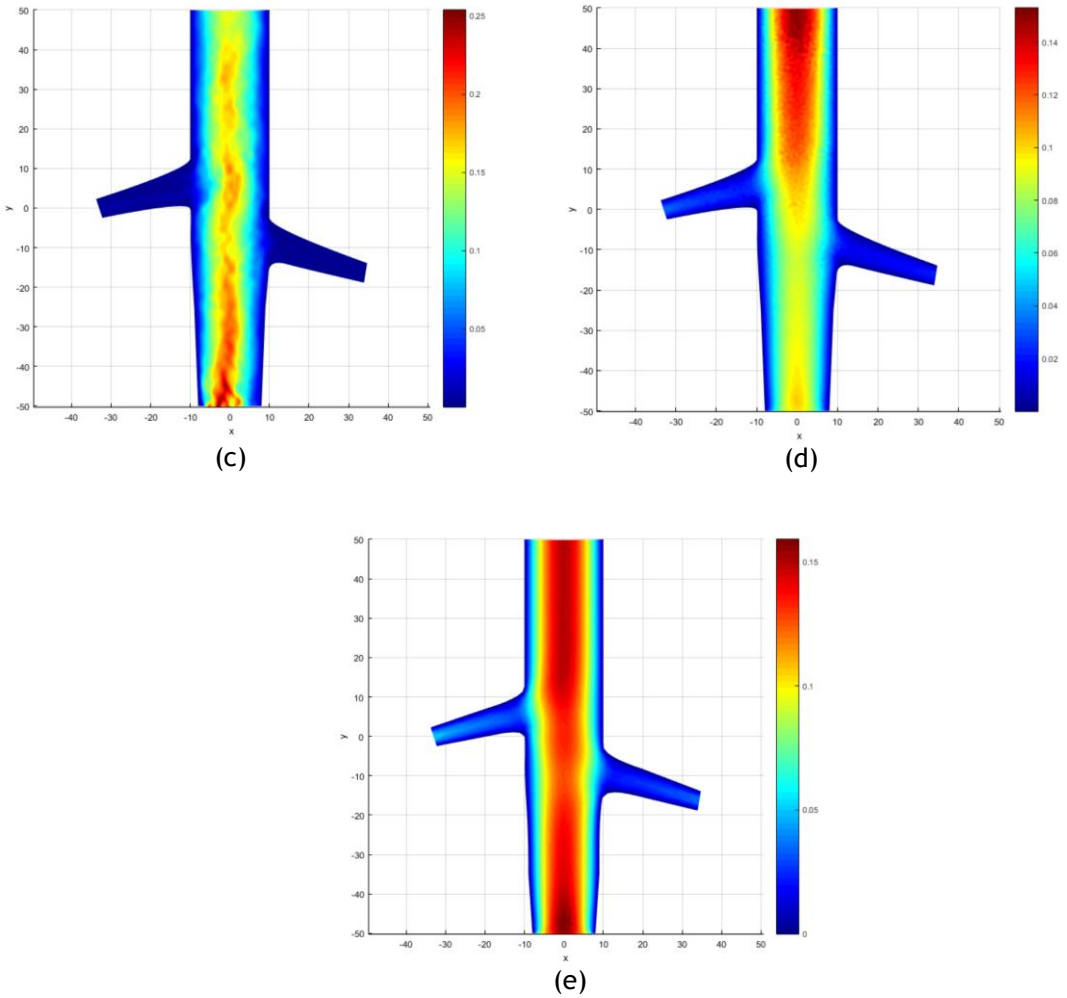

Figure A. 5 - Colour dispersion maps of the blood velocity in the branched model with 4009 nodes using: (a) FEM (colour bar up to 0.5587 mm/ms), (b) FEM saturated at 0.12 mm/ms; (c) RPIM (colour bar up to 0.2536 mm/ms), (d) NNRPIM (colour bar up to 0.1529 mm/ms) and (e) FEM 6 nodes (colour bar up to 0.1592 mm/ms).

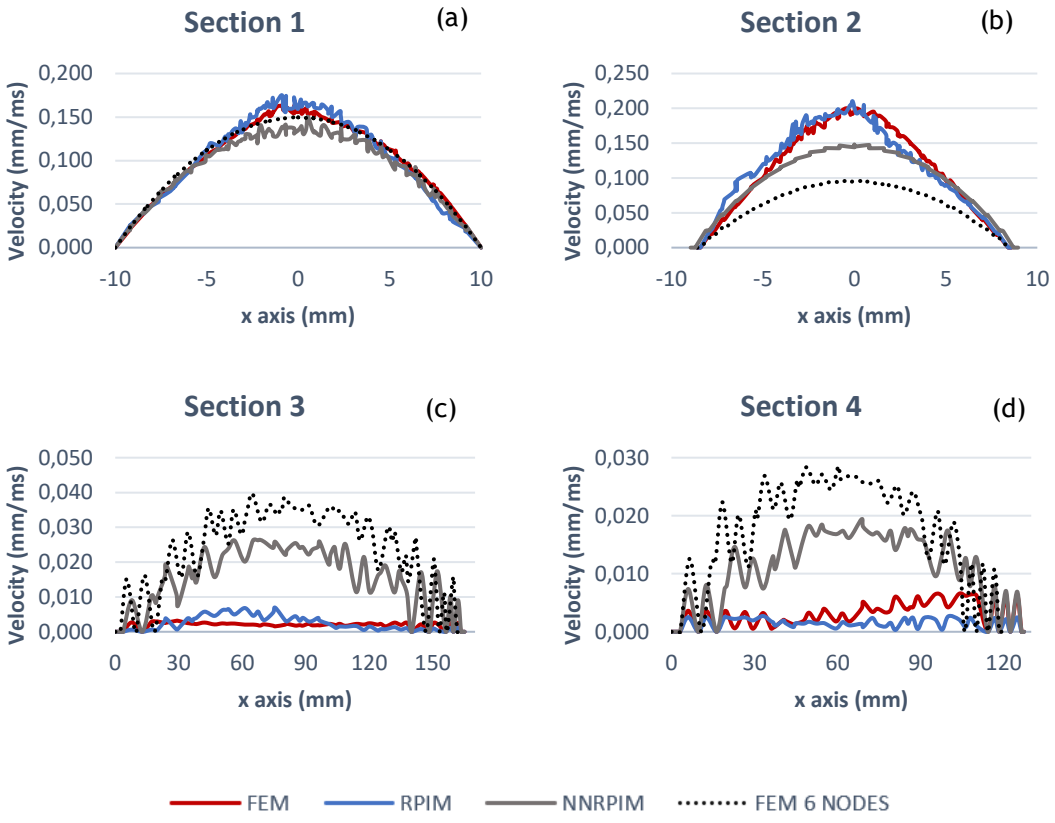

Figure A. 6 - Velocity profiles of the blood flow in: (a) section 1; (b) section 2; (c) section 3 and (d) section 4. These results were obtained from the geometrical model with 4009 nodes, using FEM, RPIM, NNRPIM and FEM 6 nodes.

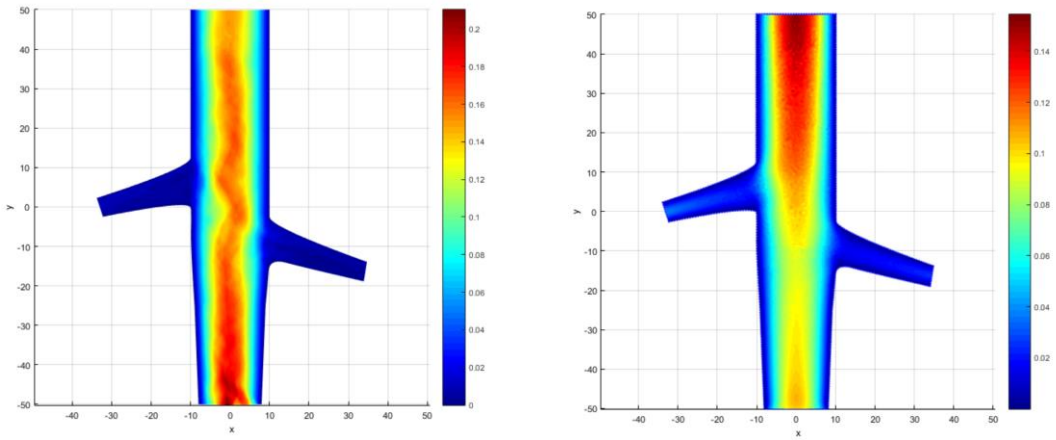

(a) (b)

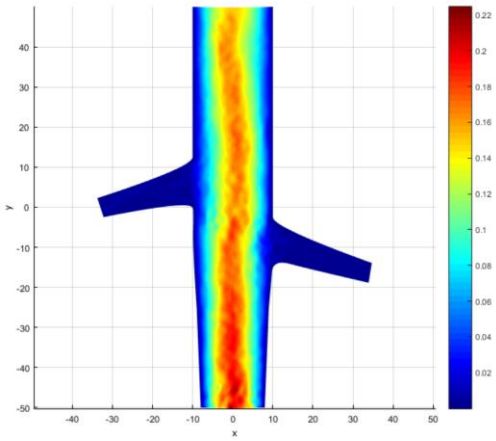

Figure A. 7 - Colour dispersion maps of the blood velocity in the branched model with 6038 nodes using: (a) FEM (colour bar up to 0.2102 mm/ms), (b) RPIM (colour bar up to 0.2245 mm/ms) and (c) NNRPIM (colour bar up to 0.1544 mm/ms).

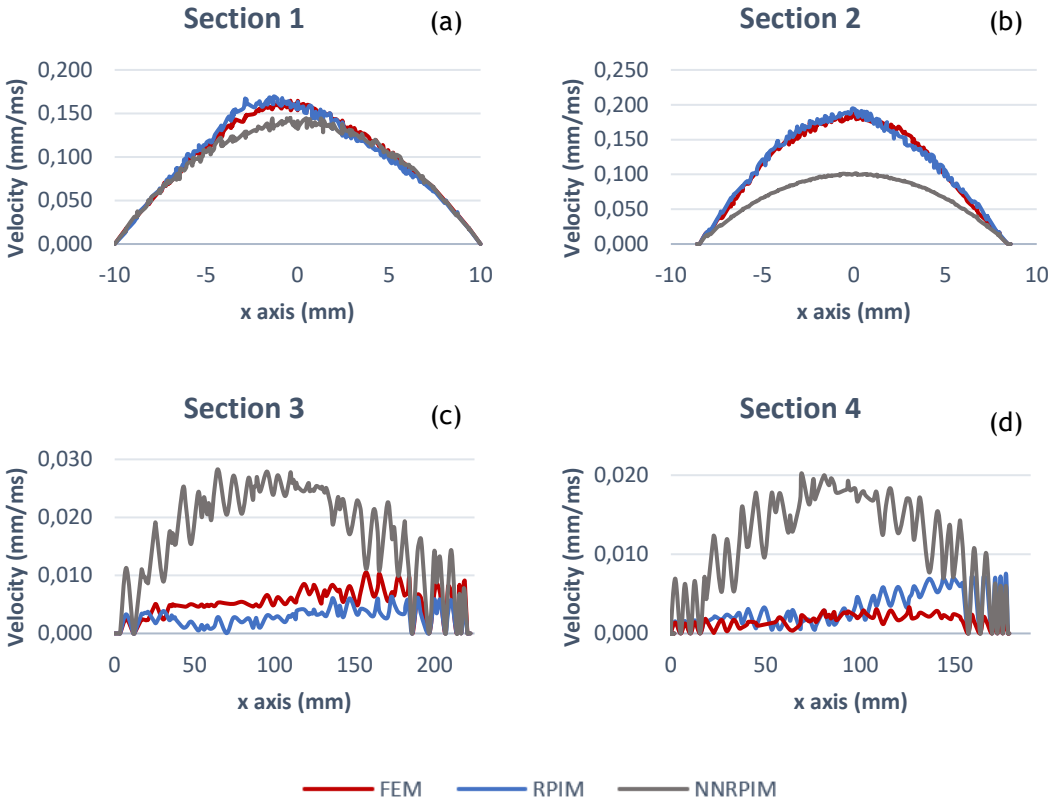

Figure A. 8 - Velocity profiles of the blood flow in: (a) section 1; (b) section 2; (c) section 3 and (d) section 4. These results were obtained from the geometrical model with 6038 nodes, using FEM, RPIM and NNRPIM.

2. Semi-structured mesh

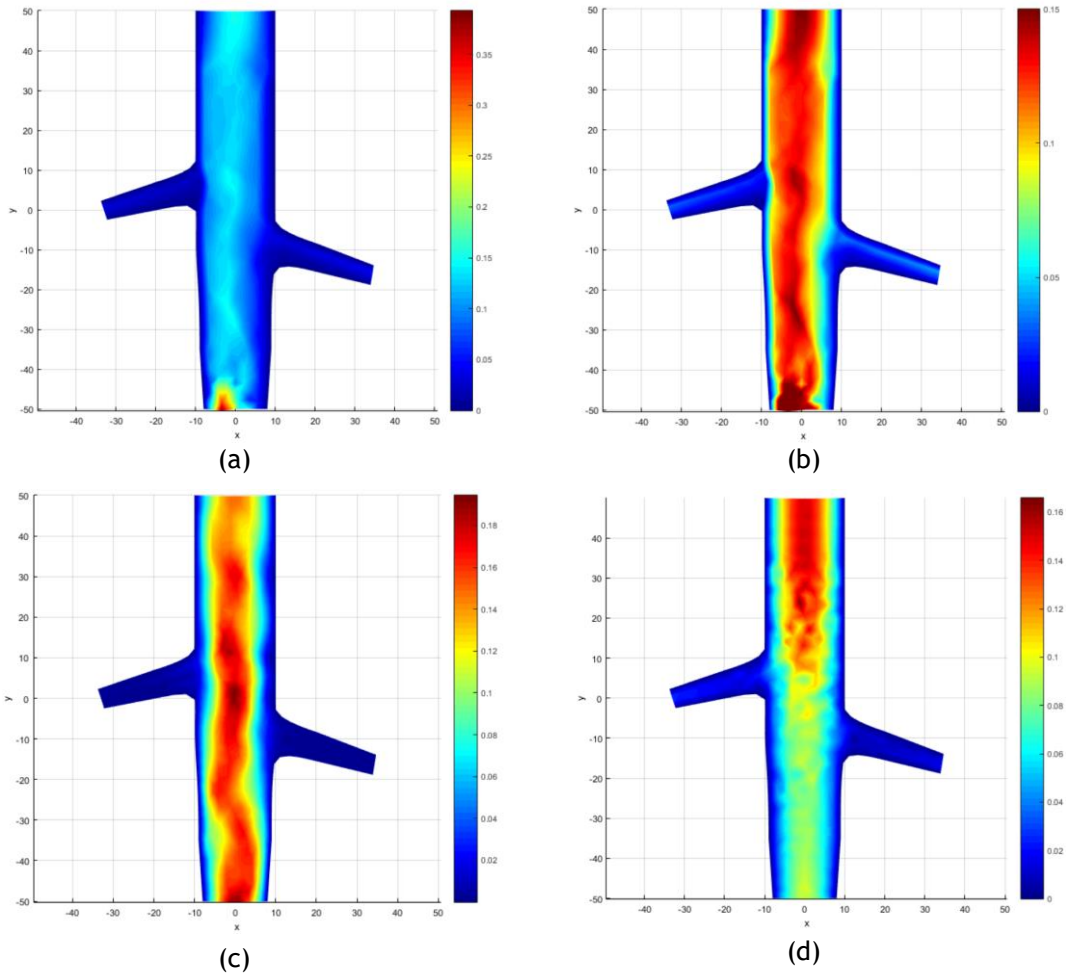

Figure A. 9 - Colour dispersion maps of the blood velocity in the branched model with 510 nodes using: (a) FEM (colour bar up to 0.3928 mm/ms), (b) FEM saturated at 0.15 mm/ms; (c) RPIM (colour bar up to 0.1944 mm/ms) and (d) NNRPIM (colour bar up to 0.1659 mm/ms).

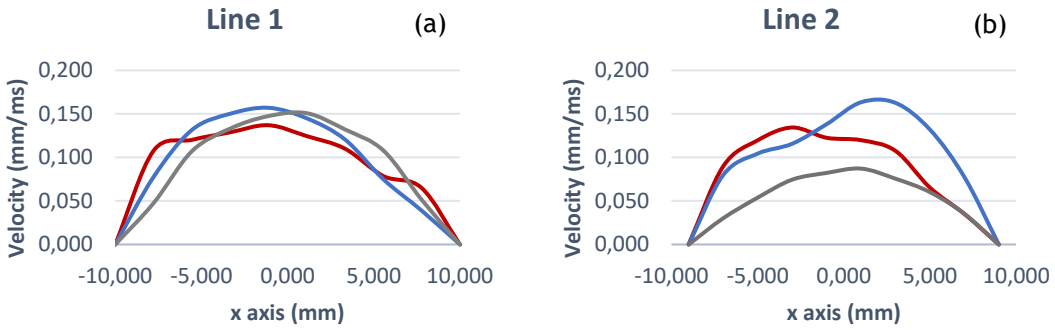

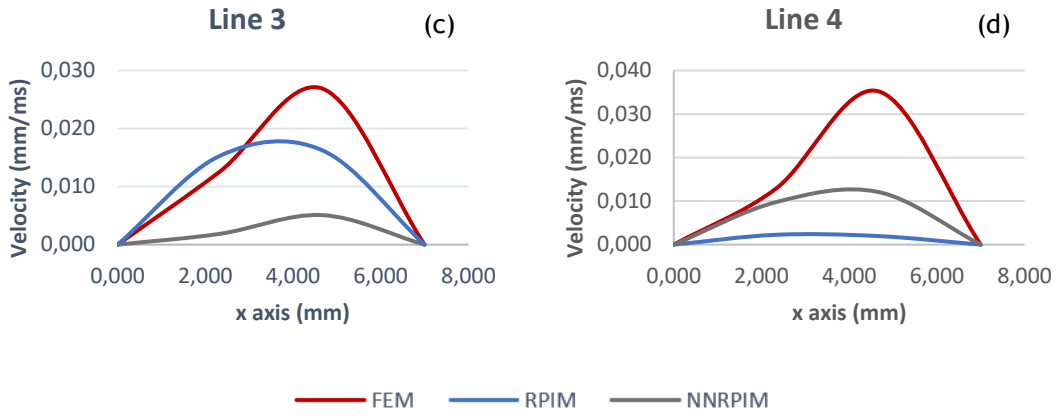

Figure A. 10 - Velocity profiles of the blood flow in: (a) section 1; (b) section 2; (c) section 3 and (d) section 4. These results were obtained from the geometrical model with 510 nodes, using FEM, RPIM and NNRPIM.

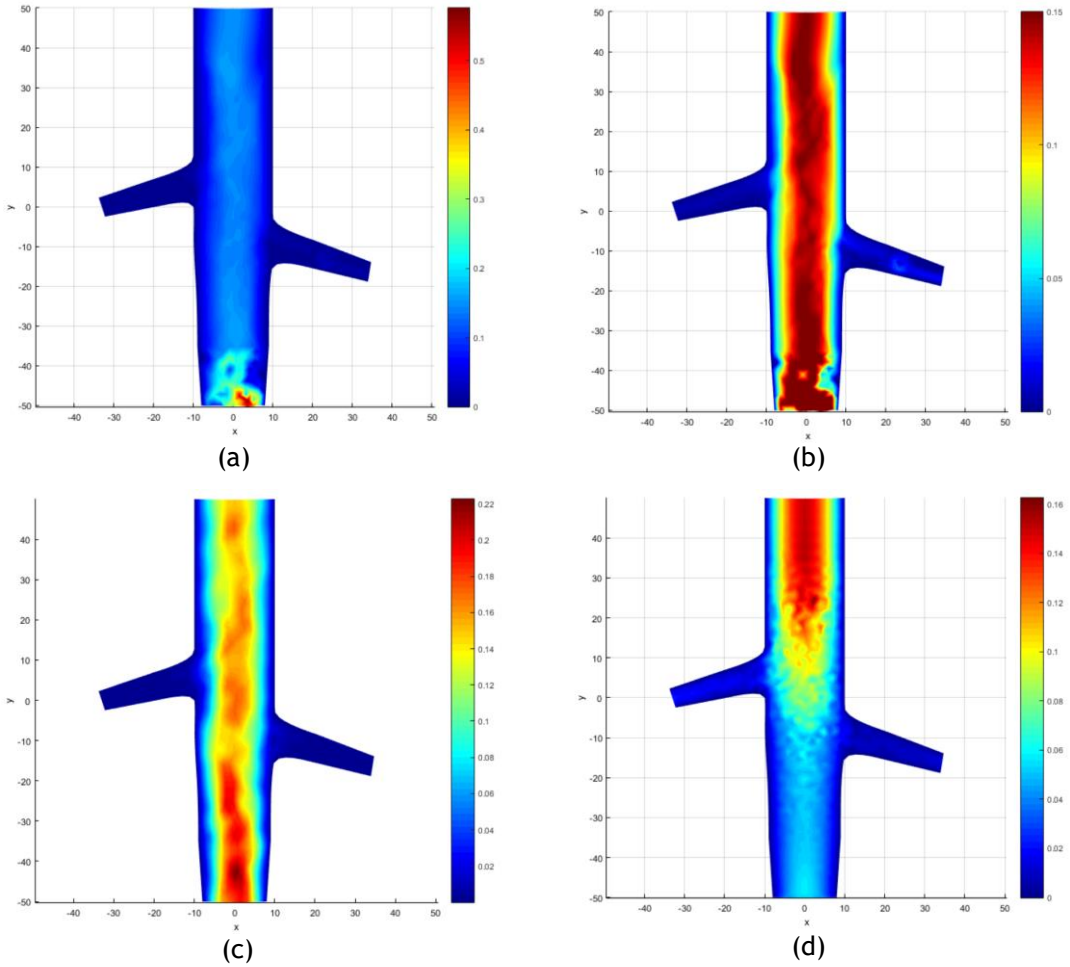

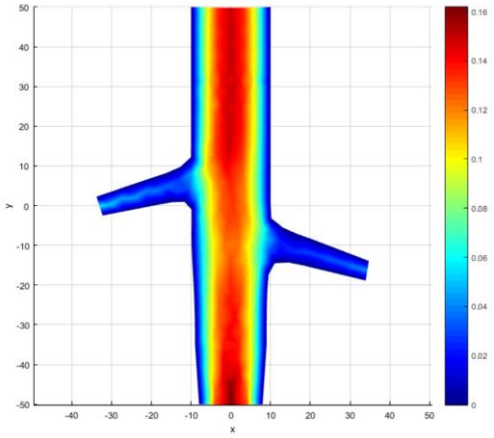

(e)

Figure A. 11 - Colour dispersion maps of the blood velocity in the branched model with 1010 nodes using: (a) FEM (colour bar up to 0.5757 mm/ms), (b) FEM saturated at 0.15 mm/ms; (c) RPIM (colour bar up to 0.2226 mm/ms), (d) NNRPIM (colour bar up to 0.1626 mm/ms) and (e) FEM 6 nodes (colour bar up to 0.1618 mm/ms).

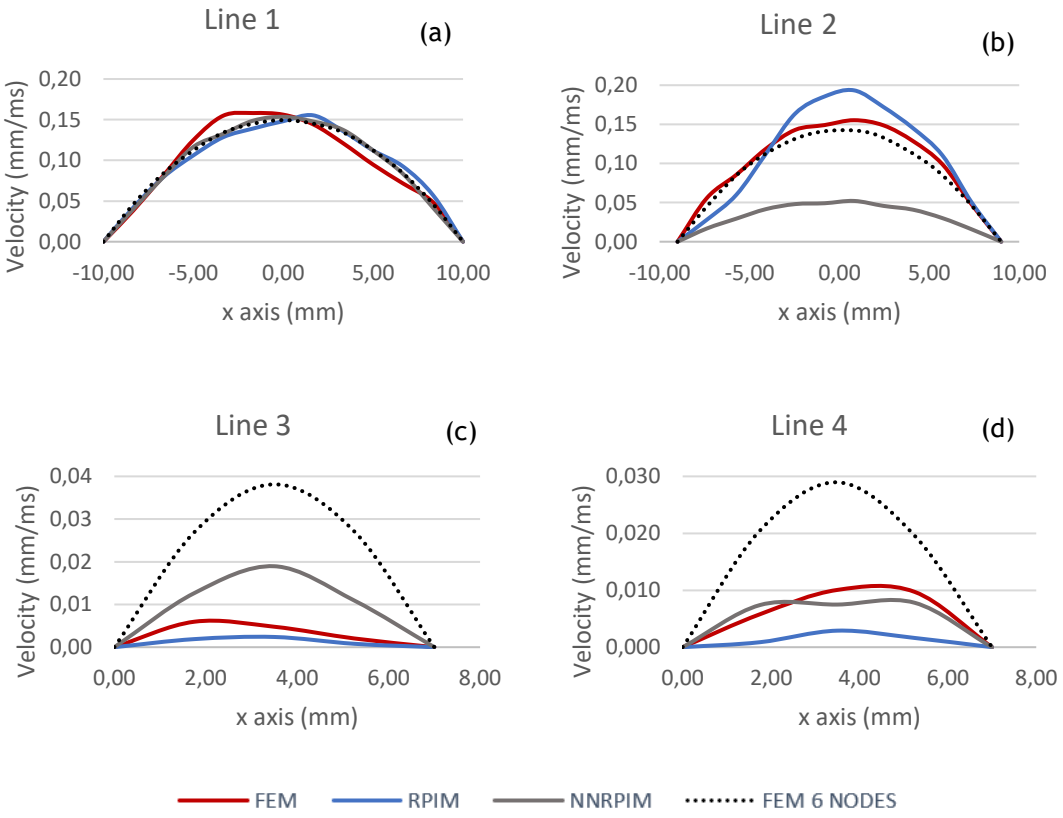

Figure A. 12 - Velocity profiles of the blood flow in: (a) section 1; (b) section 2; (c) section 3 and (d) section 4. These results were obtained from the geometrical model with 1010 nodes, using FEM, RPIM, NNRPIM and FEM 6 nodes.

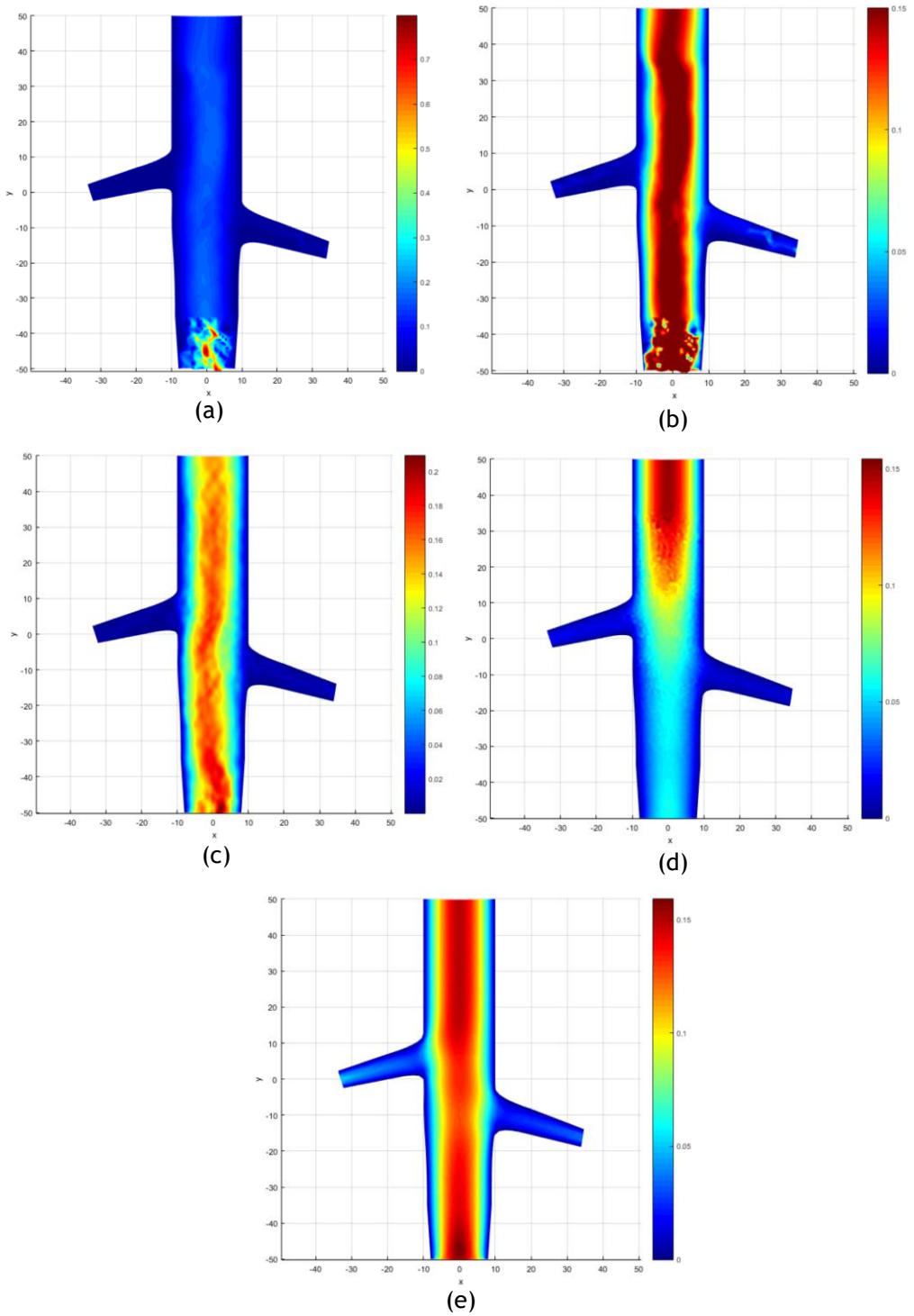

Figure A. 13 - Colour dispersion maps of the blood velocity in the branched model with 4026 nodes using: (a) FEM (colour bar up to 0.7981 mm/ms), (b) FEM saturated at 0.15 mm/ms; (c) RPIM (colour bar up to 0.2093 mm/ms), (d) NNRPIM (colour bar up to 0.1541 mm/ms) and (e) FEM 6 nodes (colour bar up to 0.1592 mm/ms).

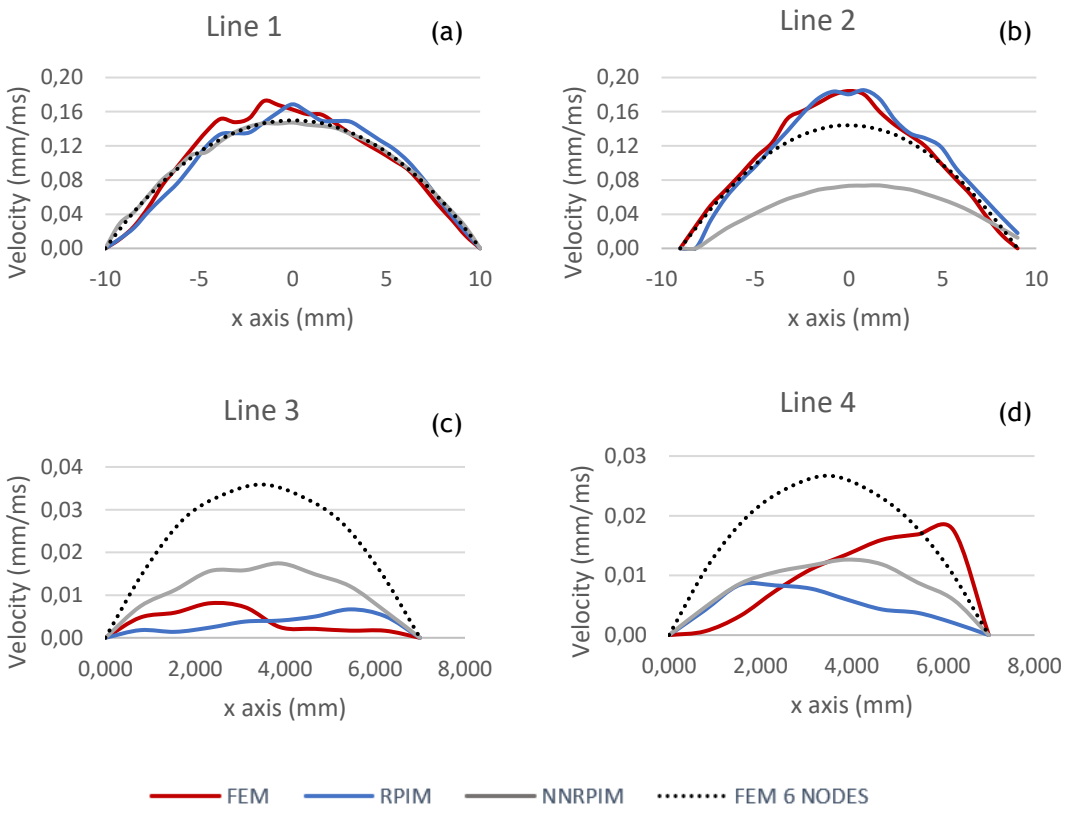

Figure A. 14 - Velocity profiles of the blood flow in: (a) section 1; (b) section 2; (c) section 3 and (d) section 4. These results were obtained from the geometrical model with 4026 nodes, using FEM, RPIM, NNRPIM and FEM 6 nodes.

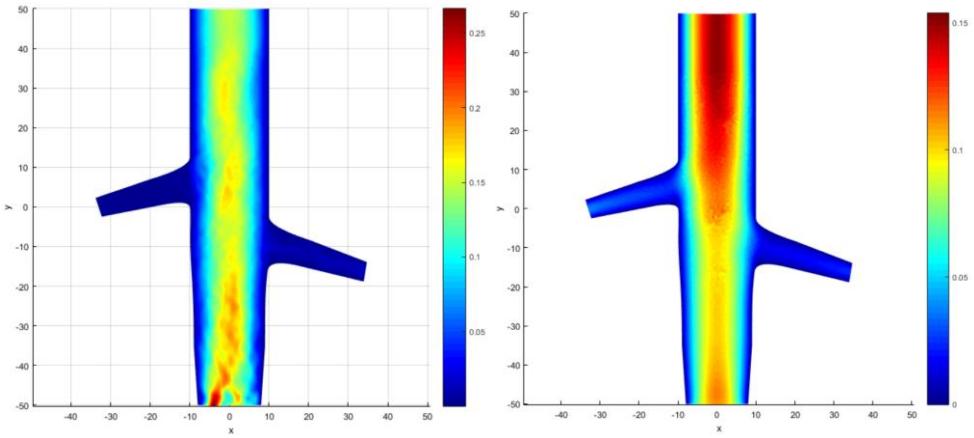

Figure A. 15 - Colour dispersion maps of the blood velocity in the branched model with 5986 nodes using: (a) RPIM (colour bar up to 0.2665 mm/ms) and (b) NNRPIM (colour bar up to 0.1537 mm/ms). In this case, the result from FEM was not viable, since it occurred an integration problem that enabled an unpractical result.

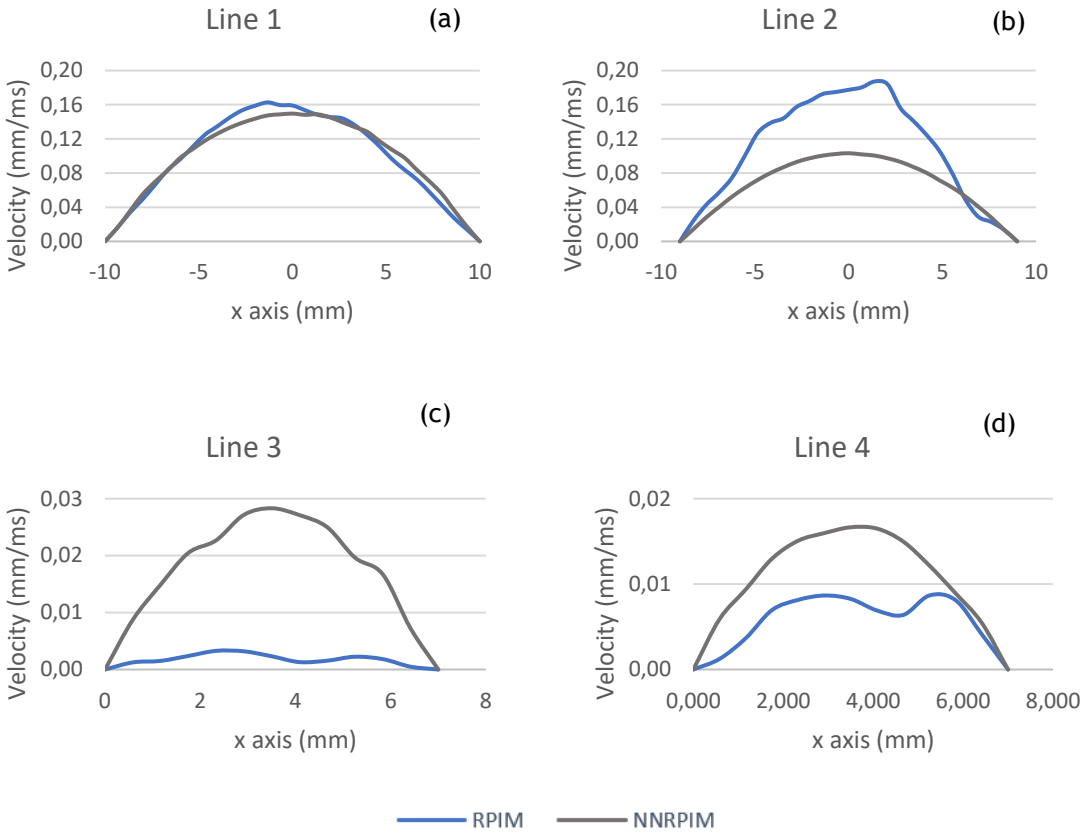

Figure A. 16 - Velocity profiles of the blood flow in: (a) section 1; (b) section 2; (c) section 3 and (d) section 4. These results were obtained from the geometrical model with 5986 nodes, using RPIM and NNRPIM.